Self-Assembling Organic–Inorganic Materials for Molecular Photovoltaic Devices

Hironobu Hayashi

Contents

General Introduction

1. Global Energy Issue

Currently the energy consumption is seriously increasing on a mass global scale due to the rapid growth of the population and of the world economic development. The total worldwide energy consumption was approximately 120×10^8 tonnes oil equivalent in 2010,[1] which corresponds to an average power of roughly 16 terawatts (TW). This number is easily expected to continue to rise gradually and show the rise of at least 10 TW by 2050 due to our mankind's activities.[2] We have been reliant on the fossil fuels to produce such an enormous amount of energy. However, of course, there is a limit of fossil fuel reserves, therefore they surely will be exhausted sooner or later. Additionally, exhaust gases such as NO_x, SO_x, and CO_2 which contribute to the air pollution and the global warming are released by the consumption of the fossil fuels, and this leads to a serious environmental problem. To break dependence on the fossil fuels, a great deal of efforts has been devoted to developing the alternative energy systems. Nuclear energy was considered as the most promising one. In fact, they provided 14% of the total power generation in the world in 2009.[3] However, they are producing the disposal of nuclear wastes which release radiation almost permanently. In addition, the nuclear accident at the Fukushima No. 1 nuclear power plant triggered by Tohoku earthquake and tsunami in 2011 leads to serious concerns on the safety of nuclear power plants, and it is no longer an option of safety and clean energy system. Therefore, there is a pressing need to develop the new and clean energy-producing systems. Wind energy, geothermal energy, biomass, methane hydrate, and solar energy are promising candidates.

2. Utilization of Solar Energy

Among the clean renewable energies the most attractive one is solar energy. Solar is a free, inexhaustible energy. Every year the sun provides the earth surface with 120,000 TW•h of radiation,[4] indicating that it supplies in about 1 hour the energy needs for 1 year. In addition, representative solar energy conversion systems (i.e., solar cells) substantially do not yield any pollutant such as NO_x, SO_x, and CO_2. In spite of such an enormous potential, however, only 0.01 TW of power was produced by solar cells in 2009, although the photovoltaic market grows at very high rates (30 – 40%).[5] The present status mainly stems from the high cost. Inorganic solar cells consisting of inorganic materials such as amorphous silicon have already been commercialized. Nevertheless, the cost of electricity from the

silicon-based solar cells is much higher than that generated by traditional energy sources such as fossil fuels and nuclear energy, which limits their widespread use.

On the other hand, organic solar cells have the advantages of potentially low production cost over inorganic solar cells. Furthermore, the merits of organic solar cells could be high flexibility, lightweight, and facile molecular design. Representative examples include dye-sensitized solar cells,[6] artificial photosynthetic solar cells,[7] and bulk heterojunction solar cells.[8] The electrical power production from sunlight in these three kinds of organic solar cells involves the following processes:[9] (i) Photons are absorbed within a photoactive layer, leading to the formation of locally confined excitons. Then, the excitons migrate to the interface of a donor–acceptor heterojunction and dissociate to electron-hole pairs (artificial photosynthetic solar cells and bulk heterojunction solar cells), or photons are absorbed by the dye adsorbed on the surface of the semiconducting electrode and the resulting dye excited state leads to rapid formation of separated electron-hole pairs at the interface of the dye-semiconducting electrode (dye-sensitized solar cells). (ii) The separated charges move toward respective electrodes, thereby yielding a photocurrent in an external circuit. To achieve high efficiency in each process and ultimately high cell performance, it is crucial to elucidate the controlling factors in the processes and optimize each process based on the fundamental information. *Especially, the interfacial geometry at semiconducting oxide/dye/electrolyte (dye-sensitized solar cell)[10] and the mixed morphology of donor-acceptor materials (artificial photosynthetic solar cell and bulk heterojunction solar cell)[11] have a direct impact on charge-transporting properties and solar cell performance*. In this context, the author decided to focus on i) the effect of molecular geometry on TiO_2 surface on electron transfer kinetics and dye-sensitized solar cell performance, and ii) the controlling the morphology of donor-acceptor composites on an electrode in a bottom-up manner for artificial synthetic solar cell.

3. Porphyrin-Sensitized Solar Cells

The detail working mechanism of dye-sensitized solar cells is as follows. The mesoporous layer deposited on a transparent conducting electrode is composed of a network of TiO_2 nanoparticles that are sintered together to establish excellent electric conduction. Dyes are self-assembled to form a

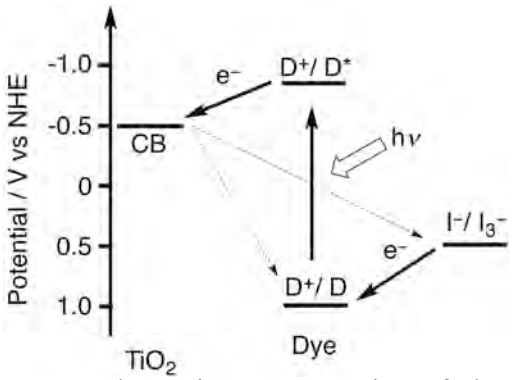

Figure 1. Schematic representation of electorn transfer process in dye-sensitized solar cells. Dashed arrows represents undesirable electron recombination processes.

monolyer on the TiO_2 nanocrystalline film. Photoexcitation of the dye results in electron injection into the conduction band of TiO_2, leaving the dye in its oxidized state. The oxidized dye is restored to its ground state by electron transfer from redox couple (i.e, I^-/I_3^-) in the electrolyte. The I_3^- ions formed by oxidation of I^- diffuse through the electrolyte to the cathode, where electron capture of I_3^- ions from the cathode regenerates I^- ions. Efficient operation of the dye-sensitized solar cells relies on the inhibition of the possible recombination pathways occurring at the TiO_2/dye/electrolyte interface (Figure 1).

To date, ruthenium(II) bipyridyl complexes have been proven to be the most efficient TiO_2 sensitizers, with most studies of device optimization focusing upon the light harvesting properties and the minimization of the possible recombination pathways.[6] However, in view of the high cost and scarcity of ruthenium, organic dyes without metal or inexpensive metal complexes are desirable for highly efficient dye-sensitized solar cells.[12] Additionally, the rather complex molecular structures with multiple binding moieties to the TiO_2 surfaces make it difficult to disclose the close relationship between the molecular structure, molecular geometry on the electrode, and the photovoltaic properties.

In this context, porphyrins are potentially promising sensitizers for highly efficient dye-sensitized solar cells due to their photostability and high light-harvesting capacities.[12h] Actually, Grätzel and Diau et al. reported the achievement of remarkably high power conversion efficiency of up to 12.3% using a push-pull porphyrin with an electron-donating diarylamino group at the *meso* position and an electron-withdrawing carboxyphenylethynyl anchoring group at the opposite *meso* position.[13] This finding corroborates that conventional ruthenium complexes could be replaced with porphyrins for highly efficient dye-sensitized solar cells. Meanwhile, for dye-sensitized solar cells with 5,10,15,20-tetrakis(4-carboxyphenyl)porphyrinatozinc(II), a wide range of power conversion efficiency and incident photon-to-current efficiency has been reported by different researchers.[14] These results imply that the cell performance of porphyrin-sensitized solar cells is susceptible to the dye adsorption conditions and dye substituents. In other words, the immersion solvent and immersion time would influence the porphyrin-TiO_2 binding geometry and electron transfer kinetics. Therefore, it is essential to elucidate the close relationship between electron transfer kinetics, porphyrin-TiO_2 binding geometries, and solar cell efficiency under various adsorption conditions using porphyrins with different substituents. Such fundamental information can be fed back to dye-sensitized solar cells to improve cell performance with reliability.

The first objective of this thesis is the systematic investigation of the effects of the porphyrin substituents and adsorption conditions on the porphyrin-TiO_2 binding

geometries, electron transfer kinetics, and solar cell performances. In this study, 5,10,15,20-tetraphenylporphyrinatozinc(II) was chosen to study because the synthetic flexibility of porphyrins offers great possibilities to modify properties such as anchoring groups, length of connecting spacer, molecule bulkiness, redox potential, excited state energy, and surface coverage.[15] A great deal of efforts has been devoted to the perturbation of the porphyrin π system and improving light-harvesting property for high cell performance.[16] However, the effects of porphyrin substituents and adsorption conditions on the photovoltaic properties of porphyrin-sensitized solar cell have not been fully understood. In Chapter 1, the author has systematically investigated the effects of porphyrin substituents and adsorption conditions (i.e. immersion solvent and immersion time) on the photovoltaic properties of porphyrin-sensitized solar cells.

Next, the author focused on the effects of electron transfer dynamics and the porphyrin-TiO_2 binding geometries on the cell performance. In dye-sensitized solar cells, ultrafast electron injection and slow charge recombination at the sensitizer-semiconductor interface have been believed. Meanwhile, the sensitizer-semiconductor binding geometry and separation distance between the sensitizer and semiconductor surface would influence the electron transfer rates significantly in light of Marcus theory for electron transfer.[17] In Chapter 2 and 3, time resolved absorption spectroscopy has been used to study the photoinduced electron injection and charge recombination dynamics in porphyrin-sensitized TiO_2 electrodes. In Chapter 3, sum frequency generation vibrational spectroscopy has also been applied to porphyrin-sensitized TiO_2 electrodes to determine the porphyrin geometry on TiO_2 as well as the environmental information on the TiO_2 surface that would not be addressed by the other conventional spectroscopic methods. The correlation between the electron transfer dynamics, porphyrin-TiO_2 binding geometry, and cell performance has been evaluated systematically.

3. Efficient Charge-Transporting Pathway

High performance bulk heterojunction solar cells possess an interpenetrating network of donor and acceptor molecules in the blend film.[8,11] Nanoscopic phase-separated morphology in the film leads to an increase in the interface area, resulting in ultrafast charge separation and subsequent efficient transport of the created charges to the electrodes through the nanohighways suppressing undesirable charge recombination. To create a desirable phase-separated network in donor-acceptor blend films, various strategies have been proposed inclusive of spin-coating solvent annealing[18] and thermal annealing.[19] However, it is still a challenge to construct such a desirable nanostructure on an electrode with the

optimization of cell fabrication process.

On the other hand, in natural photosynthesis, excitation of a special pair of chlorophylls is followed by multistep electron transfer cascade along supramolecularly assembled photofunctional chromophores in protein (Figure 2).[20] For instance, the photosynthetic core in purple photosynthetic bacteria involves light-harvesting in antenna complexes and multistep electron transfer in reaction centers, both of which are embedded in a lipid bilayer membrane. Solar energy is collected by bacteriochlorophylls (Bchl) and carotenoids (Car) in the antenna complexes. Then, the captured energy is transferred to the special pair of Bchl molecules ($(Bchl)_2$) in the reaction center, generating its singlet excited state ($^1(Bchl)_2$*) which lies about 1.4 eV above the ground state. Within ~3 ps, an electron transfer occurs from $^1(Bchl)_2$* to the bacteriopheophytin (Bph) molecule located R_{ee} ~ 9Å (edge-to-edege distance) via a two-step sequential mechanism or a one-step superexchange mechanism. The energy of $(Bchl)_2^{\bullet+}Bph^{\bullet-}$ (~1.2 eV) is lowered by ~0.2 eV, which matches the reorganization energy (λ) of electron transfer to optimize the forward electron transfer process, but the charge recombination process lies deep within the Marcus inverted region, which suppresses the charge recombination process. In a subsequent charge-shift step, an electron is transferred in ~200 ps from $Bph^{\bullet-}$ to the primary quinone (Q_A) with a R_{ee} value of ~ 9Å. This reaction yields a charge-separated state, $(Bchl)_2^{\bullet+}Q_A^{\bullet-}$, which lies only ~0.6 eV above the ground state. This implies that as much as 0.8 eV is lost to obtain the charge-separated state. In a final isoenergetic step, an electron transfer takes place from $Q_A^{\bullet-}$ to the secondary quinone (Q_B), with a time constant of ~ 100 μs. The resulting final charge-separated state with a lifetime of ~1 s across the membrane eventually leads to the production of chemical

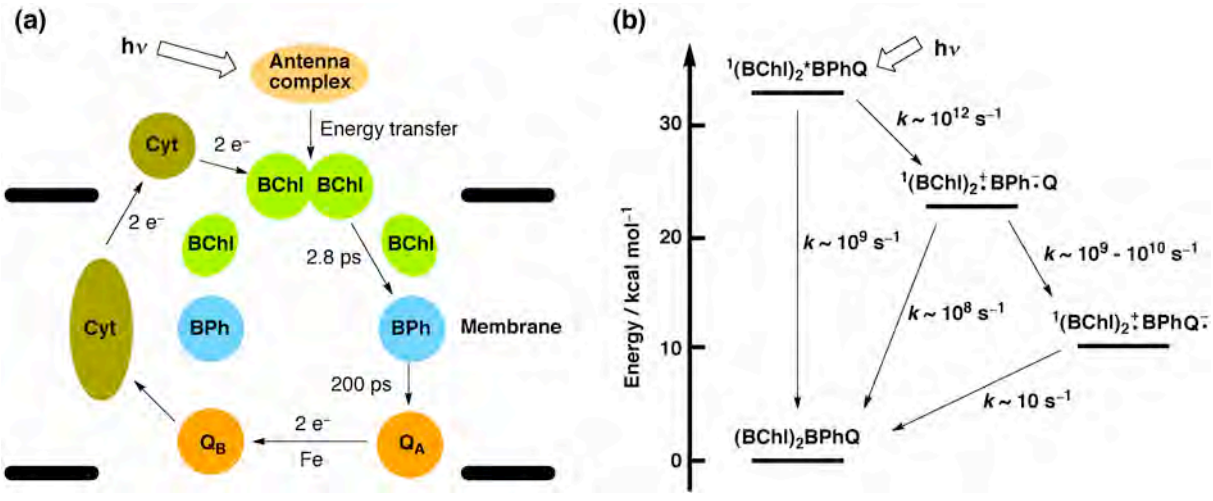

Figure 2. (a) Schematic depiction of energy transfer and multistep electron transfer in purple photosynthetic bacteria. (b) Energy diagram of natural photosynthesis.

energy. Note that the quantum efficiency for the production of $(Bchl)_2^{\bullet+}Q_B^{\bullet-}$ is ~100%. Namely, *the finely-balanced assemblies of photofunctional chromophores* within proteins allow natural photosynthesis to achieve (i) efficient energy transfer in the chromophore complexes and initial charge separation and (ii) subsequent efficient vectorial electron transport, minimizing undesirable charge recombination. Thus, natural photosynthesis is an impressive example of how to achieve efficient solar energy conversion in an artificial manner.

To mimic the finely balanced and highly efficient photosynthetic system, various attempts have been employed to fabricate donor-acceptor molecules in artificial photosynthetic systems. The methodology involves self-assembled monolayer,[21] Langmuir-Blodgett,[22] and lipid bilayer membrane.[23] However, these systems are still inferior to natural photosynthetic systems in terms of solar energy conversion. Moreover, the covalent linkage of donor-acceptor molecules is time-consuming and tedious. Therefore, there is a need to develop the facile artificial system that can reveal efficient light-harvesting, charge separation, and charge collection efficiencies, exhibiting macroscopic efficient photocurrent generation. On the other hand, ultilization of bottom-up self-assembly provides an easy means for organizing large numbers of molecules into well-defined supramolecular structures that can bridge length scales from nanometers to macroscopic dimensions.[24-26]

The second objective of this thesis is the facile construction of self-assembled donor-acceptor phase-separated architectures that exhibit efficient charge-transporting properties on electrodes. From this viewpoint, the author has focused on bottom-up self-assembly of molecular building blocks that have unique shapes, sizes, and intermolecular interactions, allowing us to construct efficient solar energy conversion system on the electrode surface. In previous studies, composite molecular nanoclusters of porphyrins and C_{60} have been successfully prepared in a mixture of polar and nonpolar solvents due to π-π and lyophobic interactions and then assembled on a SnO_2 electrode using an electrophoretic deposition technique.[27] In particular, porphyrin with specific substituents and C_{60} form the alternating donor-acceptor layer structure in the film, revealing efficient charge transport and photocurrent generation in the porphyrin–C_{60} composite film. However, relationship between the molecular structures, the film structures, and the photoelectrochemical properties at molecular level has not been fully understood due to the amorphous film with disordered structure. In Chapter 4, solid-state nuclear magnetic resonance has been applied to amorphous active layers consinsting of porphyrin-fullerene self-assembled composites to determine the molecular level complexation of porphyrin-fullerene composite, which has never been addressed by conventional

spectroscopic analysis.[28]

Utilization of one-dimensional (1-D) nanostructured semiconducting oxide that is vertically aligned with respect to a transparent conducting electrode contributes to increase the interfacial area between 1-D semiconducting oxide and donor-acceptor composite as well as to create an electron-transporting pathway through the 1-D semiconducting oxide.[29] In Chapter 5, the author has fabricated 1-D ZnO nanorod electrodes modified with porphyin-fullerene composites and examined the photoelectrochemical properties and film morphology. To prevent undesirable charge recombination at the electrode interface between ZnO nanorod electrode and porphyrin-fullerene composites, fullerene monolayer was incorporated. Furthermore, the effects of the ZnO electrode structures (i.e. nanorod vs. nanoparticle) on the film morphology and photoelectrochemical properties have been accessed.

Reduced graphene oxide is a two-dimensional (2-D) scaffold to anchoring inorganic/organic materials. Additionally it has the ability to store and shuttle electrons which can be utilized to develop semiconductor–graphene composites as 2-D nanostructured assembies for solar energy conversion system.[30] In Chapter 6, the author has developed a facile approach to construct a multistep electron transfer system exhibiting efficient photocurrent generation with porphyrin, ZnO nanoparticle, and reduced graphene oxide as donor-acceptor components. The effect of the reduced graphene oxide on the photocurrent generation has been examined in terms of film morphology and photoelectrochemical properties.

Donor-acceptor linked dyads could be used in the geometry to construct well-defined integrated two 1-D arrays of dissimilar rectifying elements.[31] If either of donor or acceptor moiety in the dyad can form 1-D discotic columnar structure, the counterpart will have more chance to be arranged closely and regularly, forming a segregated donor-acceptor columnar structure for the transport of holes and electrons. In Chapter 7, fullerene has been tethered to liquid crystalline phthalocyanine via a short, semiflexible bridge to form the segregated donor-acceptor columnar structure. The charge-transporting properties of the liquid crystalline film obtained from the phthalocyanine-fullerene linked dyad have been correlated with the segregated donor-acceptor columnar structure in terms of inter- and intra-column charge transport.

References

(1) *BP Statistical Review of World Energy June 2011*.

(2) Service, R. F. *Science* **2005**, *309*, 548.

(3) Agency for Natural Resources and Energy (http://www.iaea.org/About/Policy/GC/GC54/Agenda/index.html)

(4) Sun, S.–S.; Sariciftci, N. S. *Organic Photovoltaics: Mechanisms, Materials, and Devices*, CRC (Taylor & Francis group), **2005**.

(5) (a) Maycock, P. D. 2010 PV News, V.29, N5. (b) Razykov, T. M.; Ferekides, C. S.; Morel, D.; Stefanakos, E.; Ullal, H. S.; Upadhyaya, H. M. *Solar Energy* **2011**, *85*, 1580.

(6) (a) O'Regan, B.; Grätzel, M. *Nature* **1991**, *353*, 737. (b) Nazeeruddin, M. K.; Kay, A.; Rodicio, I.; Humphry-Baker, R.; Müller, E.; Liska, P.; Vlachopoulos, N.; Grätzel, M. *J. Am. Chem. Soc.* **1993**, *115*, 6382. (c) Grätzel, M. *Acc. Chem. Res.* **2009**, *42*, 1788.

(7) Imahori, H. *J. Mater. Chem.* **2007**, *17*, 31.

(8) (a) Tang, C. W. *Appl. Phys. Lett.* **1986**, *48*, 183. (b) Yu, G.; Gao, J.; Hummelen, J. C.; Wudl, F.; Heeger, A. J. *Science* **1995**, *270*, 1789. (c) Mayer, A. C.; Scully, S. R.; Hardin, B. E.; Rowell, M. W.; McGehee, M. D. *Mater. Today* **2007**, *10*, 28. (d) Heremans, P.; Cheyns, D.; Rand, B. P. *Acc. Chem. Res.* **2009**, *42*, 1740. (e) Liang, Y.; Xu, Z.; Xia, J.; Tsai, S.-T.; Wu, Y.; Li, Gang.; Ray, C.; Yu, L. *Adv. Mater.* **2010**, *22*, E135.

(9) (a) Hagfeldt, A.; Boschloo, G.; Sun, L.; Kloo, L.; Pettersson, H. *Chem. Rev.* **2010**, *110*, 6595. (b) Thompson, B. C.; Fréchet, M. J. *Angew. Chem., Int. Ed.* **2008**, *47*, 58.

(10) (a) Rühle, S.; Greenshtein, M.; Chen, S.–G.; Merson, A.; Sukenik, C. S.; Cahen, D.; Zaban, A. *J. Phys. Chem. B* **2005**, *109*, 18907. (b) Haque, S. A.; Handa, S.; Peter, K.; Palomares, E.; Thelakkat, M.; Durrant, J. R. *Angew. Chem., Int. Ed.* **2005**, *44*, 5740. (c) Angelis, F. D.; Fantacci, S.; Selloni, A.; Grätzel, M.; Nazeeruddin, M. K. *Nano Lett.* **2007**, *7*, 3189. (d) Kusama, H.; Orita, H.; Sugihara, H. *Langmuir* **2008**, *24*, 4411. (e) Ardo, S.; Meyer, G. J. *Chem. Soc. Rev.* **2009**, *38*, 115. (f) Koops, S. E.; O'Regan, B. C.; Barnes, P. R. F.; Durrant, J. R. *J. Am. Chem. Soc.* **2009**, *131*, 4808. (g) O'Rourke, C.; Bowler, D. R. *J. Phys. Chem. C* **2010**, *114*, 20240.

(11) (a) Günes, S.; Neugebauer, H.; Sariciftci, N. S. *Chem. Rev.* **2007**, *107*, 1324. (b) Thompson, B. C.; Fréchet, J. M. *Angew. Chem., Int. Ed.* **2008**, *47*, 58. (c) Hoppe, H.; Sariciftci, N. S. *J. Mater. Chem.* **2006**, *16*, 45. (d) Yang, X.; Loos, J. *Macromolecules* **2007**, *40*, 1353. (e) Tada, A.; Geng, Y.; Wei, Q.; Hashimoto, K.; Tajima, K. *Nat. Mater.* **2011**, *10*, 450.

(12) (a) Hara, K.; Sayama, K.; Ohga, Y.; Shinpo, A.; Suga, S.; Arakawa, H. *Chem. Commun.* **2001**, 569. (b) Horiuchi, T.; Miura, H.; Sumioka, K.; Uchida, S. *J. Am. Chem. Soc.* **2004**,

126, 12218. (c) Nazeeruddin, M. K.; Angelis, F. D.; Fantacci, S.; Selloni, A.; Viscardi, G.; Liska, P.; Ito, S.; Takeru, B.; Grätzel, M. *J. Am. Chem. Soc.* **2005**, *127*, 16835. (d) Liu, W.–H.; Wu, I.–C.; Lai, C.–H.; Lai, C.–H.; Chou, P.–T.; Li, Y.–T.; Chen, C.–L.; Hsu, Y.–Y.; Chi, Y. *Chem. Commun.* **2008**, 5152. (e) Gao, F.; Wang, Y.; Shi, D.; Zhang, J.; Wang, M.; Jing, X.; Humphry-Baker, R.; Wang, P.; Zakeeruddin, S. M.; Grätzel, M. *J. Am. Chem. Soc.* **2008**, *130*, 10720. (f) Chen, C.–Y.; Wang, M.; Li, J.–Y.; Pootrakulchote, N.; Alibabaei, L.; Ngoc-le, C.; Decoppet, J.–D.; Tsai, J.–H.; Grätzel, C.; Wu, C.–G.; Zakeeruddin, S. M.; Grätzel, M. *ACS Nano* **2009**, *3*, 3103. (g) Mishra, A.; Fischer, M. K. R.; Bäuerle, P. *Angew. Chem., Int. Ed.* **2009**, *48*, 2474. (h) Imahori, H.; Umeyama, T.; Ito, S. *Acc. Chem. Res.* **2009**, *42*, 1809.

(13) (a) Bessho, T.; Zakeeruddin, S. M.; Yeh, C.–Y.; Diau, E. W.–G.; Grätzel, M. *Angew. Chem., Int. Ed.* **2008**, *47*, 58. (b) Yella, A.; Lee, H.–W.; Tsao, H. N.; Yi, C.; Chandiran A. K.; Nazeeruddin, M.; Diau, E. W.–G.; Yeh, C.–Y.; Zakeeruddin, S. M.; Grätzel, M. *Science* **2011**, *334*, 629.

(14) (a) Boschloo, G. K.; Goossens, A. *J. Phys. Chem.* **1996**, *100*, 19489. (b) Cherian, S.; Wamser, C. C. *J. Phys. Chem. B* **2000**, *104*, 3624. (c) Ma, T. L.; Inoue, K.; Noma, H.; yao, K.; Abe, E. *J. Photochem. Photobiol. A* **2002**, *151*, 207. (d) Jasieniak, J.; Johnston, M.; Waclawik, E. R. *J. Phys. Chem. B* **2004**, *108*, 12962. (e) Rochford, J.; Chu, D.; Hagfeldt, A.; Galoppini, E. *J. Am. Chem. Soc.* **2007**, *129*, 4655.

(15) (a) Watson, D. F.; Marton, A.; Stux, A. M.; Meyer, G. J. *J. Phys. Chem. B* **2003**, *107*, 10971. (b) Huijser, A.; Marek, P. L.; Savenije, T. J.; Siebbeles, L. D. A.; Scherer, T.; Hauschild, R.; Szmytkowski, J.; Kalt, H.; Hahn, H.; Balaban, T. S. *J. Phy. Chem. C* **2007**, *111*, 11726. (c) Cíd, J.–J.; Yum, J.–H.; Jang, S.–R.; Nazeeruddin, M. K.; Martínez-Ferrero, E.; Palomares, E. J.; Ko, J.; Grätzel, M.; Torres, T. *Angew. Chem., Int. Ed.* **2007**, *46*, 8358. (d) Eu, S.; Hayashi, S.; Umeyama, T.; Oguro, A.; Kawasaki, M.; Kadota, N.; Matano, Y.; Imahori, H. *J. Phy. Chem. C* **2007**, *111*, 3528. (e) Eu, S.; Katoh, T.; Umeyama, T.; Matano, Y.; Imahori, H. *Dalton Trans.* **2008**, 5476.

(16) (a) Wang, Q.; Campbell, W. M.; Bomfantani, E. E.; Jolley, K. W.; Officer, D. L.; Walsh, P. L.; Gordon, K.; Humphery-Baker, R.; Nazeeruddin, M. K.; Grätzel, M. *J. Phys. Chem. B* **2005**, *109*, 15397. (b) Tanaka, M.; Hayashi, S.; Eu, S.; Umeyama, T.; Matano, Y.; Imahori, H. *Chem. Commun.* **2007**, 2069. (c) Campbell, W. M.; Jolley, K. W.; Wagner, P.; Wagner, K.; Walsh, P. J.; Gordon, K. C.; Schmidt-Mende, L.; Nazeeruddin, M. K.; Wang, Q.; Grätzel, M.; Officer, D. L. *J. Phys. Chem. C* **2007**, *111*, 11760. (d) Eu, S.; Hayashi, S.; Umeyama, T.; Matano, Y.; Araki, Y. Imahori, H. *J. Phys. Chem. C* **2008**, *112*, 4396. (e) Hayashi, S.; Matsubara, Y.; Eu, S.; Hayashi, H.; Umeyama, T.; Matano,

Y.; Imahori, H. *Chem. Lett.* **2008**, *37*, 846. (f) Hayashi, S.; Tanaka, M.; Hayashi, H.; Eu, S.; Umeyama, T.; MAtano, Y.; Araki, Y.; Imahori, H. *J. Phys. Chem. C* **2008**, *112*, 15576. (g) Lee, C.–W.; Lu, H.–P.; Lan, C.–M.; Huang, Y.–L.; Liang, Y.–R.; Yen, W.–N.; Liu, Y.–C.; Lin, Y.–S.; Diau, E. W.–G.; Yeh, C.–Y. *Chem.–Eur. J.* **2009**, *15*, 1403.

(17) (a) Marcus, R. A. *J. Chem. Phys.* **1956**, *24*, 966. (b) Marcus, R. A.; Sutin, N. *Biochim. Biophys. Acta* **1985**, *811*, 265.

(18) (a) Shaheen, S. E.; Brabec, C. J.; Sariciftci, N. S.; Padinger, F.; Fromherz, T.; Hummelen, J. C. *Appl. Phys. Lett.* **2001**, *78*, 841. (b) Wienk, M. M.; Kroon, J. M.; Verhees, W. J. H.; Knol, J.; Hummelen, J. C.; van Hal, P. A.; Janssen, R. A. J. *Angew. Chem., Int. Ed.* **2003**, *42*, 3371. (c) Rispens, M. T.; Meetsma, A.; Rittberger, R.; Brabec, C. J.; Sariciftci, N. S.; Hummelen J. C. *Chem. Commun.* **2003**, 2116. (d) Martens, T.; D'Haen, J.; Munters, T.; Beelen, Z.; Goris, L.; Manca, J.; D'Olieslaeger, M.; Vanderzande, D.; Schepper, L. D.; Andriessen, R. *Synth. Met.* **2003**, *138*, 243. (e) Hoppe, H.; Niggemann, M.; Winder, C.; Kraut, J.; Hiesgen, R.; Hinsch, A.; Meissner, D.; Sariciftci, N. S. *Adv. Mater.* **2004**, *14*, 1005. (f) Hoppe, H.; Glatzel, T.; Niggemann, M.; Schwinger, W.; Schaeffler, F.; Hinsch, A.; Lux-Steiner, M. C.; Sariciftci, N. S. *Thin Solid Films* **2006**, *511-512*, 587.

(19) (a) Padinger, F.; Rittberger, R. S.; Sariciftci, N. S. *Adv. Mater.* **2003**, *13*, 85. (b) Kim, Y.; Choulis, S. A.; Nelson, J.; Bradley, D. D. C.; Cook, S.; Durrant, J. R. *Appl. Phys. Lett.* **2005**, *86*, 063502. (c) Yang, X.; Loos, J.; Veenstra, S. C.; Verhees, W. J. H.; Wienk, M. M.; Kroon, J. M.; Michels, M. A. J.; Janssen, R. A. J. *Nano Lett.* **2005**, *5*, 579. (d) Erb, T.; Zhokhavets, U.; Gobsch, G.; Raleva, S.; Stühn, B.; Schilinsky, P.; Waldauf, C.; Brabec, C. J. *Adv. Funct. Mater.* **2005**, *15*, 1193. (e) Reyes-Reyes, M.; Kim, K.; Carroll, D. L. *Appl. Phys. Lett.* **2005**, *87*, 083506. (f) Ma, W.; Yang, C.; Gong, X.; Lee, K.; Heeger, A. J. *Adv. Funct. Mater.* **2005**, *15*, 1617. (g) Mihailetchi, V. D.; Xie, H.; de Boer, B.; Koster, L. J. A.; Blom, P. W. M. *Adv. Funct. Mater.* **2006**, *16*, 699. (h) Kim, J. Y.; Kim, S. H.; Lee, H.–H.; Lee, K.; Ma, W.; Gong, X.; Heeger, A. J. *Adv. Mater.* **2006**, *18*, 572. (i) Nguyen, L. H.; Hoppe, H.; Erb, T.; Günes, S.; Gobsch, G.; Sariciftci, N. S. *Adv. Funct. Mater.* **2007**, *17*, 1071. (j) Kim, K.; Liu, J.; Namboothiry, M. A. G.; Carroll, D. L. *Appl. Phys. Lett.* **2007**, *90*, 163511.

(20) (a) Fleming. G. R.; van Grondelle, R. *Physics Today* **1994**, *47*, 48. (b) McDermott, G.; Prince, S. M.; Freer, A. A.; Hawthornthwaite-Lawless, A. M.; Papiz, M. Z.; Cogdell, R. J.; Isaacs, N. W. *Nature* **1995**, *374*, 517. (c) *The Photosynthetic Reaction Center*; Deisenhofer, J., Norros, J. R., Ed.; Academic Press: San Diego, 1993. (d) *Anoxygenic*

Photosynthetic Bacteria; Blankenship, R. E., Madigan, M. T., Bauer, C. E., Ed.; Kluwer Academic Publishing: Dordrecht, 1995. (e) *In Molecular Mechanism of Photosynthesis*; Blankenship, R. E., Ed.; Willey-Blackwell: Dordrecht, 2002.

(21) (a) Imahori, H.; Norieda, H.; Yamada, Y.; Nishimura, Y.; Yamazaki, I.; Sakata, Y.; Fukuzumi, S. *J. Am. Chem. Soc.* **2003**, *123*, 100. (b) Yamada, H.; Imahori, H.; Nishimura, Y.; Yamazaki, I.; Sakata, Y.; Fukuzumi, S. *J. Am. Chem. Soc.* **2003**, *125*, 9129. (c) Yasutomi, S.; Morita, T.; Imanishi, Y.; Kimura, S. *Science* **2004**, *304*, 1944. (d) Cho, Y.-J.; Ahn, T. K.; Song, H.; Kim, K. S.; Lee, C. Y.; Seo, W. S.; Lee, K.; Kim, S. K.; Kim, D.; Park, J. T. *J. Am. Chem. Soc.* **2005**, *127*, 2380. (e) Ludlow, M. K.; Soudackov, A. V.; Hammes-Schiffer, S. *J. Am. Chem. Soc.* **2010**, *132*, 1234.

(22) (a) Tkachenko, N. V.; Vuorimaa, E.; Kesti, T.; Alekseev, A. S.; Tauber, A. Y.; Hynninen, P. H.; Lemmetyinen, H. *J. Phys. Chem. B* **2000**, *104*, 6371. (b) Tkachenko, N. V.; Vehmanen, V.; Nikkanen, J.–P.; Yamada, H.; Imahori, H.; Fukuzumi, S.; Lemmetyinen, H. *Chem. Phys. Lett.* **2002**, *366*, 245. (c) Vuorinen, T.; Kaunisto, K.; Tkachenko, N. V.; Efimov, A.; Lemmetyinen, H. *Langmuir* **2005**, *21*, 5383. (d) Kotiaho, A.; Lahtinen, R. M.; Tkachenko, N. V.; Efimov, A.; Kira, A.; Imahori, H.; Lemmetyinen, H. *Langmuir* **2007**, *23*, 13117.

(23) (a) Seta, P.; Bienvenue, E.; Moore, A. L.; Mathis, P.; Bensasson R. V.; Liddell, P.; Pessiki, P. J.; Joy, A.; Moore, T. A.; Gust, D. *Nature* **1985**, *316*, 653. (b) Steinberg-Yfrach, G.; Liddel, P. A.; Huang, S.–C.; Moore, A. L.; Gust, D.; Moore, T. A. *Nature* **1997**, *385*, 239. (c) Steinberg-Yfrach, G.; Rigaud, J.–L.; Durantini, E. N.; Moore, A. L.; Gust, D.; Moore, T. A. *Nature* **1998**, *392*, 479. (d) Drain, C. M. *Proc. Natl. Acad. Sci. USA* **2002**, *99*, 5178. (e) Bhosale, S.; Sisson, A. L.; Talukdar, P.; Fürstenberg, A.; Banerji, N.; Vauthey, E.; Bollot, G.; Mareda, J.; Röger, C.; Würthner, F.; Sakai, N.; Matile, S. *Science* **2008**, *313*, 84.

(24) (a) van der Boom, T.; Hayes, R. T.; Zhao, Y.; Bushard, P. J.; Weiss, E. A.; Wasielewski, M. R. *J. Am. Chem. Soc.* **2002**, *124*, 9582. (b) Beckers, E. H. A.; Meskers, S. C. J.; Schenning, A. P. H. J.; Chen, Z.; Würthner, F.; Marsai, P.; Beljonne, D.; Cornil, J.; Janssen, R. A. J. *J. Am. Chem. Soc.* **2006**, *128*, 649. (c) Zhou, Z.; Chen, X.; Holdcroft, S. *J. Am. Chem. Soc.* **2008**, *130*, 11711. (d) Roncali, J. *Acc. Chem. Res.* **2009**, *42*, 1719.

(25) (a) Schenning, A. P. H. J.; Herrikhuyzen, J.; Jonkheijm, P.; Chen, Z.; Würthner, F.; Meijer, E. W. *J. Am. Chem. Soc.* **2002**, *124*, 10252. (b) Segura, M.; Sánchez, L.; de Mendoza, J.; Martín, N.; Guldi, D. M. *J. Am. Chem. Soc.* **2003**, *125*, 15093. (c) Jonkheijm, P.; Stutzmann, N.; Chen, Z.; de Leeuw, D. M.; Meijer, E. W.; Schenning, A. P. H. J.; Würthner, F. *J. Am. Chem. Soc.* **2006**, *128*, 9535. (d) Wasielewski, M. R. *Acc.*

Chem. Res. **2009**, *42*, 1910.

(26) (a) Morisue, M.; Yamatsu, S.; Haruta, N.; Kobuke, Y. *Chem.–Eur. J.* **2005**, *11*, 5563. (b) Kobuke, Y. *Eur. J. Inorg. Chem.* **2006**, 2333. (c) Rodríguez-Morgade, M. S.; Torres, T.; Atienza-Castellanos, C.; Guldi, D. M. *J. Am. Chem. Soc.* **2006**, *128*, 15145. (d) Kuramochi, Y.; Sandanayaka, A. S. D.; Satake, A.; Araki, Y.; Ogawa, K.; Ito, O.; Kobuke, Y. *Chem.–Eur. J.* **2009**, *15*, 2317.

(27) (a) Kang, S.; Umeyama, T.; Ueda, M.; Matano, Y.; Hotta, H.; Yoshida, K.; Isoda, S.; Shiro, M.; Imahori, H. *Adv. Mater.* **2006**, *18*, 2549. (b) Imahori, H.; Ueda, M.; Kang, S.; Hayashi, H.; Hayashi, S.; Kaji, H.; Seki, S.; Saeki, A.; Tagawa, S.; Umeyama, T.; Matano, Y.; Yoshida, K.; Isoda, S.; Shiro, M.; Tkachenko, N. V.; Lemmetyinen, H. *Chem.–Eur. J.* **2007**, *13*, 10182.

(28) (a) Schmidt-Rohr, K.; Hu, W.; Zumbulyadis, N. *Science* **1998**, *280*, 9029. (b) Kaji, H. Schmidt-Rohr, K. *Macromolecules* **2002**, *35*, 7993. (c) Petkova, A. T.; Ishii, Y.; Balbach, J. J.; Antzutkin, O. N.; Leapman, R. D.; Delaglio, F.; Tycko, R. *Proc. Natl. Acad. Sci. U.S.A.* **2002**, *99*, 16742. (d) Sakellariou, D.; Brown, S. P.; Lesage, A.; Hediger, S.; Bardet, M.; Meriles, C. A.; Pines, A.; Emsley, L. *J. Am. Chem. Soc.* **2003**, *125*, 4376. (e) Kaji, H.; Kusaka, Y.; Onoyama, G.; Horii, F. *J. Am. Chem. Soc.* **2006**, *128*, 4292.

(29) Galoppini, E.; Rochford, J.; Chen, H.; Saraf, G.; Lu, Y.; Hagfeldt, A.; Boschloo, G. *J. Phys. Chem. B* **2006**, *110*, 16159.

(30) (a) Lightcap, I. V.; Kosel, T. H.; Kamat, P. V. *Nano Lett.* **2010**, *10*, 577. (b) Ng, Y. H.; Lightcap, I. V.; Goodwin, K.; Matsumura, M.; Kamat, P. V. *J. Phys. Chem. Lett.* **2010**, *1*, 2222. (c) Wojcik, A.; Kamat, P. V. *ACS Nano* **2010**, *4*, 6697. (d) Kamat, P. V. *J. Phys. Chem. Lett.* **2011**, *2*, 242.

(31) (a) Percec, V.; Gloddle, M.; Bera, T. K.; Miura, Y.; Shiyanovskaya, I.; Singer, K. D.; Balagurusamy, V. S. K.; Heiney, P. A.; Schnell, I.; Rapp, A.; Spiess, H.–W.; Hudson, S. D.; Duan, H. *Nature* **2002**, *419*, 384. (b) Samori, P.; yin, X.; Tchebotareva, N.; Wang, Z.; Pakula, T.; Jäckel, F.; Watson, M. D.; Venturini, A.; Müllen, K.; Rabe, J. P. *J. Am. Chem. Soc.* **2004**, *126*, 3567. (c) Pisula, W.; Kastler, M.; Wasserfallen, D.; Robertson, J. W. F.; Nolde, F.; Kohl, C.; Müllen, K. *Angew. Chem., Int. Ed.* **2006**, *45*, 819. (d) Bullock, J. E.; Carmieli, R.; Mickley, S. M.; Vura-Weis, J.; Wasielewski, M. R. *J. Am. Chem. Soc.* **2009**, *131*, 11919. (e) Charvet, R.; Acharya, S.; Hill, J. P.; Akada, M.; Liao, M.; Seki, S.; Honsho, Y.; Saeki, A.; Ariga, K. *J. Am. Chem. Soc.* **2009**, *131*, 18030. (f) Hizume, Y.; Tashiro, K.; Charvet, R.; Yamamoto, Y.; Saeki, A.; Seki, S.; Aida, T. *J. Am. Chem. Soc.* **2010**, *132*, 6628.

Chapter 1

Effects of Porphyrin Substituents and Adsorption Conditions on Photovoltaic Properties of Poprhyrin-Sensitized Solar Cells

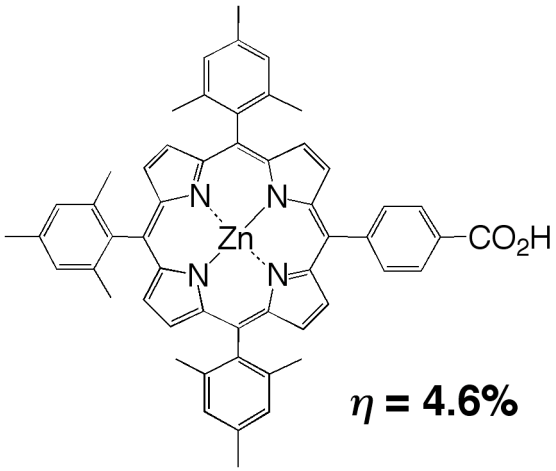

Abstract: A series of *meso*-tetraphenylzincporphyrins have been prepared to examine the effects of the porphyrin substituents and adsorption conditions on photovoltaic properties of the porphyrin-sensitized TiO_2 cells. The cell performance strongly depended on the linking bridge between the porphyrin core and the TiO_2 surface, the bulkiness around the porphyrin core, and the immersion solvents and times for the porphyrin adsorption. In particular, the high cell performance of the porphyrin-sensitized TiO_2 cells was achieved when protic solvent (i.e., methanol) and short immersion time (0.5–1 h) were used for the conditions of the dye adsorption on TiO_2, which is in sharp contrast with Ru dye-sensitized TiO_2 cells. The highest cell performance was obtained using 5-(4-carboxyphenyl)-10,15,20-tris(2,4,6-trimethylphenyl)porphyrinatozinc(II) as a sensitizer and methanol as an immersion solvent with an immersion time of 1 h: a maximal incident photon-to-current efficiency of 76 %, a short circuit photocurrent density of 9.4 mA cm^{-2}, an open-circuit voltage of 0.76 V, a fill factor of 0.64, and a power conversion efficiency of 4.6% under standard AM 1.5 sunlight. These results will provide basic and valuable information on the development of dye-sensitized solar cells exhibiting a high performance.

Introduction

Photoinduced electron transfer (ET) processes are of vital importance in versatile biological and chemical systems.[1] For instance, a cascade of photoinduced ET along a well-arranged donor-acceptor array in the photosynthetic reaction center is essential for the conversion of solar energy into chemical energy.[2] A variety of synthetic donor-acceptor systems have been prepared for better understanding of the controlling factors in ET processes.[3-5] In this context, extensive efforts have been devoted to develop interfacial photoinduced ET systems for photochemical and photovoltaic energy conversion,[6-8] including dye-sensitized nanocrystalline metal oxides[9,10] and bulk heterojunction blend films.[11-14] Specifically, Grätzel et al. developed solar cells based on the sensitization of highly porous TiO_2 by molecular dyes with power conversion efficiencies (η) of 7-11%, making practical applications feasible.[9]

To date, ruthenium(II) bipyridyl complexes have proven to be the most efficient TiO_2 sensitizers.[9,10] Nevertheless, the rather complex molecular structures with multiple binding moieties to the TiO_2 surfaces make it difficult to disclose the close relationship between the molecular structure and photovoltaic function. Attempts to employ different kinds of dyes have achieved significant success, but the cell performance is still lower or comparable to that of ruthenium dye-sensitized TiO_2 cells.[15-23] Although the substituent effects of molecular dyes relating to bridge influences, electronic coupling, and aggregation on the photochemical and photovoltaic properties have been examined,[23] relationship between the molecular structure and photovoltaic properties has remained elusive.

For photovoltaic cells with *meso*-tetraphenylporphyrin-sensitized TiO_2 electrodes, different incident photon-to-current efficiency (IPCE) and η values have been reported depending on the substituents and adsorption conditions.[17-22] Durrant et al. reported that, despite the differences in redox potential and photophysics between carboxylated porphyrin sensitizers such as **ZnTCPP** and its free-base **H_2TCPP** and the ruthenium polypyridyl **N3** dye (Figure 1), the efficiency of electron injection into a conduction band (CB) of TiO_2 and the kinetics of electron injection and charge recombination are virtually similar for all these sensitizers.[24] Furthermore, the charge recombination rate between electrons in the CB and oxidized porphyrins is in the range of several milliseconds which are sufficiently slow to permit the regeneration of the porphyrin ground state by the iodide in the electrolyte.[24] In spite of these observations, porphyrins are known to be inefficient sensitizers compared with ruthenium polypyridyl dyes. As such, the effects of porphyrin substituents and adsorption conditions on the photovoltaic properties of porphyrin-sensitized TiO_2 electrodes have not been fully understood.

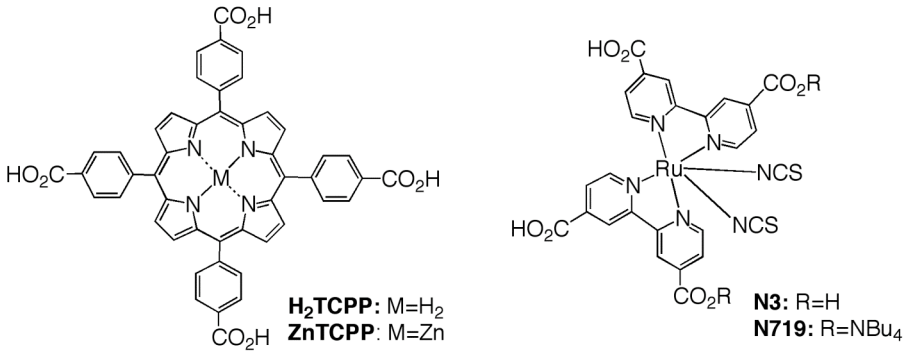

Figure 1. Molecular structures of carboxylated porphyrins and ruthenium polypyridyl dyes.

In this paper, we report the effects of porphyrin substituents and adsorption conditions (i.e., immersion solvent and time) on the photovoltaic properties of porphyrin-sensitized TiO_2 cells. 5,10,15,20-Tetraphenylporphyrinatozinc(II) (ZnP) was chosen as a sensitizer, because systematic substituents on the *meso*-phenyl groups allow us to evaluate such effects (Figure 2).[22] One carboxy group is attached on the *meso*-phenyl ring to ensure the single anchorage of the porphyrin molecule on a TiO_2 surface where the porphyrin geometry is susceptible to the molecular structure as well as the adsorption conditions. Therefore, the variations on the molecular structure and the adsorption conditions will have a large impact on molecular packing, geometry, and aggregation of the porphyrin molecules on the TiO_2 electrodes, eventually affecting the photovoltaic properties. The photovoltaic properties are also compared with those of **N719**-sensitized TiO_2 cell under the same conditions (Figure 1).

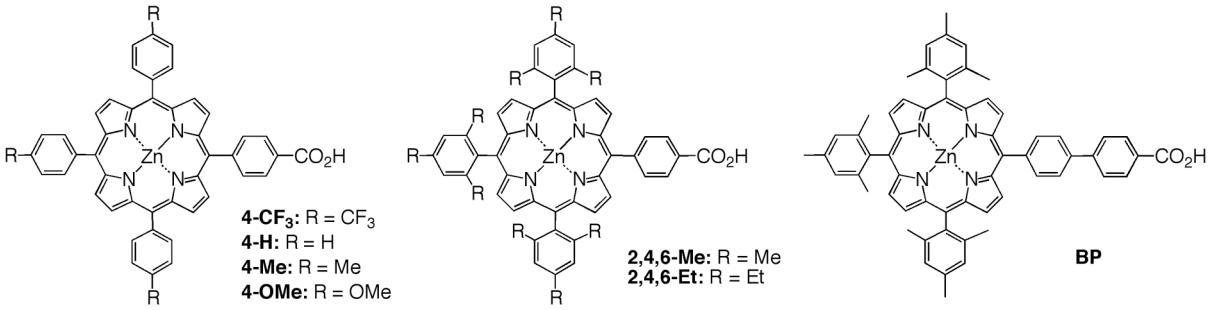

Figure 2. Molecular structures of carboxylated porphyrins used in this study.

Results and Discussion

Synthesis and Characterization. 5,10,15,20-Tetraphenylporphyrinatozinc(II)[25-29] bearing a carboxylic group, **4-CF_3**, **4-H**,[18b,28] **4-Me**, **4-OMe**,[29] **2,4,6-Me**,[8e,17b,c,22a,f,g] **2,4,6-Et**, and **BP** (Figure 2) were prepared by condensation of pyrrole with the corresponding benzaldehydes in the presence of $BF_3{\cdot}OEt_2$, followed by base hydrolysis in a mixture of THF

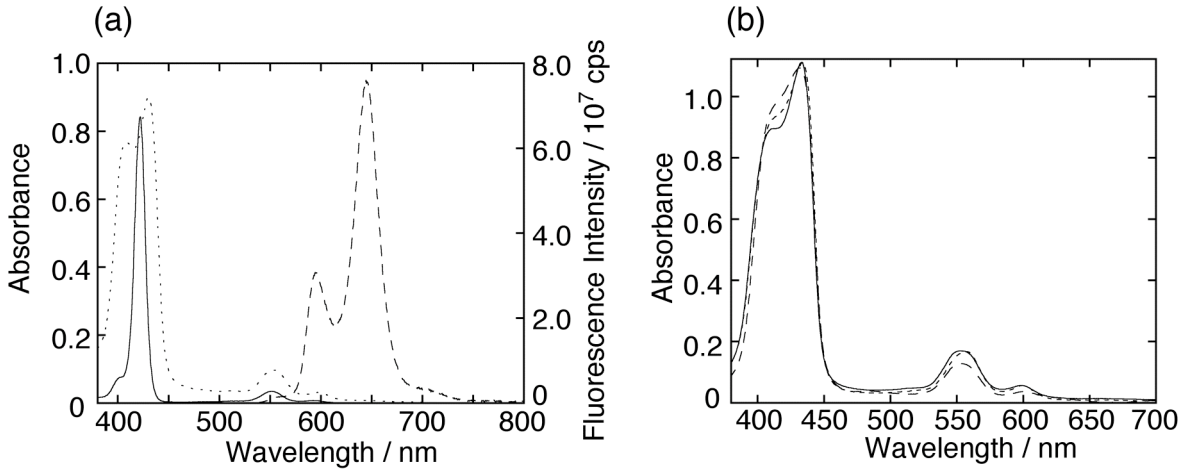

Figure 3. (a) Absorption (2.0 x 10^{-6} M, solid line) and fluorescence (dashed line) spectra of **2,4,6-Me** in CH_2Cl_2. Absorption spectrum of **2,4,6-Me** on TiO_2 electrode (dotted line) is also shown for comparison. The thickness of the TiO_2 electrode was adjusted to be 700 – 1000 nm to obtain the shape and peak position of the spectra accurately. The porphyrin-modified TiO_2 electrodes were obtained from the *t*-butylalcohol-acetonitrile mixed (1:1, v/v) solution of **2,4,6-Me** (0.2 mM) for immersion time of 12 h. (b) Absorption spectra of TiO_2/**2,4,6-Me** (solid line) electrode obtained from *t*-butylalcohol-acetonitrile mixture (1:1, v/v) for 1h, TiO_2/**2,4,6-Me** (dashed line) electrode obtained from MeOH for 12h, and TiO_2/**2,4,6-Me** (dotted line) electrode obtained from MeOH for 1h. The spectra were normalized to the spectrum at the Soret band for comparison.

and water and subsequent treatment with zinc acetate. Their molecular structures were verified by ^{1}H NMR and MALDI-TOF and high-resolution FAB mass spectrometries (see, Experimental section).

Spectroscopic and Electrochemical Studies. The UV-visible absorption spectra of zincporphyrins used for the photovoltaic measurements were measured in CH_2Cl_2 and the absorption maxima for the Soret- and Q-bands of the porphyrins are listed in Table 1. For instance, the UV-visible absorption spectrum of **2,4,6-Me** reveals characteristic strong Soret and moderate Q bands (λ_{abs} = 420, 548, 586 nm) (Figure 3, solid line). All porphyrins show approximately the same shape and the peak positions in the Soret region, as well as in the Q bands region. The fluorescence spectra of the porphyrins were also measured in CH_2Cl_2, and the emission maxima are summarized in Table 1. The fluorescence spectrum of **2,4,6-Me** exhibits emission with two peaks (λ_{em} = 595, 645 nm) arising from the porphyrin core (Figure 3, dashed line). The shape and the peak positions of the spectra are analogous for all

compounds. These results imply that the electronic structures of the porphyrin core are not perturbed largely by the substituents at the *meso*-phenyl groups.

Table 1. Optical and Electrochemical Data and Driving Forces for Electron Transfer Processes on TiO_2.

dye	λ^a_{abs} / nm	λ^b_{em} / nm	$E_{ox}{}^c$ / V	$E_{0\text{-}0}{}^d$ / eV	$E_{ox}{}^{*\,e}$ / V	$\Delta G_{inj}{}^f$ / eV	$\Delta G_{cr}{}^g$ / eV
4-CF_3	418,547,583	596,644	1.08	2.10	–1.02	–0.52	–1.58
4-H	418,547,583	597,646	1.03	2.10	–1.07	–0.57	–1.53
4-Me	420,548,588	596,648	0.99	2.10	–1.11	–0.61	–1.49
4-OMe	422,552,589	602,649	1.02	2.08	–1.06	–0.56	–1.52
2,4,6-Me	420,548,586	595,645	1.00	2.10	–1.10	–0.60	–1.50
2,4,6-Et	422,550,588	597,648	1.00	2.09	–1.09	–0.59	–1.50
BP	420,549,585	595,646	0.98	2.10	–1.12	–0.58	–1.48
N3	–	–	1.09[h]	1.75[h]	–0.64[h]	–0.14[h]	–1.59[h]

[a] Wavelengths for the maxima of Soret and Q bands in CH_2Cl_2. [b] Wavelengths for emission maxima in CH_2Cl_2 by exciting at Soret wavelength. [c] First oxidation potentials determined using cyclic voltammetry in CH_2Cl_2 containing 0.1 M n-Bu_4NPF_6 as a supporting electrolyte (vs NHE). [d] $E_{0\text{-}0}$ values were estimated from the intersection of the absorption and emission spectra. [e] Excited-state oxidation potentials approximated from E_{ox} and $E_{0\text{-}0}$ (vs NHE). [f] Driving forces for electron injection from the porphyrin excited singlet state (E_{ox}*) to the CB of TiO_2 (–0.5 V vs NHE). [g] Driving forces for charge recombination from the CB of TiO_2 to the porphyrin radical cation (E_{ox}). [h] from ref 30.

The one-electron oxidation potentials (E_{ox}) due to the porphyrins are determined using cyclic voltammetry in CH_2Cl_2 containing 0.1 M *n*-Bu_4NPF_6 as a supporting electrolyte (Table 1). From the absorption, emission, and electrochemical data, the excited state redox potentials (E_{ox}*) are approximated by extracting the zero excitation energy ($E_{0\text{-}0}$) from the potentials of the ground state couples (Table 1). Driving forces for electron injection (ΔG_{inj}) from the porphyrin excited singlet state to the CB of TiO_2 (–0.5 V vs NHE)[22] and charge recombination (ΔG_{cr}) between the resulting porphyrin radical cation and the electron in the CB of TiO_2 are determined from the values in Table 1. Note that the corresponding values of **N3** dye are also listed in Table 1 for comparison.[30] Both of the processes are thermodynamically feasible and the difference in the driving forces is virtually negligible for **4-Me**, **2,4,6-Me**, **2,4,6-Et**, and **BP**, whereas a series of the 4-substituted tetraphenylzincporphyrins (**4-CF_3**, **4-H**, **4-OMe**, and

4-Me) reveals slight difference in the driving forces depending on the electron–donating or –withdrawing substituents.

Film Preparation. Nanoporous films were prepared from colloidal suspension of TiO_2 nanoparticles (P–25) dispersed in distilled water.[22,31] The suspension was deposited on a conducting glass by using doctor blade technique. The films were annealed at 673 K for 10 min, followed by similar deposition and annealing (723 K, 2 h) for the 10-μm-thick TiO_2 films. The TiO_2 electrodes were immersed into various solvents containing 0.2 mM dye at room temperature. Finally, the dye-modified electrodes were rinsed with the same solvent as for the adsorption (denoted as TiO_2/ZnP or **N719**). Total amounts of the dyes adsorbed on the TiO_2 films were determined by measuring absorbance of the dyes that were dissolved from the dye-modified TiO_2 films into DMF containing 0.1 M NaOH. For instance, taking into account the surface area of P25 (54 m^2 g^{-1}),[22,31] the porphyrin packing densities (Γ) on the actual surface area are determined to be 1.3 x 10^{-10} mol cm^{-2} for TiO_2/**2,4,6-Me** and 1.8 x 10^{-10} mol cm^{-2} for TiO_2/**4-H** when **2,4,6-Me** and **4-H** are adsorbed onto the TiO_2 surface in *t*-butyl alcohol-acetonitrile mixture (1:1, v/v) for 12 h, respectively (Table 2). The adsorption conditions are typical for evaluating the cell performance of **N-719**-sensitized solar cell. Dye molecules bearing carboxylic groups are known to adsorb onto a TiO_2 surface, leading to the formation of monolayers on the surface.[9] Assuming that (i) the porphyrin molecule is a rectangular hexahedron and (ii) the porphyrin molecules bearing one carboxylic group are densely packed onto the TiO_2 surface to which the carboxylic group binds, the minimum occupied areas of one molecule on the TiO_2 surface are calculated to be ca. 140 $Å^2$ (7 x 20 $Å^2$) for TiO_2/**2,4,6-Me** and ca. 90 $Å^2$ (5 x 18 $Å^2$) for TiO_2/**4-H**. Accordingly, the Γ values are estimated to be 1.2 x 10^{-10} mol cm^{-2} for TiO_2/**2,4,6-Me** and 1.8 x 10^{-10} mol cm^{-2} for TiO_2/**4-H**, which agree well with the experimental values (Table 2). In the case of MeOH as an immersion solvent and the immersion time of 12 h, similar results are obtained for TiO_2/**2,4,6-Me** and TiO_2/**4-H** (Table 2). Good agreement between the experimental and calculated Γ values in the other types of porphyrins corroborates that porphyrin molecules are densely packed on the TiO_2 surface.

Spectroscopic Characterization of Porphyrin Films on TiO_2. To gain the further insight into the structures of the porphyrin monolayers on the TiO_2 surface, UV-visible absorption spectra of the TiO_2/**2,4,6-Me** electrode were measured under different adsorption conditions (Figure 3). Thickness of the TiO_2 substrate was adjusted to be 0.7 – 1.0 μm to obtain the shape and peak position of the whole spectra accurately. The split Soret bands can be attributed to the excitonic interaction between the porphyrins,[22] which is consistent with closely-packed monolayers of

the porphyrins on the TiO_2. The peak positions and the shape of the Soret and Q bands of TiO_2/**2,4,6-Me** are slightly different depending on immersion solvents (i.e., *t*-butyl alcohol-acetonitrile mixture vs MeOH) and times (i.e., 12 h vs 1 h), which would affect the photovoltaic properties in the present cell.

Table 2. Surface Coverage of Dyes on TiO_2.

electrode	experimental Γ / 10^{-10} mol cm^{-2}					calculated Γ / 10^{-10} mol cm^{-2}
	immersion solvent and time					
	t-BuOH:CH_3CN 1h	*t*-BuOH:CH_3CN 12h	MeOH 0.5h	MeOH 1h	MeOH 12h	
TiO_2/**4-CF$_3$**	1.4	1.3	1.2	1.4	1.3	1.5[a]
TiO_2/**4-H**	0.53	1.8	0.29	0.51	1.6	1.8[a]
TiO_2/**4-Me**	1.4	1.4	1.5	1.5	1.5	1.6[a]
TiO_2/**4-OMe**	1.4	1.6	0.93	1.4	1.5	1.5[a]
TiO_2/**2,4,6-Me**	1.0	1.3	0.85	1.2	1.2	1.2[a]
TiO_2/**2,4,6-Et**	0.71	0.69	0.72	0.86	0.84	0.78[a]
TiO_2/**BP**	1.2	1.1	1.1	1.1	1.2	1.2[a]
TiO_2/**N719**	0.42	2.0	0.26	0.36	1.6	1.9

[a] Assuming that the porphyrin molecules bearing one carboxylic group are densely packed onto the TiO_2 surface to which the carboxylic acid binds.

Attenuated total reflectance-Fourier transform infrared (ATR-FTIR) spectroscopy is known to be a useful tool for gaining the information on the binding mode of the molecules adsorbed on TiO_2 substrate.[22] In this study, the interpretations for the ATR-FTIR spectra of the porphyrin monolayers are aided by comparison with the FTIR spectra of the corresponding porphyrin powder in a KBr pellet. Figure 4 depicts the FTIR spectra of **2,4,6-Me** measured as a pure solid and the ATR-FTIR spectra of TiO_2/**2,4,6-Me** obtained from MeOH as an immersion solvent and the immersion times of 12 h and 1 h. The FTIR spectrum of **2,4,6-Me** obtained from a solid sample reveals the characteristic band of ν (C=O) of the carboxylic acid group at around 1700 cm^{-1} (Figure 4a).[16c,e,22,32] This diagnostic for the ν (C=O) disappears for the ATR-FTIR spectra of TiO_2/**2,4,6-Me** (Figure 4b and c). The ATR-FTIR spectra of

TiO_2/**2,4,6-Me** exhibit a marked increase in the symmetric carboxylate band, ν (COO_s^-), at around 1400 cm^{-1}.[16c,e,22,32] This diagnostic for the ν (C=O) disappears for the ATR-FTIR spectra of TiO_2/**2,4,6-Me** (Figure 4b and c). The ATR-FTIR spectra of TiO_2/**2,4,6-Me** exhibit a marked increase in the symmetric carboxylate band, ν (COO_s^-), at around 1400 cm^{-1}.[16c,e,22,32] The disappearance of ν (C=O) and the increased intensities of ν (COO_s^-) corroborate that a proton is detached from the carboxylic acid group during the adsorption of the porphyrin on the TiO_2 surface, leading to the bidentate binding of carboxylate group to the TiO_2 surface.[33] This is consistent with the previous assignment that a carboxylic acid of analogous porphyrins is bound to a TiO_2 surface via a bridging bindentate mode[16c,e] together with the fact that X-ray photoelectron spectroscopy measurement for alike tetraphenylporphyrin with a carboxylic acid group provided evidence for the bidentate binding of the carboxylate group to the TiO_2 surface.[22e]

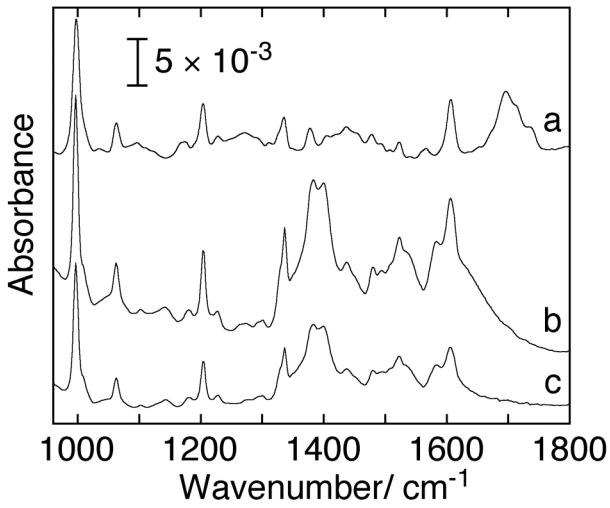

Figure 4. (a) FTIR spectra of **2,4,6-Me** measured as a pure solid. ATR-FTIR spectra of the TiO_2/**2,4,6-Me** electrode obtained from MeOH for (b) 12 h and (c) 1 h. The thickness of the TiO_2 electrode was 10 μm.

Photovoltaic Properties of Porphyrin-Sensitized TiO_2 Cells. To establish the cell performance of a reference system (i.e., Ru dye) under the present conditions using P–25, first we examined immersion time dependence of the η value for the adsorption of N719 (0.2 mM) in *t*-butyl alcohol-acetonitrile mixture (1:1, v/v). Current-voltage characteristics were measured using a 10-μm-thick TiO_2 electrode modified with N719 and a Pt counter electrode under AM 1.5 conditions. All experimental values were given as an average from six independent measurements. The η value is increased gradually with increasing the immersion time to reach a maximum η value (η_{max}) of 6.5% for 12 h (Figure 5A). Further increase of the immersion time (>12 h) does not change the η value. The η value is also increased with increasing the immersion time to become saturated for 12 h (2.0 x 10^{-10} mol cm^{-2}). The minimum occupied area of one molecule on the TiO_2 surface is calculated to be ca. 88 $Å^2$ (11 x 8 $Å^2$) for TiO_2/N719. Accordingly, the η value is estimated to be 1.9 x 10^{-10} mol cm^{-2} for TiO_2/N719, which is consistent with the experimental value (Table 2). The saturated η value is comparable to the previously reported η value in which Ru dyes are organized on the TiO_2 surface as a

densely-packed monolayer.[9,34] Accordingly, the time profile of the η value correlates well with that of the η value. It is noteworthy that the η value optimized for the immersion time (i.e., 12 h) slightly decreases in the order of *t*-butyl alcohol-acetonitrile mixture (1:1, v/v) (6.5%), CH_2Cl_2 (6.1%), and MeOH (5.5%), as shown in Figure 5B and Table 3. The cell performance of the N719-sensitized cell optimized for the immersion time is listed in Table 3.

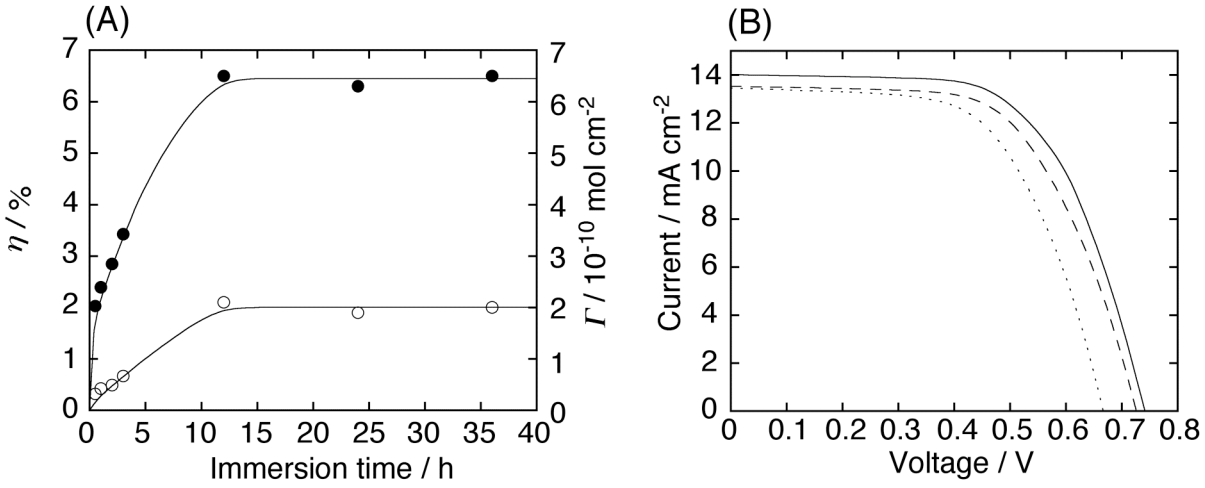

Figure 5. (A) Immersion time profiles of the η value (close circle) and of the surface density (Γ) of the **N719** dye adsorbed on a TiO_2 electrode (open circle) in *t*-butyl alcohol and acetonitrile mixture (1:1, v/v). (B) Current-voltage characteristics of **N719**-sensitized TiO_2 cells. (a) *t*-butyl alcohol and acetonitrile mixture (1:1, v/v), 12 h (solid line, η = 6.5%), (b) CH_2Cl_2, 12 h (dashed line, η = 6.1%), and (c) MeOH, 12 h (dotted line, η = 5.5%). Conditions: electrolyte 0.1 M LiI, 0.05 M I_2, 0.6 M 2,3-dimethyl-1-propyl imidazolium iodide, and 0.5 M 4-*t*-butylpyridine in acetonitrile; input power: AM 1.5 under simulated solar light (100 mW cm^{-2}). For the **N719**-sensitized cell optimized using P-25, the short-circuit photocurrent density (J_{sc}) of 14.0 mA cm^{-2}, open-circuit photovoltage (V_{oc}) of 0.74 V, and fill factor (*ff*) of 0.63 yield a power conversion efficiency (η), derived from the equation: $\eta = J_{sc}$ x V_{oc} x *ff*, of 6.5 %.

Next, we examined photovoltaic properties of the porphyrin-sensitized TiO_2 cells using **2,4,6-Me** as a representative example. For the **2,4,6-Me**-sensitized solar cell, the η value displays strong dependency of the immersion solvents (Figure 6), as contrasted with the weak solvent dependence of the **N719**-sensitized TiO_2 cell. The cell performance of **2,4,6-Me**-sensitized cell for the immersion time of 12 h in each solvent is also summarized in Table 3. The η value using **2,4,6-Me** for the immersion time of 12 h increases in the order of DMF (0.55%), CH_2Cl_2 (1.1%), *t*-butyl alcohol-acetonitrile mixture (1:1, v/v) (2.1%), EtOH (3.2%), and MeOH (3.7%). The Γ values for **2,4,6-Me** (1.2 x 10^{-10} mol cm^{-2} for EtOH and MeOH, 1.3

Table 3. Cell Performance of Dye-Sensitized Solar Cells.

cell	solvent	time / h[b]	IPCE (APCE) /%		J_{SC} / mA cm^{-2}	V_{OC} / mV	*ff*	η /%
			420 nm	560 nm				
TiO_2/ **4-CF_3**	*t*-BuOH/ MeCN[a]	1	53 (53)[d]	44 (48)	6.4	0.68	0.64	2.8
	MeOH	1	58 (58)	43 (45)	6.6	0.67	0.68	3.0
TiO_2/ **4-H**	*t*-BuOH/ MeCN[a]	1	24 (34)	8.0 (31)	3.0	0.60	0.64	1.2
	t-BuOH/ MeCN[a]	12	*c*	*c*	1.1	0.51	0.54	0.32
	MeOH	1	25 (31)	7.0 (25)	3.1	0.58	0.66	1.2
	MeOH	12	*c*	*c*	1.1	0.53	0.58	0.34
TiO_2/ **4-Me**	*t*-BuOH/ MeCN[a]	1	50 (50)	40 (42)	6.9	0.67	0.66	3.0
	MeOH	0.5	62 (62)	46 (47)	8.3	0.68	0.68	3.8
TiO_2/ **4-OMe**	*t*-BuOH/ MeCN[a]	1	60 (60)[d]	34 (37)	6.7	0.67	0.67	3.0
	MeOH	1	65 (65)	42 (44)	8.3	0.66	0.63	3.5
TiO_2/ **2,4,6-Me**	*t*-BuOH/ MeCN[a]	1	63 (63)[d]	52 (56)	7.6	0.69	0.64	3.4
	t-BuOH/ MeCN[a]	12	64 (64)	30 (32)	5.0	0.64	0.66	2.1
	EtOH	12	*c*	*c*	6.9	0.72	0.65	3.2
	MeOH	1	76 (76)	58 (60)	9.4	0.76	0.64	4.6
	MeOH	12	74 (74)	52 (53)	8.3	0.72	0.62	3.7
	DMF	1	68 (68)[d]	46 (53)	7.1	0.66	0.66	3.1
	DMF	12	*c*	*c*	1.7	0.55	0.60	0.55
	CH_2Cl_2	12	*c*	*c*	3.0	0.57	0.67	1.1
TiO_2/ **2,4,6-Et**	*t*-BuOH/ MeCN[a]	1	63 (63)[d]	52 (54)	7.7	0.71	0.61	3.3
	t-BuOH/ MeCN[a]	12	*c*	*c*	6.0	0.64	0.63	2.4
	MeOH	0.5	76 (76)[d]	52 (54)	8.6	0.69	0.63	3.7
	MeOH	12	*c*	*c*	7.1	0.66	0.62	2.9
	DMF	12	*c*	*c*	2.3	0.62	0.64	0.91
	CH_2Cl_2	12	*c*	*c*	3.6	0.60	0.66	1.4
TiO_2/ **BP**	*t*-BuOH/ MeCN[a]	1	57 (57)	40 (41)	5.6	0.64	0.66	2.4
	MeOH	1	61 (61)	41 (42)	6.0	0.65	0.66	2.6
TiO_2/ **N719**	*t*-BuOH/ MeCN[a]	12	72[e]		14.0	0.74	0.63	6.5
	MeOH	12	*c*	*c*	13.5	0.67	0.61	5.5
	CH_2Cl_2	12	*c*	*c*	13.5	0.73	0.62	6.1

[a]1:1, v/v. [b]Short immersion time giving the highest η value. [c]Not measured. [d]At 430 nm. [e]At 520 nm.

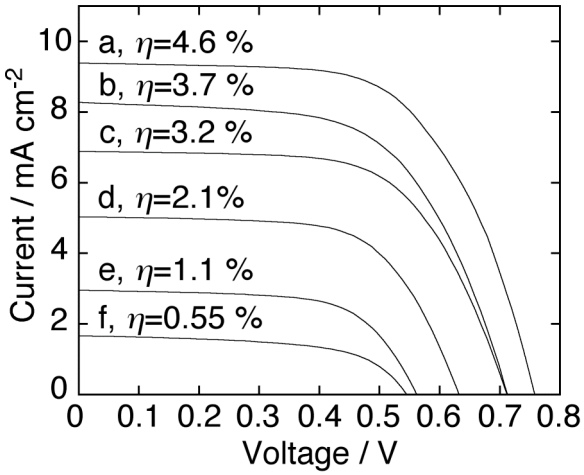

Figure 6. Current-voltage characteristics of **2,4,6-Me**-sensitized TiO_2 cells under AM 1.5 conditions. Conditions for the immersion solvent and time: (a) MeOH, 1 h, (b) MeOH, 12 h, (c) EtOH, 12 h, (d) *t*-BuOH-MeCN mixture (1:1, v/v), 12 h, (e) CH_2Cl_2, 12 h, and (f) DMF, 12 h. Conditions for the photovoltaic measurements: electrolyte 0.1 M LiI, 0.05 M I_2, 0.6 M 2,3-dimethyl-1-propyl imidazolium iodide, and 0.5 M 4-*t*-butylpyridine in acetonitrile; input power: AM 1.5 under simulated solar light (100 mW cm^{-2}). For the **2,4,6-Me**-sensitized cell optimized using P-25, J_{sc} of 9.4 mA cm^{-2}, V_{oc} of 0.76 V, and *ff* of 0.64 yield η of 4.6 % (curve a).

x 10^{-10} mol cm^{-2} for *t*-butyl alcohol-acetonitrile mixture (1:1, v/v)) are virtually the same when the protic solvents are used. On the other hand, they (Γ = 5.3 x 10^{-11} mol cm^{-2} for DMF, 8.7 x 10^{-11} mol cm^{-2} for CH_2Cl_2) are considerably lower in the case of the non-protic solvents. It is concluded that the low porphyrin density on the TiO_2 surface for the adsorption in the non-protic solvents is responsible for the low η value relative to the η value obtained with the adsorption from protic solvents. The high porphyrin density for the adsorption in the protic solvents indicates the significant contribution of the protic solvents for the formation of a densely-packed porphyrin monolayer on the TiO_2 surface.[22,35] Similar photovoltaic behavior as a function of immersion solvents was reported for the other porphyrins.[22]

To further improve the performance of **2,4,6-Me**-sensitized TiO_2 cell, immersion time dependence of the η value for the adsorption of **2,4,6-Me** was examined in MeOH, which yielded the maximum η value among all the immersion solvents under the same conditions. The η value is increased rapidly with increasing the immersion time to reach a η_{max} value of 4.6% for 1 h and then decreases gradually to reach a constant η value of 3.7% (Figure 7). In accordance with the initial trend, the Γ value also increases rapidly with increasing the immersion time, but levels off at the immersion time of 1 h (Γ = 1.2 x 10^{-10} mol cm^{-2}). Similar behavior of η and Γ values as a function of the immersion time is noted when a mixture of

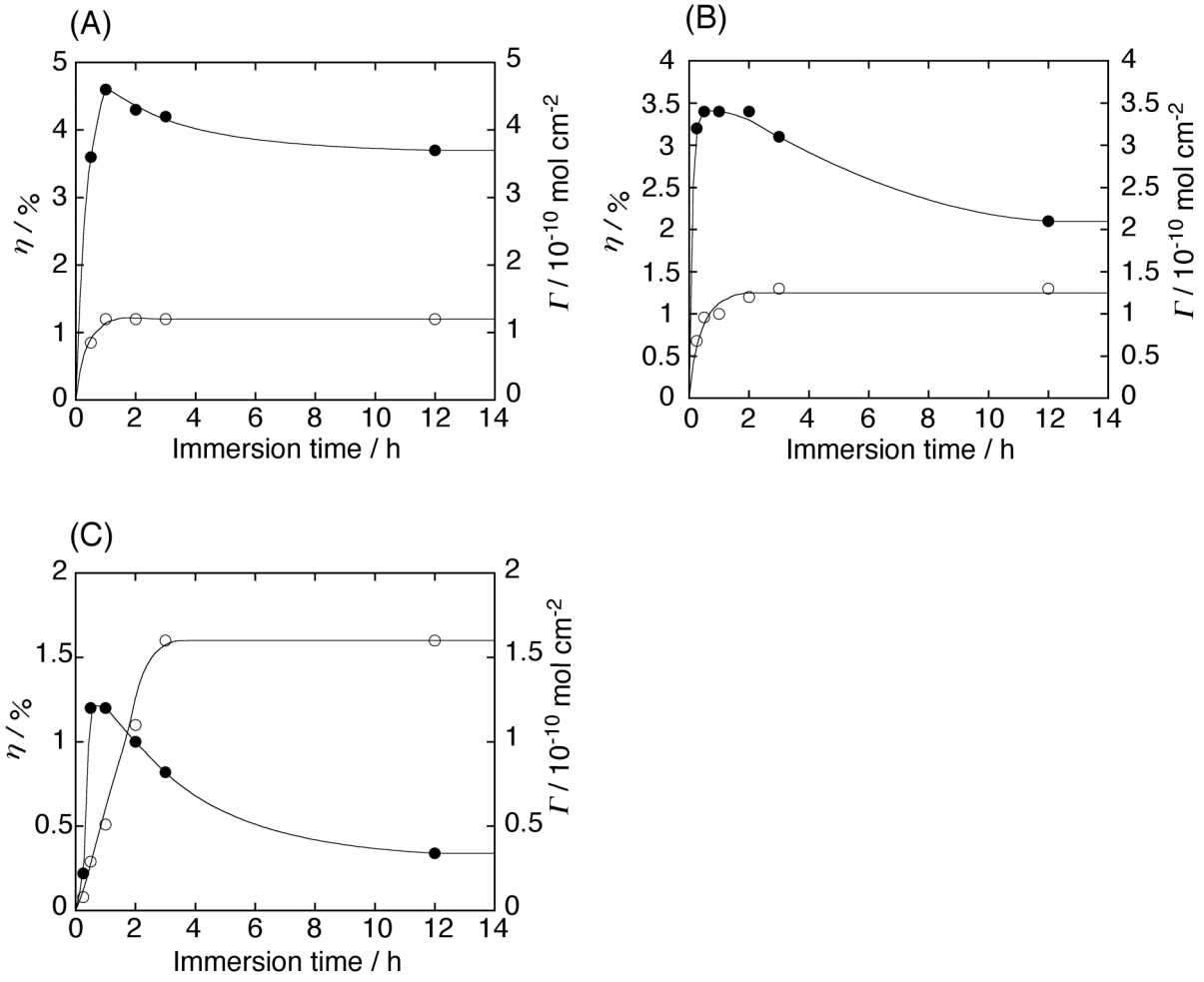

Figure 7. Immersion time profiles of η value (close circle) and of the surface density (Γ) (open circle) for (A) **2,4,6-Me** adsorbed on TiO_2 electrode in MeOH, (B) **2,4,6-Me** adsorbed on TiO_2 electrode (open circle) in *t*-butyl alcohol-acetonitrile mixture (1:1, v/v), and (C) **4-H** adsorbed on TiO_2 electrode (open circle) in MeOH.

t-butyl alcohol and acetonitrile (1:1, v/v) is used as the immersion solvents for **2,4,6-Me** (Figure 7B) or the other porphyrins that are adsorbed on the TiO_2 electrode in MeOH (Figure 7C). It should be noted here that the η_{max} value (4.6%) and the maximum incident-photon-to-current efficiency (*IPCE*) ($IPCE_{max}$ = 76%) of **2,4,6-Me**-sensitized TiO_2 cell are much larger than the corresponding values of the other porphyrin-sensitized TiO_2 cells used in this study, exhibiting the highest cell performance when MeOH as the immersion solvent and the immersion time of 0.5 or 1 h are used (Table 3). Furthermore, the η_{max} value of the present cell using **2,4,6-Me** is ~70% that of ruthenium dye (**N719**)-sensitized TiO_2 cell (6.5%) under the present optimized conditions using P-25. The photocurrent action spectrum of **2,4,6-Me**-sensitized TiO_2 cell (Figure 8) is largely similar to the absorption spectrum of **2,4,6-Me** on the TiO_2 electrode (Figure 3). Note that integration of the IPCE values for the

2,4,6-Me-sensitized TiO_2 cell with respect to wavenumber is ~70% that of the **N719**-sensitized TiO_2 cell, which parallels the ratio of the η_{max} values in the two cells. The similar ratio (~70%) reveals that the light-harvesting property of **2,4,6-Me**-sensitized TiO_2 cell limits the cell performance. Both device structure and dye are known to have a large impact on the η value of dye-sensitized solar cells.[9,15,16] Grätzel et al. reported the highest η values of 4-7% among porphyrin-sensitized solar cells[16] and of 10-11% for the **N719**-sensitized solar cell[9] under their optimized conditions using a TiO_2 double layer electrode. Thus, further increase in the cell performance of porphyrin-sensitized TiO_2 cells may be possible by improving the device fabrication as well as the light-harvesting property. It should be pointed out that the cell performance of the porphyrin-sensitized TiO_2 cells strongly depends on the immersion solvents and the times, which is in marked contrast with Ru dye-sensitized TiO_2 cells. The high cell performance in Ru dye-sensitized TiO_2 cells may originate from the robust geometry of ruthenium dyes on the TiO_2 through more than two anchoring groups, while the rather flexible geometry of the porphyrin on the TiO_2 through the single anchoring group may cause the susceptible cell performance, which is influenced by the porphyrin substituents as well as the adsorption conditions.

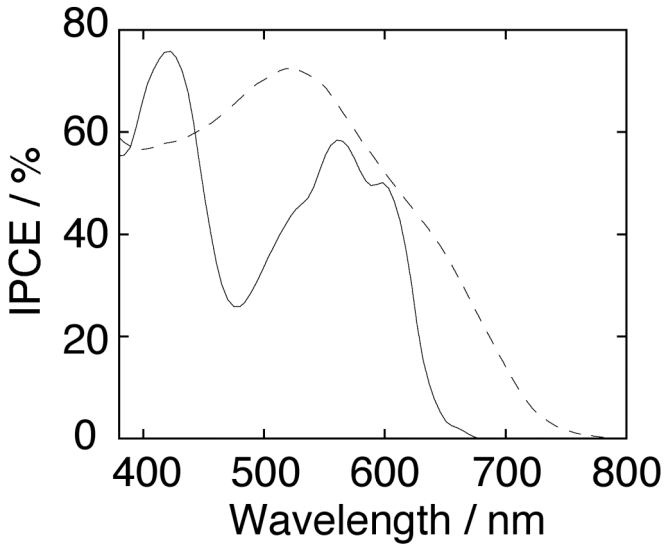

Figure 8. Photocurrent action spectra of (a) **2,4,6-Me**-sensitized solar cell (solid line, MeOH for 1 h) and (b) **N719**-sensitized solar cell (dashed line, *t*-BuOH-MeCN mixture (1:1, v/v) for 12 h) under the optimized conditions; electrolyte 0.1 M LiI, 0.05 M I_2, 0.6 M 2,3-dimethyl-1-propyl imidazolium iodide, and 0.5 M 4-*t*-butylpyridine in acetonitrile; input power: AM 1.5 under simulated solar light (100 mW cm^{-2}).

Comparison of Photovoltaic Properties. It is intriguing to compare the cell performance of **4-CF_3**, **4-H**, **4-Me**, **4-OMe**, **2,4,6-Me**, **2,4,6-Et**, and **BP**-sensitized cells under the same conditions. The results are summarized in Table 3. We consider the following points for the photovoltaic properties.

First, the cell performance of **2,4,6-Me** and **BP**-sensitized TiO_2 cells is compared to evaluate the electronic coupling effect on the photovoltaic properties. When the porphyrins are

adsorbed in MeOH for 1 h, the η_{max} and adsorbed photon-to-current efficiency (*APCE*) values of a **BP** cell (η = 2.6%, $IPCE_{max}$ = 61%) are smaller than those of a **2,4,6-Me** cell (η_{max} = 4.6%, $IPCE_{max}$ = 76%). A similar difference is noted for the comparison of **BP** (η_{max} = 2.4%, $IPCE_{max}$ = 57%) and **2,4,6-Me** cells (η_{max} = 3.4%, $IPCE_{max}$ = 63%) when adsorbed in *t*-butyl alcohol-acetonitrile mixture (1:1, v/v) for 1 h. Taking into account the same molecular structure of **2,4,6-Me** and **BP** except the spacer moiety (phenyl vs biphenyl) and full monolayer coverage of the porphyrins on the TiO_2 surface, the electronic coupling between the porphyrin and the TiO_2 has a large impact on the cell performance. Analogous spacer length dependence of the η value on zincporphyrins with conjugated phenylethylnyl spacers was reported.[18h]

Second, the driving force effects on the photovoltaic properties of **4-CF_3**, **4-OMe**, **4-H**, and **4-Me**-sensitized TiO_2 cells are evaluated. Under the adsorption conditions exhibiting the highest values (i.e., MeOH for 0.5 or 1 h), the η_{max} and $IPCE_{max}$ values are rather similar for **4-CF_3** (η_{max} = 3.0%, $IPCE_{max}$ = 58%), **4-OMe** (η_{max} = 3.5%, $IPCE_{max}$ = 65%), and **4-Me** cells (η_{max} = 3.8%, $IPCE_{max}$ = 62%) except the case of **4-H** (η_{max} = 1.2%, $IPCE_{max}$ = 25%). Similar trend is observed for the η_{max} values of **4-CF_3** (η_{max} = 2.8%), **4-OMe** (η_{max} = 3.0%), **4-H** cell (η_{max} = 1.2%), and **4-Me** cells (η_{max} = 3.0%) when adsorbed in *t*-butyl alcohol-acetonitrile mixture (1:1, v/v) for 1 h. Although the driving force for electron injection (ΔG_{inj}) from the porphyrin excited singlet state to the CB of the TiO_2 electrode increases with introducing the electron-donating substituents (-0.52 eV for **4-CF_3**, -0.56 eV for **4-OMe**, -0.57 eV for **4-H**, -0.61 eV for **4-Me**), the η_{max} and $IPCE_{max}$ values are unlikely to correlate with the driving force for the electron injection. The considerably low η_{max} value of **4-H** cell may be rationalized by the rather low porphyrin density of **4-H** on the TiO_2 in comparison of the other porphyrins at the short immersion time of 0.5 or 1 h (Table 2). Additionally, strong aggregation tendency of **4-H** on the TiO_2 due to the small steric hindrance would be also responsible for the low η value of **4-H** cell, taking into account the remarkable decrease in the η value for the long immersion time (Table 3 and Figure 7C).

The steric effect on the photovoltaic properties is examined for **4-Me**, **2,4,6-Me**, and **2,4,6-Et**-sensitized TiO_2 cells. For example, under the adsorption conditions exhibiting the highest values (i.e., MeOH for 0.5 or 1 h), the η_{max} and $IPCE_{max}$ values of **2,4,6-Me** cell (η_{max} = 4.6%, $IPCE_{max}$ = 76%) are larger than those of **4-Me** (η_{max} = 3.8%, $IPCE_{max}$ = 62%) and **2,4,6-Et** cells (η_{max} = 3.7%; $IPCE_{max}$ = 76%). Similar results are obtained for the η_{max} values of **4-Me** (η_{max} = 3.0%), **2,4,6-Me** (η_{max} = 3.4%), and **2,4,6-Et** cells (η_{max} = 3.3%) when adsorbed in *t*-butyl alcohol-acetonitrile mixture (1:1, v/v) for 0.5-1 h. Large steric repulsion between the *ortho*-methyl or -ethyl substituents and the porphyrin ring in **2,4,6-Me** and **2,4,6-Et** results in orthogonal orientation of the phenyl groups against the porphyrin ring, making large bulkiness around the porphyrin rings. In such a case, even in the densely-packed state, the rather

well-separated porphyrin cores of **2,4,6-Me** would reduce the intermolecular interaction between the porphyrins on the TiO_2 surface, thereby leading to a decrease of radiationless processes from the porphyrin excited singlet state and a subsequent increase of the electron injection efficiency, in turn an increase of the η value using **2,4,6-Me** relative to that of **4-Me**.[36] The decrease in the η value of **2,4,6-Et** cell relative to that of **2,4,6-Me** cell may be caused by the small porphyrin density (Γ = (0.71-0.72) x 10^{-10} mol cm^{-2}) on the TiO_2 electrode compared with the Γ value (Γ = (1.0-1.2) x 10^{-10} mol cm^{-2}) of **2,4,6-Me** on the TiO_2 electrode as the result of difference in the sizes of ethyl and methyl groups.

Finally, the photovoltaic properties are investigated as a function of the adsorption conditions (i.e., immersion solvent and immersion time). For all porphyrins with increasing the immersion time, the η value is increased rapidly to reach the maximum for 0.5-1 h and then decreased. Such behavior may be rationalized by an increase of the porphyrin aggregation with increasing the immersion time. Despite of similar full monolayer coverage of the porphyrins, the cell performances of the porphyrin-sensitized TiO_2 electrodes are in the order of *t*-butyl alcohol-acetonitrile < EtOH < MeOH as an immersion solvent. Although the reason is not clear at present, protic solvents may involve the adsorption process of the porphyrin on the TiO_2 surface, altering the binding mode and geometry of the porphyrin on the TiO_2 surface.[35]

Conclusions

We have systematically examined the effects of porphyrin substituents and adsorption conditions on the photovoltaic properties of the porphyrin-sensitized TiO_2 cells for the first time. The cell performance of the porphyrin-sensitized TiO_2 cells was affected greatly by the steric bulkiness around the porphyrin, the electronic coupling between the porphyrin core and the TiO_2 surface, the immersion solvent, and the immersion time. In particular, the high cell performance of the porphyrin-sensitized TiO_2 cells was realized when protic solvent (i.e., methanol) and short immersion time (0.5-1 h) were used for the conditions of the dye adsorption on TiO_2. This unique behavior is in marked contrast with little dependence of the cell performance on Ru dye-sensitized TiO_2 cells as a function of the immersion solvent and time. The TiO_2 electrode cell with 5-(4-carboxyphenyl)-10,15,20-tris(2,4,6-trimethylphenyl)porphyrinatozinc(II) as a sensitizer exhibited the maximal cell performance: IPCE value of 76 %, short circuit photocurrent density of 9.4 mA cm^{-2}, open circuit voltage of 0.76 V, fill factor of 0.64, and power conversion efficiency of 4.6% under standard AM 1.5 sunlight. These results will provide basic and important information on the development of dye-sensitized solar cells with a high performance.

Experimental Section

General Methods. Melting points were recorded on a Yanagimoto micro-melting point apparatus and not corrected. ^{1}H NMR spectra were measured on a JEOL EX-270 (400 MHz) or a JEOL JMN-AL300 (300 MHz). Matrix-assisted laser desorption/ionization (MALDI) time-of-flight mass spectra (TOF) were measured on a Shimadzu KOMPACT MALDI II using CHCA as a matrix. High-resolution mass spectra (HRMS) were recorded on a JEOL JMS-HX 110A spectrometer (FAB) using 3-nitrobenzylic alcohol as a matrix. UV-visible absorption spectra of solutions and films were recorded using a Perkin-Elmer Lambda 900 UV/VIS/NIR Spectrometer. Steady-state fluorescence spectra were acquired on a SPEX FluoroMax-3 spectrometer.

Materials. All solvents and chemicals were of reagent grade quality, purchased commercially and used without further purification unless otherwise noted. Tetrabutylammonium hexafluorophosphate used as a supporting electrolyte for the electrochemical measurements was obtained from Fluka and recrystallized from methanol. Toluene and methylene chloride were dried by refluxing and distilled from CaH_2 under an argon atmosphere just before use. Thin-layer chromatography and column chromatography were performed with Alt. 5554 DC-Alufolien Kieselgel 60 F_{254} (Merck) and UltraPure Silica Gel (230-400 mesh, SiliCycle), respectively.

Synthesis. 5,10,15,20-Tetraphenylzincporphyrins bearing carboxylic group (**4-CF$_3$**, **4-H**, **4-Me**, **4-OMe**, **2,4,6-Me**, **2,4,6-Et**, and **BP**) were prepared by condensation of pyrrole with the corresponding benzaldehydes in the presence of BF_3·OEt_2, followed by base hydrolysis in a mixture of THF and water, and subsequent treatment with zinc acetate.[25] 2,4,6-Triethylbenzaldehyde[26] and 4'-formylbiphenyl-4-carboxylic acid methyl ester[27] were synthesized by following the literature. Synthesis and characterization of porphyrins **4-H**,[18b,28] 5-(4-carboxyphenyl)-10,15,20-tris(4-methoxyphenyl)porphyrin,[29] and **2,4,6-Me**[17b,c,22a,f,g] have already been reported.

5-(4-Methoxycarbonylphenyl)-10,15,20-tris(4-trifluoromethylphenyl)porphyrin (4-CF$_3$-ester): To a solution of 4-trifluoromethylbenzaldehyde (0.78 g, 4.5 mmol) in CH_2Cl_2 (600 mL) was added methyl 4-formylbenzoate (0.25 g, 1.5 mmol) and pyrrole (0.42 ml, 6.0 mmol). Dry Ar was bubbled through the solution for 30 min before adding BF_3·OEt_2 (0.3 mL). The solution was stirred for 24 h at room temperature under Ar atmosphere. Then, DDQ (1.4 g, 6.0 mmol) was added and the reaction mixture was stirred for 1 h. After Et_3N (1 mL) was added to the reaction mixture, the solvent was removed in vacuo. Column chromatography on

silica gel (CH_2Cl_2/hexane = 4:1) afforded **4-CF_3-ester** as a purple red solid (0.055 g, 0.063 mmol, 4.2 % yield). Mp > 300°C; ^{1}H NMR (400 MHz, $CDCl_3$) δ 8.82 (s, 2H), 8.81 (s, 6H), 8.46 (d, J = 7.8 Hz, 2H), 8.34 (d, J = 7.8 Hz, 6H), 8.30 (d, J = 7.8 Hz, 2H), 8.05 (d, J = 7.8 Hz, 6H), 4.12 (s, 3H), –2.83 (s, 2H); MS (MALDI-TOF) m/z 877 ($M+H^+$); HRMS (FAB positive) *m/z* for $C_{49}H_{29}F_9N_4O_2$ 876.2147 (calcd), 876.2119 (found, M^+).

5-(4-Carboxylphenyl)-10,15,20-tris(4-trifluoromethylphenyl)porphyrin (4-CF_3-H_2): To a solution of **4-CF_3-ester** (0.030 g, 0.035 mmol) in THF (70 mL) was added 40 % KOH aqueous solution (7 mL). The solution was refluxed for 1h. After the reaction mixture was cooled to room temperature, aqueous 1M HCl (5 mL) was added. The solution was washed with saturated aqueous $NaHCO_3$ (20 mL) and H_2O (20 mL x 3), dried over anhydrous sodium sulfate, and then the solvent was removed in vacuo. Reprecipitation from CH_2Cl_2/MeOH gave **4-CF_3-H_2** as a purple red solid (0.028 g, 0.032 mmol, 92 %yield). Mp > 300°C; ^{1}H NMR (400 MHz, $CDCl_3$) δ 8.88 (m, 8H), 8.44 (d, J = 7.8 Hz, 2H), 8.29 (d, J = 7.8 Hz, 8H), 8.13 (d, J = 7.8 Hz, 6H), –2.82 (s, 2H); MS (MALDI-TOF) m/z 863 ($M+H^+$); HRMS (FAB positive) *m/z* for $C_{48}H_{27}F_9N_4O_2$ 862.1990 (calcd), 862.1972 (found, M^+).

5-(4-Carboxylphenyl)-10,15,20-tris(4-trifluoromethylphenyl)porphyrinatozinc(II) (4-CF_3): To a solution of **4-CF_3-H_2** (0.026 g, 0.028 mmol) in $CHCl_3$ (30 mL) was added a solution of $Zn(OAc)_2$ (0.1 g) in MeOH (5 mL). The solution was refluxed for 2h and cooled to room temperature. The reaction mixture was washed with H_2O (20 mL x 3), dried over anhydrous sodium sulfate, and then the solvent was removed in vacuo. Reprecipitation from CH_2Cl_2/MeOH gave **4-CF_3** as a purple red solid (0.024 g, 0.026 mmol, 92 % yield). Mp > 300°C; ^{1}H NMR (400 MHz, $CDCl_3$) δ 8.93 (m, 8H), 8.51 (d, J = 7.6 Hz, 2H), 8.35 (d, J = 7.6 Hz, 8H), 8.05 (d, J = 7.6 Hz, 6H); MS (MALDI-TOF) m/z 926 ($M+H^+$); HRMS (FAB positive) *m/z* for $C_{48}H_{25}F_9N_4O_2Zn$ 924.1125 (calcd), 924.1123 (found, M^+); UV-vis (CH_2Cl_2) λ_{max} (nm) 418, 547, 583.

5-(4-Methoxycarbonylphenyl)-10,15,20-tris(4-methylphenyl)porphyrin (4-Me-ester): To a solution of 4-methylbenzaldehyde (1.6 g, 13.5 mmol) in $CHCl_3$ (900 mL) was added methyl 4-formylbenzoate (0.74 g, 4.5 mmol) and pyrrole (1.2 mL, 18 mmol). Dry nitrogen was bubbled through the solution for 30 min before adding BF_3·OEt_2 (1.0 mL). The solution was stirred at room temperature for 1h. Then, *p*-chloranil (4.2 g) was added and stirred at room temperature for 1h. After Et_3N (1 mL) was added to the reaction mixture, the solvent was removed in vacuo. Column chromatography on silica gel (CH_2Cl_2/hexane=1:1) afforded **4-Me-ester** as a purple red solid (0.35 g, 0.50 mmol, 11 % yield). Mp > 300°C; ^{1}H NMR (400

MHz, $CDCl_3$) δ 8.87 (m, 6H), 8.77 (m, 2H), 8.43 (d, J = 7.2 Hz, 2H), 8.31 (d, J = 7.2 Hz, 2H), 8.09 (d, J = 7.2 Hz, 6H), 7.55 (d, J = 7.2 Hz, 6H), 4.11 (s, 3H), 2.71 (s, 9H), –2.76 (s, 2H); MS (MALDI-TOF) m/z 715 ($M+H^+$); HRMS (FAB positive) *m/z* for $C_{49}H_{38}N_4O_2$ 714.2995 (calcd), 714.3000 (found, M^+).

5-(4-Carboxylphenyl)-10,15,20-tris(4-methylphenyl)porphyrin (4-Me-H_2): To a solution of **4-Me-ester** (0.30 g, 0.42 mmol) in THF (150 mL) was added 40 % KOH aqueous solution (17 mL). The solution was refluxed for 1h. After the reaction mixture was cooled to room temperature, aqueous 1M HCl (10 mL) was added. The solution was washed with saturated aqueous $NaHCO_3$ (50 mL) and H_2O (50 mL x 3), dried over anhydrous sodium sulfate, and then the solvent was removed in vacuo. Reprecipitation from CH_2Cl_2/MeOH gave **4-Me-H_2** as a purple red solid (0.27 g, 0.38 mmol, 90 %yield). Mp > 300°C; ^{1}H NMR (400 MHz, $CDCl_3$) δ 8.88 (m, 6H), 8.77 (d, J = 4.5 Hz, 2H), 8.48 (d, J = 7.8 Hz, 2H), 8.34 (d, J = 7.8 Hz, 2H), 8.09 (d, J = 7.8 Hz, 6H), 7.56 (d, J = 7.8 Hz, 6H), 2.71 (s, 9H), –2.77 (s, 2H); MS (MALDI-TOF) m/z 701 ($M+H^+$); HRMS (FAB positive) *m/z* for $C_{48}H_{36}N_4O_2$ 700.2838 (calcd), 700.2816 (found, M^+).

5-(4-Carboxylphenyl)-10,15,20-tris(4-methylphenyl)porphyrinatozinc(II) (4-Me): To a solution of **4-Me-H_2** (0.25 g, 0.33 mmol) in $CHCl_3$ (100 mL) was added a solution of $Zn(OAc)_2$ (0.5 g) in MeOH (30 mL). The solution was refluxed for 2h and cooled to room temperature. The reaction mixture was washed with H_2O (50 mL x 3), dried over anhydrous sodium sulfate, and then the solvent was removed in vacuo. Reprecipitation from CH_2Cl_2/MeOH gave **4-Me** as a purple red solid (0.24 g, 0.31 mmol, 94 % yield). Mp > 300°C; ^{1}H NMR (400 MHz, $CDCl_3$) δ 8.99 (m, 6H), 8.88 (d, J = 4.8 Hz, 2H), 8.48 (d, J = 7.8 Hz, 2H), 8.34 (d, J = 7.8 Hz, 2H), 8.10 (d, J = 7.8 Hz, 6H), 7.56 (d, J = 7.8 Hz, 6H), 2.72 (s, 9H); MS (MALDI-TOF) m/z 763 ($M+H^+$); HRMS (FAB positive) *m/z* for $C_{48}H_{34}N_4O_2Zn$ 762.1973 (calcd), 762.1970 (found, M^+); UV-vis (CH_2Cl_2) λ_{max} (nm) 420, 548, 588.

5-(4-Carboxylphenyl)-10,15,20-tris(4-methoxyphenyl)porphyrinatozinc(II) (4-OMe): To a solution of 5-(4-carboxylphenyl)-10,15,20-tris(4-methoxyphenyl)porphyrin[29] (0.026 g, 0.028 mmol) in $CHCl_3$ (30 mL) was added a solution of $Zn(OAc)_2$ (0.1 g) in MeOH (5 mL). The solution was refluxed for 2h and cooled to room temperature. The reaction mixture was washed with H_2O (20 mL x 3), dried over anhydrous sodium sulfate, and then the solvent was removed in vacuo. Reprecipitation from CH_2Cl_2/MeOH gave **4-OMe** as a purple red solid (0.024 g, 0.026 mmol, 92 % yield). Mp > 300°C; ^{1}H NMR (400 MHz, $CDCl_3$) δ 8.99 (s, 6H), 8.89 (d, J = 4.0 Hz, 2H), 8.49 (d, J = 7.6 Hz, 2H), 8.34 (d, J = 7.6 Hz, 2H), 8.13 (d, J = 7.6 Hz, 6H), 7.29

(d, J = 7.6 Hz, 6H), 4.11 (s, 9H); MS (MALDI-TOF) m/z 812 ($M+H^+$); UV-vis (CH_2Cl_2) λ_{max} (nm) 422, 552, 589.

5-(4-Methoxycarbonylphenyl)-10,15,20-tris(2,4,6-triethylphenyl)porphyrin (2,4,6-Et-ester): To a solution of 2,4,6-triethylbenzaldehyde[26] (2.6 g, 13.5 mmol) in $CHCl_3$ (900 mL) was added methyl 4-formylbenzoate (0.74 g, 4.5 mmol) and pyrrole (1.2 mL, 18 mmol). Dry nitrogen was bubbled through the solution for 30 min before adding $BF_3 \cdot OEt_2$ (1.0 mL). The solution was stirred at room temperature for 1h. Then, *p*-chloranil (4.2 g) was added and stirred at room temperature for 1h. After Et_3N (1 mL) was added to the reaction mixture, the solvent was removed in vacuo. Column chromatography on silica gel (CH_2Cl_2/hexane=3:2) afforded **2,4,6-Et-ester** as a purple red solid (0.40 g, 0.48 mmol, 3.5 % yield). Mp > 300°C; ^{1}H NMR (400 Hz, $CDCl_3$) δ 8.68 (s, 4H), 8.60 (s, 4H), 8.40 (d, J = 7.8 Hz, 2H), 8.28 (d, J = 7.8 Hz, 2H), 7.30 (m, 6H), 4.10 (s, 3H), 2.95 (t, J = 6.9 Hz, 6H), 2.13 (t, J = 7.2 Hz, 12H), 1.52 (t, J = 7.2 Hz, 9H), 0.69 (q, J = 4.2 Hz, 18H), –2.51 (s, 2H); MS (MALDI-TOF) m/z 926 ($M+H^+$); HRMS (FAB positive) *m/z* for $C_{64}H_{68}N_4O_2$ 924.5342 (calcd), 924.5347 (found, M^+).

5-(4-Carboxyphenyl)-10,15,20-tris(2,4,6-triethylphenyl)porphyrin (2,4,6-Et-H_2): To a solution of **2,4,6-Et-ester** (0.38 g, 0.41 mmol) in THF (150 mL) was added 40 % KOH aqueous solution (20 mL). The solution was refluxed for 0.5h. After the reaction mixture was cooled to room temperature, aqueous 1M HCl (10 mL) was added. The solution was washed with saturated aqueous $NaHCO_3$ (50 mL) and H_2O (50 mL x 3), dried over anhydrous sodium sulfate, and then the solvent was removed in vacuo. Reprecipitation from CH_2Cl_2/MeOH gave **2,4,6-Et-H_2** as a purple red solid (0.37 g, 0.40 mmol, 99 % yield). Mp > 300°C; ^{1}H NMR (400 Hz, $CDCl_3$) δ 8.68 (s, 4H), 8.60 (s, 4H), 8.40 (d, J = 7.8 Hz, 2H), 8.28 (d, J = 7.8 Hz, 2H), 7.29 (m, 6H), 2.95 (t, J = 7.8 Hz, 6H), 2.13 (t, J = 7.8 Hz, 12H), 1.53 (t, J = 7.4 Hz, 9H), 0.70 (q, J = 4.4 Hz, 18H), –2.51 (s, 2H); MS (MALDI-TOF) m/z 910 ($M+H^+$); HRMS (FAB positive) *m/z* for $C_{63}H_{66}N_4O_2$ 910.5186 (calcd), 910.5226 (found, M^+).

5-(4-Carboxyphenyl)-10,15,20-tris(2,4,6-triethylphenyl)porphyrinatozinc(II) (2,4,6-Et): To a solution of **2,4,6-Et-H_2** (0.36 g, 0.40 mmol) in $CHCl_3$ (120 mL) was added a solution of $Zn(OAc)_2$ (0.8 g) in MeOH (30 mL). The solution was refluxed for 2h and cooled to room temperature. The reaction mixture was washed with H_2O (50 mL x 3), dried over anhydrous sodium sulfate, and then the solvent was removed in vacuo. Reprecipitation from CH_2Cl_2/MeOH gave **2,4,6-Et** as a purple red solid (0.24 g, 0.25 mmol, 63 % yield). Mp > 300°C; ^{1}H NMR (400 Hz, $CDCl_3$) δ 8.79 (s, 4H), 8.68 (s, 4H), 8.50 (d, J = 7.8 Hz, 2H), 8.36 (d, J = 7.8 Hz, 2H), 7.32 (s, 4H), 7.30 (s, 2H), 2.99 (m, 6H), 2.11 (m, 12H), 1.54 (m, 9H), 0.69 (m,

18H); MS (MALDI-TOF) m/z 974 ($M+H^+$); HRMS (FAB positive) *m/z* for $C_{63}H_{64}N_4O_2Zn$ 972.4321 (calcd), 972.4313 (found, M^+); UV-vis (CH_2Cl_2) λ_{max} (nm) 422, 550, 588.

5-(4-Methoxycarbonylbiphenyl)-10,15,20-tris(2,4,6-trimethylphenyl)porphyrin (BP-ester): To a solution of 2,4,6-trimethylbenzaldehyde (0.68 g, 4.5 mmol) in $CHCl_3$ (600 mL) was added 4'-formylbiphenyl-4-carboxylic acid methyl ester[27] (0.36 g, 1.5 mmol) and pyrrole (0.42 ml, 6.0 mmol). Dry nitrogen was bubbled through the solution for 30 min before adding $BF_3{\cdot}OEt_2$ (0.3 mL). The solution was stirred at room temperature for 1h. Then, *p*-chloranil (1.4 g) was added and stirred at room temperature for 1h. After Et_3N (1 mL) was added to the reaction mixture, the solvent was removed in vacuo. Column chromatography on silica gel (CH_2Cl_2/hexane = 1:1) afforded **BP-ester** as a purple red solid (0.10 g, 0.12 mmol, 8 % yield). Mp > 300°C; ^{1}H NMR (400 Hz, CD_2Cl_2) δ 8.87 (d, J = 4.4 Hz, 2H), 8.69 (d, J = 4.4 Hz, 2H), 8.64 (s, 4H), 8.33 (d, J = 8.4 Hz, 2H), 8.25 (d, J = 8.4 Hz, 2H), 8.06 (d, J = 8.4 Hz, 2H), 8.03 (d, J = 8.4 Hz, 2H), 7.30 (s, 6H), 3.99 (s, 3H), 2.62 (s, 9H), 1.86 (m, 18H), –2.58 (s, 2H); MS (MALDI-TOF) m/z 874 ($M+H^+$); HRMS (FAB positive) *m/z* for $C_{61}H_{54}N_4O_2$ 874.4247 (calcd), 874.4237 (found, M^+).

5-(4-Carboxybiphenyl)-10,15,20-tris(2,4,6-trimethylphenyl)porphyrin (BP-H_2): To a solution of **BP-ester** (0.09 g, 0.10 mmol) in THF (70 mL) was added 40 % KOH aqueous solution (10 mL). The solution was refluxed for 1h. After the reaction mixture was cooled to room temperature, aqueous 1M HCl (5 mL) was added. The solution was washed with saturated aqueous $NaHCO_3$ (20 mL) and H_2O (20 mL x 3), dried over anhydrous sodium sulfate, and then the solvent was removed in vacuo. Reprecipitation from CH_2Cl_2/MeOH gave **BP-H_2** as a purple red solid (0.077 g, 0.09 mmol, 90 % yield). Mp > 300°C; ^{1}H NMR (400 Hz, CD_2Cl_2) δ 8.86 (d, J = 4.4 Hz, 2H), 8.68 (d, J = 4.4 Hz, 2H), 8.63 (s, 4H), 8.33 (d, J = 8.0 Hz, 2H), 8.30 (d, J = 8.0 Hz, 2H), 8.06 (m, 4H), 7.29 (s, 6H), 2.61 (s, 9H), 1.86 (s, 6H), 1.84 (s, 12H), –2.60 (s, 2H); MS (MALDI-TOF) m/z 860 ($M+H^+$).

5-(4-Carboxybiphenyl)-10,15,20-tris(2,4,6-trimethylphenyl)porphyrinatozinc(II) (BP): To a solution of **BP-H_2** (0.070 g, 0.076 mmol) in $CHCl_3$ (30 mL) was added a solution of $Zn(OAc)_2$ (0.2 g) in MeOH (6 mL). The solution was refluxed for 2h and cooled to room temperature. The reaction mixture was washed with H_2O (20 mL x 3), dried over anhydrous sodium sulfate, and then the solvent was removed in vacuo. Reprecipitation from CH_2Cl_2/MeOH gave **BP** as a purple red solid (0.066 g, 0.071 mmol, 93 % yield). Mp > 300°C; ^{1}H NMR (400 Hz, CD_2Cl_2) δ 8.94 (br. s, 2H), 8.73 (m, 6H), 8.33 (br. s, 4H), 8.07 (br. s, 4H), 7.29 (s, 6H), 2.61 (s, 9H), 1.84 (s, 18H); MS (MALDI-TOF) m/z 924 ($M+H^+$); HRMS (FAB

positive) *m/z* for $C_{60}H_{50}N_4O_2Zn$ 922.3225 (calcd), 922.3218 (found, M^+); UV-vis (CH_2Cl_2) λ_{max} (nm) 420, 549, 585.

Electrochemical Measurements. The cyclic voltammetric measurements were performed on an ALS 630a electrochemical analyzer using a standard three-electrode system with a glassy carbon working electrode (3 mm diameter), $Ag/AgNO_3$ (0.01M in acetonitrile) reference electrode, and platinum wire counter electrode. The potentials were calibrated with ferrocenium/ferrocene [E_{mid} = +0.20 V vs $Ag/AgNO_3$]. The measured potential was converted to the normal hydrogen electrode (NHE) scale by adding +0.44 V. The stability of the reference electrode potential was confirmed under the experimental conditions.

Preparation of Porphyrin-Modified TiO_2 Electrode. Mesoporous films were prepared from colloidal suspension of TiO_2 nanoparticles (P25, Nippon Aerogel) dispersed in distilled water.[22,31] The suspension was deposited on a transparent conducting glass (Asahi Glass, SnO_2: F, 8 ohm/sq) by using doctor blade technique. The films were annealed at 723 K for 2 h for the 4-μm-thick TiO_2 films or at 673 K for 10 min, followed by similar deposition and annealing (723 K, 2 h) for the 10-μm-thick TiO_2 films. The thickness of the films was determined using surface roughness/profile measuring instrument (SURFCOM 130A, ACCRETECH). The TiO_2 electrodes were immersed in 0.2 mM porphyrin solution at room temperature. Finally, the dye-coated electrodes were rinsed with the same solvent. The amounts of the porphyrins adsorbed on the TiO_2 films were determined by measuring light absorption at the peak of Soret band of the dye molecule that was dissolved from the dye-adsorbed TiO_2 films into DMF containing 0.1 M NaOH.[22]

Photovoltaic Measurements. The photovoltaic measurements were performed in a sandwich cell consisting of the dye-sensitized electrode as the working electrode and a platinum-coated conducting glass electrode as the counter electrode.[22] The two electrodes were placed on top of each other using a thin transparent film of Surlyn polymer (DuPont) as a spacer to form the electrolyte space. A thin layer of electrolyte (0.5 M LiI, 0.01 M I_2, 0.6 M dimethylpropyl imidazolium iodide, and 0.5 M 4-t-butylpyridine in acetonitrile) was introduced onto the interelectrode space. The IPCE values and current-voltage characteristics were determined by using a potentiostat (Bunko–Keiki Co., Ltd., Model HCSSP-25) irradiated with simulated AM 1.5 solar light (100 mW cm^{-2}, Bunko–Keiki Co., Ltd., Model CEP-2000).[22] All experimental values were given as an average from six independent measurements.

References and Notes

[1] *Electron Transfer in Chemistry*; Balzani, V. Ed.; Wiley-VCH: Weinheim, 2001.

[2] (a) *The Photosynthetic Reaction Center*; Deisenhofer, J., Norris, J. R., Eds.; Academic Press: San Diego, 1993. (b) *Anoxygenic Photosynthetic Bacteria*; Blankenship, R. E., Madigan, M. T., Bauer, C. E., Eds.; Kluwer Academic Publishing: Dordrecht, 1995.

[3] (a) Closs, G. L.; Miller, J. R. *Science* **1988**, *240*, 440. (b) Wasielewski, M. R. *Chem. Rev.* **1992**, *92*, 435. (c) Gust, D.; Moore, T. A.; Moore, A. L. *Acc. Chem. Res.* **1993**, *26*, 198. (d) Kurreck, H.; Huber, M. *Angew. Chem., Int. Ed.* **1995**, *34*, 849. (e) Gust, D.; Moore, T. A.; Moore, A. L. *Acc. Chem. Res.* **2001**, *34*, 40.

[4] (a) Harriman, A.; Sauvage, J.–P. *Chem. Soc. Rev.* **1996**, *26*, 41. (b) Paddon-Row, M. N. *Acc. Chem. Res.* **1994**, *27*, 18. (c) Verhoeven, J. W. *Adv. Chem. Phys.* **1999**, *106*, 603. (d) Osuka, A.; Mataga, N.; Okada, T. *Pure Appl. Chem.* **1997**, *69*, 797. (e) Sun, L.; Hammarström, L.; Åkermark, B.; Styring, S. *Chem. Soc. Rev.* **2001**, *30*, 36.

[5] (a) Imahori, H.; Sakata, Y. *Adv. Mater.* **1997**, *9*, 537. (b) Imahori, H.; Sakata, Y. *Eur. J. Org. Chem.* **1999**, 2445. (c) Guldi, D. M. *Chem. Commun.* **2000**, 321. (d) Imahori, H.; Mori, Y.; Matano, Y. *J. Photochem. Photobiol. C* **2003**, *4*, 51. (e) Imahori, H. *Org. Biomol. Chem.* **2004**, *2*, 1425. (f) Imahori, H. *Bull. Chem. Soc. Jpn.* **2007**, *80*, 621.

[6] (a) *Organic Photovoltaics*; Sun, S. S., Sariciftci, N. S., Eds.; CRC: Boca Raton, 2005. (b) *Organic Photovoltaics*; Brabec, C. J., Dyakonov, V., Parisi, J., Sariciftci, N. S., Eds.; Springer: Berlin, 2003. (c) *Organic Photovoltaics*; Brabec, C., Dyakonov, V., Scherf, U., Eds.; Wiley-VCH: Weinheim, 2008.

[7] (a) Tang, C. W. *Appl. Phys. Lett.* **1986**, *48*, 183. (b) Peumans, P.; Yakimov, A.; Forrest, S. R. *J. Appl. Phys.* **2003**, *93*, 3693. (c) Gregg, B. A. *J. Phys. Chem. B* **2003**, *107*, 4688. (d) Coakley, K. M.; McGehee, M. D. *Chem. Mater.* **2004**, *16*, 4533.

[8] (a) Imahori, H.; Fukuzumi, S. *Adv. Funct. Mater.* **2004**, *14*, 525. (b) Imahori, H. *J. Mater. Chem.* **2007**, *17*, 31. (c) Umeyama, T.; Imahori, H. *Energy Environ. Sci.*, **2008**, *1*, 120. (d) Imahori, H.; Umeyama, T. *J. Phys. Chem. C* **2009**, *113*, 9029. (e) Imahori, H.; Umeyama, T.; Ito, S. *Acc. Chem. Res.* **2009**, *42*, 1809.

[9] (a) Hagfeldt, A.; Grätzel, M. *Chem. Rev.* **1995**, *95*, 49. (b) Hagfeldt, A.; Grätzel, M. *Acc. Chem. Res.* **2000**, *33*, 269. (c) Grätzel, M. *Nature* **2001**, *414*, 338. (d) Bignozzi, C. A.; Argazzi, R.; Kleverlaan, C. J. *Chem. Soc. Rev.* **2000**, *29*, 87. (e) Lewis, N. S. *Inorg. Chem.* **2005**, *44*, 6900. (f) Durrant, J. R.; Haque, S. A.; Palomares, E. J. *Chem. Commun.* **2006**, 3279. (g) Robertson, N. *Angew. Chem., Int. Ed.* **2006**, *45*, 2338. (h) Mishra, A.; Fischer, M. K. R.; Bäuerle, P. *Angew. Chem., Int. Ed.* **2009**, *48*, 2474.

[10] (a) Hirata, N.; Lagref, J.–J.; Palomares, E. J.; Durrant, J. R.; Nazeeruddin, M. K.; Grätzel,

M.; Di Censo, D. *Chem.–Eur. J.* **2004**, *10*, 595. (b) Piotrowiak, P.; Galoppini, E.; Wei, Q.; Meyer, G. J.; Wiewior, P. *J. Am. Chem. Soc.* **2003**, *125*, 5278. (c) Kamat, P. V.; Haria, M.; Hotchandani, S. *J. Phys. Chem. B* **2004**, *108*, 5166. (d) Huang, S. Y.; Schlichthörl, G.; Nozik, A. J.; Grätzel, M.; Frank, A. J. *J. Phys. Chem. B* **1997**, *101*, 2576.

[11] (a) Yu, G.; Gao, J.; Hummelen, J. C.; Wudl, F.; Heeger, A. J. *Science* **1995**, *270*, 1789. (b) Padinger, F.; Rittberger, R. S.; Sariciftci, N. S. *Adv. Funct. Mater.* **2003**, *13*, 85. (c) Wienk, M. M.; Kroon, J. M.; Verhees, W. J. H.; Knol, J.; Hummelen, J. C.; van Hal, P. A.; Janssen, R. A. J. *Angew. Chem., Ind. Ed.* **2003**, *42*, 3371. (d) Ma, W.; Yang, C.; Gong, X.; Lee, K.; Heeger, A. J. *Adv. Funct. Mater.* **2005**, *15*, 1617. (e) Scharber, M. C.; Mühlbacher, D.; Koppe, M.; Denk, P.; Waldauf, C.; Heeger, A. J.; Brabec, C. J. *Adv. Mater.* **2006**, *18*, 789. (f) Kim, Y.; Lee, K.; Coates, N. E.; Moses, D.; Nguyen, T.–Q.; Dante, M.; Heeger, A. J. *Science* **2007**, *317*, 222. (g) Hou, J.; Chen, H.–Y.; Zhang, S.; Li, G.; Yang, Y. *J. Am. Chem. Soc.* **2008**, *130*, 16144. (h) Liang, Y.; Feng, D.; Wu, Y.; Tsai, S.–T.; Li, G.; Ray, C.; Yu, L. *J. Am. Chem. Soc.* **2009**, *131*, 7792. (i) Park, S. H.; Roy, A.; Beaupre, S.; Cho, S.; Coates, N.; Moon, J. S.; Moses, D.; Leclerc, M.; Lee, K.; Heeger, A. J. *Nat. Photonics* **2009**, *3*, 297.

[12] (a) Halls, J. J. M.; Walsh, C. A.; Greenham, N. C.; Marseglia, E. A.; Friend, R. H.; Moratti, S. C.; Holmes, A. B. *Nature* **1995**, *376*, 498. (b) Schmidt-Mende, L.; Fechtenkötter, A.; Müllen, K.; Moons, E.; Friend, R. H.; MacKenzie, J. D. *Science* **2001**, *293*, 1119. (c) Nierengarten, J.–F. *New J. Chem.* **2004**, *28*, 1177.

[13] (a) Hiramoto, M.; Fujiwara, H.; Yokoyama, M. *Appl. Phys. Lett.* **1991**, *58*, 1062. (b) Tsuzuki, T.; Shirota, Y.; Rostalski, J.; Meissner, D. *Sol. Energy Mater. Sol. Cells* **2000**, *61*, 1. (c) Xue, J.; Uchida, S.; Rand, B. P.; Forrest, S. R. *Appl. Phys. Lett.* **2004**, *84*, 3013. (d) Xue, J.; Rand, B. P.; Uchida, S.; Forrest, S. R. *Adv. Mater.* **2005**, *17*, 66.

[14] (a) Huynh, W. U.; Dittmer, J. J.; Alivisatos, A. P. *Science* **2002**, *295*, 2425. (b) Liu, J.; Tanaka, T.; Sivula, K.; Alivisatos, A. P.; Fréchet, J. M. J. *J. Am. Chem. Soc.* **2004**, *126*, 6550.

[15] (a) Hara, K.; Kurashige, M.; Dan-oh, Y.; Kasada, C.; Shinpo, A.; Suga, S.; Sayama, K.; Arakawa, H. *New. J. Chem.* **2003**, *27*, 783. (b) Horiuchi, T.; Miura, H.; Sumioka, K.; Uchida, S. *J. Am. Chem. Soc.* **2004**, *126*, 12218. (c) Kitamura, T.; Ikeda, M.; Shigaki, K.; Inoue, T.; Anderson, N. A.; Ai, X.; Lian, T. Q.; Yanagida, S. *Chem. Mater.* **2004**, *16*, 1806. (d) Schmidt-Mende, L.; Bach, U.; Humphry-Baker, R.; Horiuchi, T.; Miura, H.; Ito, S.; Uchida, S.; Grätzel, M. *Adv. Mater.* **2005**, *17*, 813. (e) Wang, Z. S.; Hara, K.; Dan-Oh, Y.; Kasada, C.; Shinpo, A.; Suga, S.; Arakawa, H.; Sugihara, H. *J. Phys. Chem. B* **2005**, *109*, 3907. (f) Hara, K.; Sato, T.; Katoh, R.; Furube, A.; Yoshihara, T.; Murai, M.; Kurashige, M.; Ito, S.; Shinpo, A.; Suga, S.; Arakawa, H. *Adv. Funct. Mater.* **2005**, *15*,

246. (g) Koumura, N.; Wang, Z.–S.; Mori, S.; Miyashita, M.; Suzuki, E.; Hara, K. *J. Am. Chem. Soc.* **2006**, *128*, 14256. (h) Kim, S.; Lee, J. K.; Kang, S. O.; Ko, J.; Yum, J.–H.; Fantacci, S.; De Angelis, F.; Di Censo, D.; Nazeeruddin, M. K.; Grätzel, M. *J. Am. Chem. Soc.* **2007**, *128*, 16701. (i) Hwang, S.; Lee, J. H.; Park, C.; Lee, H.; Kim, C.; Park, C.; Lee, M.–H.; Lee, W.; Park, J.; Kim, K.; Park, N.–G.; Kim, C. *Chem. Commun.* **2007**, 4887. (j) Ito, S.; Miura, H.; Uchida, S.; Takata, M.; Sumioka, K.; Liska, P.; Comte, P.; Péchy, P.; Grätzel, M. *Chem. Commun.* **2008**, 5194. (k) Choi, H.; Baik, C.; Kang, S. O.; Ko, J.; Kang, M.–S.; Nazeeruddin, M. K.; Grätzel, M. *Angew. Chem., Int. Ed.* **2008**, *47*, 327. (l) Zhang, G.; Bala, H.; Cheng, Y.; Shi, D.; Lv, X.; Yu, Q.; Wang, P. *Chem. Commun.* **2009**, 2198.

[16] (a) Kay, A.; Grätzel, M. *J. Phys. Chem.* **1993**, *97*, 6272. (b) Campbell, W. M.; Burrell, A. K.; Officer, D. L.; Jolley, K. W. *Coord. Chem. Rev.* **2004**, *248*, 1363. (c) Nazeeruddin, M. K.; Humphry-Baker, R.; Officer, D. L.; Campbell, W. M.; Burrell, A. K.; Grätzel, M. *Langmuir* **2004**, *20*, 6514. (d) Schmidt-Mende, L.; Cambell, W. M.; Wang, Q.; Jolley, K. W.; Officer, D. L.; Nazeeruddin, M. K.; Grätzel, M. *ChemPhysChem* **2005**, *6*, 1253. (e) Wang, Q.; Campbell, W. M.; Bomfantani, E. E.; Jolley, K. W.; Officier, D. L.; Walsh, P. J.; Gordon, K.; Humphery-Baker, R.; Nazeeruddin, M. K.; Grätzel, M. *J. Phys. Chem. B* **2005**, *109*, 15397. (f) Campbell, W. M.; Jolley, K. W.; Wagner, P.; Wagner, K.; Walsh, P. J.; Gordon, K. C.; Schmidt-Mende, L.; Nazeeruddin, M. K.; Wang, Q.; Grätzel, M.; Officer, D. L. *J. Phys. Chem. C* **2007**, *111*, 11760.

[17] (a) Cherian, S.; Wamser, C. C. *J. Phys. Chem. B* **2000**, *104*, 3624. (b) Watson, D. F.; Marton, A.; Stux, A. M.; Meyer, G. J. *J. Phys. Chem. B* **2003**, *107*, 10971. (c) Watson, D. F.; Marton, A.; Stux, A. M.; Meyer, G. J. *J. Phys. Chem. B* **2004**, *108*, 11680. (d) Rochford, J.; Chu, D.; Hagfeldt, A.; Galoppini, E. *J. Am. Chem. Soc.* **2007**,*129*, 4655. (e) Stromberg, J. R.; Marton, A.; Kee, H. L.; Kirmaier, C.; Diers, J. R.; Muthiah, C.; Taniguchi, M.; Lindsey, J. S.; Bocian, D. F.; Meyer, G. J.; Holten, D. *J. Phys. Chem. C* **2007**, *111*, 15464. (f) Rochford, J.; Galoppini, E. *Langmuir* **2008**, *24*, 5366.

[18] (a) Boschloo, G. K.; Goossens, A. *J. Phys. Chem.* **1996**, *100*, 19489. (b) Koehorst, R. B. M.; Boschloo, G. K.; Savenije, T. J.; Goossens, A.; Schaafsma, T. J. *J. Phys. Chem. B* **2000**, *104*, 2371. (c) Clifford, J. N.; Yahioglu, G.; Milgrom, L. R.; Durrant, J. R. *Chem. Commun.* **2002**, 1260. (d) Odobel, F.; Blart, E.; Lagrée, M.; Villiera, M.; Boujtita, H.; El Murr, N.; Caramori, S.; Bignozzi, C. A. *J. Mater. Chem.* **2003**, *13*, 502. (e) Jasieniak, J.; Johnston, M.; Waclawik, E. R. *J. Phys. Chem. B* **2004**, *108*, 12962. (f) Lee, C.–W.; Lu, H.–P.; Lan, C.–M.; Huang, Y.–L.; Linag, Y.–R.; Yen, W.–N.; Liu, Y.–C.; Lin, Y.–S.; Diau, E. W.–G.; Yeh, C.–Y. *Chem.–Eur. J.* **2009**, *15*, 1403. (g) Liu, Y. J.; Xiang, N.; Feng, X. M.; Shen, P.; Zhou, W. P.; Weng, C.; Zhao, B.; Tan, S. T. *Chem. Commun.* **2009**,

2499. (h) Lin, C. Y.; Lo, C. F.; Luo, L.; Lu, H. P.; Hung, C. S.; Diau, E. W.–G. *J. Phys. Chem. C* **2009**, *113*, 755.

[19] (a) Ma, T. L.; Inoue, K.; Yao, K.; Noma, H.; Shuji, T.; Abe, E.; Yu, J. H.; Wang, X. S.; Zhang, B. W. *J. Electroanal. Chem.* **2002**, *537*, 31. (b) Ma, T. L.; Inoue, K.; Noma, H.; Yao, K.; Abe, E. *J. Photochem. Photobiol. A* **2002**, *151*, 207. (c) Hasobe, T.; Fukuzumi, S.; Hattori, S.; Kamat, P. V. *Chem. Asian J.* **2007**, *2*, 265. (d) Kamat, P. V. *J. Phys. Chem. C* **2007**, *111*, 2834. (e) Hasobe, T.; Hattroi, S.; Kamat, P. V.; Fukuzumi, S. *Tetrahedron* **2006**, *62*, 1937. (f) Wang, X.–F.; Zhan, C.–H.; Maoka, T.; Wada, Y.; Koyama, Y. *Chem. Phys. Lett.* **2007**, *447*, 79. (g) Wang, X. F.; Kitao, O.; Zhou, H. S.; Tamiaki, H.; Sasaki, S. *J. Phys. Chem. C* **2009**, *113*, 7954. (h) Park, J. K.; Lee, H. R.; Chen, J.; Shinokubo, H.; Osuka, A.; Kim, D. *J. Phys. Chem. C* **2008**, *112*, 16691.

[20] (a) Fungo, F.; Otero, L. A.; Sereno, L.; Silber, J. J.; Durantini, E. N. *J. Mater. Chem.* **2000**, *10*, 645. (b) Brune, A.; Jeong, G.; Liddell, P. A.; Sotomura, T.; Moore, T. A.; Moore, A. L.; Gust, D. *Langmuir* **2004**, *20*, 8366. (c) Huijser, A.; Marek, P. L.; Savenije, T. J.; Siebbeles, L. D. A.; Scherer, T.; Hauschild, R.; Szmytkowski, J.; Kalt, H.; Hahn, H.; Balaban, T. S. *J. Phys. Chem. C* **2007**, *111*, 11726.

[21] (a) He, J.; Benkö, G.; Korodi, F.; Polívka, T.; Lomoth, R.; Åkermark, B.; Sun, L.; Hagfeldt, A.; Sundström, V. *J. Am. Chem. Soc.* **2002**, *124*, 4922. (b) Reddy, P. Y.; Giribabu, L.; Lyness, C.; Snaith, H. J.; Vijaykumar, C.; Chandrasekharam, M.; Lakshmikantam, M.; Yum, J.–H.; Kalyanasundaram, K.; Grätzel, M.; Nazeeruddin, M. K, *Angew. Chem., Int. Ed.* **2007**, *46*, 373. (c) Cíd, J.–J.; Yum, J.–H.; Jang, S.–R.; Nazeeruddin, M. K.; Martínez-Ferrero, E.; Palomares, E. J.; Ko, J.; Grätzel, M.; Torres, T. *Angew. Chem., Int. Ed.* **2007**, *46*, 8358. (d) Eu, S.; Katoh, T.; Umeyama, T.; Matano, Y.; Imahori, H. *Dalton Trans.* **2008**, 5476. (e) Cid, J.–J.; Garcia-Iglesias, M.; Yum, J.–M.; Forneli, A.; Albero, J.; Martinez-Ferrero, E.; Vazquez, P.; Grätzel, M.; Nazeeruddin, M. K.; Palomares, E.; Torres, T. *Chem.–Eur. J.* **2009**, *15*, 5130.

[22] (a) Imahori, H.; Hayashi, S.; Umeyama, T.; Eu, S.; Oguro, A.; Kang, S.; Matano, Y.; Shishido, T.; Ngamsinlapasathian, S.; Yoshikawa, S. *Langmuir* **2006**, *22*, 11405. (b) Eu, S.; Hayashi, S.; Umeyama, T.; Oguro, A.; Kawasaki, M.; Kadota, N.; Matano, Y.; Imahori, H. *J. Phys. Chem. C* **2007**, *111*, 2777. (c) Tanaka, M.; Hayashi, S.; Eu, S.; Umeyama, T.; Matano, Y.; Imahori, H. *Chem. Commun.* **2007**, 2069. (d) Kira, A.; Tanaka, M.; Umeyama, T.; Matano, Y.; Li, G.; Ye, S.; Isosomppi, M.; Tkachenko, N. V.; Lemmetyinen, H.; Imahori, H. *J. Phys. Chem. C* **2007**, *111*, 13618. (e) Eu, S.; Hayashi, S.; Umeyama, T.; Matano, Y.; Araki, Y.; Imahori, H. *J. Phys. Chem. C* **2008**, *112*, 4396. (f) Hayashi, S.; Matsubara, Y.; Eu, S.; Hayashi, H.; Umeyama, T.; Matano, Y.; Imahori, H. *Chem. Lett.* **2008**, *37*, 846. (g) Hayashi, S.; Tanaka, M.; Hayashi, H.; Eu, S.; Umeyama,

T.; Matano, Y.; Araki, Y.; Imahori, H. *J. Phys. Chem. C* **2008**, *112*, 15576. (h) Kira, A.; Umeyama, T.; Matano, Y.; Yoshida, K.; Isoda, S.; Park, J. K.; Kim, D.; Imahori, H. *J. Am. Chem. Soc.* **2009**, *131*, 3198. (i) Hayashi, H.; Kira, A.; Umeyama, T.; Matano, Y.; Charoensirithavorn, P.; Sagawa, T.; Yoshikawa, S.; Tkachenko, N. V.; Lemmetyinen, H.; Imahori, H. *J. Phys. Chem. C* **2009**, *113*, 10819.

[23] (a) Persson, P.; Lundqvist, M. J.; Ernstorfer, R.; Goddard, W. A., III.; Willig, F. *J. Chem. Theory Comput.* **2006**, *2*, 441. (b) Anderson, N. A.; Ai, X.; Chen, D.; Mohler, D.; Lian, T. *J. Phys. Chem. B* **2003**, *107*, 14231. (c) Wang, D.; Mendelsohn, R.; Galoppini, E.; Hoertz, P. G.; Carlisle, R. A.; Meyer, G. J. *J. Phys. Chem. B* **2004**, *108*, 16642. (d) Kilså, K.; Mayo, E. I.; Kuciauskas, D.; Villahermosa, R.; Lewis, N. S.; Winkler, J. R.; Gray, H. B. *J. Phys. Chem. A* **2003**, *107*, 3379. (e) Hoertz, P. G.; Carlisle, R. A.; Meyer, G. J.; Wang, D.; Piotrowiak, P.; Galoppini, E. *Nano Lett.* **2003**, *3*, 325.

[24] (a) Tachibana, Y.; Haque, S. A.; Mercer, I. P.; Durrant, J. R.; Klug, D. R. *J. Phys. Chem. B* **2000**, *104*, 1198. (b) Clifford, J. N.; Palomares, E. J.; Nazeeruddin, M. K.; Grätzel, M.; Nelson, J.; Li, X.; Long, N. J.; Durrant, J. R. *J. Am. Chem. Soc.* **2004**, *126*, 5225.

[25] Luo, C.; Guldi, D. M.; Imahori, H.; Tamaki, K.; Sakata, Y. *J. Am. Chem. Soc.* **2000**, *122*, 6535.

[26] Fuson, R. C.; Horning, E. C.; Rowland, S. P.; Ward, M. L.; Barnes, R. P. *Org. Syntheses* **1943**, 23, 57.

[27] Blettner, C. G.; Konig, W. A.; Stenzel, W.; Schotten, T. *Synlett* **1998**, 295.

[28] Harada, A.; Shiotsuki, K.; Fukushima, H.; Yamaguchi, H.; Kamachi, M. *Inorg. Chem.* **1995**, *34*, 1070.

[29] Zaoying, L.; Jianglin, L.; Cong, L.; Wei, X. *Synth. Commun.* **2000**, *30*, 917.

[30] Nazeeruddin, M. K.; Kay, A.; Rodicio, I.; Humphry-Baker, R.; Müller, E.; Liska, P.; Vlachopoulos, N.; Grätzel, M. *J. Am. Chem. Soc.* **1993**, *115*, 6382.

[31] Nakade, S.; Matsuda, M.; Kambe, S.; Saito, Y.; Kitamura, T.; Sakata, T.; Wada, Y.; Mori, H.; Yanagida, S. *J. Phys. Chem. B* **2002**, *106*, 10004.

[32] *Spectrometric Identification of Organic Compounds*; Silverstein, R. M., Bassler, G. C., Morrill, T. C. Eds.; John Wiley & Sons: New York, 1991.

[33] Although the ATR-FTIR spectra of the TiO_2/**2,4,6-Me** exhibited new bands at 1500-1600 cm^{-1}, we could not assign these bands owing to the complex molecular structure of the porphyrin.

[34] Shklover, V.; Nazeeruddin, M. K.; Zakeeruddin, S. M.; Barbé, C.; Kay, A.; Haibach, T.; Steurer, W.; Hermann, R.; Nissen, H.–U.; Grätzel, M. *Chem. Mater.* **1997**, *9*, 430.

[35] MeOH molecules are known to adsorb onto a TiO_2 surface. There are two modes of the MeOH adsorption, molecular physisorption and dissociative chemisorption. Thus, the

protic solvents may influence the adsorption and geometry of the porphyrins on the TiO_2 surface. (a) Wang, C.−Y.; Groenzin, H.; Shultz, M. J. *J. Phys. Chem. B* **2004**, *108*, 265. (b) Wang, C.−Y.; Groenzin, H.; Shultz, M. J. *J. Am. Chem. Soc.* **2005**, *127*, 9736.

[36] Addition of chenodeoxycholic acid (0.2 mM) as an inhibitor of dye aggregation to MeOH solution of **2,4,6-Me** for adsorption onto the TiO_2 surface led to a virtually same η value (4.4% vs 4.6%) for the immersion time of 1 h, while the long immersion time (12 h) results in slight increase of the η value (4.1% vs 3.7%).

Chapter 2

Photoiduced Charge Carrier Dynamics of Zn-Porphyrin-TiO_2 Electrodes: The Key Role of Charge Recombination for Solar Cell Performance

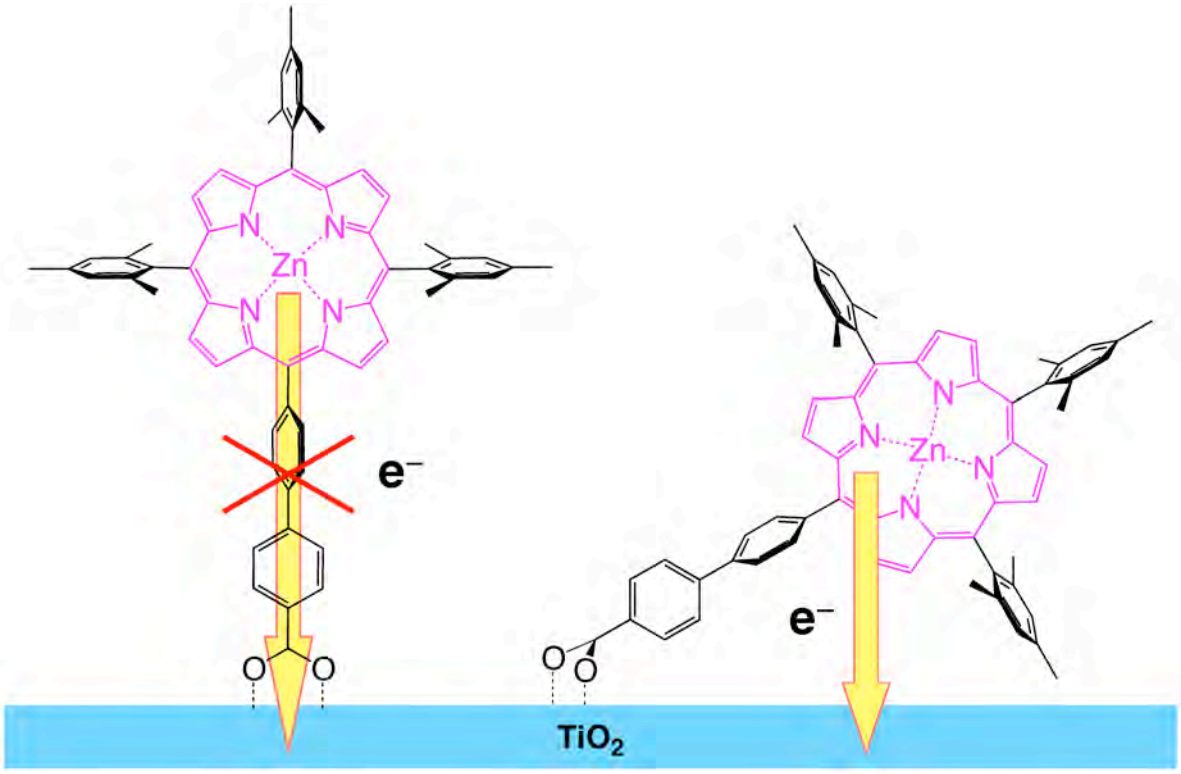

Abstract: Time resolved absorption spectroscopy has been used to study photoinduced electron injection and charge recombination in Zn-porphyrin sensitized nanostructured TiO_2 electrodes. The electron transfer dynamics is correlated to the performance of dye sensitized solar cells based on the same electrodes. We find that the dye/semiconductor binding can be described with a heterogeneous geometry where the Zn-porphyrin molecules are attached to the TiO_2 surface with a distribution of tilt angles. The binding angle determines the porphyrin-semiconductor electron transfer distance and charge transfer occurs through space, rather than through the bridge connecting the porphyrin to the surface. For short immersion times (1 h), there is a direct correlation between solar cell efficiency and amplitude of the kinetic component due to long-lived conduction band electrons, once variations in light harvesting (surface coverage) have been taken into account. Long immersion time (12 h) results in decreased solar cell efficiency because of decreased efficiency of electron injection.

Introduction

Thin film dye-sensitized solar cells (DSC) hold great promise to become inexpensive and sustainable devices for solar energy conversion with high power conversion efficiency.[1] These prospects have triggered many research efforts toward optimizing the performance of functioning practical devices, including the development of innovative sensitizers, solid state electrolytes, and novel semiconductor materials and morphologies. The DSC with the highest power conversion efficiency manufactured to this date employs Ru-polypyridyl dyes for sensitization.[2] The light initiated processes in the active electrodes of these solar cells have been extensively studied.[3] Electron injection and recombination at the sensitizer-semiconductor interface are key processes for solar cell power conversion efficiency. For maximum efficiency electron injection should be much faster than the intrinsic excited state decay of the sensitizer and charge recombination should be sufficiently slow so that there is time for re-reduction of the oxidized sensitizer by the redox couple of the electrolyte. On the one hand, it is expected that the sensitizer–semiconductor binding geometry and distance are important factors in controlling the electron transfer rates. On the other hand, the complex nanostructured interface leads to less than straightforward, sometimes contra-intuitive, relation between molecular structure and electron transfer rates. The distance dependence of electron injection and charge recombination has been extensively studied for polypyridyl and other dyes attached to nanostructured semiconductor surfaces.[3a] With the idea that electron transfer occurs through the spacer (molecular or insulating metal oxide shell) connecting the sensitizer chromophore to the semiconductor surface, the distance dependence has been studied by varying the spacer length (thickness of the shell). With only a few exceptions[4] a very weak distance dependence of the electron transfer rates was observed.[5] This unexpected behavior was suggested to be due to flexibility of the one-carboxyl sensitizer attachment that allowed proximity of the Ru^{II}-metal center and the TiO_2 surface. For the metal oxide shell spacer,[6] the weak distance dependence was suggested to be a result of the presence of intraband gap states within the metal oxide coating layer.[7] From these results it is clear that there is a great need for sensitizer molecules that can bind in a well-defined geometry to the semiconductor surface. Having such a system would greatly help the manufacturing of a DSC material with predictable properties, as well as provide a testing ground for interfacial electron transfer. Understanding of the factors controlling dye–semiconductor binding geometry appears to be a route to this goal.

For Ru–polypyridyl dyes (e.g., Ru–N3, the black dye) resulting in the most efficient solar cells, electron-cation recombination has been shown to be very slow (microsecond time scale)[8] and slower than regeneration of the oxidized sensitizer by the redox mediators,[9] and therefore not a limiting factor for the efficiency of a solar cell based on these dyes. This fact, established for some Ru–polypyridyl sensitizers often seems to have been extrapolated to

suggest that this is also the case for other dyes,[10] leading to a picture where variations of solar cell efficiency have been directly correlated to the efficiency and rate of electron injection.[10] One objective of this paper is to show that electron–cation recombination can be a more important process for controlling solar cell efficiency. Another objective is to provide new results that allow us to correlate electron injection and recombination rates to the binding geometry of the sensitizer and thus take the first steps toward the goal of designing nanostructured dye-sensitizer materials with predictable properties. For this work we have chosen to study Zn-porphyrin sensitizers for two reasons. For large-scale production of DSC, sensitizers free of noble or rare metals are desirable; the wide variety of porphyrins available are of great interest in this respect. As discussed above, the complex nature of the nanostructured semiconductor surface to which the sensitizer binds makes prediction of optimal sensitizer properties a nontrivial task. The synthetic flexibility of porphyrins offers great possibilities to modify properties such as anchoring group(s), length of connecting spacer, molecule bulkiness, redox potential, excited state energy, and surface coverage.[11] This will allow us to explore factors such as dye binding, packing on the semiconductor surface, and dye–semiconductor interaction, which ultimately control electron injection and charge recombination. The dye–semiconductor interactions have been characterized in two ways: information on electron transfer rates was obtained from ultrafast laser spectroscopy measurements and information on dye attachment to the TiO_2 surface was obtained from transmission electron microscopy (TEM) measurements. Referring to Marcus theory,[12] the rate of electron transfer between a discrete donor and acceptor level in the nonadiabatic regime is given by

$$k_{\mathrm{ET}} = \frac{2\pi}{\hbar}\frac{|H|^2}{\sqrt{4\pi\lambda k_{\mathrm{B}}T}}\exp\left(-\frac{(\lambda+\Delta G_0)^2}{4\lambda k_{\mathrm{B}}T}\right) \tag{1}$$

where H^2 is the electronic coupling between the donor and acceptor states, ΔG_0 is the sum of the free energy difference, and λ is the total reorganization energy. The electronic coupling (H^2) decreases exponentially with increasing distance d between the donor and the acceptor as

$$H^2 = H_0{}^2\exp(-\beta d) \tag{2}$$

where $H_0{}^2$ is the value at $d = 0$ and the constant β is related to the properties of the intervening medium. For electron injection from the excited state of the sensitizer to the density of states in the conduction band of the semiconductor, Gerischer formulated a modified theory.[13] According to this theory, the interfacial electron transfer rate can be altered by varying the free energy of electron transfer, ΔG_0 (driving force), electronic coupling, and reorganization energy

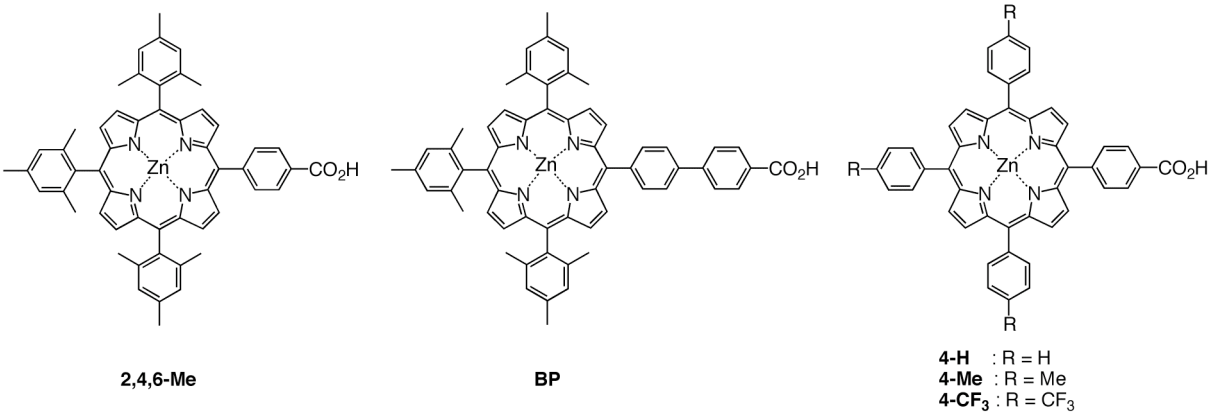

Figure 1. Molecular structure of zinc porphyrins used in this study.

(and for injection the density of acceptor states). For quantitative calculations of electron transfer rates in dye-sensitized systems this theory should be used. In the present work we only perform relative comparisons between sensitizers with very similar energetic attached to the same semiconductor; we can therefore use Marcus' version of electron transfer theory. The present work focuses on several porphyrins **4-H**, **2,4,6-Me**, **4-CF$_3$**, **4-Me**, and **BP** (displayed in Figure 1) tailored at the molecular level with systematic substitutions that allow assessing several of these parameters. The rates of electron injection from the photoexcited sensitizer to the conduction band of the TiO_2 semiconductor, as well as recombination between conduction band electrons and oxidized sensitizer were measured with transient absorption laser spectroscopy. The samples for these measurements were Zn-porphyrin sensitized TiO_2 electrodes in contact with solvent (a 1:1 mixture of *t*-BuOH/acetonitrile).

An important aim of the present work is to seek a correlation between solar cell efficiency and electron transfer dynamics of the active Zn-porphyrin/TiO_2 electrode. This was achieved by considering the key factors contributing to the solar cell conversion efficiency, and we will show that there is a direct correlation between the solar cell efficiency corrected for surface coverage (η_{rel}) and the amplitude of long-lived (~50 ns) charges measured for the Zn-porphyrin/TiO_2 electrode. This shows that minimizing fast recombination in these electrodes is an important way to obtain high solar cell efficiency.

Result and Discussion

Photophysics in Solution. *Steady State Spectra.* Figure 2a shows the steady-state absorption and fluorescence spectra of 2,4,6-Me dissolved in MeOH. The strongly absorbing Soret band centered at 423 nm corresponds to the $S_2 \leftarrow S_0$ transition, whereas the two much weaker Q-bands observed at 558 and 597 nm correspond to the $S_1[1] \leftarrow S_0[0]$ and $S_1[0] \leftarrow$

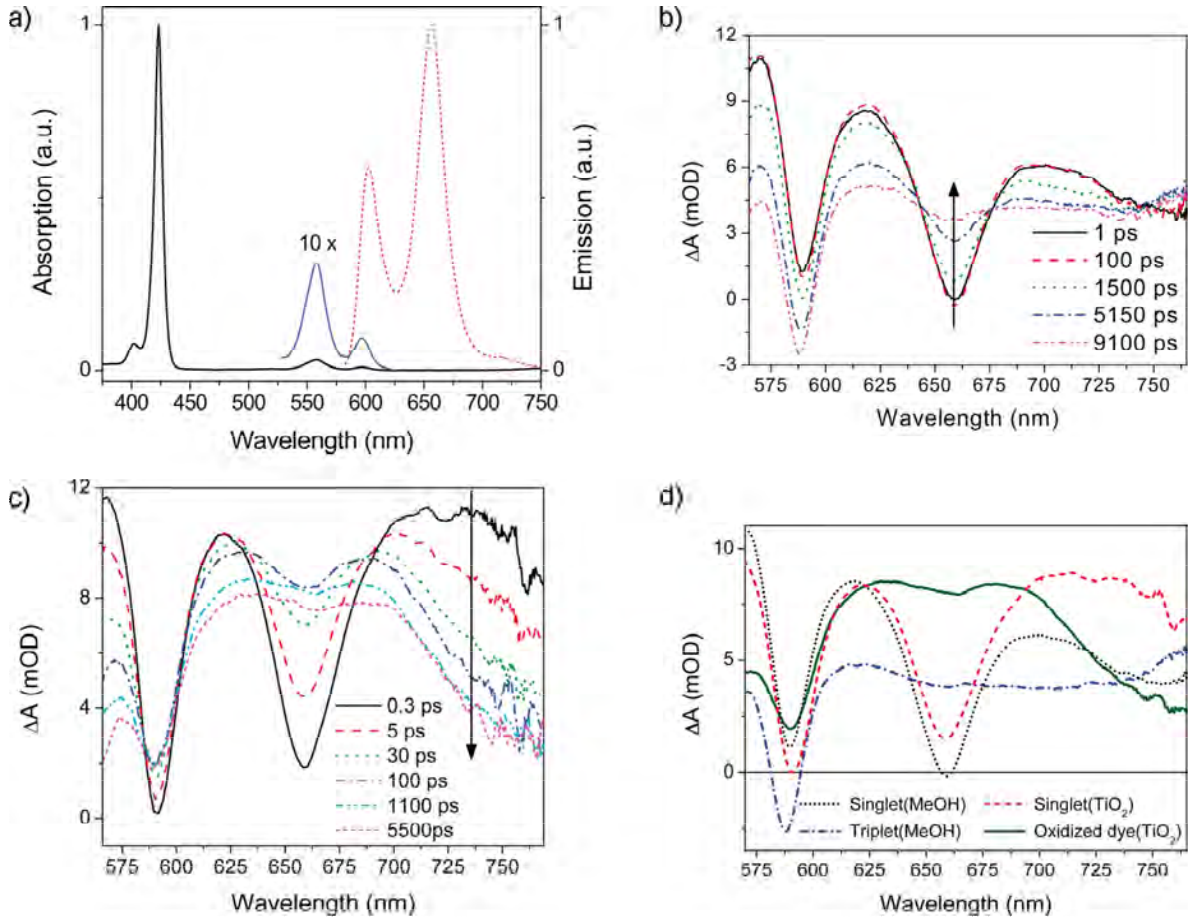

Figure 2. (a) Normalized steady-state absorption (solid black) and emission (dashed red) spectra of **2,4,6-Me** in MeOH. The absorption spectrum is magnified by a factor of 10 in the Q-band region (blue). (b) Transient absorption spectra of **2,4,6-Me** in MeOH solution recorded at different times after excitation. The arrow indicates the direction of increasing delay time. (c) Transient absorption spectra of TiO_2 film sensitized by **2,4,6-Me** in *t*-BuOH/ACN for 12 h, recorded at different times after excitation. The arrow indicates the direction of increasing delay time. (d) Spectral components extracted from the measured transient absorption spectra. The dotted line represents the singlet excited-state spectrum (including stimulated emission) in methanol solution, while the singlet excited-state spectrum on TiO_2 is the dashed line. The triplet spectrum in methanol solution is the blue dash-dot line and the oxidized dye on TiO_2 is represented by a solid green line.

$S_0[0]$ transitions, respectively. Fluorescence from the S_1 state is detected at 601 and 655 nm and assigned to the $S_1[0] \rightarrow S_0[0]$ and $S_1[0] \rightarrow S_0[1]$ transitions, presenting only a small Stokes shift. All the dyes studied exhibit very similar spectroscopic features, indicating that the electronic structure of the porphyrin moiety is not perturbed by the substituents at the meso-phenyl positions. In this respect, **2,4,6-Me**, **BP**, **4-H**, **4-Me**, and **4-CF_3** are appropriate

models to examine the effects of dye–TiO_2 distance, driving force and steric effects on aggregation, while preserving the electronic properties of the porphyrin ring.

Transient Absorption Spectra. Spectral characterization of the laser excited porphyrins in solution is the first step for the time-resolved studies of the interfacial electron transfer dynamics in the dye–sensitized TiO_2 electrode. Transient absorption spectra obtained in solution give the properties of the involved excited states and allow identifying the optimal spectral regions for subsequent probing of the electron transfer processes in the films. The measured transient absorption spectrum has contributions from the ground state bleaching (GSB), singlet excited state stimulated emission (SE) and absorption (ESA) and triplet state absorption (TSA), according to eq 3:

$$\Delta A(\lambda) = \Delta A_{ESA}(\lambda) + \Delta A_{TSA}(\lambda) - \Delta A_{GSB}(\lambda) - \Delta A_{SE}(\lambda) \qquad (3)$$

The transient absorption spectra of **2,4,6-Me** in MeOH solution measured at several delay times from ~1 ps to 9.1 ns after excitation at 560 nm in the Q(1,0) band with an excitation intensity of 4.35×10^{13} photons/cm^2 per pulse are shown in Figure 2b. Since the triplet state is populated through the nanosecond time scale decay of the singlet excited state, the measured transient absorption spectrum at early time 1 ps can be used to obtain the singlet excited state spectrum ($\Delta A_{ESA}(\lambda) - \Delta A_{SE}(\lambda)$, shown in Figure 2d), whereas the spectrum measured at ~5 ns yields the triplet spectrum, ($\Delta A_{TSA}(\lambda)$ (shown in Figure 2d). The procedure to obtain the component spectra is described in the Experimental Section. The singlet state spectrum has two pronounced bands at ~590 and ~660 nm due to stimulated emission (the 590 nm band also carries some contribution from ground state bleaching since it has not been subtracted). These bands are superimposed on the broad and structureless singlet excited state absorption (ESA). The triplet absorption spectrum also shown in Figure 2d, is broad and featureless and extends over the entire measured wavelength range, in good agreementwith the triplet spectrum of a similar compound reported by Rogers et al.[16] The triplet spectrum shown in Figure 2d also carries the ground state bleach at ~590 nm.

Electron Injection and Recombination in Porphyrin/TiO_2 Films. The intermediates (excited states) and products (oxidized dye and electrons) of electron injection have characteristic absorption spectra, implying that the processes can be monitored by measuring the time evolution of the transient absorption spectrum. In that way we obtain information about the nature of intermediates and products as well as the variation of their concentrations. Figure 2c shows the transient absorption spectrum of **2,4,6-Me**/TiO_2 measured at several delay times from 0.3 ps to 5.5 ns. At 5 ns electron injection is complete (see below) and the only

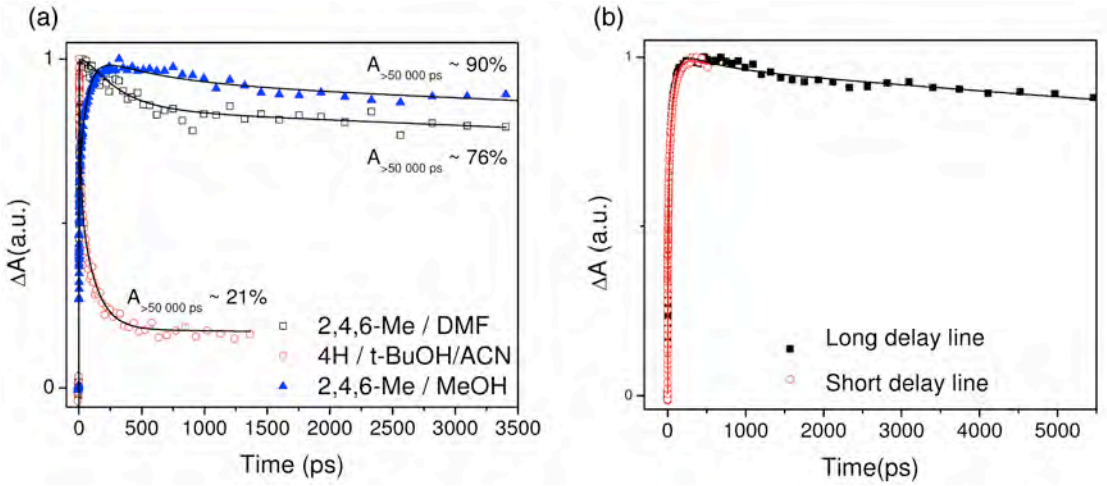

Figure 3. (a) Long delay line kinetics (at 660 nm) of **2,4,6-Me** on TiO_2 sensitized in MeOH (closed blue triangle) and DMF (open, black square) and of **4-H** on TiO_2 sensitized in *t*-BuOH/ACN (open, red circle) for 12 hours. All kinetics are normalized to maxima and solid black lines represents fits of the kinetics.

Table 1. Time Constants (τ) and Amplitudes (A) for the Measured TA Kinetics at 660 nm.[a]

dye	immersion solvent	immersion time (h)	rise τ (ps) [A (%)]			decay τ (ps) [A (%)]		
4-CF_3	*t*-BuOH/ACN	1	0.4	-	-	9 [29]	137 [35]	>50000 [36]
4-H	*t*-BuOH/ACN	1	<0.1 [7]	0.4 [32]	-	12 [50]	87 [35]	>50000 [15]
4-Me	*t*-BuOH/ACN	1	0.4	-	-	13 [29]	112 [36]	>50000 [35]
2,4,6-Me	*t*-BuOH/ACN	1	<0.1 [52]	2.4 [18]	-	59 [17]	391 [18]	>50000 [65]
2,4,6-Me	*t*-BuOH/ACN	12	<0.1 [21]	4 [16]	53 [12]	-	268 [9]	>50000 [91]
2,4,6-Me	MeOH	1	<0.1 [31]	5 [18]	60 [43]	-	547 [5]	>50000 [95]
2,4,6-Me	MeOH	12	<0.1 [29]	3.5 [11]	64 [47]	-	547 [5]	>50000 [95]
2,4,6-Me	DMF	1	<0.1 [6]	1.2 [33]	-	32 [39]	259 [33]	>50000 [28]
BP	*t*-BuOH/ACN	1	<0.1 [72]	0.9 [18]	-	43 [37]	256 [32]	>50000 [32]

[a] Accuracy of time constants (τ) and corresponding amplitudes (A) are ± 5%.

species contributing to the transient spectrum are the depleted ground state and the oxidized dye (possibly with some small contribution from the weak absorption of electrons[31,3m]). The spectrum is shown in Figure 2d and agrees closely with previously reported spectra of the Zn-porphyrin radical cation.[17] In particular, it should be noted that the long time spectrum of the Zn-porphyrin/TiO_2 films is distinct from that of the triplet state (Figure 2d). From the **2,4,6-Me**/TiO_2 TA spectrum measured at early times (0.3 ps), the singlet excited state spectrum can be obtained and it is very similar to the singlet excited state spectrum measured in solution (Figure 2d), showing that the singlet excited state of the Zn-porphyrin is not significantly perturbed by the binding to TiO_2. The time evolution of the TA spectrum of **2,4,6-Me**/TiO_2 can be described as a nonexponential process involving only two species, the singlet excited state and the Zn-porphyrin radical cation. Thus, it is seen that the excited state of the sensitizer is formed within the time resolution (<100 fs) of the experiment oxidized sensitizer, which then decays back to the ground state through charge recombination with conduction band electrons. This recombination can for most dyes be described with two lifetimes on the tens and hundreds of picoseconds time scale and a very slow ~50 ns component. The lifetime and amplitude of the very slow decay cannot be obtained with high precision from the 500 ps time window measurements. To obtain this, the 500 ps measurements were complemented with measurements covering a longer 5 ns time window for several Zn-porphyrin/TiO_2 samples. As illustrated by a few examples in Figure 3a, all studied Zn-porphyrin/TiO_2 samples at all conditions exhibit the ~50 ns slow charge recombination process but at greatly varying amplitude depending on dye and immersion conditions. The superimposed 500 ps and 5 ns measurements (Figure 3b) also show that the agreement between the measurements on the two time scales is very good over the overlapping time range. In fitting the 500 ps time window kinetics the slowest ~50 ns decay component obtained from the long delay line measurements was set as a fixed lifetime. The exact time constants and amplitudes of the various kinetic components vary depending on sensitizer molecule and immersion conditions (all kinetic parameters are summarized in Table 1). The finding that the electron injection/recombination dynamics is dominated by two species, the singlet excited state and dye radical cation, in addition to the ground state, implies that kinetic measurements at a single wavelength can be used for precise characterization of the temporal evolution of the reactions. With the help of the spectra of Figure 2d we can choose the most appropriate wavelength for this. We see that stimulated emission of the sensitizer is at ~660 nm and the oxidized dye absorbs strongly at the same wavelength. Thus, by measuring kinetics at 660 nm we can monitor the formation of the sensitizer excited state, its decay and formation of the oxidized sensitizer, as well as the ensuing decay of the sensitizer radical cation through recombination with conduction band electrons. Having now established the conditions for probing the electron transfer dynamics we

proceed with a systematic examination of how a number of factors influencing sensitizer–TiO_2 and sensitizer-sensitizer interactions control the electron injection and recombination dynamics. Finally, we correlate electron transfer dynamics of the Zn-porphyrin sensitized TiO_2 electrodes to photovoltaic properties of the solar cells based on these electrodes. As was discussed above, charge recombination kinetics are nonexponential, with time constants ranging from several tens of picoseconds to several tens of nanoseconds, or longer (see Figure 3 and Figure 4). Recombination covering a wide time scale has earlier been observed in many sensitizer/semiconductor systems and interpreted as due to heterogeneity or flexibility of the dye/semiconductor binding and/or heterogeneous electron transfer coupling.[3,18] For the Zn-porphyrin/TiO_2 electrodes studied here, we will show that the widely varying recombination times can be understood as being a result of a dye/semiconductor binding geometry where the Zn-porphyrin attachment to the TiO_2 surface is characterized by a distribution of tilt angles (Figure 5) and electron transfer occurs through space rather than through the spacer connecting the porphyrin core to the anchoring COOH group. The binding tilt angle is sensitive to the exact sensitizer structure and immersion conditions (solvent and time), which results in greatly varying recombination times.

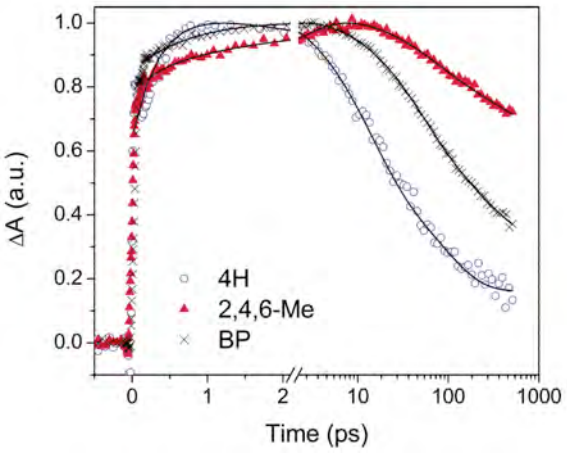

Figure 4. Transient absorption kinetics at 660 nm of **2,4,6-Me** (full, red triangles), **BP** (black cross) sensitized TiO_2 in *t*-BuOH/ACN for 1 h. See Table 1 for time constants and amplitudes. Kinetics are normalized to their maxima and black solid lines represent fits of the kinetics.

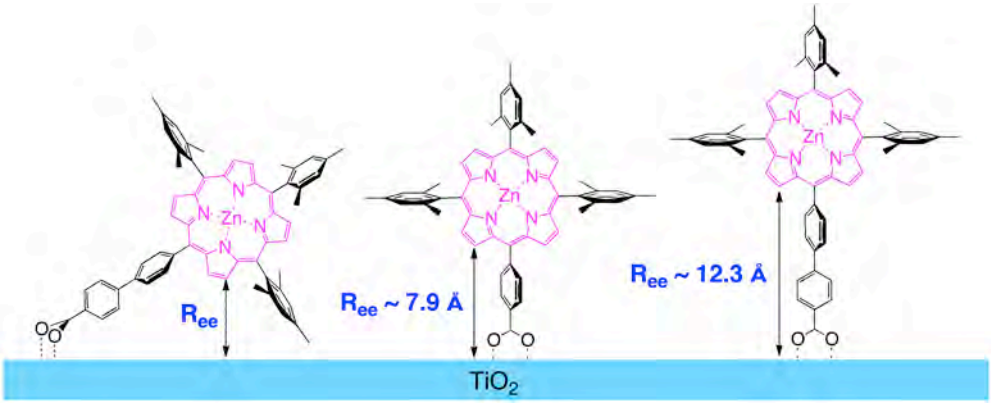

Figure 5. Binding model for Zn-porphyrins to TiO_2. The edge-to-edge distance (R_{ee}) is decreased upon tilting of the dye molecule.

Dye Binding Length of Porphyrin–TiO_2 Connector. From eq 2 it is clear that the distance over which electron transfer occurs has a strong impact on its rate. If electron transfer between the porphyrin core and semiconductor occurs through the connecting spacer, making this spacer longer should slow down the transfer. With the help of the sensitizers **2,4,6-Me** and **BP** we can test this expectation; introduction of the extra phenyl moiety in the biphenyl spacer of **BP**/TiO_2 relative to **2,4,6-Me**/TiO_2 would result in approximately 1.5 times longer edge-to-edge distance (R_{ee}) between the porphyrin core and the TiO_2 surface (R_{ee} = 12.3 Å for **BP**/TiO_2 and R_{ee} = 7.9 Å for **2,4,6-Me**/TiO_2, see Figure 5) and therefore in considerably smaller electronic coupling and much slower electron injection and recombination. The TA kinetics of these molecules attached to the TiO_2 film (*t*-BuOH/ACN as immersion solvent) measured over a time window of 500 ps are shown in Figure 4. Already a superficial glance at the two kinetic curves shows that both electron injection (rise of the curves) and charge recombination (decay of the curves) do not meet this expectation: the **BP** sensitizer with the longer connecting spacer has a faster injection and a much higher amplitude of fast recombination components, as well as a lower amplitude of long-lived signal (32% vs 65% for **2,4,6-Me**) that accounts for long-lived charges that can be harvested as photocurrent in a solar cell. Not only is the amplitude of the ~50 ns decay component higher for **2,4,6-Me**/TiO_2 than for **BP**/TiO_2, but also the lifetimes of the faster decays are shorter for **BP**/TiO_2. All lifetimes and amplitudes are summarized in Table 1. This shows that both electron injection and recombination are overall faster for the sensitizer with the longer connecting spacer. Obviously, electron transfer does not occur as could be anticipated through the spacer connecting the porphyrin core to the TiO_2 surface. Instead, we suggest a picture where the single carboxyl anchoring group allows a flexible binding geometry; for some of the porphyrins, depending on length of the spacer group, bulkiness of the porphyrin core, etc., a fraction of the molecules are bound at an angle to the semiconductor surface (see Figure 5) and electron transfer occurs through space rather than through the linker group connecting the porphyrin core to the anchoring COOH group. When the tilt angle is changed as a result of a change of porphyrin molecule size or shape, the distance between the porphyrin core and semiconductor surface is changed, which will lead to a change of the through-space electron transfer rate. Due to the expected exponential distance dependence of electron transfer (eq 2) only a modest change of distance (and thus angle) will have dramatic impact on the transfer rate. As an example let us consider the situation when an upright (perpendicular) orientation of the porphyrin results in an edge-to-edge distance of 7.9 Å between the porphyrin core and the TiO_2 surface (the distance for **2,4,6-Me**/TiO_2) and a recombination time of 50 ns (the measured slow part of the recombination is ~50 ns). A decrease of the porphyrin–TiO_2 distance (R_{ee}) as illustrated in Figure 5 to 3.5 Å would result in a dramatic shortening of the recombination time to 100 ps, the

same order of magnitude as the short recombination times observed (Table 1), assuming all other factors in the rate equation constant. Keeping in mind the extended dimensions of the porphyrin core and the bulky aryl (and methyl) substituents, it is not difficult to imagine that only a quite small tilt of the porphyrin molecule relative to the surface can lead to very short porphyrin–semiconductor distances, and thus very fast electron transfers; this is illustrated in the binding model of Figure 5. This crude illustration of the distance dependence of the electron transfer rate does not consider the possibly different distance dependencies of electron transfer through the molecular framework and through space, or changes in free energy and reorganization energy. Its only purpose is to demonstrate that relatively small changes in binding geometry can have dramatic effects on the electron transfer rate. A question that should be answered is whether there are discrete binding geometries (tilt angles) or if there is a distribution of angles giving rise to a distribution of electron transfer distances. The fact that for most of the studied dyes we observe nonexponential injection and recombination kinetics (see Table 1) shows that there at least are several geometries for most dyes, and it is therefore reasonable to assume that in most cases there is a distribution of binding geometries.

Transmission electron microscopy (TEM) measurements on TiO_2 nanoparticles sensitized with **BP** and **2,4,6-Me** for 1 h (Figure 6) provide support for the tilted binding geometry suggested above (Figure 5). The samples for the TEM measurements were prepared in the same way as for time-resolved measurements, yielding complete monolayers of the porphyrins. The TEM images reveal ~20 nm sized TiO_2 nanoparticles, covered with a thin porphyrin layerwith an average thickness of 1.0 ± 0.2 nm. Similar average thicknesses are seen for TiO_2 nanoparticles sensitized with the other porphyrins. Considering that the molecular lengths of **BP** and **2,4,6-Me** along the molecular long axis are 2.4 and 2.0 nm, this suggests a considerable tilt angle of the axis with respect to the surface normal for both molecules. Taking into account the lengths of **BP** and **2,4,6-Me** molecules, the average tilt angles of the molecular axis with respect to the surface normal are estimated as 60 ± 6º and 53 ± 7º, respectively. Additional support for the suggested binding geometry comes from recent calculations on pyrene sensitizers attached to anchoring groups (one or two COOHs) with spacers similar to those used here.[19a] For single-anchor binding, rotational freedom between the surface-binding anchor group and the main part of the sensitizer was shown to cause the spacer-axis to be tilted nearly parallel to the substrate surface opening up for a close contact between the sensitizer moiety and the TiO_2 surface. The double-anchor binding modes make the sensitizer geometry somewhat more predictable and lead to fixed binding geometries with a well-defined axial direction for the spacer-chromophore part of the sensitizer. However, the binding geometry was still characterized by a significant tilt of the entire sensitizer relative to the surface normal; for the particular case when the spacer is a single-triple-single bond attached to a phenyl ring

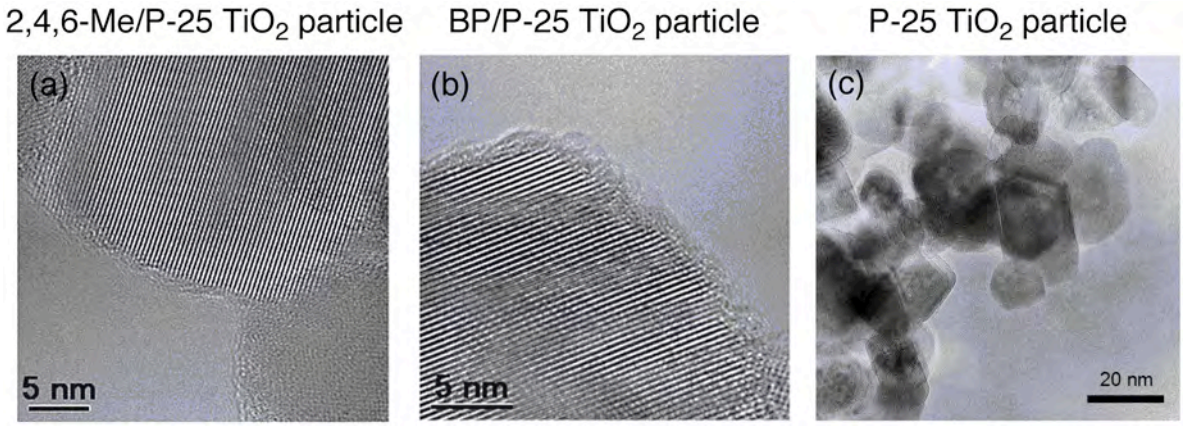

Figure 6. TEM images of TiO_2 nanoparticles sensitized with (a) **2,4,6-Me** and (b) **BP** for 1 h in *t*-BuOH/ACN that yielded complete monolayers of the dyes. The average thickness of the Zn-porphyrin layers were determined as 1.0 ± 0.2 nm for **BP** and **2,4,6-Me**. (c) TEM image of TiO_2 nanoparticles with out porphyrin is also shown for comparison.

with the two COOH anchors attached in meta position to a phenyl moiety, the sensitizer tilt angle was estimated to be approximately 45º relative to the surface normal. It should be mentioned that the calculations were performed for a model system consisting of the dye attached to a $(TiO_2)_{46}$ cluster model in the absence of solvent. These results show that it is far from straightforward to design a sensitizer-spacer-anchor assembly such that an upright binding geometry is obtained with electron transfer controlled by the length of the spacer. Two requirements should be met if this binding model is to reflect reality: (1) it must be possible to define a planar surface on the semiconductor particle, of at least the size of the sensitizer; (2) the sensitizer does not make other contacts than through the anchoring group (that lead to electron transfer) with other nanoparticles in the film. If the sensitizer molecules make multiple contacts with more than one nanoparticle, at for instance necking regions between nanoparticles, this may give rise to multiple electron transfer times and thus contribute to observed nonexponential electron transfer. Sensitizers of different size could in addition be expected to have a varying degree of multiple contacts. The first requirement seems to be fulfilled since electron micrographs show that the TiO_2 nanoparticles (P25, Nippon Aerogel, diameter ~20 nm) have relatively flat crystal faces of dimensions significantly larger than the sensitizer molecules (Figure 6c). Several observations indicate that multiple contacts in necking regions are not a major cause to the observed nonexponential electron transfer kinetics. (i) for electron injection and recombination in dye sensitized colloidal semiconductor systems and nanoparticle thin films (based on similar size nanoparticles),[18] both show similar electron transfer dynamics; (ii) for the dye **2,4,6-Me** studied here, attached to the same TiO_2 film, we

observe greatly varying electron transfer dynamics depending on experimental conditions (e.g., varying immersion solvent, see below). We believe this is a strong indication that electron transfer in multiple contact regions of the TiO_2 film does not significantly contribute to the observed dynamics. (iii) the upper limit of the total film surface area which would contribute to the multiple contacts is ~10%. This estimate also supports our interpretation. According to a previous model of charge recombination in mesoporous TiO_2[19b,19c] the nanoparticles contain electron traps with different depths and cation-electron recombination occurs through escape of electrons from the traps. A distribution of trap depths leads to many different recombination times and this is a likely contributing factor to the generally observed nonexponential kinetics of charge recombination in dye-sensitized nanostructured systems. The distribution of traps and the resulting nonexponentiality of charge recombination are expected to be a property of the semiconductor film. Here we see a strong variation in both electron injection and recombination rates depending on the properties of the sensitizer, for the same film material. This shows that detrapping of electrons cannot be the major process controlling charge recombination. Recent time-resolved THz measurements on dye-sensitized TiO_2 and ZnO nanostructured films[19d] show that the electron dynamics in these systems is best described by the so-called "random flight model",[19e] showing that the majority of electrons in the semiconductor particle are not located in deep traps characterized by slow detrapping. In what follows we will present results and discuss how varying experimental conditions (immersion solvent, packing, substituents, etc.) influence the charge transfer dynamics and rationalize it in terms of varying sensitizer-semiconductor interactions.

Steric Effects: Bulky Substituents on the Porphyrin Core. Some studies suggest that the low efficiency of porphyrin-based solar cells could originate from enhanced probability of exciton annihilation and radiationless processes.[20] At high surface coverage, dipole-dipole interactions could result in rapid migration of energy between neighboring dyes, or quenching of the excited states, both processes affecting the electron injection yield. It is a well-known fact that time-resolved laser spectroscopy measurements may suffer from exciton annihilation effects due to high excitation densities available in such experiments. However, at the low light intensities prevailing for solar cells under solar illumination, these effects are negligible and cannot explain observed low power conversion efficiencies. High pigment packing and aggregate formation can nevertheless reduce solar cell efficiency by excited state quenching or reduced electron injection efficiency. To examine the effect of such interactions on electron transfer dynamics and solar cell efficiency, steric hindrance between the porphyrins was introduced through attachment of bulky aryl substituents, which was expected to decrease loss channels by increasing the molecular distances and thereby reduce dye-dye interactions. Of the

molecules studied here, **2,4,6-Me** and **4-H** represent the extremes in steric hindrance and bulkiness around the porphyrin core. In **2,4,6-Me** the 2,6-methyl groups on the phenyl ring force the phenyls to twist out of the porphyrin plane and thus make the molecule bulkier along an axis perpendicular to the porphyrin plane. On the other hand, the less bulky **4-H** is expected to have its phenyl rings less twisted from the plane of the porphyrin core. This difference in bulkiness will affect the way the molecules can pack and interact: in closed packed organization of the molecules we expect **4-H** to come closer to each other and interact more strongly. This is verified by the more pronounced splitting and broader Soret band of **4-H** (Figure 7). The influence of bulky substituents on the dynamics of electron injection and recombination is illustrated by the kinetic traces in Figure 4. We observe a dramatic shortening of both electron injection and recombination times of **4-H** as compared to **2,4,6-Me** (for lifetimes and amplitudes, see Table 1). Of most importance for solar cell efficiency, the slow recombination phase (~50 ns) only carries 15% of the amplitude for **4-H**, as compared to 65% for **2,4,6- Me** (both immersed in *t*-BuOH/ACN, Table 2). This difference nicely correlates with the difference in power conversion efficiency, 1.2% vs 3.4% (Table 3) for solar cells based on electrodes of **4-H**/TiO_2 and **2,4,6-Me**/TiO_2. The fact that both electron injection and recombination rates are affected in a similar manner upon going from **2,4,6-Me**/TiO_2 to **4-H**/TiO_2 suggests that somehow the dye-semiconductor coupling is increased in **4-H**/TiO_2. Substitution of the phenyl rings with methyl groups at the 2- and 6-positions forces them to twist out of the porphyrin plane. Within the binding model of Figure 5 it can be anticipated that the bulkiness of the porphyrin imposed by the 2- and 6-methyl substituents forces the porphyrins to take a more upright position as a result of the interaction of these groups with the TiO_2 surface. Consequently, recombination on the hundreds of picoseconds time scale is slower for **2,4,6-Me**/TiO_2 than for **4-H**/TiO_2 and the amplitude of the ~50 ns recombination component is much higher for the former. The decreased excitonic effects of the Soret band of **2,4,6-Me**/TiO_2 as compared to **4-H**/TiO_2 can be seen as a result of dye–dye steric interaction: the bulky substituents prevent the chromophores from very close approach. The consequence

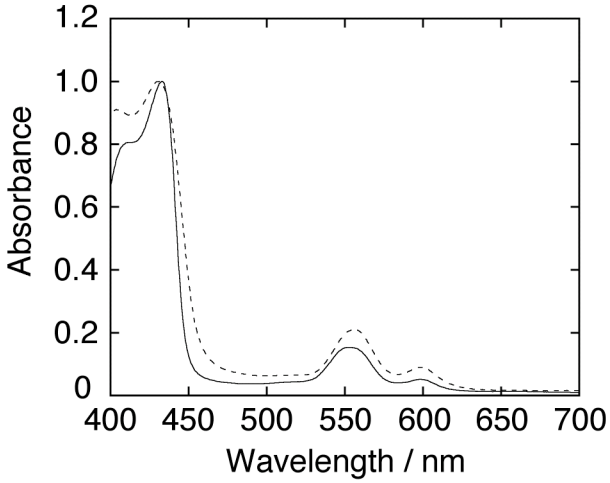

Figure 7. UV-visible absorption spectra of **2,4,6-Me**/TiO_2 (solid line) and **4-H**/TiO_2 (dashed line) electrodes sensitized in *t*-BuOH/ACN for 1 h. The spectra are normalized.

of all this is that the throughspace Zn-porphyrin–TiO_2 distance for electron transfer on average is shorter for **4-H**/TiO_2, leading to faster electron injection and recombination.

Table 2. Power Conversion Efficiencies Normalized for Surface Coverage (η_{rel}) Correlated to Amplitude of Long Lived (~50 ns) Electrons

dye	immersion solvent	immersion time (h)	η_{rel}	$A_{>50\ ns}$ (%)
4-CF_3	*t*-BuOH/ACN	1	2.8	36
4-H	*t*-BuOH/ACN	1	3.2	15
4-Me	*t*-BuOH/ACN	1	3.0	35
2,4,6-Me	*t*-BuOH/ACN	1	4.8	65
2,4,6-Me	*t*-BuOH/ACN	12	2.3	91
2,4,6-Me	MeOH	1	5.4	95
2,4,6-Me	MeOH	12	4.3	95
BP	*t*-BuOH/ACN	1	2.8	32

Table 3. Cell Performance of Porphyrin-Sensitized Solar Cells.[a]

dye	immersion solvent	immersion time (h)	J_{SC} (mA cm^{-2})	V_{OC} (mV)	*ff*	η (%)
2,4,6-Me	*t*-BuOH/ACN[b]	1	7.6	0.69	0.64	3.4
		12	5.0	0.64	0.66	2.1
	MeOH	1	9.4	0.76	0.64	4.6
		12	8.3	0.72	0.62	3.7
	DMF	1	7.1	0.66	0.66	3.1
		12	1.7	0.55	0.60	0.55
BP	*t*-BuOH/ACN[a]	1	5.6	0.64	0.66	2.4
4-H	*t*-BuOH/ACN[a]	1	3.0	0.60	0.64	1.2
4-Me	*t*-BuOH/ACN[a]	1	6.9	0.67	0.66	3.0
4-CF_3	*t*-BuOH/ACN[a]	1	6.4	0.68	0.64	2.8

[a] Taken from ref 14. [b] 1/1=v/v.

Immersion Solvent and Time Effects. Solar cells based on the porphyrin sensitizers studied here, prepared using different immersion solvents have significantly different performances, even for the same dye[14] (Tables 2 and 3). As an example, a **2,4,6- Me**/TiO_2 solar cell prepared with methanol as immersion solvent has the highest efficiency (η = 4.6%), whereas the same cell sensitized using *t*-BuOH/ACN and DMF are substantially worse (η = 3.4% and 3.1%, respectively). When the solar cell efficiency is normalized for dye surface coverage,[14] the **2,4,6-Me**/TiO_2 cell made with methanol as immersion solvent is still the most efficient cell and those made using *t*-BuOH/ACN and DMF are considerably less efficient (Table 2). This shows that factors other than surface coverage and light harvesting control the cell efficiency. For other sensitizers, surface coverage has been observed to depend on immersion solvents used, but it has been difficult to establish clear trends between surface coverage and cell efficiency. Since charge recombination is expected to have direct influence on the cell efficiency, variations in this process in different immersion solvents could be part of the reason for immersion solvent dependence of solar cell efficiency. Figure 8 shows the injection/recombination kinetics of **2,4,6-Me**/TiO_2 immersed in MeOH, *t*-BuOH/ACN, and DMF (we remind that the solvent in contact with the electrode during measurement is *t*-BuOH/ACN in all cases, see the Experimental Section). It is seen that following electron injection there is no recombination on the nanosecond time scale for **2,4,6-Me**/TiO_2 immersed in MeOH, whereas in both the other solvents there are substantial fast recombinations on the tens and hundreds of picoseconds timescale. Solar cell efficiencies normalized to surface coverage (η_{rel}) are nicely correlated to the amplitude of the slow, ~50 ns, recombination process (Table 2 and Figure 9). Once again, we see that the number of long-lived charge carriers in the electrode is directly related to cell efficiency. The strong dependence of charge recombination kinetics on immersion solvent, for electrodes made from the same TiO_2

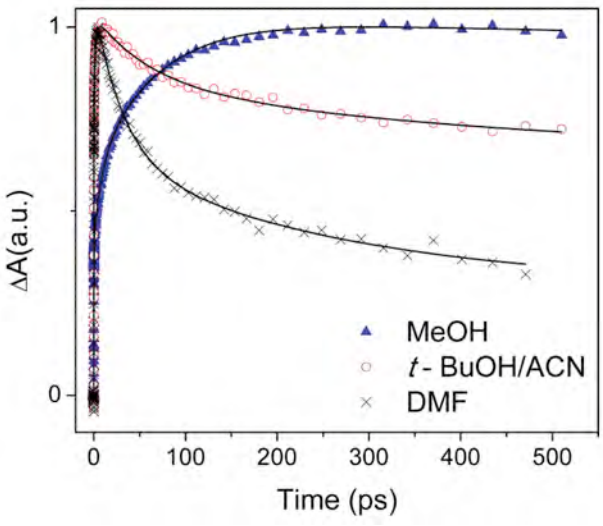

Figure 8. Transient absorption kinetics of **2,4,6-Me** on TiO_2 sensitized in MeOH (closed, blue triangles), *t*-BuOH/ACN (open, red circle), and DMF (black cross) for 1 h. Kinetics are normalized to their maxima and solid lines represent fits of the kinetics. See table 1 for time constants and amplitudes.

particles, also excludes the possibility that dye molecules situated in necking regions of the semiconductor film contribute significantly (with different behavior) to the observed dynamics, as already mentioned above.

The observed solvent effect on solar cell efficiency and charge carrier dynamics is indeed remarkable; the solvent effect concerns the immersion solvent, whereas the solvent in contact with the sensitized electrode during measurement of cell characteristics and electrode dynamics is always the same, *t*-BuOH/ACN (1:1). This result implies that there is some memory in the dye/TiO_2 system of the immersion solvent used, despite the fact that another solvent may be in contact with the electrode during measurement. At least two reasons for this can be envisaged: (1) the immersion solvent organizes the sensitizer in a specific manner, which depends on solvent, surface coverage, etc., and (2) the solvent plays an active role in the sensitizer binding by forming a stable sensitizer–solvent–TiO_2 complex. The current data cannot distinguish between these possibilities, but measurements with surface sensitive techniques are in progress and will hopefully provide an answer.

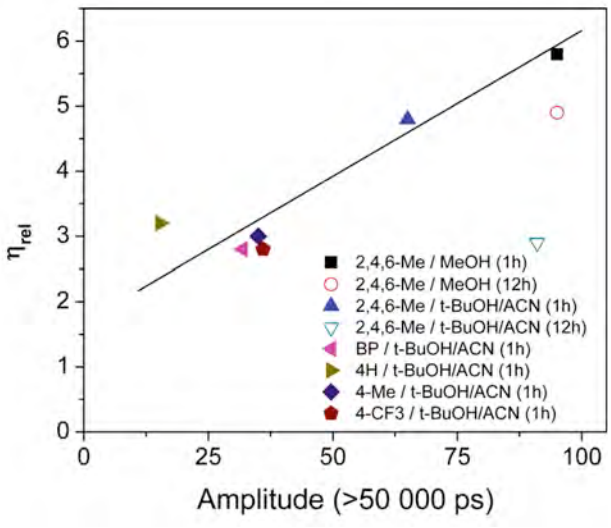

Figure 9. Solar cell power conversion normalized for surface coverage (η_{rel}) as a function of long-lived recombination signal ($A_{>50ns}$). Closed symbols represent measurements of TiO_2 films sensitized for 1 h. Particular dye and solvent are in figure legend.

Long immersion times are known to cause aggregation of the dye on the semiconductor surface,[21] but different dyes have very different tendencies to aggregate. For instance, phthalocyanines exhibit strong aggregation,[22] whereas polypyridyl transition metal complexes (e.g., Ru–N3) show much less aggregation.[23] The nature of aggregates and therefore the effects of aggregation can also be envisaged to vary.[24] Even for monolayer dye coverage on the semiconductor surface one can think of aggregation effects in the sense that close packing of the molecules give rise to strong dye–dye interactions and modified photophysical properties. Aggregation, in the sense of multilayer formation of the dye on the semiconductor surface, has also been discussed in the literature[23] and may reduce the efficiency of charge injection if energy transfer between dyes is slow. Infrared spectroscopy of the studied Zn-porphyrins on TiO_2[14] showed that all sensitizers are bound to the surface, thus excluding multilayer type of aggregation. Strong dye–dye interactions may lead to short excited state lifetimes and therefore

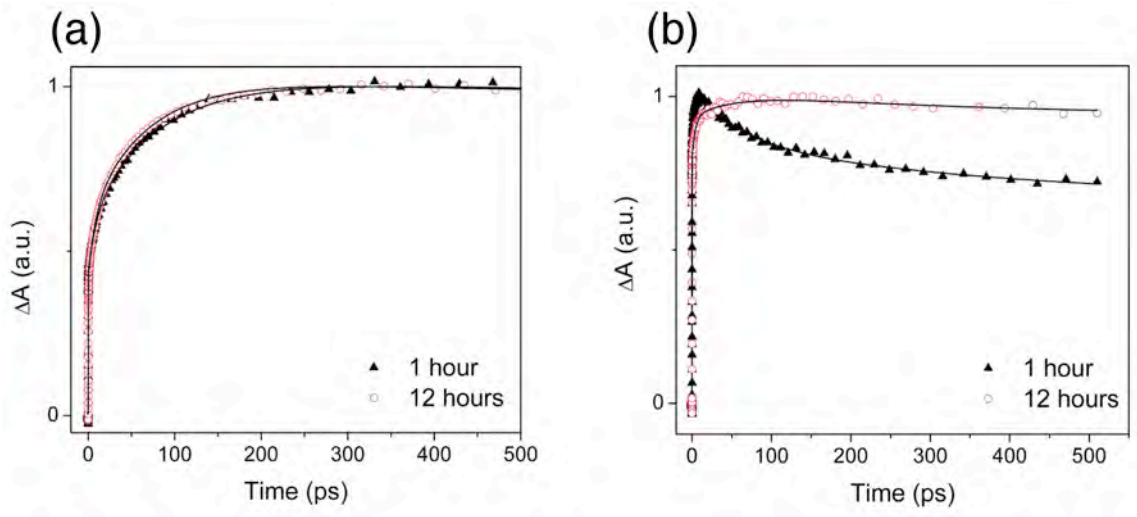

Figure 10. (a) Transient absorption kinetics of **2,4,6-Me** on TiO_2 sensitized in MeOH for 1 h (open, red circle) and 12 h (closed, black triangle). Kinetics are normalized and solid black lines represent fits of the kinetics. See Table 1 for time constants and amplitudes. (b) **2,4,6-Me** on TiO_2 senesitized in *t*-BuOH/ACN for 1 h (open circle) and 12 h (closed triangle). All kinetics are normalized to maxima, and solid black lines represent fits of the kinetics. See Table 1 for time constants and amplitudes.

diminish the efficiency of charge injection if the excited state lifetime of the aggregate is short relative the injection time. The solar cell performance of the studied Zn-porphyrins is generally worse for 12 h immersion than for 1 h, but the extent of the effect is quite different for different dyes and solvents[14] (Table 3). Thus, for **4-H**, the molecule with the smallest substituents and therefore probably most prone to aggregation, the cell efficiency corrected for surface coverage drops by a factor of approximately 10 when the immersion time increases from 1 to 12 h.[14] **2,4,6-Me**/TiO_2 immersed in methanol, on the other hand, only exhibits minor changes of η_{rel} with immersion time (Table 2). The same molecule in DMF exhibits a strong dependence on immersion time: increasing it from 1 to 12 h reduces η_{rel} by a factor of 6.[14] From this it is clear that for the Zn-porphyrins studied here, prolonged immersion adversely affects the power conversion efficiency of the solar cell. The results displayed in Figure 10a,b illustrate the effects of immersion time on the injection/recombination dynamics. For **2,4,6-Me**/TiO_2 immersed in methanol (Figure 10a), 1 and 12 h immersion have almost identical kinetics. In particular, the recombination is in both cases entirely controlled by the ~50 ns decay component, but the solar cell made with 12 h immersion has considerably lower efficiency (η_{rel} = 4.3% (12 h) vs 5.4% (1 h))[14] (Tables 1 and 2). Solar cells of **2,4,6-Me**/TiO_2 immersed in *t*-BuOH/ACN exhibit an interesting behavior: the conversion efficiency η_{rel} drops from 4.8% to

2.3% in going from 1 to 12 h immersion, but the amplitude of the ~50 ns recombination is higher for the longer immersion time (Figure 10b and Table 1). Obviously, long immersion time (12 h) results in decreased solar cell performance for **2,4,6-Me**/TiO_2 with both *t*-BuOH/ACN and MeOH as immersion solvent, but this is not correlated with an increased rate of charge recombination. Above we discussed various detrimental effects of aggregation on solar cell performance. The results presented here suggest that for solar cells with long immersion time part of the light energy absorbed by the sensitizer molecules is quenched by efficient radiationless processes competing with electron injection and therefore never reaches the TiO_2 surface. The series of Zn-porphyrins studied here also represents a modest variation of driving force ΔG (~0.1 eV) for electron injection and recombination. No significant change of electron transfer dynamics or solar cell performance was, however, observed, in agreement with previous observations.[3a]

Correlation Solar Cell Performance and Electron Transfer Dynamics. The results of the kinetic studies were compared to those of photovoltaic measurements on complete solar cells of the same sensitizers,[14] enabling us to correlate solar cell performance to photophysics and electron transfer dynamics in the half-cell electrode (sensitized TiO_2 film in contact with solvent). Here, it is important to keep in mind that our comparison of solar cell performance with electron injection and recombination kinetics can be used to test the assumption that these processes are not qualitatively different in the solar cell and on the electrode. The operating conditions of the solar cell could certainly be envisaged to influence the electron transfer processes as well as add new reactions (e.g., electron transfer reactions involving the electrolyte redox couple). The quantum efficiency (η) of a solar cell is generally defined as the external quantum efficiency (EQE = number of extracted electrons/number of incident photons). For a discussion of how key processes contribute to the overall quantum efficiency it can be defined as

$\eta \sim$ (efficiency of light harvesting)
× (yield of electron injection) × (yield of electron long-lived
conduction band electrons that can be extracted) × (1 – other losses)

Light harvesting is related to the surface coverage of the dye and how well it absorbs the wavelengths of the solar spectrum, and it varies substantially between the different dyes and various experimental conditions. Thus, variations in η are to a certain extent a result of variation in light-harvesting. To distinguish the various factors contributing to the quantum efficiency of a particular solar cell, we have therefore measured the dye surface coverage of all

used dye–TiO_2 electrodes.[14] The absorption spectra are very similar for all studied porphyrin dyes. Variation in spectral coverage and its contribution to light harvesting efficiency can therefore be ignored. For short immersion (1 h) electron injection is more or less the same for all the molecules and injection is also fast as compared to the excited state lifetime of the sensitizer, so injection is close to 100% efficiency. Thus, in most of the dye/TiO_2 combinations studied, injection will not influence the efficiency significantly. For 12 h immersion we concluded above that solar cell efficiency is decreased without increasing the recombination rate, suggesting that sensitizer excited state quenching induced by strong dye–dye interaction decreases the efficiency of injection. Recombination directly controls the number of long-lived electrons in the conduction band contributing to the quantum efficiency of the solar cell, and thus the photocurrent. If there is fast recombination, faster than the extraction of electrons or oxidized dye regeneration by electrolyte, this will decrease the photocurrent and thereby the power conversion efficiency of the solar cell. Since the fill factor is almost constant (Table 3[14]) competition of electron extraction and oxidized dye regeneration by electrolyte with the conductive looses because of slow recombination of electrons with oxidized dye and electrolyte is similar for all sensitizers. Therefore the number of long-lived conduction band electrons, monitored by the amplitude of longlived oxidized dye signal ($A_{>50ns}$), is expected to be correlated to the solar cell power conversion. From the relation above we see that with variations in light harvesting (i.e., surface coverage) taken into account recombination should be the major determining factor for solar cell efficiency, if other losses are of minor importance. The correctness of this expectation for the studied Zn-porphyrin/TiO_2 electrodes and corresponding solar cells may be examined by plotting solar cell power conversion normalized to surface coverage (η_{rel}) versus the amplitude of long-lived (~50 ns) charge recombination ($A_{>50ns}$) for all the studied electrodes (Figure 9). For the 1 h immersion time data points, there is a linear relationship between η_{rel} and A_{50ns}: higher η_{rel} corresponds to higher $A_{>50ns}$. This shows that for the series of Zn-porphyrins studied here and 1 h immersion, no factors other than those considered in the expression for solar cell efficiency have a significant impact on solar cell performance. It also suggests that electron injection and recombination processes in the solar cell and on the electrode are similar qualitatively and even quantitatively. Although we cannot exclude that injection and recombination dynamics in solar cells may differ from those in electrodes, from the presented correlation it seems that the time ranges and the relative rates of these processes do not change much for the studied dyes. For 12 h immersion the situation is different; in both solvents examined, the solar cell efficiency is relatively low, despite the fact that there is no fast recombination. As discussed above, this suggests that aggregation of the sensitizer decreases the efficiency of electron injection to the TiO_2 electrode.

Conclusion

• There is a heterogeneous dye/semiconductor binding geometry; the Zn-porphyrin molecules are attached to the TiO_2 surface with a distribution of tilt angles, where the angle determines the porphyrin–semiconductor electron transfer distance and charge transfer occurs through space, rather than through the spacer connecting the porphyrin core and anchoring COOH group.

• From measurements of transient absorption spectra of the dyes on TiO_2 and analysis of the spectral evolution we conclude that the oxidized dye, D^+, is the only photoproduct and its spectrum is quantified.

• For short immersion time (1 h), there is a direct correlation between solar cell efficiency and amplitude of long-lived conduction band electrons, once variations in light harvesting (surface coverage) have been taken into account.

• Long immersion time (12 h) results in decreased solar cell efficiency because of decreased efficiency of electron injection.

Experimental Section

Synthesis and Sample Preparation. 5,10,15,20-Tetraphenylzinc porphyrins bearing a carboxylic group for attachment to the TiO_2 surface, **2,4,6-Me**, **BP**, **4-H**, **4-Me**, and **4-CF_3** (Figure 1), were prepared by condensation of pyrrole with the corresponding benzyl aldehydes in the presence of BF_3•OEt_2, followed by base hydrolysis in a mixture of THF and ethanol and subsequent treatment with zinc acetate.[14] Nanoporous films were prepared from a colloidal suspension of TiO_2 nanoparticles (P25, Nippon Aerogel) dispersed in distilled water that was deposited on a transparent glass substrate by using the doctor blade technique and annealed for 2 h at 723 K for the 4 μm thick TiO_2 film used in transient absorption measurements.[14] For photovoltaic measurements,[14] 10 μm thick films were used and made by two successive depositions and drying procedures. The thickness of the films was determined using a surface roughness tester (SURFCOM 130A, ACCRETECH). The TiO_2 electrodes were immersed in a 0.2 mM porphyrin solution of *t*-BuOH/ acetonitrile (denoted *t*-BuOH/ACN in the following), methanol (MeOH), or dimethylformamide (DMF) at room temperature. After removal from the dye bath, the nonadsorbed molecules were washed off by rinsing the film with the same solvent and the filmwas dried at room temperature for ~20 s. The amount of porphyrins adsorbed on the TiO_2 films was determined by measuring the absorbance at the peak of the Soret band for each dye molecule dissolved from the dye-sensitized TiO_2 films into a known amount of DMF containing 0.1 M NaOH. For transient absorption measurements, a spacer frame with a thickness of 0.13 mm was placed on top of the porphyrin–TiO_2 glass sheet, together with

another thin microscope coverslip, and this volume was filled with the *t*-BuOH/ACN 1:1 mixture. Paper clips were used to press the glass assembly to prevent solvent evaporation during measurements. Here it is important to point out that although immersion was performed in a few different solvents (*t*-BuOH/ACN, MeOH, DMF), the transient absorption measurements and solar cell characterization were always performed with the same solvent, *t*-BuOH/ACN 1:1 mixture, in contact with the electrode.

Transient Absorption Spectroscopy. Transient absorption (TA) studies were performed using an experimental setup based on a commercial 1 kHz Clark MXR CPA 2001 femtosecond laser, pumping a noncollinear optical parametric amplifier (TOPAS White, Light Conversion) for generation of pump pulses at 560 nm. Another amplifier (Clark MXR Inc. NOPA) was used to generate the probe pulses, either at 660 nm for kinetic measurements or in the broad spectral region from 560 to 750 nm for differential spectra. The pump and probe (660 nm) pulses were compressed to ~40 fs. Undispersed probe and reference pulses for TA kinetics were measured by silicon photodiodes. A pair of diode arrays was used to measure probe and reference beams for differential spectra. Uncompressed probe pulses were used to measure spectra. Different arrival time for different probe wavelength has been accounted for in the fitting procedure. The pump and probe beams were set at the magic angle, 54.7º, relative polarization. Experiments were performed using both short (550 ps, 30 fs instrumental function) and long (5 ns, ~1 ps resolution) delay lines. In kinetic measurements, an excitation pulse fluency of 4.35×10^{12} (photons/cm^2)/pulse was used. Differential spectra required 10 times higher fluency for good signal/noise. Both fluencies were in the linear response region as can be seen in Figure S1, which displays the recorded signal amplitude as a function of excitation fluency. Multiexponential modeling of kinetics was performed by the Origin software. Differential spectra were globally fitted using in-house written software.[15] To account for inhomogeneous character of

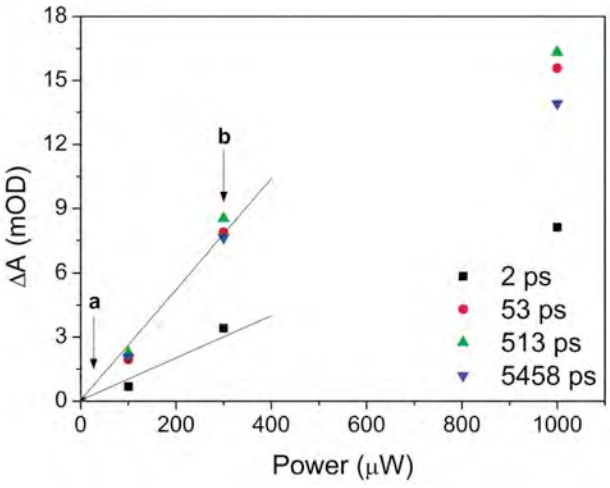

Figure S1. Recorded signal amplitude as function of excitation intensity to demonstrate linearity of measurements. Arrow "a" corresponds to an excitation pulse fluency of 4.35×10^{12} (photons/cm^2)/pulse used in kinetics measurements, while arrow "b" corresponds to 10 times higher excitation pulse fluency than was used in spectral measurements.

dye–semiconductor interactions, a special algorithm has been used. Each transient species has been assigned to a specific spectral shape whereas three decay components were associated with it. Although four additional variables are needed for each transient species with this approach, only two species, namely photogenerated excited state and oxidized dye, were required to fit the data successfully. When a conventional exponential decay associated spectra approach was used, up to three extra species with several hundreds of additional variables of spectral amplitude at each wavelength were required to obtain an equally good fit.

References and Notes

[1] (a) Hagfeldt, A.; Grätzel, M. *Chem. Rev.* **1995**, *95*, 49. (b) Hagfeldt, A.; Grätzel, M. *Acc. Chem. Res.* **2000**, *33*, 269. (c) Grätzel, M. Nature **2001**, *414*, 338. (d) Grätzel, M. *Acc. Chem. Res.* **2009**, *42*, 1788.

[2] (a) Hirata, N.; Lagref, J.–J.; Palomares, E. J.; Durrant, J. R.; Nazeeruddin, M. K.; Grätzel, M.; Di Censo, D. *Chem.–Eur. J.* **2004**, *10*, 595. (b) Piotrowiak, P.; Galoppini, E.; Wei, Q.; Meyer, G. J.; Wiewior, P. *J. Am. Chem. Soc.* **2003,** *125*, 5278. (c) Kamat, P. V.; Haria, M.; Hotchandani, S. *J. Phys. Chem. B* **2004**, *108*, 5166. (d) Lewis, N. S. *Inorg. Chem.* **2005**, *44*, 6900. (e) Durrant, J. R.; Haque, S. A.; Palomares, E. J. *Chem. Commun.* **2006**, 3279. (f) Robertson, N. *Angew. Chem., Int. Ed.* **2006**, *45*, 2338. (g) Mishra, A.; Fischer, M. K. R.; Bäuerle, P. *Angew. Chem., Int. Ed.* **2009**, *48*, 2474.

[3] (a) Ardo, S.; Meyer, G. *J. Chem. Soc. Rev.* **2009**, *38*, 115. (b) Tachibana, Y.; Moser, J. E.; Grätzel, M.; Klug, D. R.; Durrant, J. R. *J. Phys. Chem.* **1996**, *100*, 20056. (c) Hannappel, T.; Burfeindt, B.; Storck, W.; Willig, F. *J. Phys. Chem. B* **1997**, *101*, 6799. (d) Moser, J. E.; Noukakis, D.; Bach, U.; Tachibana, Y.; Klug, D. R.; Durrant, J. R.; Humphry-Baker, R.; Grätzel, M. *J. Phys. Chem. B* **1998**, *102*, 3649. (e) Hannappel, T.; Zimmermann, C.; Meissner, B.; Burfeindt, B.; Storck, W.; Willig, F. *J. Phys. Chem. B* **1998**, *102*, 3651. (f) Ellingson, R. J.; Asbury, J. B.; Ferrere, S.; Hirendra, N. G.; Sprague, J. R.; Lian, T.; Nozik, A. J. *J. Phys. Chem. B* **1998**, *102*, 6455. (g) Asbury, J. B.; Ellingson, R. J.; Ghosh, H. N.; Ferrere, S.; Nozik, A. J.; Lian, T. *J. Phys. Chem. B* **1999**, *103*, 3110. (h) Durrant, J. R.; Tachibana, Y.; Mercer, I. P.; Moser, J. E.; Grätzel, M.; Klug, D. R. Z. *Phys. Chem.* **1999**, *212*, 93. (i) Tachibana, Y.; Haque, S. A.; Mercer, I. P.; Durrant, J. R.; Klug, D. R. *J. Phys. Chem. B* **2000**, *104*, 1198. (j) Heimer, T. A.; Heilweil, E. J.; Bignozzi, C. A.; Meyer, G. J. *J. Phys. Chem. A* **2000**, *104*, 4256. (k) Kallioinen, J.; Lehtovuori, V.; Myllyperkiö, P.; Korppi–Tommola, *J. Chem. Phys. Lett.* **2001**, *340*, 217. (l) Benkö, G.; Kallioinen, J.; Korppi-Tommola, J. E. I.; Yartsev, A. P.; Sundström, V. *J. Am. Chem. Soc.* **2002**, *124*,

489. (m) Kallioinen, J.; Benkö, G.; Sundström, V.; Korppi–Tommola, J. E. I.; Yartsev, A. P. *J. Phys. Chem. B* **2002**, *106*, 4396. (n) Tachibana, Y.; Nazeeruddin, M. K.; Grätzel, M.; Klug, D. R.; Durrant, J. R. *Chem. Phys.* **2002**, *285*, 127. (o) Asbury, J. B.; Hao, E.; Wang, Y.; Ghosh, H. N.; Lian, T. *J. Phys. Chem. B* **2001**, *105*, 4545.

[4] (a) Wang, Y.; Asbury, J. B.; Lian, T. *J. Phys. Chem. A* **2000**, *104*, 4291. (b) Asbury, J. B.; Hao, E.; Wang, Y.; Lian, T. *J. Phys. Chem. B* **2000**, *104*, 11957. (c) Palomares, E.; Martinez-Diaz, M. V.; Haque, S. A.; Torres, T.; Durrant, J. R. *Chem. Commun.* **2004**, 2112. (d) Wang, D.; Mendelsohn, R.; Galoppini, E.; Hoertz, P. G.; Carlisle, R. A.; Meyer, G. J. *J. Phys. Chem. B* **2004**, *108*, 16642.

[5] (a) Kilsa, K.; Mayo, E. I.; Kuciauskas, D.; Villahermosa, R.; Lewis, N. S.; Winkler, J. R.; Gray, H. B. *J. Phys. Chem.* **2003**, *107*, 3379. (b) Galoppini, E. *Coord. Chem. Rev.* **2004**, *248*, 1283. (c) Piotrowiak, P.; Galoppini, E.; Wei, Q.; Meyer, G. J.; Wiewior, P. *J. Am. Chem. Soc.* **2003**, *125*, 5278. (d) Bonhote, P.; Moser, J. E.; Humphry-Baker, R.; Vlachopoulos, N.; Zakeeruddin, S. M.; Walder, L.; Grätzel, M. *J. Am. Chem. Soc.* **1999**, *121*, 1324. (e) Hasselmann, G. M.; Meyer, G. J. *J. Phys. Chem. B* **1999**, *103*, 7671. (f) Wang, D.; Mendelsohn, R.; Galoppini, E.; Hoertz, P. G.; Carlisle, R. A.; Meyer, G. J. *J. Phys. Chem. B* **2004**, *108*, 16642.

[6] (a) Palomares, E.; Clifford, J. N.; Haque, S. A.; Lutz, T.; Durrant, J. R. *J. Am. Chem. Soc.* **2003**, *125*, 475. (b) Kortan, A. R.; Hull, R.; Opila, R. L.; Bawendi, M. G.; Steigerwald, M. L.; Carroll, P. J.; Brus, L. E. *J. Am. Chem. Soc.* **1990**, *112*, 1327. (c) Diamant, Y.; Chappel, S.; Chen, S. G.; Melamed, O.; Zaban, A. *Coord. Chem. Rev.* **2004**, *248*, 1271.

[7] Rippard, W. H.; Perrella, A. C.; Albert, F. J.; Buhrman, R. A. *Phys. Rev. Lett.* **2002**, *88*, No. 046805.

[8] (a) Haque, S. A.; Handa, S.; Peter, K.; Palomares, E.; Thelakkat, M.; Durrant, J. R. *Angew. Chem., Int. Ed.* **2005**, *44*, 5740. (b) O'Regan, B.; Moser, J.; Anderson, M.; Grätzel, M. *J. Phys. Chem.* **1990**, *94*, 8720. (c) Moser, J. E.; Grätzel, M. *Chem. Phys.* **1993**, *176*, 493.

[9] Fitzmaurice, D. J.; Frei, H. *Langmuir* **1991**, *7*, 1129.

[10] Imahori, H.; Umeyama, T.; Ito, S. *Acc. Chem. Res.* **2009**, *42*, 1809.

[11] (a) Watson, D. F.; Marton, A.; Stux, A. M.; Meyer, G. J. *J. Phys. Chem. B* **2003**, *107*, 10971. (b) Rochford, J.; Chu, D.; Hagfeldt, A.; Galoppini, E. *J. Am. Chem. Soc.* **2007**, *129*, 4655. (c) Huijser, A.; Marek, P. L.; Savenije, T. J.; Siebbeles, L. D. A.; Scherer, T.; Hauschild, R.; Szmytkowski, J.; Kalt, H.; Hahn, H.; Balaban, T. S. *J. Phys. Chem. C* **2007**, *111*, 11726. (d) Cíd, J.–J.; Yum, J.–H.; Jang, S.–R.; Nazeeruddin, M. K.; Martínez-Ferrero, E.; Palomares, E. J.; Ko, J.; Grätzel, M.; Torres, T. *Angew. Chem., Int. Ed.* **2007**, *46*, 8358. (e) Eu, S.; Hayashi, S.; Umeyama, T.; Oguro, A.; Kawasaki, M.;

Kadota, N.; Matano, Y.; Imahori, H. *J. Phys. Chem. C* **2007**, *111*, 3528. (f) Eu, S.; Katoh, T.; Umeyama, T.; Matano, Y.; Imahori, H. *Dalton Trans.* **2008**, 5476.

[12] (a) Marcus, R. A. *J. Chem. Phys.* **1956**, *24*, 966. (b) Marcus, R. A.; Sutin, N. Biochim. *Biophys. Acta* **1985**, *811*, 265.

[13] (a) Gerischer, H.; Willig, F. *Top. Curr. Chem.* **1976**, *61*, 31. (b) Gerischer, H. *Photochem. Photobiol.* **1972**, *16*, 243.

[14] Imahori, H.; Hayashi, S.; Hayashi, H.; Oguro, A.; Eu, S.; Umeyama, T.; Matano, Y. *J. Phys. Chem. C* **2009**, *113*, 18406.

[15] (a) Pascher, T. *Biochemistry* **2001**, *40*, 5812. (b) De, S.; Pascher, T.; Maiti, M.; Jespersen, K. G.; Kesti, T.; Zhang, F.; Inganäs, O.; Yartsev, A. P.; Sundström, V. *J. Am. Chem. Soc.* **2007**, *129*, 8466.

[16] Rogers, J. E.; Nguyen, K. A.; Hufnagle, D. C.; McLean, D. G.; Su, W. J.; Gossett, K. M.; Burke, A. R.; Vinogradov, S. A.; Pachter, R.; Fleitz, P. A. *J. Phys. Chem. A* **2003**, *107*, 11331.

[17] (a) Kira, A.; Tanaka, M.; Umeyama, T.; Matano, Y.; Li, G.; Ye, S.; Isosomppi, M.; Tkachenko, N. V.; Lemmetyinen, H.; Imahori, H. *J. Phys. Chem. C* **2007**, *111*, 13618. (b) Hayashi, H.; Kira, A.; Umeyama, T.; Matano, Y.; Charoensirithavorn, P.; Sagawa, T.; Yoshikawa, S.; Tkachenko, N. V.; Lemmetyinen, H.; Imahori, H. *J. Phys. Chem. C* **2009**, *113*, 10819.

[18] (a) Hilgendorff, M.; Sundström, V. *Chem. Phys. Lett.* **1998**, *287*, 709. (b) Hilgendorff, M.; Sundström, V. *J. Phys. Chem. B* **1998**, *102*, 10505. (c) Benkö, G.; Hilgendorff, M.; Yartsev, A. P.; Sundström, V. *J. Phys. Chem. B* **2001**, *105*, 967. (d) Clifford, J. N.; Palomares, E.; Nazeeruddin, M. K.; Grätzel, M.; Nelson, J.; Li, X.; Long, N. J.; Durrant, J. R. *J. Am. Chem. Soc.* **2004**, *126*, 5225. (e) Santos, T. D.; Morandeira, A.; Koops, S.; Mozer, A. J.; Tsekouras, G.; Dong, Y.; Wagner, P.; Wallace, G.; Earles, J. C.; Gordon, K. C.;Officer, D.; Durrant, J. R. *J. Phys. Chem. C* **2010**, *114*, 3276.

[19] (a) Pal, S.; Galoppini, E.; Sundström, V.; Persson, P. *Dalton Trans.* **2009**, 10021. (b) Haque, S. A.; Tachibana, Y.; Klug, D. R.; Durrant, J. R. *J. Phys. Chem. B* **1998**, *102*, 1745. (c) Haque, S. A.; Tachibana, Y.; Willis, R. L.; Moser, J. E.; Grätzel, M.; Klug, D. R.; Durrant, J. R. *J. Phys. Chem. B* **2000**, *104*, 538. (d) Nemec, H.; Rochford, J.; Taratula, O.; Galoppini, E.; Kuzel, P.; Polívka, T.; Yartsev, A.; Sundström, V. *Phys. Rev. Lett.* **2010**, *104*, 197401. (e) Barzykin, A. V.; Tachiya, M. *J. Phys. Chem. B* **2002**, 106, 4356.

[20] (a) Lee, C. W.; Lu, H. P.; Lan, C. M.; Huang, Y. L.; Liang, Y. R.; Yen, W. N.; Liu, Y. C.; Lin, Y. S.; Diau, E. W. G.; Yeh, C. Y. *Chem.–Eur. J.* **2009**, *15*, 1403. (b) Lee, M. W.; Lee, D. L.; Yen, W. N.; Yeh, C. Y. J. *Macromol. Sci.* **2009**, *46*, 730.

[21] (a) Rochford, J.; Galoppini, E. *Langmuir* **2008**, *24*, 5366. (b) Tacconi, N. R.; Chanmanee,

W.; Rajeshwar, K.; Rochford, J.; Galoppini, E. *J. Phys. Chem. C* **2009**, *113*, 2996. (c) Wang, Q.; Campbell, W. M.; Bonfantani, E. E.; Jolley, K. W.; Officer, D. L.; Walsh, P. J.; Gordon, K.; Baker, R. H.; Nazeeruddin, M. K.; Grätzel, M. *J. Phys. Chem. B* **2005**, *109*, 15397. (d) Hasobe, T.; Imahori, H.; Fukuzumi, S.; Kamat, P. V. *J. Mater. Chem.* **2003**, *13*, 2515. (e) Nogueira, A. F.; Furtado, L. F. O.; Formiga, A. L. B.; Nakamura, M.; Araki, K.; Toma, H. E. *Inorg. Chem.* **2004**, *43*, 396.

[22] (a) Gulbinas, V.; Chachisvilis, M.; Valkunas, L.; Sundström, V. *J. Phys. Chem.* **1996**, *100*, 2213. (b) He, J. J.; Benkö, G.; Korodi, F.; Polivka, T.; Lomoth, R.; Åkermark, B.; Sun, L.; Hagfeldt, A.; Sundström, V. *J. Am. Chem. Soc.* **2002**, *124*, 4922.

[23] (a) Pellnor, M.; Myllyperkiö, P.; Korppi–Tommola, J.; Yartsev, A. P.; Sundström, V. *Chem. Phys. Lett.* **2008**, *462*, 205. (b) Wenger, B.; Grätzel, M.; Moser, J. E. *J. Am. Chem. Soc.* **2005**, *127*, 12150.

Chapter 3

Role of Binding Structures of Zn-Porphyrin on TiO_2 Surface in Dye-Sensitized Solar Cells: Systematic Investigation by Ultrafast Spectroscopy and Sum Frequency Generation

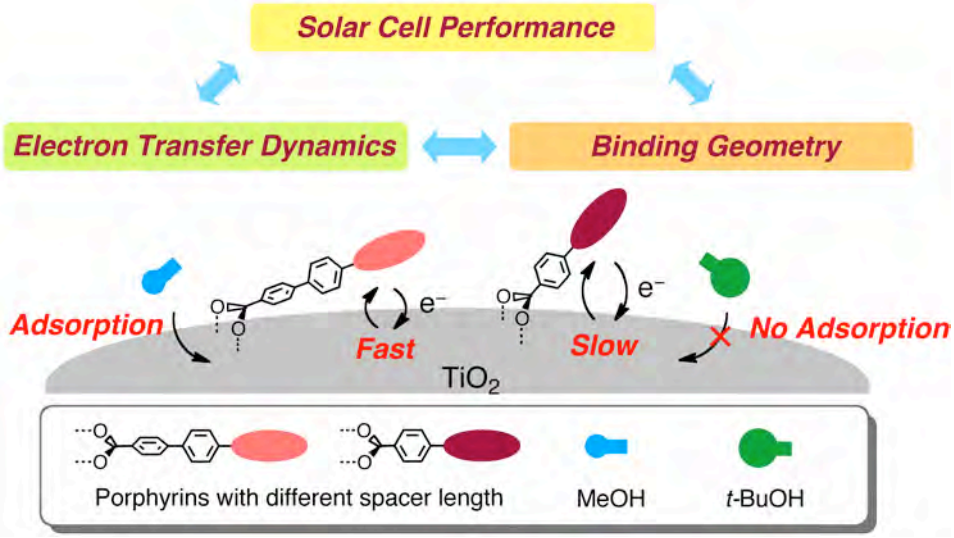

Abstract: Zn-porphyrins (ZnP) anchored to nanocrystalline TiO_2 films have been used for dye-sensitized solar cells. Binding geometry of the porphyrins on the TiO_2 surface in different immersion solvents was characterized by vibrational sum frequency generation (SFG) on CN-labeled ZnPs, and the average tilt angles of the porphyrin molecules on the surface were determined. Almost identical electron transfer dynamics of labeled and non-labeled sensitizers proved that sensitizer binding is largely unaffected by the CN-label. By correlating binding geometry, electron transfer dynamics and solar cell efficiency, guidelines to efficient material design are obtained. Thus, a linear correlation between average tilt angle and solar cell efficiency normalized for surface coverage (η_{rel}) is demonstrated, and since tilt angle determines the distance of through-space electron transfer between porphyrin and TiO_2, the electron transfer rate is directly related to tilt angle. Therefore, the more upright (relative to the TiO_2 surface) orientation of the porphyrin molecule, the higher concentration of long lived electrons in the conduction band contributing to the photocurrent and higher solar cell efficiency. The results also show that long immersion time (12 h) leads to decreased solar cell efficiency through two aggregation induced effects – changes of binding geometry and increased radiationless quenching decreasing injection efficiency. It is also revealed that the immersion solvent (methanol) may affect binding geometry through co-adsorption with the porphyrin molecule and modify the electron transfer dynamics and consequently solar cell efficiency.

Introduction

Dye-sensitized solar cells (DSCs) as introduced by Grätzel and co-workers, have received extensive development efforts over the past two decades and now stand out as one of the most promising alternatives for photovoltaic solar energy conversion.[1] Till now, ruthenium polypyridyl complexes have been demonstrated as excellent photosensitizers of TiO_2 and have yielded the highest solar energy-to-electricity power conversion efficiencies (η) up to 12.2%.[2] However, in view of the cost and environmental demand, organic dyes are strongly desired for their high extinction coefficients and the diversity of molecular structures.[3] Therefore, organic dyes and their derivatives have been investigated as potential sensitizers for DSCs.[4-12] To date, the highest η obtained for organic-dye based DSCs have reached a considerable level of 10.3%.[13] On the other hand, porphyrins have been frequently employed as sensitizers for DSCs (so called porphyrin sensitized solar cells, PSSCs) due to their strong Soret (400-450 nm) and moderate Q bands (550-600 nm), and they have demonstrated η values approaching the highest reported for other types of dyes, i.e up to 11 %.[14,15]

In DSCs, after light absorption, an excited state of the sensitizer injects an electron into the conduction band of the semiconductor.[16] Measuring the electron injection kinetics between the sensitizer and inorganic semiconductor has been a subject of intense research because understanding the interfacial injection process is essential for designing interfaces that are favorable for charge injection and high solar cell efficiency.[17-19] Both electron injection and recombination at the dye/semiconductor interface can be anticipated to be key processes, directly controlling the solar cell efficiency. High power conversion efficiency can be attributed to efficient solar energy harvesting by the sensitizer, efficient electron injection and slow recombination, resulting in a high incident photon to current conversion efficiency (IPCE).[20] Experimentally, ultrafast spectroscopy has shown that excited-state electron injection into TiO_2 often is characterized by non-exponential kinetics, a behavior attributed to the presence of a distribution of sensitizer-semiconductor binding geometries, distances and energetics.[21] This has been thoroughly studied for both Ru polypyridyl complexes and other dye/TiO_2 systems.[19a,21] Also electron-cation recombination has been observed to have highly non-exponential kinetics covering wide timescales from hundreds of picoseconds to nanoseconds and microseconds.[22] Trap energy landscapes[23] and sensitizer-semiconductor binding geometries[24] have been suggested as explanations.

With PSSC now belonging to the most efficient DSSC it is becoming increasingly interesting to obtain detailed knowledge of the factors controlling power conversion efficiency, with the aim to further improve performance. On the other hand, for photovoltaic cells with zinc(II)-5,10,15,20-tetrakis(4-carboxyphenyl)porphyrin-sensitized TiO_2 electrodes, a wide range of IPCE and η values have been reported.[25] These results imply that the performance of

PSSC is quite sensitive to the experimental conditions such as immersion solvent and immersion time. To achieve high performance and reproducibility of cell performance it is essential to elucidate the relationship between rates and efficiency of electron injection and recombination, porphyrin-semiconductor binding geometries, and solar cell efficiency, which are expected to have direct impact on PSSC performance.

Recently, we took the first steps in this direction by investigating the photoinduced electron injection and recombination in Zn-porphyrin sensitized TiO_2 electrodes.[26] Electron injection and electron-cation recombination rates were studied for several different Zn-porphyrin molecules at various conditions of immersion (different solvents and immersion times). Contrary to expectation, it was observed that the electron transfer rates (both injection and recombination) varied in a way inconsistent with electron transfer occurring through the molecular connecting spacer. Based on these results it was suggested that the sensitizer binding to the semiconductor surface is characterized by a distribution of tilt-angles and electron transfer occurs through space rather than through the molecular spacer. For the family of studied Zn-porphyrin molecules a direct correlation between amount of long lived electrons in the conduction band (measured as amplitude of very slow (~50 ns) electron-cation recombination) and solar cell power conversion efficiency was observed.[26] Transmission electron microscopy (TEM) of the studied nanostructured electrodes provided support for the tilted binding geometry.[26]

With the work reported here we now take next step towards a material characterization that can lead to design and manufacturing DSC materials with predictable and controlled properties. To achieve this we need methods that can report on both interfacial sensitizer-semiconductor structure and electron transfer dynamics. By combining surface sensitive sum frequency generation (SFG) to characterize dye-binding geometry and time resolved transient absorption spectroscopy to measure electron transfer rates, we obtain a detailed picture of how sensitizer binding and electron injection/recombination dynamics are correlated and how they control solar cell performance (power conversion efficiency). The binding geometry of the sensitizer is obtained from SFG measurements on Zn-porphyrin molecules (the same as in[26]) labeled with a CN infrared-active chromophore (see **Figure 1**) that can be selectively identified in the SFG spectrum. The IR transition dipole moment of the CN-group is along the symmetry axis of the Zn-porphyrin molecules – SFG will therefore give the orientation of the porphyrin core relative to the semiconductor surface (the tilt angle (θ) relative to the surface normal). In order for the CN-labeled molecules to be good reporters on the binding geometry of non-labeled molecules, labeled and non-labeled molecules of course have to have the same binding. Since electron transfer is a sensitive measure of distance we can use the rates of electron injection and recombination as a critical test of the similarity of

sensitizer binding geometry for labeled and non-labeled molecules – except for the small CN-label the molecules are identical (**Figure 1**) and we do not expect that other factors than binding geometry will influence the electron transfer. This approach to correlate sensitizer surface binding geometry, electron transfer dynamics and solar sell performance is graphically illustrated in **Scheme 1**.

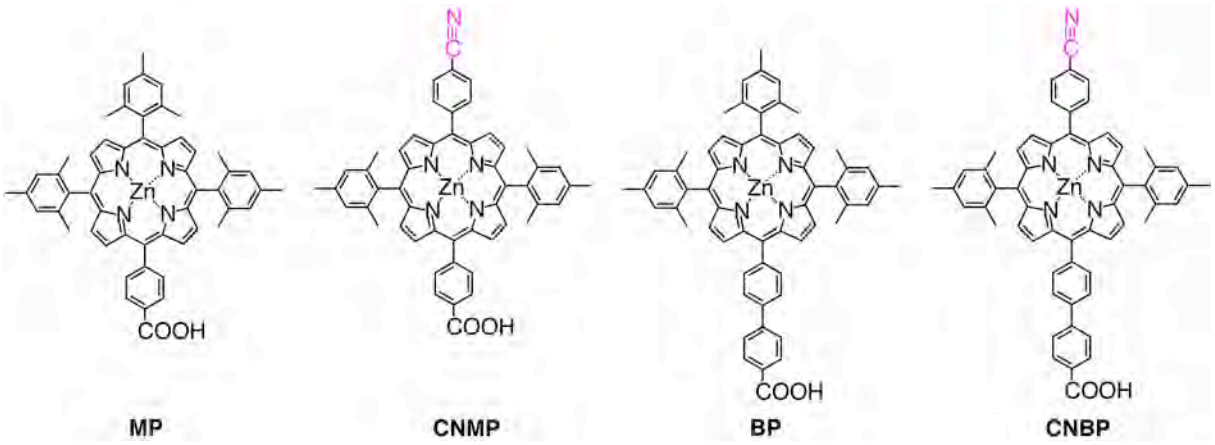

Figure 1. Molecular structure of CN-labeled and non-labeled Zn-porphyrins. MP was defined as **2,4,6-Me** in Chapters 1 and 2.

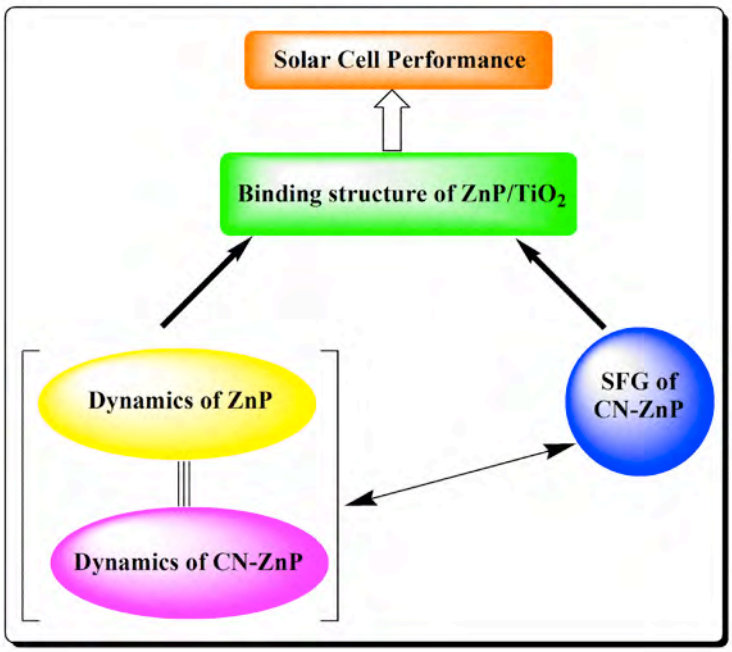

Scheme 1. Illustration of the experimental approach used in this work – Sum Frequency Generation (SFG) measures the binding geometry on the TiO_2 surface of CN-labeled Zn-porphyrin molecules, and comparison of electron transfer dynamics of CN-labeled and non-labeled molecules reveals the suitability of the CN-ZnPs as structural probes. Finally, binding geometry and electron transfer dynamics are correlated to solar cell performance.

Results and Discussion

Photophysics of CN-labeled Zn-porphyrins in solution

Figures 2a, **b** show the normalized steady state absorption and fluorescence spectra of CN-labeled and non-labeled Zn-porphyrins in MeOH. The absorption and fluorescence maximum wavelengths of CN-labeled molecules are quite similar to those of non-labeled molecules. Interestingly, the CN-labeled molecules show a ~3 nm red shift of the $Q_{(0,0)}$ absorption band as compared to non-labeled molecules. This is because the bulky 2,4,6-trimethylphenyl group has large steric hindrance with the porphyrin macrocycle so that the phenyl group is twisted out of the porphyrin plane, resulting in less conjugation. On the other hand, the 4-cyanophenyl group has less steric hindrance, leading to more effective conjugation between them. The effect of this difference in conjugation is also visible as a broadening of the absorption and fluorescence bands of the CN-labeled molecule relative to the non-labeled ones. Further, both monophenyl (CNMP) and biphenyl (CNBP) spacer molecules show very similar absorption and fluorescence spectra, implying that the electronic structure of the porphyrin core is not perturbed by the different spacers.

Figure 3a shows the transient absorption spectra of BP and CNBP in MeOH measured at 1 ps after excitation (the corresponding spectra of MP and CNMP are given in **Figure 3b**); the negative peak at ~553 nm represents the ground state bleach, the band at ~660 nm is assigned to stimulated emission, and the 595 nm band carries contribution from both ground state bleach and stimulated emission. These bands are superimposed on the broad and structureless singlet excited state absorption (ESA), which can be obtained from a spectral analysis of the measured transient spectra[26] (see **Figure 3f**). The detailed spectral description of non-labeled molecules

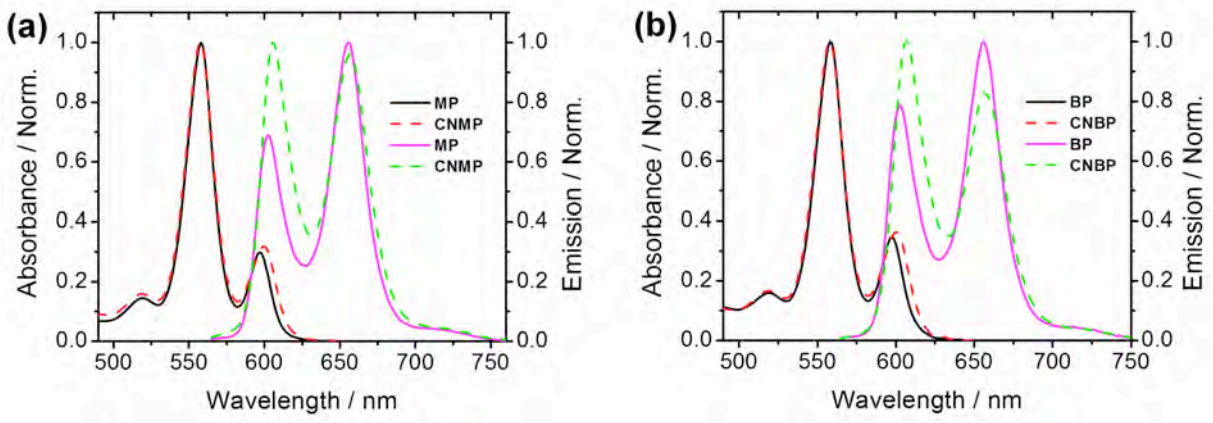

Figure 2. Normalized absorption spectra of (a) **MP** (black solid line) vs **CNMP** (red dotted line) and (b) **BP** (black solid line) vs **CNBP** (red dotted line) in MeOH and normalized steady state fluorescence spectra of (a) **MP** (magenda solid line) vs **CNMP** (green dotted line) and (b) **BP** (magenda solid line) vs **CNBP** (green dotted line) in MeOH.

already has been reported.[26] Here we can see that the wavelength positions of the bands in the transient absorption spectrum of the CN-labeled molecules are consistent with the positions of the corresponding bands in the steady state absorption and fluorescence spectra. These spectral assignments will be used to determine probe wavelengths for monitoring the electron transfer dynamics.

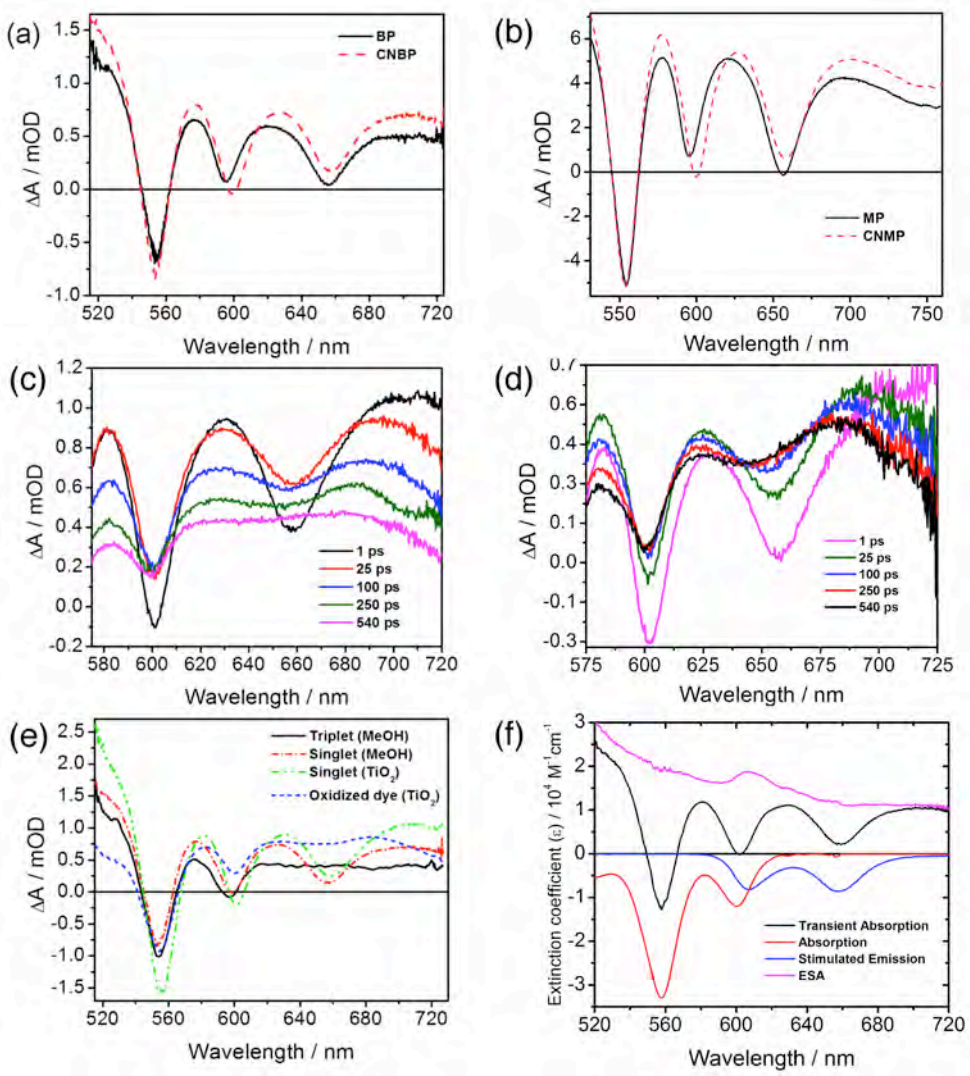

Figure 3. Transient absorption singlet excited state spectra of (a) **BP** (solid black) vs **CNBP** (dotted red) (b) **MP** (solid black) vs **CNMP** (dotted red) in MeOH solution (at 1 ps after excitation at 558 nm). Transient absorption spectra of TiO_2 film sensitized by (c) **CNBP** and (d) **CNMP** in MeOH for 1h, recorded at different times after excitation at 558 nm. (e) Transient absorption (black), ground state bleach (red), stimulated emission (blue), and singlet excited state absorption (magenda) spectra of **CNBP** in MeOH. (f) Spectral components extracted from the measured transient absorption spectra of **CNBP** in MeOH and TiO_2 film of **CNBP**: Triplet excited state in MeOH (solid black), Singlet excited states in MeOH (dotted red) and on TiO_2 (dotted green), porphyrin radical cation on TiO_2 (dotted blue).

Electron transfer dynamics of Zn-porphyrin sensitized TiO_2 films

In this section we provide information that makes it possible to interpret and understand the results of the time resolved transient absorption measurements of electron transfer in Zn-porphyrin sensitized TiO_2 films. **Figure 3c** shows the transient absorption spectrum of CNBP/TiO_2 measured at several delay times from ~1 ps to 540 ps after excitation (spectrum of CNMP/TiO_2 is presented in **Figure 3d**). The early time (1 ps) spectrum shows strong contribution from the dye excited state spectrum (ground state bleach, excited state absorption and stimulated emission). A comparison between this spectrum and the corresponding solution spectrum (**Figure 3a**) shows that the two spectra are somewhat different. This difference may be due to a component of ultrafast (< 1 ps) electron injection (see below). The transient absorption spectrum at 540 ps corresponds to the oxidized dye and the depleted ground state and the spectral evolution from 1 ps to 540 ps represents the electron injection and concomitant cation formation. The spectral shape changes very little beyond 250 ps, suggesting that electron injection is complete on this time scale. **Figure 3e** presents spectra obtained as a result of fitting of species associated spectra (SAS). One can see that the SAS related to the singlet excited state are quite similar for CNBP in solution and adsorbed to TiO_2 whereas the SAS of the triplet excited state obtained at later time for CNBP in solution (nearly flat featureless triplet state absorption) is clearly different from the long-time SAS observed for the CNBP on TiO_2 and assigned to the oxidized CNBP (stronger photo-induced absorption with a characteristic two-humps shape).[26]

More precise temporal information on the electron transfer dynamics can be obtained by measuring kinetics at ~660 nm; since at this wavelength the differential absorption spectrum has contributions from both excited state (SE and ESA) and oxidized dye, the kinetics provides information on both electron injection and recombination. **Figures 4a**, **b** illustrate typical appearances of the measured kinetics of both labeled and non-labeled molecules immersed in MeOH and *t*-BuOH:ACN. The rise of each kinetic trace represents the electron injection and is described by two exponentials and a certain portion of a very fast rise (<0.1 ps), whereas the decay representing electron-cation recombination can be described by one to three time constants, ranging from a few hundred ps to more than several tens of ns (> 50 ns). All fitted time constants and the corresponding amplitudes are summarized in **Table 1**.

Table 1. Fitting Parameters of Electron Injection and Recombination Dynamics in Zn-Porphyrin-Sensitized TiO_2 Films (at 660 nm)

cell	immersion solvent	immersion time (h)	rise			decay		
			τ (ps) amplitudes [%]			τ (ns) amplitudes [%]		
MP/ TiO_2	MeOH	1	<0.1	0.8	40	-	-	>50
			[28]	[21]	[51]	-	-	[100]
		12	<0.1	6	70	-	0.7	>50
			[28]	[21]	[51]	-	[3]	[97]
	t-BuOH:ACN	1	<0.1	1.6	95	-	2.6	>50
			[52]	[12]	[36]	-	[12]	[88]
		12	<0.1	7.1	140	-	0.7	>50
			[31]	[14]	[55]	-	[18]	[82]
CNMP/ TiO_2	MeOH	1	<0.1	0.6	48	-	-	>50
			[24]	[25]	[51]	-	-	[100]
		12	<0.1	5.5	119	-	0.95	>50
			[45]	[18]	[37]	-	[10]	[90]
	t-BuOH:ACN	1	<0.1	4	92	-	1.2	>50
			[66]	[10]	[24]	-	[18]	[82]
		12	<0.1	4.5	217	-	0.89	>50
			[52]	[14]	[34]	-	[30]	[70]
BP/ TiO_2	MeOH	1	<0.1	0.7	42	-	1.2	>50
			[63]	[19]	[18]	-	[15]	[85]
		12	<0.1	2.3	55	-	1.4	>50
			[60]	[11]	[29]	-	[14]	[86]
	t-BuOH:ACN	1	<0.1	1.9	-	0.12	1.31	>50
			[88]	[12]	-	[33]	[30]	[37]
		12	<0.1	0.5	-	0.18	1.28	>50
			[78]	[22]	-	[18]	[35]	[46]
CNBP/ TiO_2	MeOH	1	<0.1	0.5	-	-	0.8	>50
			[74]	[26]	-	-	[10]	[90]
		12	<0.1	1.3	-	-	0.68	>50
			[79]	[21]	-	-	[36]	[64]
	t-BuOH:ACN	1	<0.1	0.7	-	0.08	0.67	>50
			[90]	[10]	-	[30]	[23]	[47]
		12	<0.1	0.5	-	0.02	0.17	>50
			[87]	[13]	-	[12]	[27]	[61]

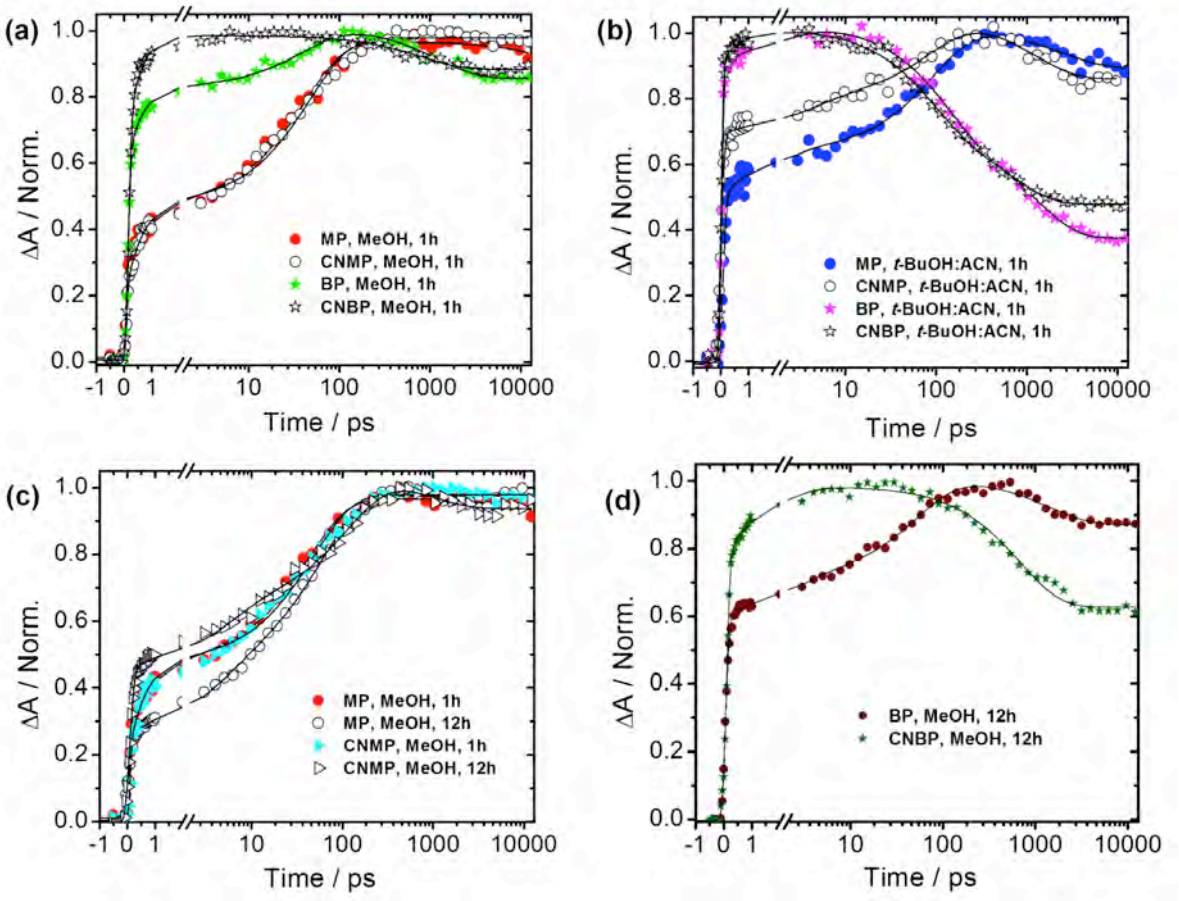

Figure 4. (a) Transient absorption kinetics of **MP** (full, red circles), **BP** (full, green star), **CNMP** (open, black circles), and **CNBP** (open, black star) sensitized TiO_2 in MeOH for 1h. (b) Transient absorption kinetics of **MP** (full, blue circles), **BP** (full, magenta star), **CNMP** (open, black circles), and **CNBP** (open, black star) sensitized TiO_2 in *t*-BuOH:ACN for 1h. (c) Transient absorption kinetics of **MP** (full, red circles) and **CNMP** (full, cyan triangles) sensitized TiO_2 in MeOH for 1h and of **MP** (open, black circles) and **CNMP** (open, black triangle) sensitized TiO_2 in MeOH for 12h. (d) Transient absorption kinetics of **BP** (full, wine circles) and **CNBP** (full, olive stars) sensitized TiO_2 in MeOH for 12h.

Effect of CN-labeling on electron transfer dynamics

We examine this with the help of the results in **Figures 4a**, **b.** We can see that the electron transfer (both injection and recombination) kinetics at 660 nm are very similar for both dyes (i.e. MP vs. CNMP and BP vs. CNBP). This is particularly true for monophenyl spacers (MP and CNMP) where the kinetics with both MeOH and *t*-BuOH:ACN as immersion solvents are more or less identical. There are some minor differences between labeled and non-labeled molecules in the amplitude of fast rise, often coupled to a very small difference in amplitude of

the very slow recombination process. We will discuss this in more detail below. The time constants and amplitudes characterizing the electron injection and recombination processes obtained by the fitting procedure are summarized in **Table 1** and will be discussed in detail below when we compare electron transfer, SFG orientation data and solar cell performance.
The key conclusion to be drawn from these results is that the close similarity of injection and recombination kinetics of labeled and non-labeled molecules shows that both types of molecules must have very similar interaction with the TiO_2 surface and, thus, very similar binding geometry controlling the electron transfer rates. Therefore, we expect that measurements of orientation of the CN-labeled molecules relative to the semiconductor surface with the SFG technique is also representative for the orientation of the non-labeled molecules.

Influence of spacer length on electron transfer

Taking into account that the spacer lengths between porphyrin core and carboxylic group (i.e. MP and CNMP vs. BP and CNBP) are different, we can find the spacer dependence of the electron transfer dynamics in **Figures 4a**, **b**. Both labeled and non-labeled molecules with the longer biphenyl spacer (BP and CNBP) generally have higher amplitudes of fast electron injection and recombination, i.e. overall faster electron transfer. This observation was the main topic of our previous paper;[26] it is counterintuitive if electron transfer occurs through the molecular spacer connecting the molecule to the TiO_2 surface, and it led to the proposed "tilted molecule" binding model and through-space electron transfer (see illustration in inset of **Figure 11**). Thus, we see that for biphenyl spacer molecules, injection is essentially complete after ~10 ps and there is a large component (10-50 %) of recombination on the time scale of several hundred picoseconds (**Table 1**), whereas for the monophenyl spacer molecules there is a large fraction of slowly (~100 ps) injecting molecules and most of the recombination occurs with >50 ns time constant. With the help of SFG measurements on CN-labeled porphyrins we will below provide direct evidence for the "tilted molecule" binding geometry and see how binding geometry correlates to electron transfer dynamics.

Influence of immersion solvent and time on electron transfer dynamics

The molecules with monophenyl and biphenyl spacers respond quite differently to a change of immersion solvent and long immersion time. Both MP/TiO_2 and CNMP/TiO_2 exhibit only small changes in electron transfer dynamics upon changing the immersion solvent from MeOH to the *t*-BuOH:ACN mixture (**Figures 4a**, **b**), or extending immersion time from 1 h to 12 h (**Figure 4c** and **Figure 5a**). For the molecules with biphenyl spacers (BP and CNBP), changing the immersion solvent from MeOH to the *t*-BuOH:ACN mixture leads to a dramatic change of the injection and recombination dynamics (compare the kinetics in **Figures 4a**, **b**) –

the recombination kinetics in MeOH has only a ~10 % amplitude on the several hundred ps time scale, which in the *t*-BuOH:ACN mixture increases to ~50 %. This change in recombination kinetics is coupled to a change in injection kinetics – higher amplitude of fast recombination (~100 ps) is associated with higher amplitude of ultrafast (<< 1 ps) injection. It is known that protic solvents such as alcohols adsorb on a TiO_2 surface,[29] which may affect the porphyrin geometry on the TiO_2 surface. To shed light on the effect of immersion solvent on the electron transfer and solar cell performance in PSSC, SFG vibrational spectroscopy has been employed to investigate the solvent adsorption on the TiO_2 surface. **Figure 6** shows SFG spectra of a TiO_2 surface after immersion into (a) MeOH (red trace) and (b) the *t*-BuOH:ACN mixture (black trace), in the frequency region of the C-H stretch (2800 – 3000 cm^{-1}). After adsorption in MeOH, the SFG spectrum shows three broad peaks around 2825, 2880 and 2945 cm^{-1} and a shoulder around 2970 cm^{-1}. These peaks disappear after ozone treatment for 5 min and thus can be attributed to an adsorbed species from MeOH. Shultz and co-workers reported that methanol adsorbs to the TiO_2 surface in two adsorption modes: physisorbed as molecular methanol and chemisorbed as a methoxy species.[29] Two pairs of C-H stretch peaks were observed and ascribed to the methoxy species (2828 and 2935 cm^{-1}) and molecular MeOH (2855 and 2968 cm^{-1}), which are consistent with the results obtained from the SFG measurements. One can expect that the co-adsorption of MeOH could strongly affect the binding geometry of a porphyin molecule on the TiO_2 surface.

On the other hand, after immersion in the *t*-BuOH:ACN mixed solvent no SFG peak on TiO_2 surface is observed both in the C-H region (**Figure 6**, black trace) and C-N stretching region (spectrum is not given here), indicating that neither *t*-BuOH nor ACN form ordered adsorption structures on the TiO_2 surface. The *t*-butyl group of *t*-BuOH is bulkier than the methyl group of MeOH and probably this is the main reason why *t*-BuOH cannot adsorb to the TiO_2 surface. It should be noted here that we could find the peaks which was attributed to the adsorbed MeOH species even when a porphyrin without methyl group (4-CF_3)[26a] was sensitized with MeOH, but we could not find the peaks when the *t*-BuOH:ACN mixed solvent was used for immersion (**Figure 6b**). This supports that the porphyrin and MeOH molecules can bind to the TiO_2 surface at the same time. The electron transfer kinetics in **Figure 4** show that for all dyes MeOH immersion gives the highest amplitudes of slow injection and slow recombination. This suggests that co-adsorption of MeOH molecules with the porphyrins allows them to adopt a more upright binding geometry of the porphyrin on the TiO_2 surface, making the through-space electron transfer processes slower.

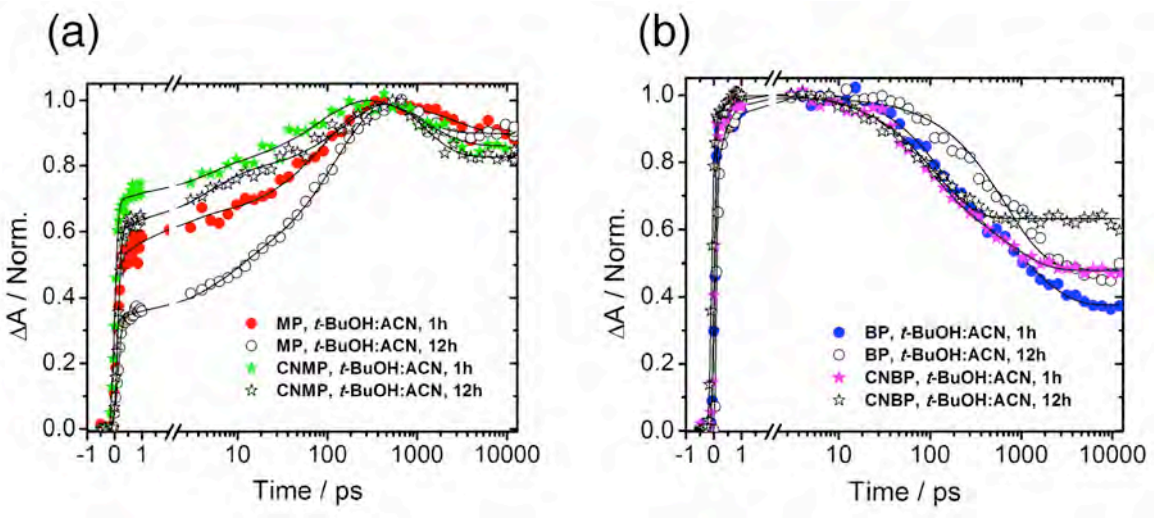

Figure 5. (a) Transient absorption kinetics of **MP** (full, red circles) and **CNMP** (full, green stars) sensitized TiO_2 in *t*-BuOH:ACN for 1h and of **MP** (open, black circles) and **CNMP** (open, black stars) sensitized TiO_2 in *t*-BuOH:ACN for 12h. (b) Transient absorption kinetics of **BP** (full, blue circles) and **CNBP** (full, magenta star) sensitized TiO_2 in *t*-BuOH:ACN for 1h and of **BP** (open, black circles) and **CNBP** (open, black stars) sensitized TiO_2 in *t*-BuOH:ACN for 12h.

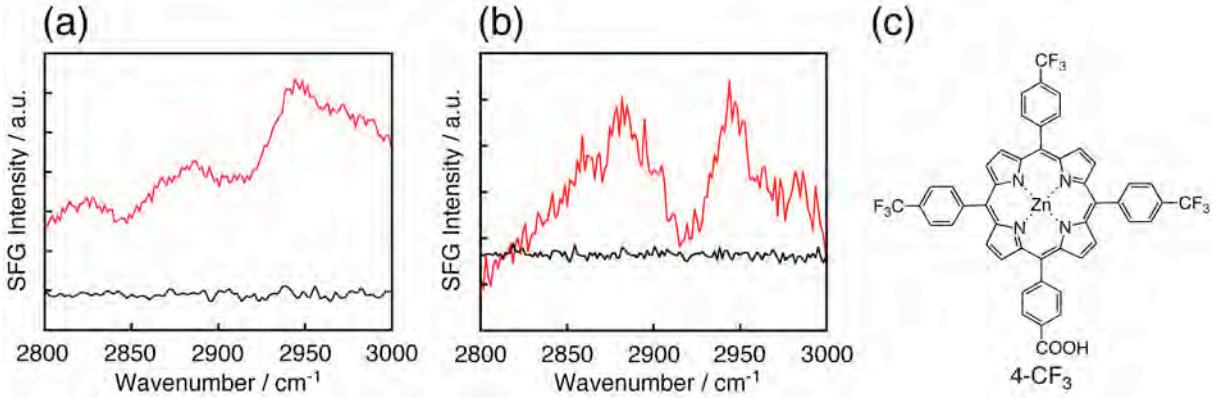

Figure 6. (a) SFG spectra of TiO_2 films sensitized with MeOH (red) and with *t*-BuOH:ACN (black). The spectra in the C-H region of 2800 – 3000 cm^{-1} are shown without normalization. The background signal was subtracted. (b) SFG spectra in the C-H region (2800 – 3000 cm^{-1}) of TiO_2 films sensitized by **4-CF$_3$** in MeOH for 1h (red) and in *t*-BuOH:ACN for 1h (black). The background signal was subtracted. (c) Molecular structure of **4-CF$_3$**.

The effect of long immersion time (12 h in MeOH) on BP and CNBP molecules is more complex than for MP and CNMP and there is some difference between labeled and non-labeled molecules. For the non-labeled molecule (BP) in MeOH long immersion time only changes the kinetics to a small extent (compare **Figure 4a** and **Figure 4d**), whereas long immersion of CNBP leads to higher amplitude of fast (~100 ps time scale) recombination (and ultrafast injection). In the *t*-BuOH:ACN mixed solvent there are some minor differences in recombination between 1 h and 12 h immersion (**Figure 5b**). The increase in fast recombination and ultrafast injection for the TiO_2 film sensitized by CNBP in MeOH for 12 h relative to the non-labeled molecule (**Figure 4d**) could perhaps be a consequence of interaction between the CN-group and the TiO_2 surface.[30] To investigate if this is the case we examined the direct interaction between the CN-group and the TiO_2 surface by using ATR-IR spectroscopy. ATR-IR spectra of CNBP and the TiO_2 films sensitized by CNBP for 1 h and 12 h are depicted in **Figure 7**. The ATR-IR spectrum of the TiO_2 film sensitized by CNMP for 12 h is also shown for comparison. At first, the ATR-IR spectrum of pristine CNBP reveals the characteristic ν(C=O) band of the carboxylic acid group at around 1700 cm^{-1} (**Figure 7a**).[14a,31] This diagnostic for the ν(C=O) disappears for the ATR-IR spectra of the TiO_2 films sensitized by CNMP and CNBP (**Figures 7b-d**) and a marked increase in the symmetric carboxylate band, $\nu(COO_s^-)$, at around 1400 cm^{-1} emerges.[14a,31] These spectral features corroborate that a proton is detached from the carboxylic acid group during the adsorption of the porphyrin on the TiO_2 surface. Similar behavior has also been observed by SFG vibration spectroscopy in the same frequency region. Besides, this is consistent with the previous assignment that a carboxylic acid of analogous porphyrins is bound to the TiO_2 surface via a bridging bindentate mode.[14a] On the other hand, no shift in C≡N frequencies at 2230 cm^{-1} was seen when comparing the CNBP and TiO_2 film with CNBP, implying no interaction between the cyano group and the TiO_2 surface. Moreover, the immersion time (1 h vs. 12 h) does not affect the peak position of the C≡N vibration for the TiO_2 films sensitized by CNMP and CNBP. These results corroborate that there is no direct interaction between the CN-group and TiO_2 surface in this system. Porphyrin aggregation is another possible reason for the increase in fast recombination and ultrafast injection for the TiO_2 film sensitized by CNBP in MeOH for 12 h relative to the non-labeled molecule. Long immersion time often leads to an increase in the degree of porphyrin aggregation[26] and this would affect the porphyrin geometry on the TiO_2 surface and in turn the electron transfer dynamics. In addition, considering the difference in the substituent at the opposite meso-position of the 4-carboxyphenyl group (i.e. 2,4,6-trimethylphenyl group vs. 4-cyanophenyl group), the degree of aggregation in CNBP could be anticipated to be larger than that in BP, which would explain the observed difference in recombination dynamics between BP and CNBP for 12 h immersion time (**Figure 4d**).

The solvent in contact with the dye-semiconductor surface, the covering solvent, could perhaps also be expected to have some influence on the binding geometry[19h,32] and thus the electron transfer dynamics. Work in progress, suggests that such an effect indeed exists and is sensitizer molecule dependent.

In summary of the electron transfer dynamics, perhaps the most striking result is that the molecules with the longer spacer on the TiO_2 surface (BP and CNBP) have faster electron injection and higher amplitude of decay components representing recombination on the hundreds of ps time scale than the molecules with shorter spacer (MP and CNMP). It is also evident that factors such as solvent used in the immersion of the TiO_2 and immersion time may have a significant influence on the electron transfer dynamics through co-adsorption and dye aggregation effects. In the next section we will present the results of the SFG and TEM measurements and see how the electron transfer dynamics is correlated to the binding geometry – i.e. the tilting angle of the porphyrin molecule symmetry axis relative to the surface normal.

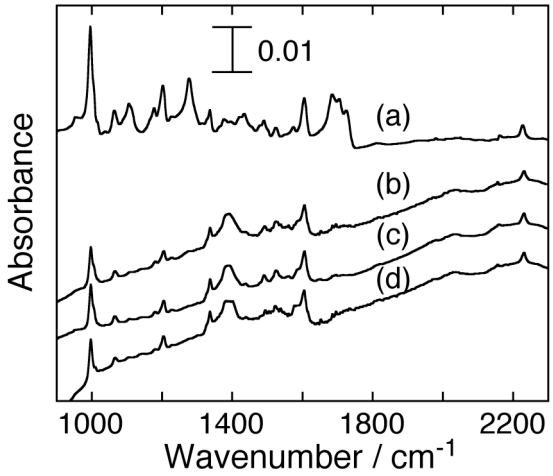

Figure 7. ATR-IR spectra of (a) **CNBP**, (b) TiO_2 film sensitized by **CNBP** for 1 h, (c) TiO_2 film sensitized by **CNBP** for 12 h, and (d) TiO_2 film sensitized by **CNMP** for 12 h. ATR-IR intensities for the powders from TiO_2 films sensitized by **CNMP** and **CNBP** were normalized at the CN peak of the pristine TiO_2 powder (2230 cm^{-1}). The pristine TiO_2 powder was used as a background for the TiO_2 film sensitized by **CNBP**.

Binding geometry of CN-labeled Zn-porphyrins from SFG measurements

Figures 8, **9** show (a,c) *ssp*– and (b,d) *sps*–polarized SFG spectra in the frequency region of the C≡N stretch (2150-2300 cm^{-1}) of the CN-labeled porphyrin sensitized TiO_2 films (CNMP: black trace, CNBP: red trace). By monitoring the SFG signal of the C≡N stretch mode under different polarization combinations, we are able to estimate the orientation of these molecules adsorbed on the TiO_2 surface. A vibration mode around 2230 cm^{-1} is observed in both *ssp*- and *sps*- polarized SFG spectra, which can be assigned as the C-N stretch mode of the

CN group in the CN-labeled porphyrins. Based on eq. 1, we are able to get the exact spectral component for the C-N stretch, and thus to estimate the average tilt angle of the CN group, and the orientation of the dye molecules adsorbed on the surface. A description of the calculation method to obtain the average tilt angle can be found in Experimental Section.

The tilt angles estimated by the SFG measurements are summarized in **Table 2** and two observations can be made: a) both CNMP and CNBP are attached to the TiO_2 surface at a considerable angle relative to the surface normal, and b) the molecule with the longer spacer (CNBP) has on the average a somewhat larger angle. The tilt angles obtained from the SFG measurements are in addition similar to those found for MP and BP with TEM measurements in our previous report.[26] As a further verification of the binding geometries obtained from the SFG measurements we performed TEM measurements on TiO_2 nanoparticles sensitized by CNMP and CNBP (**Figure 10**). The TEM images for the TiO_2 nanoparticles modified with CNMP and CNBP reveal 20-nm sized P25 TiO_2 nanoparticles, covered with a thin porphyrin layer with an average thickness of 0.9-1.5 nm depending on the immersion conditions. Given that respective molecular lengths of CNMP and CNBP along the molecular long axis are 2.0 nm and 2.4 nm (**Figure 10**), the average tilt angles of the porphyrins within the densely-packed monolayer of CNMP and CNBP can be calculated (**Table 2**). The tilt angles of CNBP estimated by the TEM measurements are on the average larger than those of CNMP under the same immersion conditions. In addition, the tilt angles estimated by the SFG measurements largely agree with the TEM measurements, assuring that the SFG method is reliable for determining the molecular geometry of the porphyrin on the TiO_2 surface. Here, it should be noted that considering the positional relationship between the TiO_2 surface and the neighboring terminal proton in the biphenyl spacer of CNBP, the tilt angle of CNBP is limited to ~60º, indicating that CNBP cannot adopt more tilted geometry on the TiO_2 surface. Finally, we notice that an X-ray reflectometry study on Zn-porphyrin molecules adsorbed as a mono-layer on a planar TiO_2 surface arrived at a very similar picture of the sensitizer binding geometry as presented here.[33]

As shown in **Figure 8**, the spectral intensities of the SFG spectra with *t*-BuOH:ACN as immersion solvent are much stronger than that with MeOH. The SFG intensity at the interface depends on both the molecular density and ordering. In the present work, an independent measurement for the dye coverage demonstrated that coverages for CNMP and CNBP on the TiO_2 surface are comparable (**Table 2**). Therefore, higher SFG intensity with *t*-BuOH:ACN immersion solvent suggests that the porphyrins are adsorbed on the TiO_2 surface in a more ordered geometry in *t*-BuOH:ACN as compared to MeOH.

As already discussed in relation to **Figure 6**, MeOH strongly adsorbs to the TiO_2 surface together with the porphyrin, while *t*-BuOH and ACN do not adsorb. The co-adsorption of

MeOH solvent on the TiO_2 surface may weaken the direct intermolecular interaction between the porphyrin molecules, leading to a more random arrangement of the porphyrins on the TiO_2 surface. In contrast, porphyrins immersed in *t*-BuOH:ACN would form a more ordered arrangement on the TiO_2 surface due to the direct interaction between the porphyrins including the bulky 2,4,6-trimethylphenyl groups. Additionally, the SFG intensities of the *ssp*- and *sps*-spectra with immersion time of 1 h are stronger than those with immersion time of 12 h (**Figure 9**). Knowing that long immersion time leads to an increase in the porphyrin aggregation on the TiO_2 surface,[26] this suggests enhanced disorder among sensitizer molecules with increased immersion time.

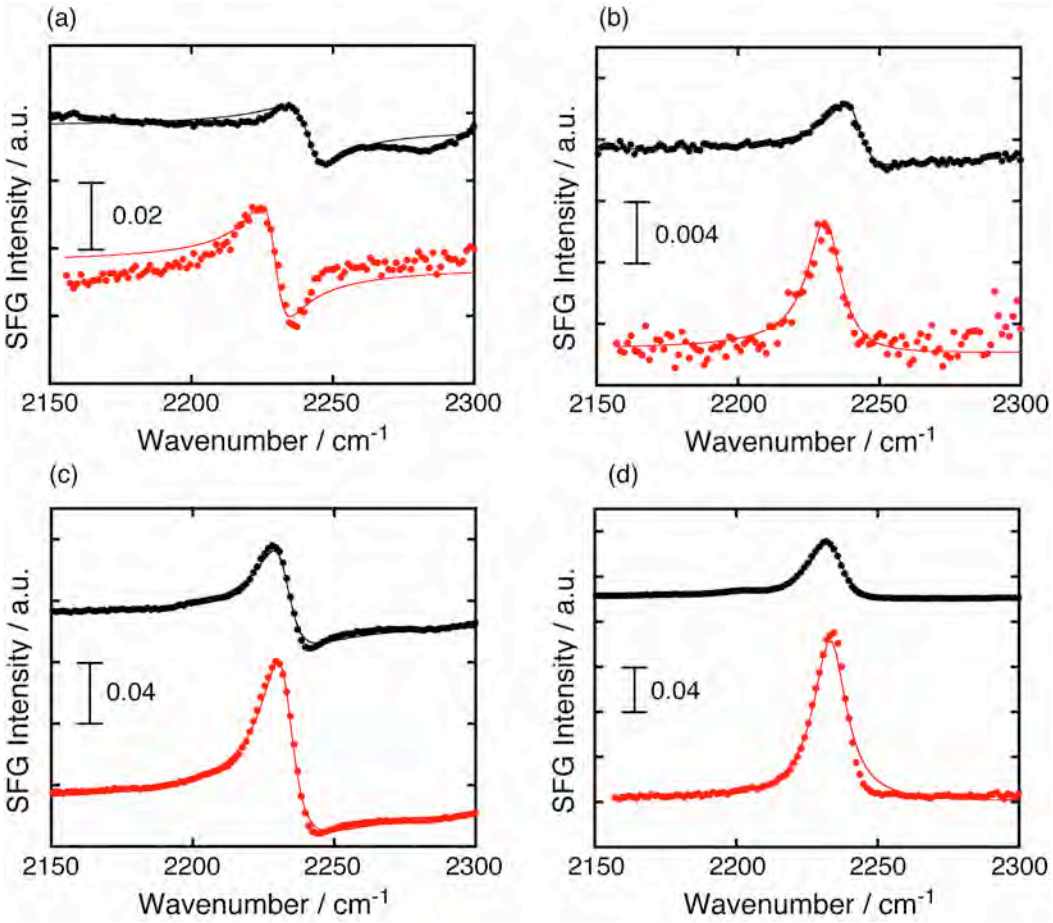

Figure 8. (a) *ssp*- and (b) *sps*-Polarized SFG spectra of CNMP sensitized (black) and CNBP sensitized (red) TiO_2 films with immersion solvent of MeOH. (c) *ssp*- and (d) *sps*-Polarized SFG spectra of CNMP sensitized (black) and CNBP sensitized (red) TiO_2 films with immersion solvent of *t*-BuOH:ACN mixture. Immersion time is 1 h.

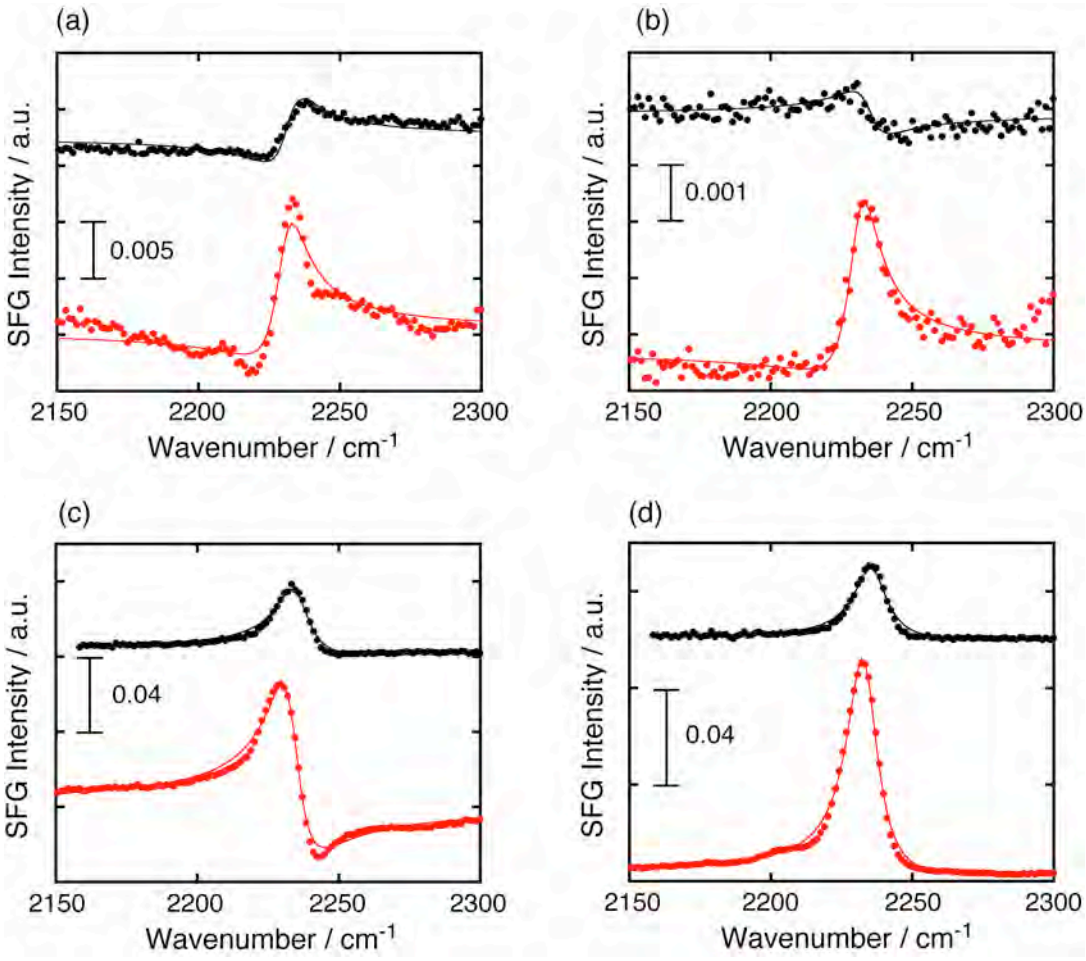

Figure 9. (a) *ssp*- and (b) *sps*-polarized SFG spectra of **CNMP** sensitized (black) and **CNBP** sensitized (red) TiO_2 films with MeOH as immersion solvent. (c) *ssp*- and (d) *sps*-polarized SFG spectra of **CNMP** sensitized (black) and **CNBP** sensitized (red) TiO_2 films with the *t*-BuOH:ACN mixture as immersion solvent. Immersion time is 12 h.

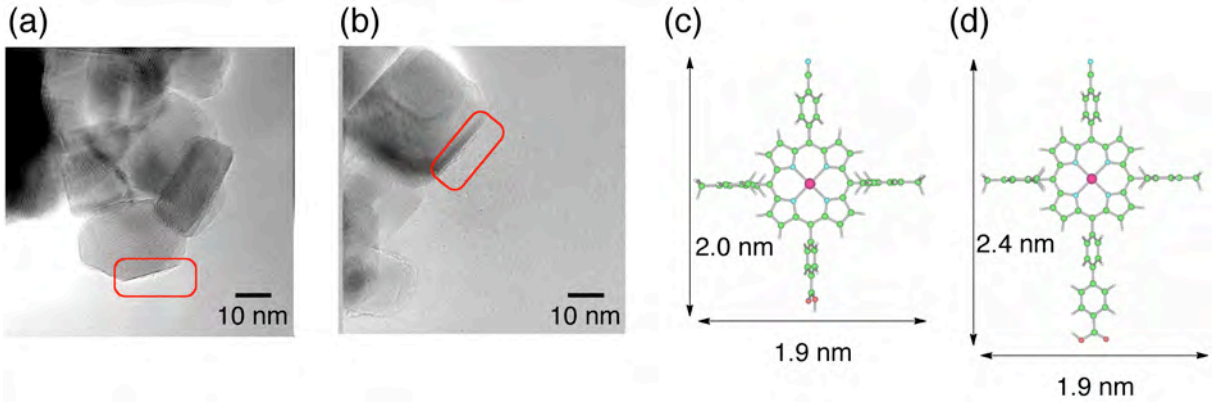

Figure 10. Typical TEM images of TiO_2 nanoparticles sensitized with (a) **CNMP** and (b) **CNBP** in MeOH for 1 h. The average thickness of the porphyrin layers was determined as ca. 1.1 nm for the both porphyrin films. Molecular lengths along the molecular long and short axis of (a) **CNMP** and (b) **CNBP** are also shown for comparison.

Table 2. Tilt Angle and Surface Coverage of Zn-Porphyrin on TiO_2

cell	solvent	time/h	tilt angle[a]	tilt angle[b]	experimental Γ / 10^{-10} mol cm^{-2}	calculated Γ[c] / 10^{-10} mol cm^{-2}
MP/ TiO_2	MeOH	1	d	d	1.2[e]	1.2[e]
	MeOH	12	d	d	1.2[e]	1.2[e]
	t-BuOH:ACN	1	d	53±7° [e]	1.0[e]	1.2[e]
	t-BuOH:ACN	12	d	d	1.3[e]	1.2[e]
BP/ TiO_2	MeOH	1	d	d	1.1[e]	1.2[e]
	MeOH	12	d	d	1.2[e]	1.2[e]
	t-BuOH:ACN	1	d	60±6° [e]	1.2[e]	1.2[e]
	t-BuOH:ACN	12	d	d	1.1[e]	1.2[e]
CNMP/ TiO_2	MeOH	1	51±4°	59±3°	1.1	1.2
	MeOH	12	47±3°	44±4°	1.2	1.2
	t-BuOH:ACN	1	56±4°	63±2°	1.2	1.2
	t-BuOH:ACN	12	59±5°	44±8°	1.2	1.2
CNBP/ TiO_2	MeOH	1	58±5°	64±4°	1.1	1.2
	MeOH	12	55±4°	56±7°	1.3	1.2
	t-BuOH:ACN	1	58±5°	69±2°	1.2	1.2
	t-BuOH:ACN	12	57±5°	58±7°	1.3	1.2

[a] Estimated from SFG measurements. [b] Estimated from TEM measurements. [c] Assuming that the porphyrin molecules bearing one carboxylic group are densely packed onto the TiO_2 surface to which the carboxylic acid binds. [d] Not measured. [e] Taken from ref 26.

Correlation between binding geometry and electron transfer

Now we are in a position to compare the SFG and electron transfer results. **Figure 11** displays that there is a linear relationship between the amplitude of the long lived kinetic component ($A_{>50ns}$) corresponding to very slow electron-cation recombination (and thus long lived conduction band electrons) and tilt angle (**Table 1** and **Table 2**) – small tilt angle results in more long lived electrons. This is of course a result of the strong distance dependence of electron transfer – a small tilt angle corresponds to a larger fraction of molecules having a

larger electron transfer distance and therefore more of slower electron transfer. The tilt angle for one particular type of molecule should not be seen as a fixed and well-defined orientation of the molecules. Heterogeneity of the molecules as well as the TiO_2 surface leads to a distribution of tilt angles. Thus, the measured angle rather represents the average of a distribution of angles. The very slow recombination, in our fitting procedure modeled as one lifetime, > 50 ns, most likely in reality corresponds to a range of very long recombination times corresponding to the part of the tilt angle distribution representing the most up-right molecules and thus the slowest recombination. All this means that a small tilt angle should be seen as a larger fraction of sensitizers exhibiting slow recombination. This view nicely agrees with the correlation between tilt angle and amplitude of very slow recombination, $A_{>50\ ns}$.

A change in dye-semiconductor distance, through a change of tilt angle, should of course influence both the electron injection and recombination processes. If this is correct there should exist a correlation between the rate of electron injection and rate of recombination. **Figures 12** show that there in fact exists such a correlation – the higher amplitude of instantaneous rise of the transient absorption signal (<< 1 ps electron injection) the lower amplitude of slow recombination. The very fast injection corresponds to a fraction of molecules making close contact with the TiO_2 surface, and thus also very fast recombination (~100 ps time scale recombination). From this we can see that both injection and recombination give the same picture of the binding geometry, which is corroborated by the tilt angle from the SFG measurements.

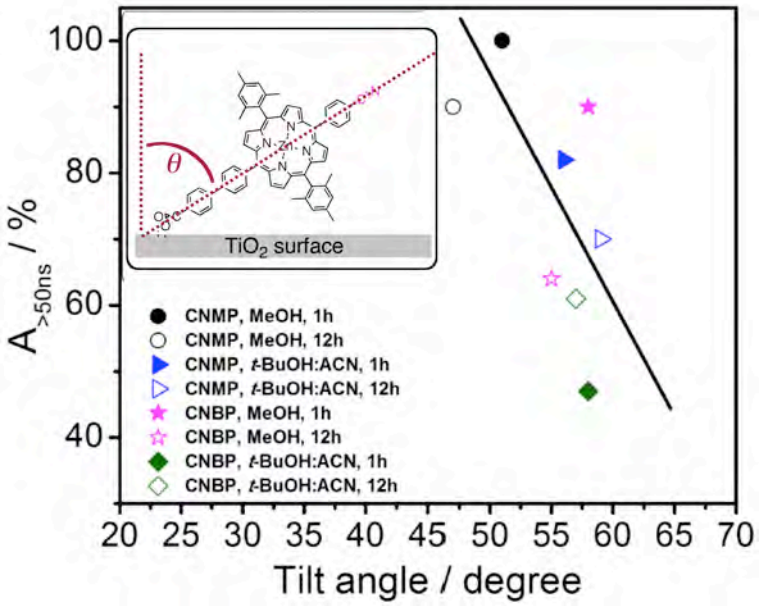

Figure 11. Long lived recombination signal ($A_{>50\ ns}$) as a function of tilt angle. Closed and opened symbols are representing for 1 h and 12 h respectively. Inset shows the illustration of the "tilted molecule" binding geometry.

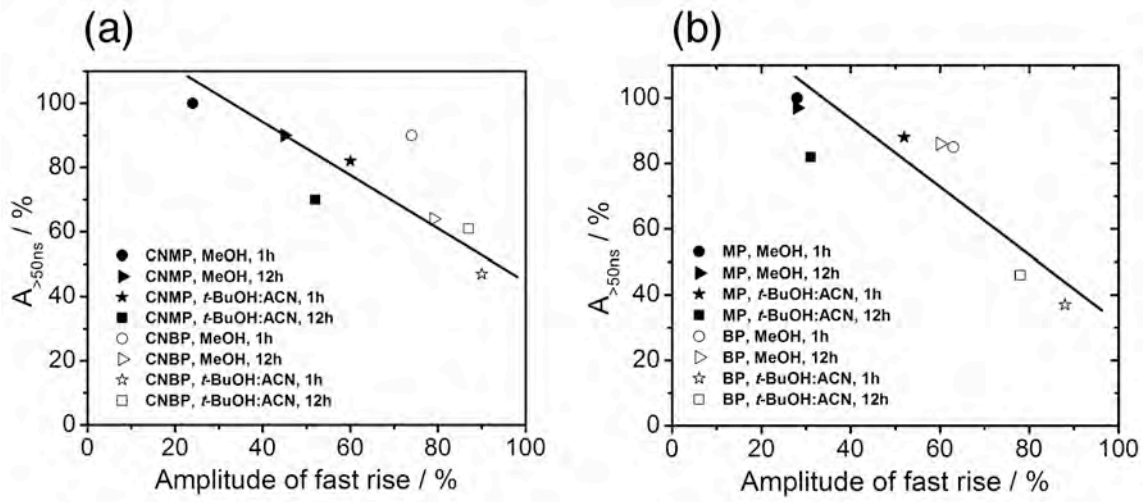

Figure 12. (a) Instantaneous rise as a function of long-lived recombination signal ($A_{>50\ ns}$) of CN-labeled molecules. Closed and opened symbols correspond to monophenyl and biphenyl spacer molecules, respectively. (b) $A_{>50ns}$ vs. amplitude of instantaneous rise of transient absorption kinetics of non-labeled molecules. Closed and opened symbols correspond to monophenyl and biphenyl spacer molecules, respectively.

Photovoltaic properties of CN-labeled Zn-porphyrins sensitized TiO_2 electrodes

To investigate the correlation between the electron transfer kinetics, porphyrin geometry on the TiO_2 surface, and solar cell performance, we examined the photovoltaic properties of the CN-labeled PSSCs. At first, total amounts of the porphyrins adsorbed on the TiO_2 films were determined by measuring the absorbance of the porphyrins that were dissolved from the porphyrin-modified TiO_2 films into DMF containing 0.1 M NaOH aqueous solution. After immersion, labeled porphyrins reached almost saturated surface coverage (Γ) in 1 h. The trend was very similar to that of the non-labeled porphyrins as seen in our previous report.[26] For instance, the saturated Γ values of CNMP that was sensitized with MeOH were determined to be $1.1\times\ 10^{-10}$ mol cm^{-2} for 1 h immersion and $1.2\ \times\ 10^{-10}$ mol cm^{-2} for 12 h (**Table 2**). Analogous Γ values were obtained when the *t*-BuOH:ACN mixture as immersion solvent was used for CNBP. By assuming that the porphyrins are densely packed to form a complete monolayer on a flat TiO_2 surface, theoretical Γ values of CNMP and CNBP were calculated to be $\Gamma = 1.1\times10^{-10}$ mol cm^{-2}. By taking into account the good agreement between the calculated and experimental Γ values together with the saturated adsorption behavior of CNMP and CNBP, we conclude that densely packed monolayers of CNMP and CNBP are formed on the TiO_2 surface.[26] Then, we evaluated the solar cell performance of the CN-labeled porphyrin-sensitized TiO_2 electrodes. The η value is derived from the equation: $\eta = J_{sc} \times V_{oc} \times ff$, in which J_{sc} is the short-circuit current, V_{oc} is the open-circuit potential, and ff is the fill factor. In the case of CNMP sensitized with MeOH, the η value increased rapidly with

increasing immersion time to reach a maximum η value of 3.4% in 1 h and then decreased gradually to reach a constant η value of 2.9% for 12 h immersion. Similar behavior of η for both CNMP and CNBP as a function of the immersion time was noted when the *t*-BuOH:ACN mixture was used as the immersion solvent. The maximum η value (3.4%) and the maximum IPCE (incident photo-to-current efficiency) (59%) of the CNMP-sensitized TiO_2 cell with MeOH as immersion solvent are much larger than the corresponding values (2.0%, 37%) of the CNBP-sensitized TiO_2 cell. The photovoltaic parameters of CNMP and CNBP are listed in **Table 3** (Those of MP and BP are also shown in **Table 3** for comparison).

Table 3. Cell Performance of Zn-Porphyrin-Sensitized Solar Cells.

cell	solvent	time/ h[b]	IPCE (APCE)/%		J_{SC}/ mA cm^{-2}	V_{OC}/ V	*ff*	η/%
			420 nm	560 nm				
MP /TiO_2	MeOH	1	76 (76)	58 (60)	9.4	0.76	0.64	4.6
	MeOH	12	74 (74)	53 (53)	8.3	0.72	0.62	3.7
	t-BuOH: ACN[a]	1	63 (63)	52 (56)	7.6	0.69	0.64	3.4
	t-BuOH: ACN[a]	12	64 (64)	30 (32)	5.0	0.64	0.66	2.1
BP /TiO_2	MeOH	1	61 (61)	41 (42)	6.0	0.65	0.65	2.6
	MeOH	12	34 (34)	13 (13)	5.2	0.62	0.64	2.3
	t-BuOH: ACN[a]	1	57 (57)	40 (41)	5.6	0.64	0.66	2.4
	t-BuOH: ACN[a]	12	41 (41)	20 (20)	4.7	0.61	0.68	1.9
CNMP /TiO_2	MeOH	1	59 (59)	46 (46)	7.3	0.69	0.67	3.4
	MeOH	12	54 (54)	37 (37)	6.3	0.69	0.65	2.9
	t-BuOH: ACN[a]	1	53 (53)	28 (28)	4.9	0.64	0.68	2.1
	t-BuOH: ACN[a]	12	34 (34)	6 (6)	3.4	0.62	0.63	1.3
CNBP /TiO_2	MeOH	1	37 (37)	16 (16)	4.6	0.66	0.67	2.0
	MeOH	12	32 (32)	6 (6)	3.5	0.61	0.66	1.4
	t-BuOH: ACN[a]	1	21 (21)	7 (7)	2.9	0.63	0.67	1.2
	t-BuOH: ACN[a]	12	16 (16)	4 (4)	1.7	0.56	0.64	0.6

[a]1:1, v/v. [b]Short immersion time giving the highest η value.

Correlation between binding geometry (tilt angle), electron-cation recombination and solar cell efficiency

Now we are in a position to discuss the correlation between binding geometry, electron-cation recombination, and solar cell efficiency, η. The solar cell efficiency η correlates with J_{sc}, which is a wave number integrated value of IPCE. For a discussion of how key processes contribute to the efficiency it can be defined as,

η ~ (efficiency of light harvesting) × (yield of electron injection) × (yield of long-lived conduction band electrons that can be extracted) × (1 – other losses)

Light harvesting is related to the surface coverage of the dye and how well it absorbs the wavelengths of the solar spectrum, and it varies substantially between the different dyes and various experimental conditions. Thus, variations in the η value are to a certain extent a result of variation in light-harvesting. The absorption spectra are quite similar for all studied porphyrin dyes, but the surface coverage may vary somewhat for the studied porphyrin-TiO_2 electrodes. When discussing solar cell efficiency-electron transfer dynamics correlations below, we therefore use an efficiency normalized to surface coverage (η_{rel}) to remove any uncertainly that stems from variations in light-harvesting efficiency (**Table 4**).[26] Electron injection is more or less the same for all the porphyrins and condition for short immersion time (i.e. 1 h). Furthermore electron injection is also fast as compared to the excited state lifetime of the porphyrin, so electron injection is close to 100% efficient (except for some of the 12 h immersions where porphyrin excited state quenching induced by strong dye-dye interaction decreases the efficiency of electron injection). Thus, in most cases electron injection does not influence the efficiency. In contrast, recombination directly controls the number of long-lived electrons in the conduction band contributing to the IPCE value, and thus the photocurrent, suggesting that recombination should be the major determining factor for solar cell efficiency. This expectation was verified in our previous work,[26] where high solar cell efficiency was shown to be directly coupled to a high concentration of long lived (> 50 ns) conduction band electrons injected from the photoexcited sensitizer. Also in this paper we use the same characteristics and now in addition extend the studies to a direct measurement of the dye binding geometry, using SFG. A plot of solar cell efficiency normalized to surface coverage (η_{rel}) vs. $A_{>50ns}$ (**Figure 13**) for CN-labeled molecules illustrates that there is a direct correlation between efficiency and amplitude of slow recombination, similarly to that shown earlier for non-labeled molecules.[26] Thus, higher efficiency corresponds to higher amplitude of slow recombination (and thus long lived conduction band electrons).

Table 4. Power Conversion Efficiencies Normalized for Surface Coverage (η_{rel}) Correlated to Amplitude of Long Lived ($A_{>50ns}$) Recombination.

cell	immersion solvent	immersion time (h)	η_{rel}	$A_{>50ns}$ (%)
MP/TiO$_2$	MeOH	1	5.4[a]	100
	MeOH	12	4.3[a]	97
	t-BuOH:ACN	1	4.8[a]	88
	t-BuOH:ACN	12	2.3[a]	82
BP/TiO$_2$	MeOH	1	3.31[a]	85
	MeOH	12	2.68[a]	86
	t-BuOH:ACN	1	2.8[a]	37
	t-BuOH:ACN	12	2.41[a]	46
CNMP/TiO$_2$	MeOH	1	4.32	100
	MeOH	12	3.38	90
	t-BuOH:ACN	1	2.45	82
	t-BuOH:ACN	12	1.52	70
CNBP/TiO$_2$	MeOH	1	2.54	90
	MeOH	12	1.51	64
	t-BuOH:ACN	1	1.4	47
	t-BuOH:ACN	12	0.65	61

[a] Taken from ref 26.

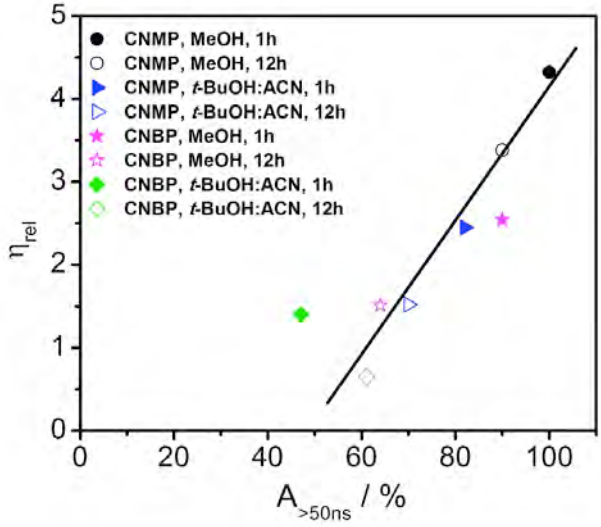

Figure 13. Solar cell efficiency normalized for surface coverage (η_{rel}) as a function of long-lived recombination signal ($A_{>50\ ns}$). Closed and opened symbols correspond to the immersion time of 1 h and 12 h, respectively.

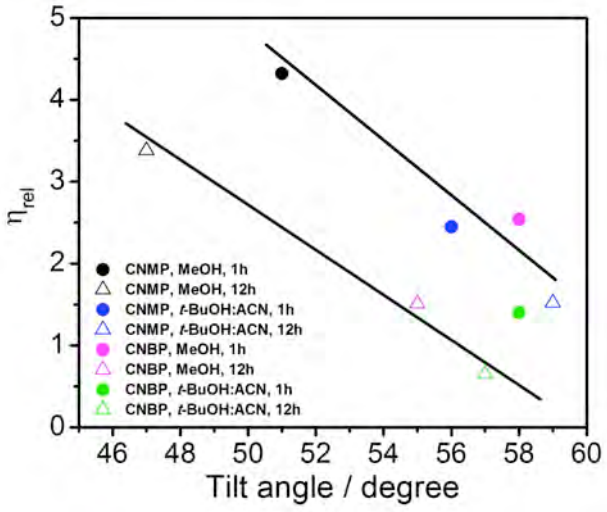

Figure 14. Solar cell efficiency normalized for surface coverage (η_{rel}) as a function of tilt angle. Closed circle and triangle symbols correspond to the immersion time of 1 h and 12 h, respectively.

If the binding geometry and average tilt angle are the controlling factors for the rate of electron transfer, then there should exist a correlation between solar cell efficiency and tilt angle as measured by SFG, similar to the efficiency vs. long lived recombination relationship. This expectation is verified in **Figure 14** where we see that there is a linear correlation (with some scatter) between η_{rel} and tilt angle – the larger the angle the lower the solar cell efficiency. The η_{rel} vs. tilt angle plots depict that 12 h immersion leads to lower efficiency than 1 h, for the same tilt angle. This suggests that efficiency is lost in the injection step and it is reasonable to suggest that long immerison leads to aggregation that decreases the injection efficiency by radiationless quenching processes competing with the injection, a phenomenon already observed in our earlier study of the non-labeled Zn-porphyrin molecules.[26] We discussed above how aggregation induced changes of binding geometry may change the electron transfer and therefore solar cell efficiency. These results taken together thus suggest that aggregation may influence solar cell efficiency through two effects – changed binding geometry and increased excited state quenching.

We have seen that the DSC active electrodes based on CN-labeled and non-labeled porphyrin molecules exhibit very similar electron transfer dynamics (**Figure 4**) and that trends of solar cell efficiency variations with degree of slow (> 50 ns) charge recombination also are very similar (**Figure 13**). Nevertheless, the CN-labeled porphyrins exhibit lower absolute value of solar cell efficiency (η_{rel}, normalized for surface covarage) than the non-labeled porphyrins (**Table 4**) under the same experimental conditions. It is known that the dipole moment of the sensitizer may influence the solar cell performance[34] through a shift of the position of the TiO_2

conduction band, which ultimately causes a variation of the V_{oc} value. The interfacial dipole moment could also change the electron injection rate, which would result in a variation of the J_{sc} value. However, our measurements reveal that there is no significant difference in the V_{oc} values for labeled and non-labeled sensitizers, nor is there any significant difference in electron injection rates. Therefore, the effects of dipole moment on the cell performance are likely to be negligible for the studied porphyrin molecules. A difference in re-reduction (regeneration) kinetics between the oxidized porphyrin and the I^-/I_3^- redox couple in the electrolyte could be another possible explanation for the lower cell performance of CN-labeled porphyrins. A difference in driving force of the re-reduction could give rise to a difference in rate. However, the first oxidation potentials of CNMP (0.98 V vs. NHE) and CNBP (0.97 V vs. NHE) in dichloromethane containing 0.1 M Bu_4NPF_6 as a supporting electrolyte are virtually identical to those of the non-labeled porphyrins (1.00 V vs. NHE for MP, 0.98 V vs. NHE for BP),[26a] implying that difference in driving force cannot rationalize that in the re-reduction rate. On the other hand, it is known that the re-generation reaction proceeds via a transient intermediate complex [$dye^+ \bullet I^-$] formed by the reaction of a photogenerated dye cation with iodide ions.[35] If the interaction between the cyano group of the porphyrin cation and iodide ion in the electrolyte solution inhibits the [$dye^+ \bullet I^-$] formation,[36] the regeneration kinetics between the oxidized porphyrin and I^-/I_3^- redox couple would slow down, resulting in a decrease in the photocurrent and solar cell efficiency.

Conclusions

We have successfully established CN-labeled molecules as probes of the binding geometry of non-labeled molecules by using vibrational SFG and transient absorption spectroscopy. The transient absorption kinetic results of labeled and non-labeled molecules show that they have very similar dynamics, demonstrating that the labeled molecules are good probes for binding geometry of non-labeled molecules. The SFG measurements reveal that all Zn-porphyrin molecules studied here are attached to the TiO_2 surface under an appreciable tilt angle, and this angle depends on the specifics of the porphyrin as well as properties of the immersion solvent and duration of the immersion. There is a linear correlation between average tilt angle and solar cell efficiency normalized for surface coverage (η_{rel}) – the smaller the angle the higher solar cell efficiency. Since electron transfer exhibits a strong distance dependence, the rate of electron injection and recombination constitutes a complimentary measure (to SFG-measured tilt angle) of sensitizer binding geometry. Long immersion (i.e. 12 h vs. 1 h) of the TiO_2 electrode causes aggregation induced decrease of solar cell efficiency through two effects – changes of binding geometry and increased radiationless quenching decreasing injection efficiency.

Experimental Section

Porphyrin synthesis

The target compounds were synthesized as illustrated in the schemes below. Synthesis of the non-labeled molecules has been reported in a previous publication.[26a]

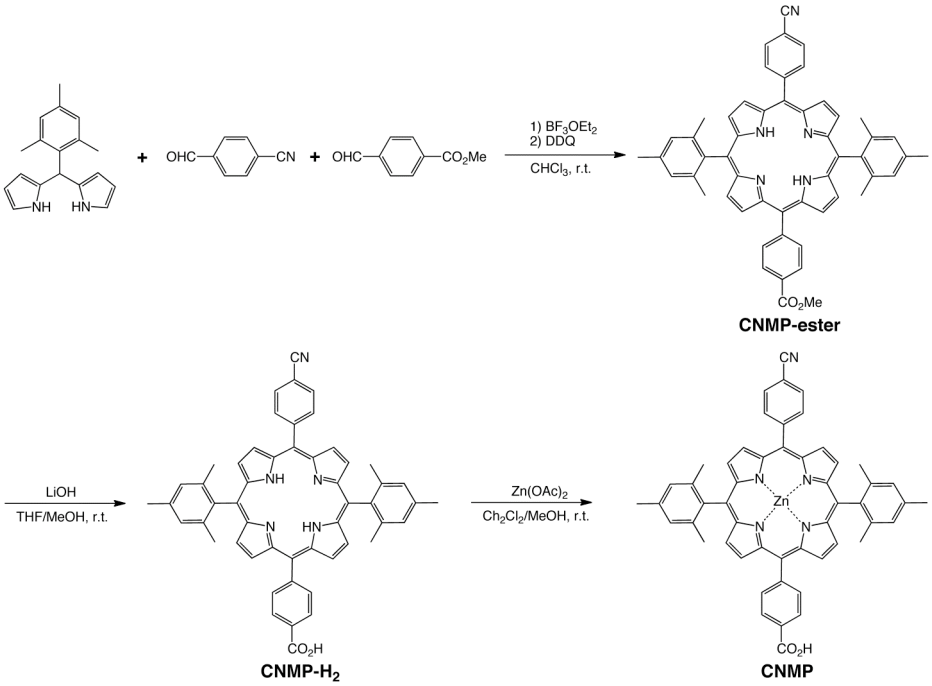

5-(4-Cyanophenyl)-15-(4-methoxycarbonylphenyl)-10,20-bis(2,4,6-trimethylphenyl) porphyrin (CNMP-ester): To a solution of (2,4,6-trimethylphenyl)dipyrromethane[37] (1.8 g, 6.8 mmol) in $CHCl_3$ (800 mL) was added 4-cyanobenzaldehyde (446 mg, 3.4 mmol) and methyl 4-formylbenzoate (558 mg, 3.4 mmol). Dry nitrogen was bubbled through the solution for 30 min before adding BF_3•OEt_2 (0.113 mL, 0.9 mmol). The solution was stirred at room temperature in dark for 2 h. Then, 2,3-dichloro-5,6-dicyano-1,4-benzoquinone (DDQ, 681 mg, 3 mmol) was added and stirred at room temperature for 1 h. After triethylamine (Et_3N, 0.125 mL, 0.9 mmol) was added to the reaction mixture, the solvent was removed in vacuo. Column chromatography on silica gel (toluene/EtOAc = 200:1) afforded **CNMP-ester** as a purple red solid (0.23 g, 0.3 mmol, 9% yield). Mp > 300°C; ^{1}H NMR (400 MHz, CD_2Cl_2) δ 8.79 (d, J = 4.9 Hz, 2H), 8.72 (s, 4H), 8.71 (d, J = 4.9 Hz, 2H), 8.42 (d, J = 8.3 Hz, 2H), 8.36 (d, J = 8.3 Hz, 2H), 8.32 (d, J = 8.3 Hz, 2H), 8.07 (d, J = 8.3 Hz, 2H), 7.30 (s, 4H), 4.08 (s, 3H), 2.62 (s, 6H), 1.82 (s, 12H), –2.69 (s, 2H); MS (MALDI-TOF) *m/z* 782 ($M+H^+$); HRMS (FAB positive) *m/z* for $C_{53}H_{43}N_5O_2$ 781.3417 (calcd), 781.3429 (found, M^+).

5-(4-Carboxyphenyl)-15-(4-cyanophenyl)-10,20-bis(2,4,6-trimethylphenyl)porphyrin (CNMP-H_2): To a solution of **CNMP-ester** (78 mg, 0.1 mmol) in THF (80 mL) was added MeOH (20 mL) and LiOH•H_2O (0.63 g, 15 mmol) in H_2O (10 mL). The solution was stirred at room temperature for 36 h. The reaction mixture was extracted with CH_2Cl_2/H_2O, and then the

aqueous phase was acidified to pH 2 with 1 M HCl and back extracted with CH_2Cl_2. The organic phase was washed with brine and H_2O, dried over anhydrous sodium sulfate. Column chromatography on silica gel (CH_2Cl_2/MeOH = 10:1) afforded **CNMP-H_2** as a purple solid (72 mg, 0.09 mmol, 93% yield). Mp > 300°C; ^{1}H NMR (400 MHz, C_4D_8O) δ 8.68 (d, J = 4.4 Hz, 2H), 8.63 (d, J = 4.4 Hz, 2H), 8.58 (t, J = 9.8 Hz, 4H), 8.32 (d, J = 8.3 Hz, 2H), 8.29 (d, J = 8.3 Hz, 2H), 8.20 (d, J = 8.3 Hz, 2H), 8.03 (d, J = 7.8 Hz, 2H), 7.21 (s, 4H), 2.50 (s, 6H), 1.72 (s, 12H), –2.64 (s, 2H); MS (MALDI-TOF) *m/z* 768 ($M+H^+$); HRMS (FAB positive) *m/z* for $C_{52}H_{41}N_5O_2$ 767.3260 (calcd), 767.3263 (found, M^+).

5-(4-Carboxyphenyl)-15-(4-cyanophenyl)-10,20-bis(2,4,6-trimethylphenyl)-porphyrinatozinc(II) (CNMP): To a solution of **CNMP-H_2** (50 mg, 0.065 mmol) in CH_2Cl_2 (60 mL) was added a solution of saturated $Zn(OAc)_2$ in MeOH (20 mL). The solution was stirred at room temperature for 2 h. The reaction mixture was washed with H_2O (50 mL x 3), dried over anhydrous sodium sulfate, and then the solvent was removed in vacuo. Reprecipitation from $CHCl_3$/hexane gave **CNMP** as a purple solid (53 mg, 0.063 mmol, 97% yield). Mp > 300°C; ^{1}H NMR (400 MHz, CD_2Cl_2) δ 8.88 (d, J = 4.4 Hz, 2H), 8.81 (s, 4H), 8.79 (s, 2H), 8.48 (d, J = 8.3 Hz, 2H), 8.38 (d, J = 8.3 Hz, 4H), 8.07 (d, J = 8.3 Hz, 2H), 7.31 (s, 6H), 2.63 (s, 6H), 1.82 (s, 12H); MS (MALDI-TOF) *m/z* 829 ($M+H^+$); HRMS (FAB positive) *m/z* for $C_{52}H_{39}N_5O_2Zn$ 829.2395 (calcd), 829.2369 (found, M^+): UV-vis (CH_2Cl_2) λ_{max} (nm) 423, 552, 595.

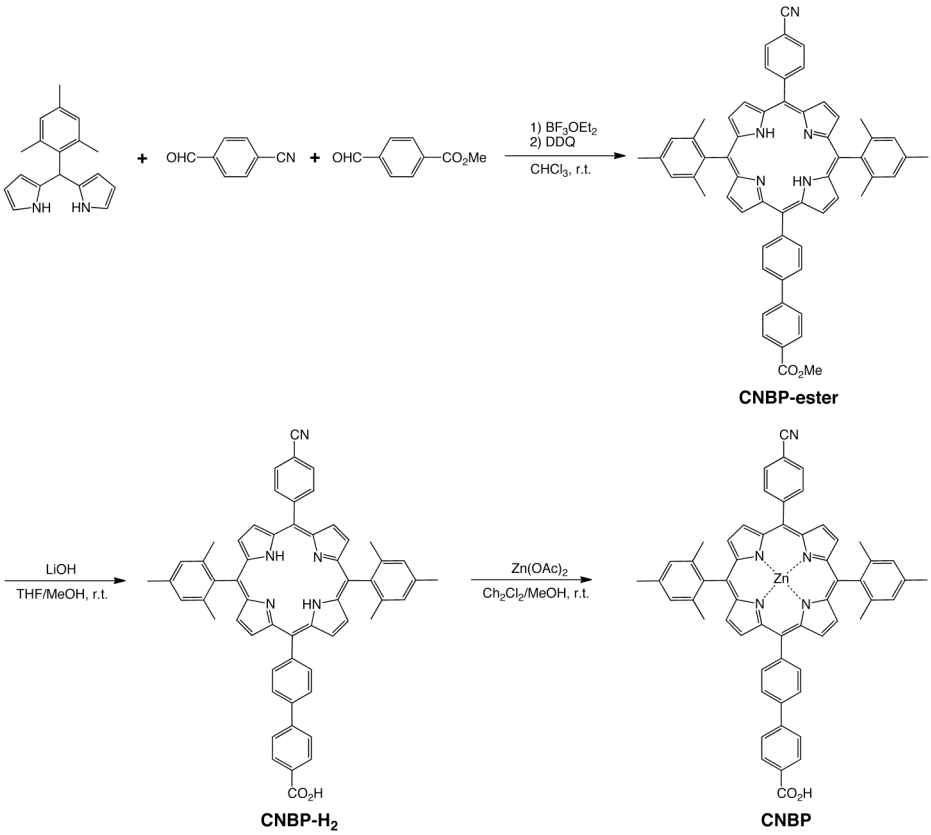

5-(4-Cyanophenyl)-15-(4-methoxycarbonylbiphenyl)-10,20-bis(2,4,6-trimethyl-

phenyl)porphyrin (CNBP-ester): To a solution of (2,4,6-trimethylphenyl)-dipyrromethane (1.8 g, 6.8 mmol) in $CHCl_3$ (800 mL) was added 4-cyanobenzaldehyde (446 mg, 3.4 mmol) and methyl 4-(4-formylphenyl)benzoate (817 mg, 3.4 mmol). Dry nitrogen was bubbled through the solution for 30 min before adding BF_3•OEt_2 (0.113 mL, 0.9 mmol). The solution was stirred at room temperature in dark for 2 h. Then, DDQ (681 mg, 3 mmol) was added and stirred at room temperature for 1h. After Et_3N (0.125 mL, 0.9 mmol) was added to the reaction mixture, the solvent was removed in vacuo. Column chromatography on silica gel (toluene/EtOAc = 200:1) afforded **CNBP-ester** as a purple red solid (0.32 g, 0.37 mmol, 11 % yield). Mp > 300°C; ^{1}H NMR (400 MHz, CD_2Cl_2) δ 8.90 (d, J = 4.9 Hz, 2H), 8.73 (t, 4H), 8.71 (s, 2H), 8.37 (d, J = 8.3 Hz, 2H), 8.34 (d, J = 8.3 Hz, 2H), 8.25 (d, J = 8.3 Hz, 2H), 8.08 (d, J = 4.9 Hz, 2H), 8.06 (d, J = 4.9 Hz, 2H), 8.03 (d, J = 8.8 Hz, 2H), 7.31 (s, 4H), 3.98 (s, 3H), 2.62 (s, 6H), 1.83 (s, 12H), –2.66 (s, 2H); MS (MALDI-TOF) *m/z* 858 ($M+H^+$); HRMS (FAB positive) *m/z* for $C_{59}H_{47}N_5O_2$ 857.3730 (calcd), 857.3730 (found, M^+).

5-(4-Carboxybiphenyl)-15-(4-cyanophenyl)-10,20-bis(2,4,6-trimethylphenyl)-porphyrin (CNBP-H_2): To a solution of **CNBP-ester** (64 mg, 0.075 mmol) in THF (240 mL) was added MeOH (60 mL) and LiOH•H_2O (1.57 g, 37.5 mmol) in H_2O (30 mL). The solution was stirred at room temperature for 36 h. The reaction mixture was extracted with $CHCl_3$/MeOH (v/v = 10:1) and H_2O, and then the aqueous phase was acidified to pH 2 with 1M HCl and back extracted with $CHCl_3$/MeOH (v/v = 10:1). The organic phase was washed with brine and H_2O, dried over anhydrous sodium sulfate. Column chromatography on silica gel (toluene/MeOH = 9:1) afforded **CNBP-H_2** as a purple solid (62 mg, 0.074 mmol, 98% yield). Mp > 300°C; ^{1}H NMR (400 MHz, $C_2D_2Cl_4$ + $(CD_3)_2CO$) δ 8.9 (d, J = 4.4 Hz, 2H), 8.75 (d, J = 2.4 Hz, 2H), 8.73 (d, J = 2.4 Hz, 2H), 8.7 (d, J = 4.4 Hz, 2H), 8.33 (m, 6H), 8.06 (m, 6H), 7.30 (s, 4H), 2.64 (s, 6H), 1.87 (s, 12H), –2.69 (s, 2H); MS (MALDI-TOF) *m/z* 844 ($M+H^+$); HRMS (FAB positive) *m/z* for $C_{58}H_{45}N_5O_2$ 843.3573 (calcd), 843.3577 (found, M^+).

5-(4-Carboxybiphenyl)-15-(4-cyanophenyl)-10,20-bis(2,4,6-trimethylphenyl)-porphyrinatozinc(II) (CNBP): To a solution of **CNBP-H_2** (43 mg, 0.05 mmol) in $CHCl_3$ (60 mL) was added a solution of saturated $Zn(OAc)_2$ in MeOH (20 mL). The solution was stirred at room temperature for 2 h. The reaction mixture was washed with H_2O (50 mL x 3), dried over anhydrous sodium sulfate, and then the solvent was removed in vacuo. Reprecipitation from $CHCl_3$/hexane gave **CNBP** as a purple solid (42 mg, 0.046 mmol, 92% yield). Mp > 300°C; ^{1}H NMR (400 MHz, C_4D_8O) δ 8.87 (d, J = 4.4 Hz, 2H), 8.72 (d, J = 4.4 Hz, 2H), 8.69 (d, J = 4.4 Hz, 4H), 8.37 (d, J = 8.3 Hz, 2H), 8.30 (d, J = 8.3 Hz, 2H), 8.23 (d, J = 8.3 Hz, 2H), 8.10 (m, 6H), 7.29 (s, 4H), 2.60 (s, 6H), 1.84 (s, 12H); MS (MALDI-TOF) *m/z* 907 ($M+H^+$); HRMS (FAB positive) *m/z* for $C_{58}H_{43}N_5O_2Zn$ 905.2708 (calcd), 905.2717 (found, M^+); UV-vis (CH_2Cl_2) λ_{max} (nm) 423, 552, 593.

Orientation of CN-labeled porphyrins on a TiO_2 surface as determination by SFG.

The SFG intensity is proportional to the power densities of the visible pump (I_{vis}) and IR (I_{IR}) beams (eq. S1),

$$I_{SFG}(\omega_s) \propto \left| \sum_i \sum_{j,k} L_{ii}(\omega_{SFG}) \chi^{(2)}_{ijk} L_{jj}(\omega_{vis}) L_{kk}(\omega_{IR}) \right|^2 I_{vis} I_{IR} \qquad \text{(S1)}$$

where i, j and k are non-specific labels, representing x, y or z, which is the three elements in an interface-fixed reference frame. $\chi^{(2)}_{ijk}$ is the second-order susceptibility of the interface, which carries the surface structural information such as molecular density, orientation and conformation on the surface. As a third rank tensor, $\chi^{(2)}_{ijk}$ contains 27 elements. The independent $\chi^{(2)}_{ijk}$ is reduced to four on an azimuthally isotropic surface, i.e. $\chi^{(2)}_{zzz}$, $\chi^{(2)}_{yyz}$ ($=\chi^{(2)}_{xxz}$), $\chi^{(2)}_{yzy}$ ($=\chi^{(2)}_{xzx}$) and $\chi^{(2)}_{zyy}$ ($=\chi^{(2)}_{zxx}$). These susceptibility tensors can be related to molecular hyperpolarizabilities, $\beta^{(2)}_{\xi\eta\zeta}(\xi,\eta,\zeta=a,b,c)$ in a molecular frame (a,b,c), through Euler transformation matrices. Generally, the vibrational modes from a $C_{\infty v}$ symmetry group, which is the case for the present dye system, will only exhibit non-zero symmetric hyperpolarizability terms as eq. S2-i and eq. S2-ii,[38]

$$\chi^{(2)}_{xxz} \equiv \chi^{(2)}_{yyz} = \frac{1}{2} N_s \beta^{(2)}_{ccc} [\langle \cos\theta \rangle (1+R) - \langle \cos^3\theta \rangle (1-R)] \qquad \text{(S2-i)}$$

$$\chi^{(2)}_{xzx} \equiv \chi^{(2)}_{yzy} \equiv \chi^{(2)}_{zxx} \equiv \chi^{(2)}_{zyy} = \frac{1}{2} N_s \beta^{(2)}_{ccc} (1-R)[\langle \cos\theta \rangle - \langle \cos^3\theta \rangle] \qquad \text{(S2-ii)}$$

where N_s is the number of molecules at the interface, the hyperpolarizability ratio R is defined as a ratio between $\beta^{(2)}_{aac}$ and $\beta^{(2)}_{ccc}$ for the molecules. For the C≡N groups in the present study, 0.72 is adopted.[39] The expression < > carries out an ensemble average of the orientation angle (i.e., tilt angle) via the distribution function eq. S3,

$$\langle \cos^n\theta \rangle = \int_{-1}^{1} \cos^n\theta \, f(\cos\theta) \, d(\cos^n\theta) \qquad \text{(S3)}$$

$f(\cos\theta)$ in the equation denotes a distribution function, which can be expressed as a Gaussian (eq. S4),

$$f(\theta) = \frac{1}{\sqrt{2\pi}\sigma} \exp\left[-\frac{(\theta - \theta_0)^2}{2\sigma^2}\right] \quad \text{(S4)}$$

where θ_0 is the mean orientation angle and σ is the root-mean-square width. In the present paper, only δ-distribution is used for calculation (σ=0).

L_{ii}, L_{jj} and L_{kk} (i, j, k = x, y, z) in eq. S1 are the Fresnel coefficients or so-called the local field factors (L factors) relating input macroscopic electric fields to the macroscopic fields at the interface.[40] The values of these L factors depend on experimental setups, such as the refractive index of the medium, the incident beams angles and can be accurately calculated according the experimental geometry employed. In the present study, the calculation of the L factors for thin film systems of TiO_2 was as described in our previous work.[41] The moduli of L_{ssp} and L_{sps} are shown in **Figure SI 1**. As ~420 nm in thick film was employed, the calculated ratio is found to be 0.82±0.03.

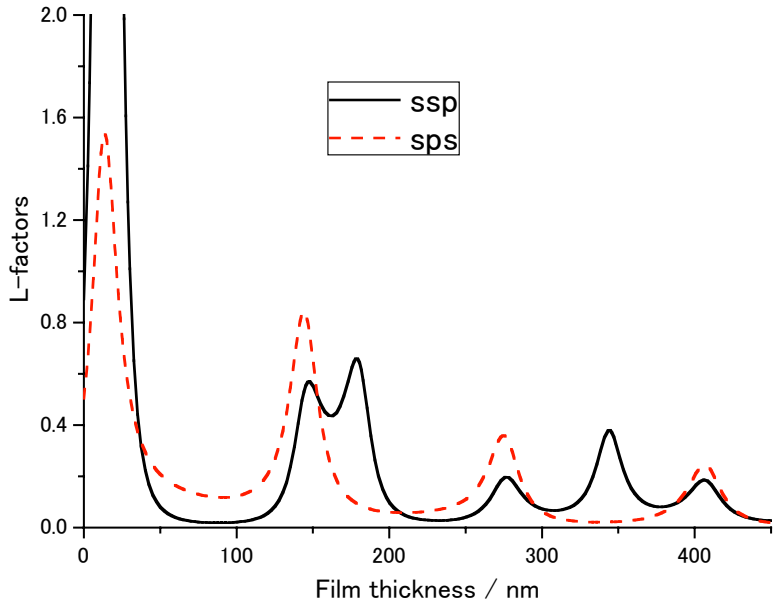

Figure SI 1. Calculated L factors for *ssp* (black solid traces) and *sps* (red dashed traces) as a function of film thickness of TiO_2.

Based on Eqs. S1-S4, the orientation angle (θ) of the porphyrin molecules can be determined from the SFG spectra with *ssp*- and *sps*-polarization combinations by the following procedures: first, obtain the L factors involving the effective refractive susceptibility (A_{ssp}, A_{sps}) by fitting the SFG spectra; second, obtain the molecular susceptibility ($\chi^{(2)}_{yzy}$, $\chi^{(2)}_{yyz}$) after removal of L

factors (L_{ssp}, L_{sps}); finally, acquire the molecular orientation by comparing the experimental observations with calculated results from Eqs. S-2i and S-2ii, as shown in **Figure SI 2**.

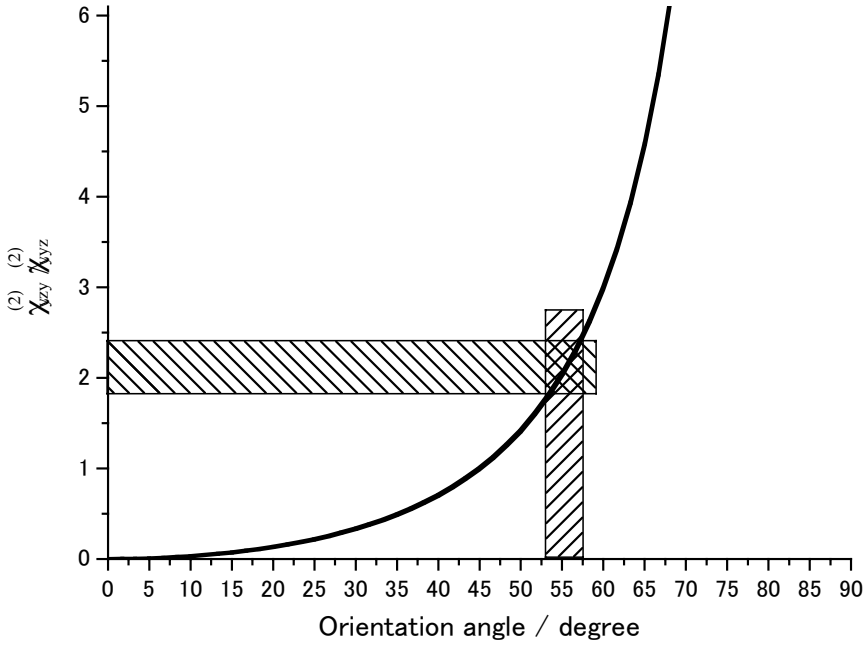

Figure SI 2. Simulation for the relationship between $\chi_{yzy}^{(2)}/\chi_{yyz}^{(2)}$ and orientation angle for δ angle distribution (σ=0°).

Sample preparation

Preparation of porphyrin sensitized TiO_2 electrode and photovoltaic measurements.

Nanoporous films were prepared from a colloidal suspension of TiO_2 nanoparticles (P25, Nippon Aerogel) dispersed in distilled water. This TiO_2 colloidal suspension was deposited on a transparent conducting glass substrate (Asahi Glass, SnO_2:F, 8 ohm/sq) by using the doctor blade technique. The films were annealed for 10 min at 673 K for the 4-μm-thick TiO_2 film, followed by similar deposition and annealing (723 K, 2 h) for the 10-μm-thick TiO_2 films. The thickness of the films was determined using a surface roughness tester (SURFCOM 130A, ACCRETECH). The TiO_2 electrodes were immersed in a 0.2 mM *t*-butyl alcohol:acetonitrile (v/v=1:1) (denoted as *t*-BuOH:ACN) or methanol (MeOH) solution of the porphyrins at room temperature. After removal from the dye bath, the non-adsorbed molecules were washed off by rinsing the film with the same solvent and the film was dried at room temperature for ~20 s. The amount of porphyrins adsorbed on the TiO_2 films was determined by measuring the absorbance at the peak of the Soret band for each dye molecule dissolved from the dye-sensitized TiO_2 films into a known amount of DMF containing 0.1 M NaOH aqueous solution.

The samples for SFG characterization were spin-coated on a CaF_2 substrate and sintered in 673 K for 10 min and then at 723 K for 2 h. The thickness of the TiO_2 layer was ca. 420 nm, which was determined by sectional profiles using atomic force microscopy (AFM). Other procedures were the same as those mentioned above. The samples for attenuated total reflectance-Fourier transform infrared (ATR-IR) spectroscopy and TEM were prepared with a similar procedure as described above. The powder peeled off from the porphyrin-coated TiO_2 film was used for the measurements.

The photovoltaic measurements were performed in a sandwich cell consisting of the dye-sensitized electrode as the working electrode and a platinum-coated conducting glass electrode as the counter electrode. The two electrodes were placed on top of each other using a thin transparent film of Surlyn polymer (Dupont) as a spacer to form the electrolyte space. A thin layer of electrolyte (0.5 M LiI, 0.01 M I_2, 0.6 M dimethylpropyl imidazolium iodide, and 0.5 M 4-*t*-butylpyridine in acetonitrile) was introduced onto the interelectrode space. The IPCE values and current-voltage characteristics were determined by using a PECL 11 solar simulator (Peccell, Japan) irradiated with simulated air mass (AM) 1.5 solar light (100 mW cm^{-2}). All experimental values were given as an average of five independent measurements. The cell performances of the CN-labeled and non-labeled ZnP/TiO_2 electrodes are summarized in **Table 1**.

For transient absorption measurements, a similar procedure as described above was used for making the porphyrin-TiO_2 films. A spacer frame with a thickness of 0.13 mm was placed on top of the porphyrin-TiO_2 film together with a thin glass slide, and the volume between the slides was filled with ACN. Paper clips were used to press the glass assembly to prevent solvent evaporation during measurements.

Transient absorption spectroscopy

Two femtosecond laser setup were used; both based on a 1 kHz repetition rate amplified Ti:Sapphire laser system: one with central output wavelength of 795 nm and 6 mJ per pulse (Spectra-Physics) and the other centered at 775 nm with 0.9 mJ (Clark MXR). The output beam of the 6 mJ laser system was split into two parts, each for pumping one of two collinear optical parametric amplifiers (TOPAS) to generate pump and probe beams, and transient absorption kinetics were measured as previously described whereas the other laser system was used to pump two broad-band non-collinear parametric amplifiers and used to measure transient spectra.[26] In both transient experiments, excitation in the linear range of fluency (10^{13} photons/cm^2/pulse) centered at 558 nm was utilized. Multi-exponential fit of kinetics was performed in Matlab software. Two or three components were necessary to describe the rise of the kinetics, whereas for fitting of the kinetic decay one to three components were necessary.

Results of the fitting procedure are summarized in **Table 1**. The transient absorption spectra were globally fitted to a sum of exponentials using in-house written data-fitting software DAFit (Pascher Instruments), assuming that the excited system is evolving according to an irreversible sequential model.[27] Subsequently, for each of the particular transient species with a specific spectral shape, three parallel decay channels were used to represent the heterogeneous character of the material.[26] Obviously, with this model, four additional variables (two lifetimes and two amplitudes) were used for each transient species. Yet, only two species, namely photo-generated excited state and oxidized dye were required to obtain a random distribution of residuals in the fit. Using a model with only one decay component for each transient species, a random distribution of residuals could be achieved with up to five transient species, each of them adding several hundreds of variables to the fit.[26]

Sum frequency generation (SFG) vibrational spectroscopy

SFG measurements were carried out with a broad-band SFG system with a femtosecond Ti:Sapphire laser developed in Hokkaido Univeristy.[28] A narrow band visible pulse (ca. 10 ps at 800 nm) and a tunable broad-band infrared (IR) pulse (ca. 100 fs from 4000–1000 cm^{-1}) were overlapped on the sample surface and SFG signals were recorded by a CCD camera attached to a spectrograph. Due to the limited spectral width of the IR pulse (typically ca. 250 cm^{-1}), SFG spectra were obtained at several central IR wavelengths, and finally these SFG spectra were added together to get the complete spectrum. To remove effects of IR pulse shape and beam overlap, the SFG spectra were normalized by a SFG spectrum recorded for a gold substrate.[28] Two polarization combinations of the sum frequency, visible and IR beams were used, i.e., *ssp*, and *sps*. Generally, SFG measurement in *ssp* polarization can probe a vibrational mode that has an IR dipole perpendicular to the surface, while *sps* polarization is sensitive to a vibrational mode that has an IR dipole parallel to the surface; this fact can be employed to detect different vibrational modes of *ssp*- and *sps*-polarized SFG spectra. The SFG spectra were quantitatively analyzed and fitted by the following equation,

$$I_{SFG} = \left| \sum_{\nu} \frac{A_\nu}{\omega_{IR} - \omega_\nu + i\Gamma_\nu} e^{i\phi_\nu} + \chi^{(2)}_{NR} \right|^2 \qquad (1)$$

where A_ν and Γ_ν are the amplitude and the damping constant, respectively, of the vibrational mode ν at a frequency ω_ν. ϕ_ν is the phase angle between the resonance mode and non-resonant background which can significantly affect the shape of the SFG spectra. Details of the calculation method to obtain the average tilt angle are described in Supporting Information

(**Figure SI 1** and **Figure SI 2**).

Attenuated total reflectance-Fourier transform infrared (ATR-IR) spectroscopy

The ATR data reported here were taken with the golden gate diamond anvil ATR accessory (NICOLET 6700, Thermo Scientific), using typically 256 scans at a resolution of 2 cm^{-1}. All samples were placed in contact with the diamond window using the same mechanical force. Neat TiO_2 powder was used as a background for the porphyrin-coated TiO_2 samples.

References and Notes

[1] O'Regan, B. C.; Grätzel, M. *Nature* **1991**, *353*, 737.

[2] (a) Grätzel, M. *Nature* **2001**, *414*, 338. (b) Nazeeruddin, M. K.; Pechy, P.; Renouard, T.; Zakeeruddin, S. M.; Humphry-Baker, R.; Comte, P.; Liska, P.; Cevey, L.; Costa, E.; Shklover, V.; Spiccia, L.; Deacon, G. B.; Bignozzi, C. A.; Grätzel, M. *J. Am. Chem. Soc.* **2001**, *123*, 1613. (c) Nazeeruddin, M. K.; De Angelis, F.; Fantacci, S.; Selloni, A.; Viscardi, G.; Liska, P.; Ito, S.; Bessho, T.; Grätzel, M. *J. Am. Chem. Soc.* **2005**, *127*, 16835. (d) Chiba, Y.; Islam, A.; Watanabe, Y.; Komiya, R.; Koide, N.; Han, L. *Jpn. J. Appl. Phys.* **2006**, *45*, 638. (e) Nazeeruddin, M. K.; Bessho, T.; Cevey, L.; Ito, S.; Klein, C.; De Angelis, F.; Fantacci, S.; Comte, P.; Liska, P.; Imai, H.; Grätzel, M. *J. Photochem. Photobiol. A* **2007**, *185*, 331. (f) Gao, F.; Wang, Y.; Zhang, J.; Shi, D.; Wang, M.; Humphry-Baker, R.; Wang, P.; Zakeeruddin, S. M.; Grätzel, M. *Chem. Commun.* **2008**, *23*, 2635. (g) Gao, F.; Wang, Y.; Shi, D.; Zhang, J.; Wang, M.; Jing, X.; Humphry-Baker, R.; Wang, P.; Zakeeruddin, S. M.; Grätzel, M. *J. Am. Chem. Soc.* **2008**, *130*, 10720. (h) Chen, C. Y.; Wang, M.; Li, J. Y.; Pootrakulchote, N.; Alibabaei, L.; Ngoc-le, C.; Decoppet, J. D.; Tsai, J. H.; Grätzel, C.; Wu, C. G.; Zakeeruddin, S. M.; Grätzel, M. *ACS Nano* **2009**, *3*, 3103. (i) Hagfeldt, A.; Boschloo, G.; Sun, L.; Kloo, L.; Pettersson, H. *Chem. Rev.* **2010**, *110*, 6595. (j) Cao, Y.; Bai, Y.; Yu, Q.; Cheng, Y.; Liu, S.; Shi, D.; Gao, F.; Wang, P. *J. Phys. Chem. C* **2009**, *113*, 6290. (k) Grätzel, M. Historical development of the DSC, from its inception to its current state. In: 3rd International Conference on the Industrialization of DSC, Nara, Japan, April 22-24 (2009). <http://www.dyesol.com/download/DSCIC09/22Apr09Graetzel.pdf>.

[3] (a) Tian, H.; Yang, X.; Cong, J.; Chen, R.; Liu, J.; Hao, Y.; Hagfeldt, A.; Sun, L. *Chem. Commun.* **2009**, 6288. (b) Wang, Z.–S.; Koumura, N.; Cui, Y.; Miyashita, M.; Mori, S.; Hara, K. *Chem. Mater.* **2009**, *21*, 2810. (c) Qin, H.; Wenger, S.; Xu, M.; Gao, F.; Jing, X.;

Wang, P.; Zakeeruddin, S. M.; Grätzel, M. *J. Am. Chem. Soc.* **2008**, *130*, 9202. (d) Zhou, G.; Pschirer, N.; Schöneboom, J.; Eickemeyer, F.; Baumgarten, M.; Müllen, K. *Chem. Mater.* **2008**, *20*, 1808. (e) Xu, W.; Peng, B.; Chen, J.; Liang, M.; Cai, F. *J. Phys. Chem. C* **2008**, *112*, 874. (f) Horiuchi, T.; Miura, H.; Sumioka, K.; Uchida, S. *J. Am. Chem. Soc.* **2004**, *126*, 12218. (g) Li, G.; Jiang, K.–J.; Li, Y.–F.; Li, S.–L.; Yang, L.–M. *J. Phys. Chem. C* **2008**, *112*, 11591. (h) Ning, Z.; Zhang, Q.; Wu, W.; Pei, H.; Liu, B.; Tian, H. *J. Org. Chem.* **2008**, *73*, 3791. (i) Zhang, X. H.; Wang, Z.–S.; Cui, Y.; Koumura, N.; Furube, A.; Hara, K. *J. Phys. Chem. C* **2009**, *113*, 13409.

[4] (a) Hara, K.; Sayama, K.; Ohga, Y.; Shinpo, A.; Suga, S.; Arakawa, H. *Chem. Commun.* **2001**, 569. (b) Hara, K.; Kurashige, M.; Danoh, Y.; Kasada, C.; Shinpo, A.; Suga, S.; Arakawa, H. *New. J. Chem.* **2003**, *27*, 783. (c) Wang, Z.–S.; Cui, Y.; Dan-oh, Y.; Kasada, C.; Shinpo, A.; Hara, K. *J. Phys. Chem. C* **2007**, *111*, 7224. (d) Wang, Z.–S.; Cui, Y.; Dan-oh, Y.; Kasada, C.; Shinpo, A.; Hara, K. *J. Phys. Chem. C* **2008**, *112*, 17011.

[5] (a) Horiuchi, T.; Miura, H.; Uchida, S. *Chem. Commun.* **2003**, 3036. (b) Ito, S.; Zakeeruddin, S. M.; Humphry-Baker, R.; Liska, P.; Charvet, R.; Comte, P.; Nazeeruddin, M. K.; Péchy, P.; Takata, M.; Miura, H.; Uchida, S.; Grätzel, M. *Adv. Mater.* **2006**, *18*, 1202.

[6] (a) Hara, K.; Kurashige, M.; Ito, S.; Shinpo, A.; Suga, S.; Sayama, K.; Arakawa, H. *Chem. Commun.* **2003**, 252. (b) Kitamura, T.; Ikeda, M.; Shigaki, K.; Inoue, T.; Anderson, N. A.; Ai, X.; Lian, T.; Yanagida, S. *Chem. Mater.* **2004**, *16*, 1806. (c) Hwang, S.; Lee, J. H.; Park, C.; Lee, H.; Kim, C.; Park, C.; Lee, M.–H.; Lee, W.; Park, J.; Kim, K.; Park, N.–G.; Kim, C. *Chem. Commun.* **2007**, 4887. (d) Kim, C.; Choi, H.; Kim, S.; Baik, C.; Song, K.; Kang, M.–S.; Kang, S. O.; Ko, J. *J. Org. Chem.* **2008**, *73*, 7072. (e) Im, H.; Kim, S.; Park, C.; Jang, S.–H.; Kim, C.–J.; Kim, K.; Park, N.–G.; Kim, C. *Chem. Commun.* **2010**, 1335.

[7] (a) Tan, S.; Zhai, J.; Fang, H.; Jiu, T.; Ge, J.; Li, Y.; Jiang, L.; Zhu, D. *Chem.–Eur. J.* **2005**, *11*, 6272. (b) Liu, W.–H.; Wu, I.–C.; Lai, C.–H.; Lai, C.–H.; Chou, P.–T.; Li, Y.–T.; Chen, C.–L.; Hsu, Y.–Y.; Chi, Y. *Chem. Commun.* **2008**, 5152. (c) Choi, H.; Baik, C.; Kang, S. O.; Ko, J.; Kang, M.–S.; Nazeeruddin, M. K.; Grätzel, M. *Angew. Chem., Int. Ed.* **2008**, *47*, 327. (d) Wang, Z.–S.; Koumura, N.; Cui, Y.; Takahashi, M.; Sekiguchi, H.; Mori, A.; Kubo, T.; Furube, A.; Hara, K. *Chem. Mater.* **2008**, *20*, 3993.

[8] (a) Ehret, A.; Stuhl, L.; Spitler, M. T. *Electrochim. Acta* **2000**, *45*, 4553. (b) Wu, W.; Hua, J.; Jin, Y.; Zhan, W.; Tian, H. *Photochem. Photobiol. Sci.* **2008**, *7*, 63.

[9] (a) Wang, Z.–S.; Li, F.–Y.; Huang, C.–H.; Wang, L.; Wei, M.; Jin, L.–P.; Li, N.–Q. *J. Phys. Chem. B* **2000**, *104*, 9676. (b) Yao, Q.–H.; Shan, L.; Li, F.–Y.; Yin, D.–D.; Huang, C.–H. *New J. Chem.* **2003**, *27*, 1277. (c) Chen, Y.–S.; Li, C.; Zeng, Z.–H.; Wang, W.–B.; Wang, X.–S.; Zhang, B.-W. *J. Mater. Chem.* **2005**, *15*, 1654.

[10] (a) Chen, Y.; Zeng, Z.; Li, C.; Wang, W.; Wang, X.; Zhang, B. *New J. Chem.* **2005**, *29*, 773. (b) Yum, J.–H.; Walter, P.; Huber, S.; Rentsch, D.; Geiger, T.; Nüesch, F.; Angelis, F. D.; Grätzel, M.; Nazeeruddin, M. K. *J. Am. Chem. Soc.* **2007**, *129*, 10320.

[11] (a) Reddy, P. Y.; Giribabu, L.; Lyness, C.; Snaith, H. J.; Vijaykumar, C.; Chandrasekharam, M.; Lakshmikantam, M.; Yum, J.–H.; Kalyanasundaram, K.; Grätzel, M.; Nazeeruddin, M. K. *Angew. Chem., Int. Ed.* **2007**, *46*, 373. (b) Cid, J.–J.; Yum, J.–H.; Jang, S.–R.; Nazeeruddin, M. K.; Martínez-Ferrero, E.; Palomares, E. J.; Ko, J.; Grätzel, M.; Torres, T. *Angew. Chem., Int. Ed.* **2007**, *46*, 8358. (c) Eu, S.; Katoh, T.; Umeyama, T.; Matano, Y.; Imahori, H. *Dalton Trans.* **2008**, 5476. (d) Cid, J.–J.; García-Iglesias, M.; Yum, J.–M.; Forneli, A.; Albero, J.; Martínez-Ferrero, E.; Vázquez, P.; Grätzel, M.; Nazeeruddin, M. K.; Palomares, E.; Torres, T. *Chem.–Eur. J.* **2009**, *15*, 5130. (e) Martínez-Díaz, M. V.; de la Torre, G.; Torres, T. *Chem. Commun.* **2010**, *46*, 7090. (f) Wang, X.–F.; Tamiaki, H.; Wang, L.; Tamai, N.; Kitao, O.; Zhou, H.; Sasaki, S.–I. *Langmuir* **2010**, *26*, 6320. (g) Mori, S.; Nagata, M.; Nakahata, Y.; Yasuta, K.; Goto, R.; Kimura, M.; Taya, M. *J. Am. Chem. Soc.* **2010**, *132*, 4054.

[12] (a) Ferrere, S.; Zaban, A.; Gregg, B. A. *J. Phys. Chem. B* **1997**, *101*, 4490. (b) Shibano, Y.; Umeyama, T.; Matano, Y.; Imahori, H. *Org. Lett.* **2007**, *9*, 1971. (c) Li, C.; Yum, J.–H.; Moon, S.–J.; Herrmann, A.; Eickemeyer, F.; Pschirer, N. G.; Erk, P.; Schöneboom, J.; Müllen, K.; Grätzel, M.; Nazeeruddin, M. K. *ChemSusChem.* **2008**, *1*, 615.

[13] (a) Ito, S.; Miura, H.; Uchida, S.; Takata, M.; Sumioka, K.; Liska, P.; Comte, P.; Péchy, P.; Grätzel, M. *Chem. Commun.* **2008**, 5194. (b) Zhang, G.; Bala, H.; Cheng, Y.; Shi, D.; Lv, X.; Yu, Q.; Wang, P. *Chem. Commun.* **2009**, 2198. (c) Zeng, W.; Cao, Y.; Bai, Y.; Wang, Y.; Shi, Y.; Zhang, M.; Wang, F.; Pan, C.; Wang, P. *Chem. Mater.* **2010**, *22*, 1915.

[14] (a) Wang, Q.; Campbell, W. M.; Bonfantani, E. E.; Jolley, K. W.; Officer, D. L.; Walsh, P. J.; Gordon, K.; Humphry-Baker, R.; Nazeeruddin, M. K.; Grätzel, M. *J. Phys. Chem. B* **2005**, *109*, 15397. (b) Campbell, W. M.; Jolley, K. W.; Wagner, P.; Wagner, K.; Walsh, P. J.; Gordon, K. C.; Schmidt-Mende, L.; Nazeeruddin, Md. K.; Wang, Q.; Grätzel, M.; Officer, D. L. *J. Phys. Chem. C* **2007**, *111*, 11760. (c) Lee, C. Y.; She, C.; Jeong, N. C.; Hupp, J. T. *Chem. Commun.* **2010**, *46*, 6090. (d) Imahori, H.; Umeyama, T.; Ito, S. *Acc. Chem. Res.* **2009**, *42*, 1809. (e) Walter, M. G.; Rudine, A. B.; Wamser, C. C. *J. Porphyrins Phthalocyanines* **2010**, *14*, 759. (f) Imahori, H.; Matsubara, Y.; Iijima, H.; Umeyama, T.; Matano, Y.; Ito, S.; Niemi, M.; Tkachenko, N. V.; Lemmetyinen, H. *J. Phys. Chem. C* **2010**, *114*, 10656. (g) Kira, A.; Matsubara, Y.; Iijima, H.; Umeyama, T.; Matano, Y.; Ito, S.; Niemi, M.; Tkachenko, N. V.; Lemmetyinen, H.; Imahori, H. *J. Phys. Chem. C* **2010**, *114*, 11293. (h) Mathew, S.; Iijima, H.; Toude, Y.; Umeyama, T.; Matano, Y.; Ito, S.; Tkachenko, N. V.; Lemmetyinen, H.; Imahori, H. *J. Phys. Chem. C* **2011**, *115*,

14415. (i) Ishida, M.; Park, S. W.; Hwang, D.; Koo, Y. B.; Sessler, J. L.; Kim, D. Y.; Kim, D. *J. Phys. Chem. C* **2011**, *115*, 19343.

[15] (a) Bessho, T.; Zakeeruddin, S. M.; Yeh, C.–Y.; Diau, E. W.–G.; M. Grätzel, M. *Angew. Chem., Int. Ed.* **2010**, *49*, 6646. (b) Wang, C.–L.; Chang, Y.–C.; Lan, C.–M.; Lo, C.–F.; Diau, E. W. –G.; Lin, C.-Y. *Energy Environ. Sci.* **2011**, *4*, 1788. (c) Chang, Y.–C.; Wang, C.–L.; Pan, T.–Y.; Hong, S.–H.; Lan, C.–M.; Kuo, H.–H.; Lo, C.–F.; Hsu, H.–Y.; Lin, C.–Y.; Diau, E. W.–G. *Chem. Commun.* **2011**, *47*, 8910.

[16] (a) Asbury, J. B.; Hao, E.; Wang, Y.; Ghosh, H. N.; Lian, T. *J. Phys. Chem. B* **2001**, *105*, 4545. (b) Robertson, N. *Angew. Chem., Int. Ed.* **2006**, *45*, 2338.

[17] (a) Pelet, S.; Grätzel, M.; Moser, J.–E. *J. Phys. Chem. B* **2003**, *107*, 3215. (b) Haque, S. A.; Tachibana, Y.; Willis, R. L.; Moser, J.–E.; Grätzel, M.; Klug, D. R.; Durrant, J. R. *J. Phys. Chem. B* **2000**, *104*, 538. (c) Chen, C.; Wang, M.; Wang, K. *J. Phys. Chem. C* **2009**, *113*, 1624. (d) Szarko, J. M.; Neubauer, A.; Bartelt, A.; Socaciu-Siebert, L.; Birkner, F.; Schwarzburg, K.; Hannappel, T.; Richberger, R. *J. Phys. Chem. C* **2008**, *112*, 10542. (e) Myllyperkio, P.; Manzoni, C.; Polli, D.; Cerullo, G.; Korppi-Tommola, J. *J. Phys. Chem. C* **2009**, *113*, 13985. (f) Wiberg, J.; Marinado, T.; Hagberg, D. P.; Sun, L.; Hagfeldt, A.; Albinsson, B. *J. Phys. Chem. C* **2009**, *113*, 3881. (g) Punniamoorthy, R.; Peir, A. M.; Nazeeruddin, M. K.; Grätzel, M.; Bradley, D. D. C.; Durrant, J. R.; Nelson, J. *J. Phys. Chem. B* **2006**, *110*, 7635.

[18] Anderson, S.; Constable, E. C.; Dare-Edwards, M. P.; Goodenough, J. B.; Hamnett, A.; Seddon, K. R.; Wright, R. D. *Nature*, **1979**, *280*, 571.

[19] (a) Ardo, S.; Meyer, G. J. *Chem. Soc. Rev.* **2009**, *38*, 115. (b) Tachibana, Y.; Moser, J. E.; Grätzel, M.; Klug, D. R.; Durrant, J. R. *J. Phys. Chem.* **1996**, *100*, 20056. (c) Hannappel, T.; Burfeindt, B.; Storck, W.; Willig, F. *J. Phys. Chem. B* **1997**, *101*, 6799. (d) Moser, J. E.; Noukakis, D.; Bach, U.; Tachibana, Y.; Klug, D. R.; Durrant, J. R.; Humphry-Baker, R.; Grätzel, M. *J. Phys. Chem. B* **1998**, *102*, 3649. (e) Hannappel, T.; Zimmermann, C.; Meissner, B.; Burfeindt, B.; Storck, W.; Willig, F. *J. Phys. Chem. B* **1998**, *102*, 3651. (f) Ellingson, R. J.; Asbury, J. B.; Ferrere, S.; Hirendra, N. G.; Sprague, J. R.; Lian, T.; Nozik, A. J. *J. Phys. Chem. B* **1998**, *102*, 6455. (g) Asbury, J. B.; Ellingson, R. J.; Ghosh, H. N.; Ferrere, S.; Nozik, A. J.; Lian, T. *J. Phys. Chem. B* **1999**, *103*, 3110. (h) Durrant, J. R.; Tachibana, Y.; Mercer, I. P.; Moser, J. E.; Grätzel, M.; Klug, D. R. *Z. Phys. Chem.* **1999**, *212*, 93. (i) Tachibana, Y.; Haque, S. A.; Mercer, I. P.; Durrant, J. R.; Klug, D. R. *J. Phys. Chem. B* **2000**, *104*, 1198. (j) Heimer, T. A.; Heilweil, E. J.; Bignozzi, C. A.; Meyer, G. J. *J. Phys. Chem. A* **2000**, *104*, 4256. (k) Kallioinen, J.; Lehtovuori, V.; Myllyperkiö, P.; Korppi-Tommola, J. *Chem. Phys. Lett.* **2001**, *340*, 217. (l) Benkö, G.; Kallioinen, J.; Korppi-Tommola, J. E. I.; Yartsev, A. P.; Sundström, V. *J. Am. Chem. Soc.* **2002**, *124*,

489. (m) Kallioinen, J.; Benkö , G.; Sundström, V.; Korppi-Tommola, J. E. I.; Yartsev, A.P. *J. Phys. Chem. B* **2002**, *106*, 4396. (n) Tachibana, Y.; Nazeeruddin, M. K.; Grätzel, M.; Klug, D. R.; Durrant, J. R. *Chem. Phys.* **2002**, *285*, 127.

[20] (a) Hagfeldt, A.; Gratzel, M. *Chem. Rev.* **1995**, *95*, 49. (b) Moser, J. E.; Bonnote, P.; Grätzel, M. *Coord. Chem. Rev.* **1998**, *171*, 245. (c) Kay, A.; Grätzel, M. *Sol. Energy Mater. Sol. Cells* **1996**, *44*, 99.

[21] (a) Anderson, N.A.; Lian, T.; *Coord. Chem. Rev.* **2004**, *248*, 1231. (b) Schwarzburg, K.; Ernstorfer, R.; Felber, S.; Willig, F. *Coord. Chem. Rev.* **2004**, *248*, 1259. (c) Watson, D. F.; Meyer, G. J. *Annu. Rev. Phys. Chem.* **2005**, *56*, 119. (d) Durrant, J. R. *J. Photochem. Photobiol. A Chem.* **2002**, *148*, 5.

[22] (a) Haque, S. A.; Handa, S.; Peter, K.; Palomares, E.; Thelakkat, M.; Durrant, J. R. *Angew. Chem., Int. Ed.* **2005**, *44*, 5740. (b) O'Regan, B.; Moser, J.; Anderson, M.; Grätzel, M. *J. Phys. Chem.* **1990**, *94*, 8720. (c) Moser, J. E.; Grätzel, M. *Chem. Phys.* **1993**, *176*, 493.

[23] (a) Nelson, J.; Haque, S. A.; Klug, D. R.; Durrant, J. R. *Phys. Rev. B* **2001**, *63*, 205321. (b) Barzykin, A. V.; Tachiya, M. *J. Phys. Chem. B* **2002**, *106*, 4356. (c) Katoh, R.; Furube, A.; Barzykin, A.V.; Arakawa, H.; Tachiya, M. *Coord. Chem. Rev.* **2004**, *248*, 1195. (d) Barzykin, A.V.; Tachiya, M. *J. Phys. Chem. B* **2004**, *108*, 8385.

[24] (a) Pan, J.; Benkö, G.; Xu, Y.; Pascher, T.; Sun, L.; Sundström, V.; Polivka, T. *J. Am. Chem. Soc.* **2002**, *124*, 13949. (b) Anderson, N. A.; Ai, X.; Chen, D.; Mohler, D.; Lian, T. *J. Phys. Chem. B* **2003**, *107*, 14231. (c) Wang, D.; Mendelsohn, R.; Galoppini, E.; Hoertz, P. G.; Carlisle, R. A.; Meyer, G. J. *J. Phys. Chem. B* **2004**, *108*, 16642. (d) Kilså, K.; Mayo, E. I.; Kuciauskas, D.; Villahermosa, R.; Lewis, N. S.; Winkler, J. R.; Gray, H. B. *J. Phys. Chem. A* **2003**, *107*, 3379. (e) Hoertz, P. G.; Carlisle, R. A.; Meyer, G. J.; Wang, D.; Piotrowiak, P.; Galoppini, E. *Nano Lett*. **2003**, *3*, 325.

[25] (a) Boschloo, G. K.; Goossens, A. *J. Phys. Chem.* **1996**, *100*, 19489. (b) Cherian, S.; Wamser, C. C. *J. Phys. Chem. B* **2000**, *100*, 19489. (c) Ma, T. L.; Inoue, K.; Noma, H.; Yao, K.; Abe, E. *J. Photochem. Photobiol. A* **2002**, *151*, 207. (d) Jasieniak, J.; Johnston, M.; Waclawik, E. R. *J. Phys. Chem. B* **2004**, *108*, 12962. (e) Rochford, J.; Chu, D.; Hagfeldt, A.; Galoppini, E. *J. Am. Chem. Soc.* **2007**, *129*, 4655.

[26] (a) Imahori, H.; Hayashi, S.; Hayashi, H.; Oguro, A.; Eu, S.; Umeyama, T.; Matano, Y. *J. Phys. Chem. C* **2009**, *113*, 18406. (b) Imahori, H.; Kang, S.; Hayashi, H.; Haruta, M.; Kurata, H.; Isoda, S.; Canton, S.E.; Infahsaeng, Y.; Kathiravan, A.; Pascher, T.; Chábera, P.; Yartsev, A.P.; Sundström, V. *J. Phys. Chem. A* **2011**, 115, 3679.

[27] (a) Pascher, T. *Biochemistry* **2001**, *40*, 5812. (b) De, S.; Pascher, T.; Maiti, M.; Jespersen, K. G.; Kesti, T.; Zhang, F.; Inganäs, O.; Yartsev, A. P.; Sundström, V. *J. Am. Chem. Soc.*

2007, *129*, 8466.

[28] (a) Ye, S.; Noda, H.; Morita, S.; Uosaki, K.; Osawa, M. *Langmuir* **2003**, *19*, 2238. (b) Ye, S.; Noda, H.; Nishida, T.; Morita, S.; Osawa, M. *Langmuir* **2004**, *20*, 357. (c) Holman, J.; Davies, P. B.; Nishida, T.; Ye, S.; Neivandt, D. J. *J. Phys. Chem. B* **2005**, *109*, 18723. (d) Nishida, T.; Johnson, M.; Holman, J.; Osawa, M.; Davies, P. B.; Ye, S. *Phys. Rev. Lett.* **2006**, *96*, 77402. (e) Ye, S.; Nihonyanagi, S.; Uosaki, K. *Phys. Chem. Chem. Phys.* **2001**, *3*, 3463. (f) Wei, Q.; Tajima, K.; Tong, Y.; Ye, S.; Hashimoto, K. *J. Am. Chem. Soc.* **2009**, *131*, 17597. (g) Tong, Y.; Li, N.; Liu, H.; Ge, A.; Osawa, M.; Ye, S. *Angew. Chem., Int. Ed.* **2010**, *49*, 2319. (h) Tong, Y.; Zhao, Y.; Li, N.; Ma, Y.; Osawa, M.; Davies, P. B.; Ye, S. *J. Chem. Phys.* **2010**, *133*, 034705. (i) Tong, Y.; Zhao, Y.; Li, N.; Osawa, M.; Davies, P. B.; Ye, S. *J. Chem. Phys.* **2010**, *133*, 034704. (j) Ye, S.; Osawa, M. *Chem. Lett.* **2009**, *38*, 386.

[29] (a) Wang, C.; Groenzin, H.; Shultz, M. J. *J. Phys. Chem. B* **2004**, *108*, 265. (b) Wang, C.; Groenzin, H.; Shultz, M. J. *J. Am. Chem. Soc.* **2005**, *127*, 9736.

[30] (a) Ferrere, S.; Gregg, B. A. *J. Am. Chem. Soc.* **1998**, 120, 843. (b) Yang, M.; Thompson, D.W.; Meyer, G.J. *Inorg. Chem.* **2000**, 39, 3738. (c) Khoudiakov, M.; Parise, A.R.; Brunschwig, B.S. *J. Am. Chem. Soc.* **2003**, 125, 4637. (d) Harris, J.A.; Trotter, K.; Brunschwig, B.S. *J. Phys. Chem. B* **2007**, 111, 6695.

[31] *Spectrometric Identification of Organic Compounds*; Silverstein, R. M., Bassler, G. C., Morrill, T. C., Eds.; John Wiley & Sons: New York, 1991.

[32] She, C.; Guo, J.; Lian, T. *J. Phys. Chem. B* **2007**, *111*, 6903.

[33] Wagner, K.; Griffith, M. J.; James, M.; Mozer, A. J.; Wagner, P.; Triani, G.; Officer, D.L.; Wallace, G. G. *J. Phys. Chem. C*, **2011**, *115*, 317.

[34] (a) Rühle, S.; Greenshtein, M.; Chen, S.–G.; Merson, A.; Pizem, H.; Sukenik, C. S.; Cahen, D.; Zaban, A. *J. Phys. Chem. B* **2005**, *109*, 18907. (b) Angelis, F. D.; Fantacci, S.; Selloni, A.; Grätzel, M.; Nazeeruddin, M. K. *Nano Lett.* **2007**, *7*, 3189. (c) Kusama, H.; Orita, H.; Sugihara, H. *Langmuir* **2008**, *24*, 4411. (d) Meng, S.; Kaxiras, E. *Nano Lett.* **2010**, *10*, 1238. (e) O'Rourke, C.; Bowler, D. R. *J. Phys. Chem. C* **2010**, *114*, 20240.

[35] Clifford, J. N.; palomares, E.; Nazeeruddin, M. K.; Grätzel, M.; Durrant, J. R. *J. Phys. Chem. C* **2007**, *111*, 6561.

[36] Kusaka, H.; Sugihara, H.; Sayama, K. *J. Phys. Chem. C* **2011**, *115*, 2544.

[37] Laha, J. K.; Dhanalekshmi, S.; Taniguchi, M.; Ambroise, A.; Lindsey, J. S. *Org. Process. Res. Dev.* **2003**, 7, 799.

[38] (a) Du, Q.; Superfine, R.; Freysz, E.; Shen, Y. R. *Phys. Rev. Lett.* **1993**, *70*, 2313. (b) Chin, R. P.; Huang, J. Y.; Shen, Y. R.; Chuang, T. J.; Seki, H.; Buck, M. *Phys. Rev. B* **1992**, *45*, 1522.

[39] Stähelin, M. *J. Chem. Phys.* **1993**, *98*, 5595.

[40] Feller, M. B.; Chen, W.; Shen, Y. R. *Phys. Rev. A* **1991**, *43*, 6778.

[41] Tong, Y.; Zhao, Y.; Li, N.; Osawa, M.; Davies, P. B.; Ye, S. *J. Chem. Phys.* **2010**, *133*, 034704. (b) Tong, Y.; Zhao, Y.; Li, N.; Ma, Y.; Osawa, M.; Davies, P. B.; Ye, S. *J. Chem. Phys.* **2010**, *133*, 034705. (c) Feller, M. B.; Chen, W.; Shen, Y. R. *Phys. Rev. A* **1991,** *43*, 6778.

Chapter 4

Local Stoichiometry in Amorphous Supramolecular Composites Analyzed by Solid-State ^{13}C Nuclear Magnetic Resonance

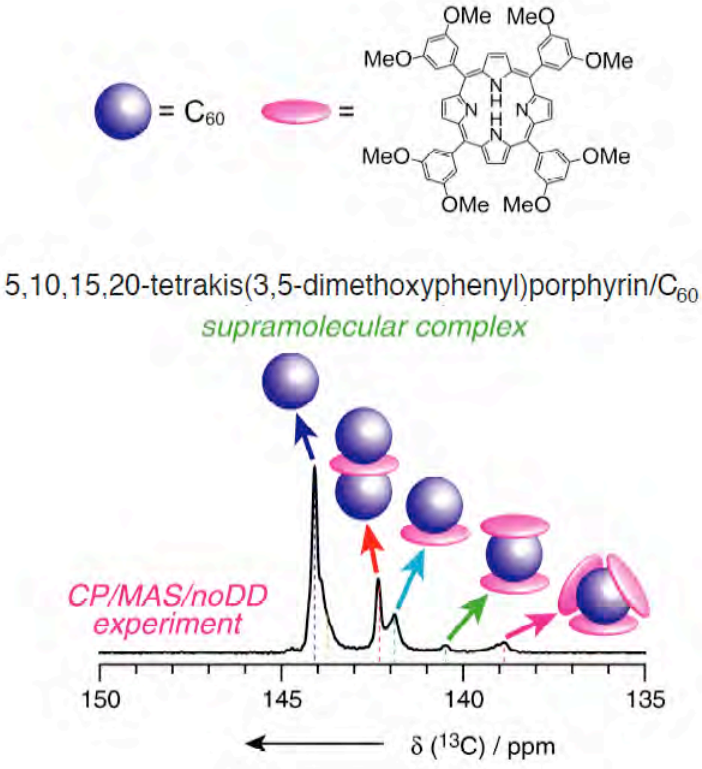

Abstract: Solid-state nuclear magnetic resonance (NMR) has been applied to "*amorphous*" active layers consisting of donor-acceptor self-assembled composites in organic solar cells. Several stoichiometric supramolecular complexation states as well as the charge-transfer states are revealed by the solid-state NMR, which have been difficult to access by conventional spectroscopy. The spectra show clear correlation between local self-assembled supramolecular structures and the organic solar cell performances.

Introduction

Donor-acceptor (D-A) systems have attracted significant interest in supramolecular chemistry as well as organic electronics including organic solar cells (OSCs).[1,2] In particular, fabrication of '*amorphous*' D-A systems is one of the cost-effective approaches to develop highly-efficient, large-area OSCs. In this regard, the characterization of the molecular-level D-A structure is crucial to design high-performance OSCs, however, the details have been unrevealed for such *amorphous* systems.

Solid-state nuclear magnetic resonance (NMR) is a powerful tool for elucidating the structure of disordered or amorphous systems.[3-7] Recent application of solid-state NMR to organic light-emitting materials with disordered structures has disclosed a relationship between the local structure and the light-emitting properties.[8,9] The application to OSCs is also expected to be highly useful to evaluate the D-A structure, as examplifed by Ref. 10. Here, we present solid-state NMR experiments for two supramolecular OSC systems composed of tetraphenylporphyrin-derivatives (TPP) and C_{60}; 3,5-OMeTPP/C_{60} and 3,4,5-OMeTPP/C_{60} composites (Figure 1). The 3,5-OMeTPP/C_{60} supramolecular composite led to a remarkably high cell performance with an incident photon-to-current efficiency (IPCE) of up to ca. 60%.[11-13] In contrast, additional introduction of methoxy group at 4-position of 3,5-OMeTPP (i.e., 3,4,5-OMeTPP) resulted in a remarkable decrease in the IPCE values (<10 %). One of the purposes in this study is to reveal the origin of the difference. From solid-state NMR experiments, we find the existence of several different supramolecular elementary units possessing local stoichiometry between TPP and C_{60} in an amorphous state, as shown below. The quantitative molar ratio and the degree of charge transfers for the respective elementary units would have a large impact on the cell performance, which has never been addressed by conventional spectroscopic analyses.

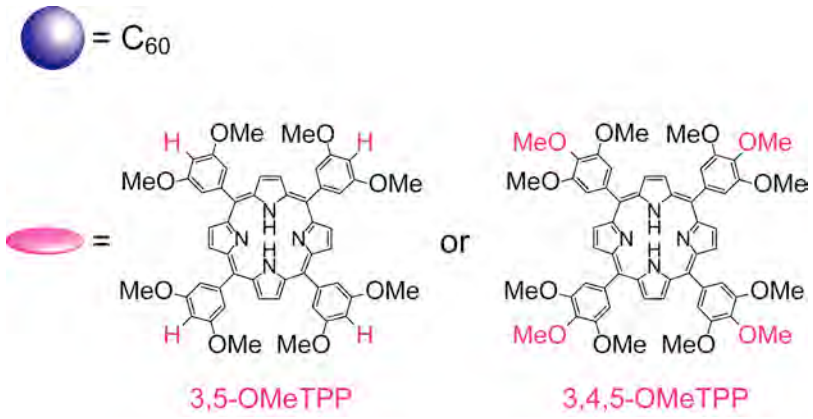

Figure 1. Materials used in this study. Purple sphere indicates fullerene (C_{60}). Pink disk indicates 5,10,15,20-tetrakis(3,5-dimethoxyphenyl)porphyrin (3,5-OMeTPP) or 5,10,15,20-tetrakis(3,4,5-trimethoxyphenyl)porphyrin (3,4,5-OMeTPP).

The above two D-A composites were prepared as follows. The TPP and C_{60}, dissolved in toluene, were rapidly injected into acetonitrile. This resulted in the formation of supramolecular composite clusters, TPP/C_{60}. The gently centrifuged and dried clusters were employed for two different solid-state NMR experiments. First experiments, fully-relaxed direct polarization / magic angle spinning ^{13}C NMR experiments *without* ^{1}H dipolar decoupling (DP/MAS/noDD experiments), distinguished the C_{60}s in different states with quantitative molar ratios. Second experiments, cross polarization (CP) / MAS ^{13}C NMR experiments *without* DD (CP/MAS/noDD experiments), gave information on the spatial proximity of C_{60} and ^{1}H in TPP (see Ref. 14 for more experimental details).

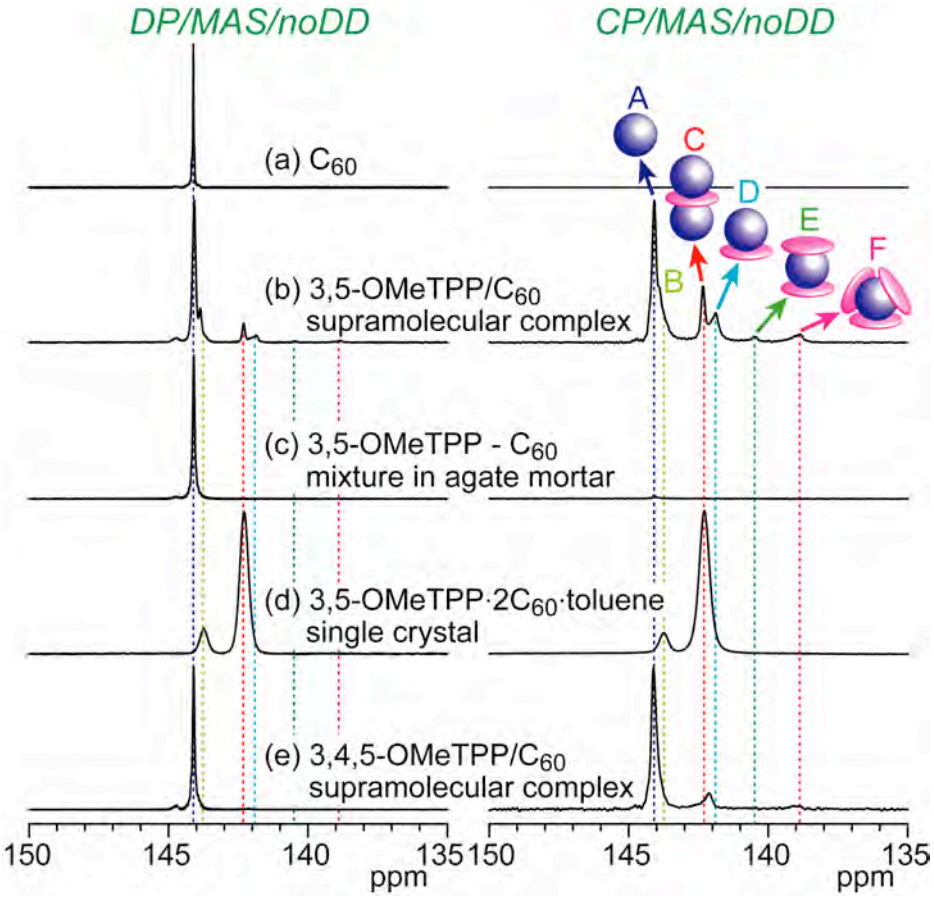

Figure 2. Fully-relaxed DP/MAS/noDD (left) and CP/MAS/noDD (right) ^{13}C NMR spectra of (a) pristine C_{60}, (b) 3,5-OMeTPP/C_{60} supramolecular clusters, (c) 3,5-OMeTPP–C_{60} mixed in agate mortar, (d) 3,5-OMeTPP•2C_{60}•toluene single crystals, and (e) 3,4,5-OMeTPP/C_{60} supramolecular clusters.

Figure 2(a) shows a DP/MAS/noDD ^{13}C NMR spectrum of pristine C_{60}. A single resonance line appears at 144.1 ppm. In Figure 2(b), the DP/ and CP/MAS/noDD ^{13}C NMR spectra of 3,5-OMeTPP/C_{60} clusters in the amorphous states are presented in the left and right, respectively. The resonance lines are denoted as **A** to **F**. Compared with the spectrum of

pristine C_{60}, the 3,5-OMeTPP/C_{60} clusters display several upfield-shifted resonance lines, **B** – **F**, which indicate the occurrence of molecular-level complexation between 3,5-OMeTPP and C_{60}. Here, these resonance lines in both the DP/ and CP/MAS/noDD spectra in Figure 2 do not originate from 3,5-OMeTPP, because the resonance lines of 3,5-OMeTPP are effectively suppressed by not applying DD. This is clearly confirmed by the fact that the NMR spectrum of 3,5-OMeTPP and C_{60} mixture only ground in an agate mortar does not show any detectable upfield resonance lines as shown in Figure 2(c). Therefore, C_{60} carbons can be selectively detected in all the experiments in Figure 2. To further confirm the molecular-level complexation, we carried out a two-dimensional (2D) ^{1}H-^{13}C heteronuclear correlation (HETCOR) experiment. ^{13}C resonance lines of 3,5-OMeTPP are suppressed by not applying DD as described above and C_{60} does not possess ^{1}H. Therefore, 2D ^{1}H-^{13}C heteronuclear correlation experiment can show further evidence for the molecular-level complexation. The result, shown in Figure. 3, clearly exhibits the correlation between ^{1}H in 3,5-OMeTPP and ^{13}C in C_{60}.

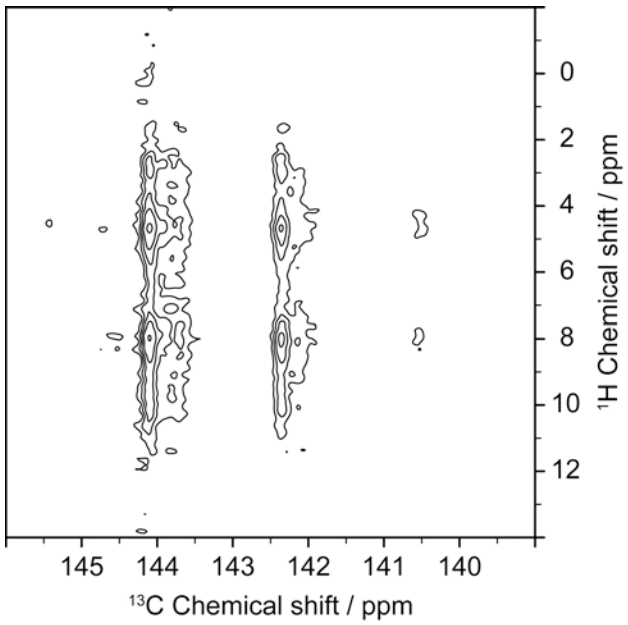

Figure 3. ^{1}H-^{13}C HETCOR spectrum of 3,5-OMeTPP/C_{60} supramolecular clusters without ^{1}H dipolar decoupling during the detection of free induction decay.

Our preceding study[11-13] suggests the formation of a single crystal-like structure even in the amorphous sample. Figure 2(d) depicts the DP/ and CP/MAS/noDD ^{13}C NMR spectra of the single crystals, 3,5-OMeTPP·2C_{60}·toluene. A resonance line which emerged at 142.3 ppm in Figure 2(d) corresponds to the peak **C** in Figure 2(b). This implies that the elementary unit in the single crystals, consisting of two C_{60} molecules and an intervening single 3,5-OMeTPP molecule,[11-13] really exist in the amorphous sample. Note that a small resonance line, observed

at 143.7 ppm in Figure 2(d), is considered to be C_{60}s in defects, which are farther from the second neighbors of 3,5-OMeTPP. The ^{13}C chemical shift anisotropy (CSA) NMR measurement on the single crystals (Figure 4) provides a motionally averaged ^{13}C CSA spectrum, indicating that isotropic rotational motion occurs at a rate larger than the CSA width of ~20 kHz.[15-18] This isotropic rotational motion provides the essentially single resonance line at 142.3 ppm in Figure 2(d). Otherwise, the resonance lines of the respective carbons in C_{60} should split due to the interaction with 3,5-OMeTPP. The Jahn-Teller distortion was reported for C_{60} in some complex systems.[10,19,20] However, in our case, the X-ray diffraction of the 3,5-OMeTPP·2C_{60}·toluene single crystals did not reveal the distortion.[11-13] Even if the Jahn-Teller distortion takes place, the resonance lines would coalesce into a single line due to the above-mentioned isotropic rotational motion, which is faster than the NMR detection time scale. Therefore, we can safely conclude that the appearance of the several resonance lines in Figure 2(b) does not stem from the Jahn-Teller effect.

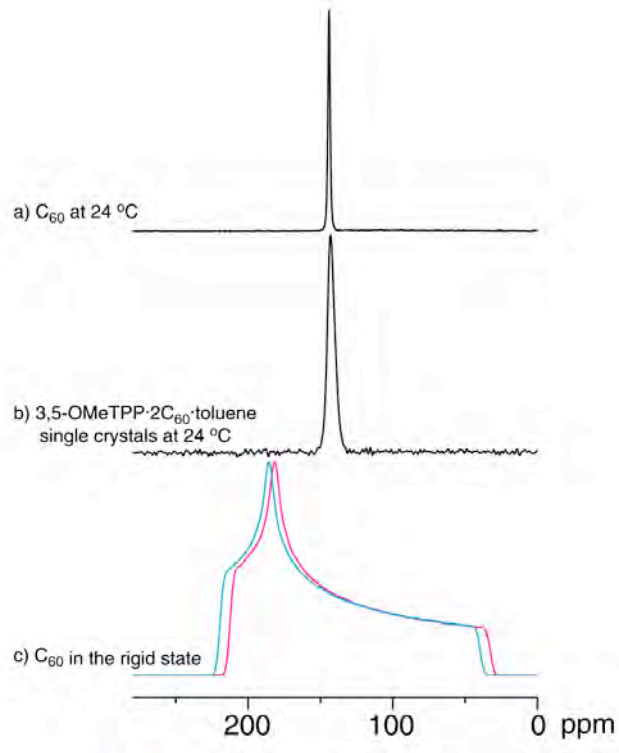

Figure 4. DP/CSA/noDD ^{13}C NMR spectra of (a) pristine C_{60}, (b) 3,5-OMeTPP·2C_{60}·toluene single-crystals at 24°C. Calculated ^{13}C CSA spectra of C_{60} in the rigid state are also shown in (c) for reference. For (c), the experimentally-obtained CSA tensor principal values of (σ_{11}, σ_{22}, σ_{33}) = (220, 186, 40) ppm (Ref. 21) and (213, 182, 33) ppm (Refs. 22, 23) are used, as shown in blue and red lines, respectively.

For the 3,5-OMeTPP/C_{60} clusters in Figure 2(b), signals other than the peak **C** are also observed, showing that the molecular-level structure in the amorphous sample cannot be explained simply by the single crystals structure. Different types of elementary units exist. A host-guest system consisting of C_{60} sandwiched between two porphyrins in Refs.[24-27] is a suitable reference to characterize the structure; C_{60} sandwiched between the two porphyrins exhibits 3.1,[24] 3.6,[25] and 3.4[26,27] ppm upfield shift relative to pristine C_{60} in solution ^{13}C NMR. This shift corresponds to the peak **E** in Figure 2(b). Seemingly sterically-hindered complexation between three 3,5-OMeTPP and one C_{60}, corresponding to peak **F**, is possible as seen in similar systems.[28-30] From these considerations, the peaks **A**, **C**, **E**, and **F** are assigned to free C_{60}, the C_{60} in C_{60}/3,5-OMeTPP/C_{60} unit, the C_{60} in 3,5-OMeTPP/C_{60}/3,5-OMeTPP unit, and C_{60} surrounded by three 3,5-OMeTPP molecules, respectively. Therefore, stoichiometric complexations between 3,5-OMeTPP and C_{60} are responsible for the discrete resonance lines in Figure 2(b). The peak **D** appears between the two peaks due to supramolecular complexations with the molar ratios of 3,5-OMeTPP : C_{60} = 1 : 2 (peak **C**) and 2 : 1 (peak **E**), suggesting the stoichiometric composition of 1 : 1. The upfield shoulder of peak **A** (i.e., peak **B**) can be attributed to C_{60} in the second neighbor of or farther from 3,5-OMeTPP. Although the assignments of **B** and **D** are tentative, the discrete resonance lines reflect the nature of stoichiometric complexations. To confirm the above assignments, we carried out density functional theory (DFT) calculations for these complexations (the details of the DFT calculations and the results are shown in Ref. 14). The experimental upfield shifts from pristine C_{60}, 1.7, 2.2, 3.6, and 5.1 ppm for the 3,5-OMeTPP/C_{60} supramolecular complexes with molar ratios of 1 : 2, 1 : 1, 2 : 1, and 3 : 1, respectively, are well reproduced by the DFT calculations for the respective complexes (Table 1, Figure 5). This also supports the above assignments. A sample in which 3,5-OMeTPP and C_{60} are mixed in a powder form and only ground in an agate mortar exhibits no upfield shifts (Figure 2(c)). This unequivocally corroborates that the upfield resonance lines arise from the supramolecular complexation at the molecular level.

The dominant origin of the upfield shifts of the C_{60} resonance lines is charge-transfer (CT) from porphyrin to C_{60}. This is confirmed by the fact that the ^{13}C resonance lines of 3,5-OMeTPP show downfield shifts on average by complexation with C_{60}; the 3,5-OMeTPP becomes electron-deficient by the CT to form 3,5-OMeTPP$^{\delta+}$. Further supporting evidence for the CT is provided in similar systems in Ref. 21 and 22. The electron-enriched fullerene, $C_{60}^{\delta-}$, is more shielded compared to free C_{60}. Therefore, the peaks **C** to **F** result from four distinctly different degrees of CTs in this system, which would greatly affect the cell performance of the solar cell.

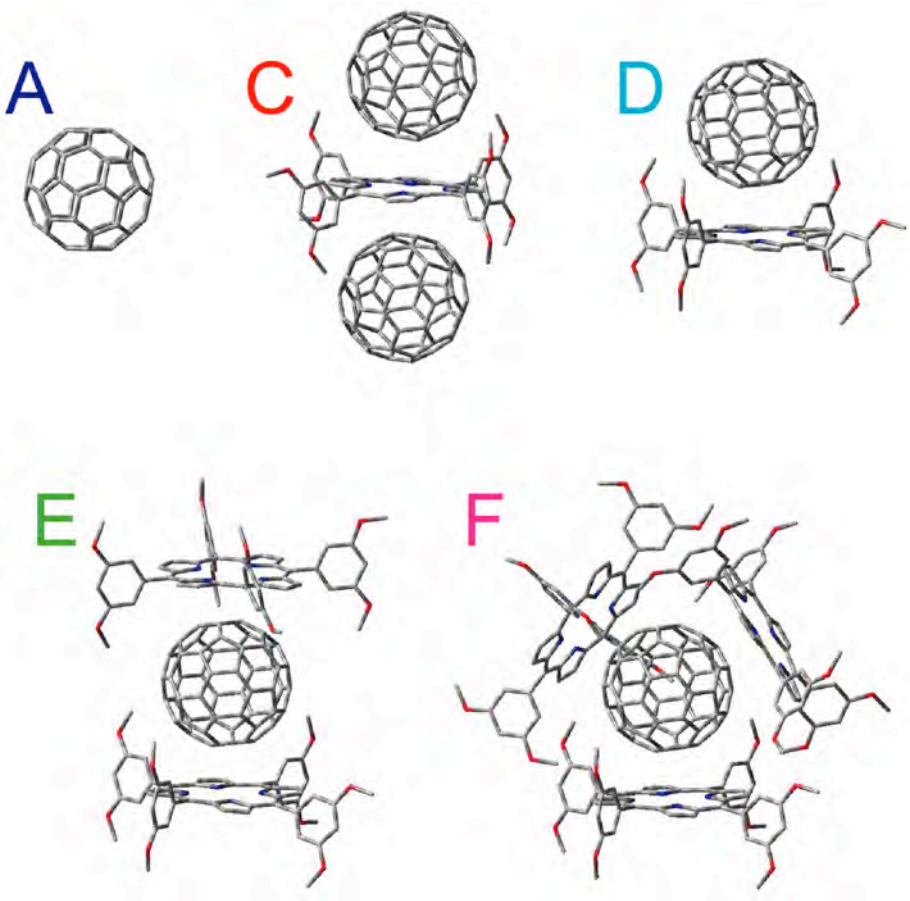

Figure 5. Graphic representation of supramolecular clusters. (A) Free C_{60} and 3,5-OMeTPP/C_{60} supramolecular complexes with the 3,5-OMeTPP/C_{60} molar ratio of (C) 1 : 2, (D) 1 : 1, (E) 2 : 1, and (F) 3 : 1. Hydrogen atoms are omitted for clarity. These possible 3,5-OMeTPP/C_{60} supramolecular clusters are used for the isotropic chemical shift calculations.

TABLE 1. Upfield Shifts of Resonance Lines for 3,5-OMeTPP/C_{60} Supramolecular Complexes from Pristine C_{60}.

Molar ratio of 3,5-OMeTPP : C_{60}	Upfield shifts from pristine C_{60} (ppm)	
	Experimental values	DFT-calculated values
1 : 2	1.7	1.58
1 : 1	2.2	1.62
2 : 1	3.6	3.30
3 : 1	5.1	4.89

Finally, we compare the difference between 3,5-OMeTPP/C_{60} and 3,4,5-OMeTPP/C_{60} supramolecular self-assembled systems. The quantitative molar ratios of the respective species, **A** to **F**, are obtained from the integrated intensities of the fully-relaxed DP/MAS/noDD resonance lines. The molar ratios of **A**, **B**, **C**, **D**, **E**, and **F** are determined to be 100 : 22 : 12 : 9 : 1 : 4 and 100 : 0 : 2 : 0 : 0 : 0 for 3,5-OMeTPP/C_{60} and 3,4,5-OMeTPP/C_{60} clusters, respectively. Obviously, the amounts of charge transferred C_{60} are greater for the 3,5-OMeTPP/C_{60} system. Considering that CT plays an important role in the OSCs,[12,13] an increase in molar ratios of the CT complexes exhibiting the larger degree of CTs for 3,5-OMeTPP/C_{60} relative to 3,4,5-OMeTPP/C_{60} system is consistent with the large IPCE value of 3,5-OMeTPP/C_{60}-based cell (about 60%) in comparison with 3,4,5-OMeTPP/C_{60}-based cell (<10 %).

Because C_{60} does not have any protons, the CP from ^{1}H to ^{13}C is not expected, as shown in Figs. 2(a) and 2(c), where no resonance lines are observed for the CP/MAS/noDD spectra. Interestingly, however, resonance lines are unequivocally detected in the CP/MAS/noDD spectra of Figs. 2(b), 2(d), and 2(e), showing the existence of dipolar coupling between ^{1}H in TPP and ^{13}C in C_{60}. This also demonstrates the formation of supramolecular complexation between TPP and C_{60} in close proximity. The intensities of the CP/MAS/noDD signals in Fig. 2(b) are enhanced by a factor of 1.7, 2.9, 3.3, 3.4 and 3.7 (within ±0.1) relative to the DP/MAS/noDD for peaks **B**, **C**, **D**, **E**, and **F**, respectively (we define the enhancement factor of free C_{60} as unity). This confirms that the number of the nearest 3,5-OMeTPP molecules around C_{60} increases from **A** to **F**.

In conclusion, we have characterized self-assembled amorphous D-A solids consisting of porphyrin derivatives and C_{60} by solid-state NMR. The DP/MAS/noDD, CP/MAS/noDD, and ^{1}H-^{13}C HETCOR experiments provide molecular-level information on the disordered TPP/C_{60} composites, which explains the remarkable difference in OSC performances arising from subtle structural difference. Such analyses for amorphous solids will become increasingly important in organic electronics as well as in supramolecular chemistry.

Experimental Section

Solid-State NMR Experiments. The following solid-state ^{13}C nuclear magnetic resonance (NMR) measurements were carried out in this study. In all the experiments, ^{1}H dipolar decoupling (DD) was "*not*" applied during the detection of free induction decay (FID). Without applying DD, the resonance lines of C_{60}, which does not possess ^{1}Hs, were selectively detected. The resonance lines of the molecules possessing ^{1}Hs, that is, 5,10,15,20-tetrakis(3,5-dimethoxyphenyl)porphyrin (3,5-OMeTPP), 5,10,15,20-tetrakis(3,4,5-trimethoxyphenyl)porphyrin (3,4,5-OMeTPP) for all the samples, and

toluene for the 3,5-OMeTPP·2C_{60}·toluene single crystals were significantly broadened due to the ^{13}C-^{1}H dipolar interaction and effectively suppressed in the experiments.

For a fully-relaxed direct polarization / magic angle spinning without DD (DP/MAS/noDD) experiment on pristine C_{60}, the pulse delay was set to be 310 s, which was longer than five times the ^{13}C spin-lattice relaxation time (T_{1C}). Fully-relaxed DP/MAS/noDD spectra with a pulse delay of 140 s were measured for the 3,5-OMeTPP/C_{60} and 3,4,5-OMeTPP/C_{60} supramolecular complex clusters. For the DP/MAS/noDD experiments on 3,5-OMeTPP·2C_{60}·toluene single crystals and the 3,5-OMeTPP – C_{60} mixture only ground in an agate mortar, a pulse delay of 140 s was used in order to set all the experimental parameters the same as those for the 3,5-OMeTPP/C_{60} and 3,4,5-OMeTPP/C_{60} supramolecular complex clusters. The T_{1C} values were measured by the saturation-recovery method (Table SI). The T_{1C} value of pristine C_{60} is consistent with previous reported values.[23,31] The contact time for the cross polarization (CP) process was set to be 5.0 ms for CP/MAS without DD (CP/MAS/noDD) experiments. For all the above solid-state NMR experiments, the MAS spinning speed was set to 6 kHz (±2 Hz), and the experiments were carried out at 28 °C.

TABLE SI. T_{1C} values of respective resonance lines in Figure 2.

Complexation states	T_{1C} values (s)					
	A	**B**	**C**	**D**	**E**	**F**
C_{60}	55.2					
3,5-OMeTPP/C_{60} supramolecular complex	24.0	20.1	19.8	15.2	9.6	8.4
3,5-OMeTPP·2C_{60}·toluene single crystals		40.8	37.9			
3,5-OMeTPP – C_{60} mixture in agate mortar	52.4					
3,4,5-OMeTPP/C_{60} supramolecular complex	26.4		20.9			

^{13}C chemical shift anisotropy (CSA) measurements with DP preparation were also performed without DD (DP/CSA/noDD experiments, Figure 4). For the CSA measurement of the single crystals, a background, originating from the rotor spacers and the housing, was obvious. Therefore, the background was suppressed by subtracting the spectrum of an empty rotor under the same experimental conditions. The CSA experiments were carried out at 24 °C.

All the above solid-state NMR measurements were conducted on a Chemagnetics CMX-400 Infinity spectrometer operating at a ^{13}C frequency of 100.28 MHz (under a static magnetic field of 9.4 T). A double resonance probe with a 7.5-mm MAS probehead was used,

and the ^{1}H and ^{13}C field strengths $\gamma B_1/2\pi$ of 62.5 kHz were used for all the applied pulses.

^{1}H-^{13}C heteronuclear correlation (HETCOR) measurements were carried out on a Bruker Avance III 400 MHz NMR spectrometer equipped with a 4 mm double resonance MAS probe. Also in this experiment, ^{1}H dipolar decoupling (DD) was "*not*" applied during the detection of free induction decay (FID). The ^{1}H and ^{13}C field strengths $\gamma B_1/2\pi$ of 80 kHz were used for all the applied pulses. The contact time was 10 ms and the MAS spinning speed was 15 kHz (±4 Hz). The experiments were carried out at 27 ^{o}C.

The ^{13}C chemical shifts were expressed as values relative to tetramethylsilane (Me_4Si) using the C_{60} resonance line (the line width was ~2.5 Hz) at 144.1 ppm for pristine C_{60} crystals.[22]

DFT Calculations. Figure 5 displays a C_{60} and four classes of clusters with molar ratios of 3,5-OMeTPP : C_{60} = 1 : 2 (cluster **C**), 1 : 1 (cluster **D**), 2 : 1 (cluster **E**), and 3 : 1 (cluster **F**) for the nuclear magnetic shielding calculations. The calculations were performed by the gauge including atomic orbitals (GIAO) method[32-34] using density functional theory (DFT) at the B3LYP/6-31G(d) level.[35-38] For cluster **C** with 3,5-OMeTPP : C_{60} = 1 : 2, the geometry obtained from the single crystals was used. For cluster **D** with 3,5-OMeTPP : C_{60} = 1 : 1, one C_{60} molecule was deleted from the cluster **C**. For cluster **E** with 3,5-OMeTPP : C_{60} = 2 : 1, one 3,5-OMeTPP molecule was added to **D** and the structure was generated with the following restriction; the structures of 3,5-OMeTPP and C_{60}, and the distances between the centers of gravity of 3,5-OMeTPP and C_{60} were fixed to be the same as those of the single crystals, and the centers of gravity of the three molecules were positioned in a straight line. The cluster **F** was constructed, as in the case of the cluster **E**; two 3,5-OMeTPP molecules were added to **D**, followed by the structure generation with the restriction; the structures of 3,5-OMeTPP and C_{60}, and the distances between the centers of gravity of 3,5-OMeTPP and C_{60} were fixed to be the same as those of the single crystals, and the three 3,5-OMeTPP molecules were positioned as far as possible from each other (the 3,5-OMeTPP molecules form a triangle).

The calculated isotropic chemical shifts of the respective carbons of C_{60} in the supramolecular complexes were different due to the complexations with 3,5-OMeTPP. These chemical shift values were averaged for the respective complexes, because it was experimentally found that these resonance lines are motionally averaged by the isotropic rotational motion of C_{60}. All the calculations were performed with the Gaussian 03 program.[39]

Additional Results

^{13}C CSA Measurements. Figures 4(a) and 4(b) show DP/CSA/noDD ^{13}C NMR spectra of pristine C_{60} and C_{60} in 3,5-OMeTPP·2C_{60}·toluene single crystals at 24 °C, respectively.

Compared to the CSA of pristine C_{60} in the rigid state (the CSA width was 180 ppm) in Figure 4(c),[21-23] the pristine C_{60} at 24 °C provides a narrow CSA spectrum with a line width of 1.8 ppm. This is an indication of the isotropic rotational motion of C_{60} molecules at room temperature, as previously investigated in detail.[21-23] The C_{60} in 3,5-OMeTPP·2C_{60}·toluene single-crystals at 24 °C also provides a narrow CSA spectrum with a line width of 5.8 ppm. The slightly greater line width compared with that of pristine C_{60} would be due to dynamically-weakened dipolar coupling with ^{1}Hs in 3,5-OMeTPP and toluene. However, the line width (5.8 ppm) in Figure 4(b) is still much smaller than that in the rigid state (180 ppm) in Figure 4(c), indicating that the C_{60} molecules in the single crystals are also isotropically rotating on the NMR detection time scale.

References and Notes

[1] Troshin, P. A.; Koeppe, R.; Peregudov, A. S.; Peregudova, S. M.; Egginger, M.; Lyubovskaya, R. N.; Sariciftci, N. S.; *Chem. Mater.* **2007**, *19*, 5363.

[2] Imahori, H.; Umeyama, T. *J. Phys. Chem. C* **2009**, *113*, 9029.

[3] Schmidt-Rohr, K.; Hu, W.; Zumbulyadis, N. *Science* **1998**, *280*, 714.

[4] Kaji, H.; Schmidt-Rohr, K. *Macromolecules* **2001**, *34*, 7368.

[5] Kaji, H.; Schmidt-Rohr, K. *Macromolecules* **2002**, *35*, 7993.

[6] Petkova, A. T.; Ishii, Y.; Balbach, J. J.; Antzutkin, O. N.; Leapman, R. D.; Delaglio, F.; Tycko, R. *Proc. Natl. Acad. Sci. USA* **2002**, *99*, 16742.

[7] Sakellariou, D.; Brown, S. P.; Lesage, A.; Hediger, S.; Bardet, M.; Meriles, C. A.; Pines, A.; Emsley, L. *J. Am. Chem. Soc.* **2003**, *125*, 4376.

[8] Kaji, H.; Kusaka, Y.; Onoyama, G.; Horii, F. *Jpn. J. Appl. Phys.* **2005**, *44*, 3706.

[9] Kaji, H.; Kusaka, Y.; Onoyama, G.; Horii, F. *J. Am. Chem. Soc.* **2006**, *128*, 4292.

[10] Yang, C. Y.; Hu, J. G.; Heeger, A. J. *J. Am. Chem. Soc.* **2006**, *128*, 12007.

[11] Hasobe, T.; Imahori, H.; Fukuzumi, S.; Kamat, P. V. *J. Phys. Chem. B* **2003**, *107*, 12105.

[12] Kang, S.; Umeyama, T.; Ueda, M.; Matano, Y.; Hotta, H.; Yoshida, K.; Isoda, S.; Shiro, M.; Imahori, H. *Adv. Mater.* **2006**, *18*, 2549.

[13] Imahori, H.; Ueda, M.; Kang, S.; Hayashi, H.; Hayashi, S.; Kaji, H.; Seki, S.; Saeki, A.; Tagawa, S.; Umeyama, T.; Matano, Y.; Yoshida, K.; Isoda, S.; Shiro, M.; Tkachenko, N. V.; Lemmetyinen, H. *Chem.–Eur. J.* **2007**, *13*, 10182.

[14] See experimental section for solid-state experiments, DFT calculations, and additional results.

[15] Tycko, R.; Dabbagh, G.; Fleming, R. M.; Haddon, R. C.; Makhija, A. V.; Zahurak, S. M. *Phys. Rev. Lett.* **1991**, *67*, 1886.

[16] Tycko, R.; Haddon, R. C.; Dabbagh, G.; Glarum, S. H.; Douglass, D. C.; Mujsce, A. M. *J. Phys. Chem.* **1991**, *95*, 518.

[17] Yannoni, C. S.; Johnson, R. D.; Meijer, G.; Bethune, D. S.; Salem, J. R. *J. Phys. Chem.* **1991**, *95*, 9.

[18] Johnson, R. D.; Yannoni, C. S. ; Dorn, H. C.; Salem, J. R.; Bethune, D. S. *Science* **1992**, *255*, 1235.

[19] Wachowiak, A.; Yamachika, R.; Khoo, K. H.; Wang, Y.; Grobis, M.; Lee, D. H.; Louie, S. G.; Crommie, M. F. *Science* **2005**, *310*, 468.

[20] Chancey, C. C.; O'Brien, M. C. M. *The Jahn-Teller Effect in C_{60} and Other Icosahedral Complexes*. (Princeton Univ. Pr., 1997), p.204 Pages.

[21] Yannoni, C. S.; Johnson, R. D.; Meijer, G.; Bethune, D. S.; Salem, J. R. *J. Phys. Chem.* **1991**, *95*, 9.

[22] Tycko, R.; Haddon, R. C.; Dabbagh, G.; Glarum, S. H.; Douglass, D. C.; Mujsce, A. M. *J. Phys. Chem.* **1991**, *95*, 518.

[23] Tycko, R.; Dabbagh, G.; Fleming, R. M.; Haddon, R. C.; Makhija, A. V.; Zahurak, S. M. *Phys. Rev. Lett.* **1991**, *67*, 1886.

[24] Tashiro, K.; Aida, T.; Zheng, J. Y.; Kinbara, K.; Saigo, K.; Sakamoto, S.; Yamaguchi, K. *J. Am. Chem. Soc.* **1999**, *121*, 9477.

[25] Zheng, J. Y.; Tashiro, K.; Hirabayashi, Y.; Kinbara, K.; Saigo, K.; Aida, T.; Sakamoto, S.; Yamaguchi, K. *Angew. Chem. Int. Ed.* **2001**, *40*, 1858.

[26] Yamaguchi, T.; Ishii, N.; Tashiro, K.; Aida, T. *J. Am. Chem. Soc.* **2003**, *125*, 13934.

[27] Ouchi, A.; Tashiro, K.; Yamaguchi, K.; Tsuchiya, T.; Akasaka, T.; Aida, T. *Angew. Chem. Int. Ed.* **2006**, *45*, 3542.

[28] Olmstead, M. M.; Nurco, D. J. *Cryst. Growth Des.* **2006**, *6*, 109.

[29] Hosseini, A.; Hodgson, M. C.; Tham, F. S.; Reed, C. A.; Boyd, P. D. W. *Cryst. Growth Des.* **2006**, *6*, 397.

[30] Schmittel, M.; He, B.; Mal, P. *Org. Lett.* **2008**, *10*, 2513.

[31] Johnson, R. D.; Yannoni, C. S.; Dorn, H. C.; Salem, J. R.; Bethune, D. S. *Science* **1992**, *255*, 1235.

[32] Ditchfield, R. *Mol. Phys.* **1974**, *27*, 789.

[33] Wolinski, K.; Hinton, J. F.; Pulay, P. *J. Am. Chem. Soc.* **1990**, *112*, 8251.

[34] Rauhut, G.; Puyear, S.; Wolinski, K.; Pulay, P. *J. Phys. Chem.* **1996**, *100*, 6310.

[35] Becke, A. D. *J. Chem. Phys.* **1993**, *98*, 5648.

[36] Becke, A. D. *J. Chem. Phys.* **1993**, *98*, 1372.

[37] Becke, A. D. *Phys. Rev. A* **1988**, *38*, 3098.

[38] Lee, C. T.; Yang, W. T.; Parr, R. G. *Phys. Rev. B* **1988**, *37*, 785.

[39] Frisch, M. J.; Trucks, G. W.; Schlegel, H. B.; Scuseria, G. E.; Robb, M. A.; Cheeseman, J. R.; Montgomery, Jr. J. A.; Vreven, T.; Kudin, K. N.; Burant, J. C.; Millam, J. M.; Iyengar, S. S.; Tomasi, J.; Barone, V.; Mennucci, B.; Cossi, M.; Scalmani, G.; Rega, N.; Petersson, G. A.; Nakatsuji, H.; Hada, M.; Ehara, M.; Toyota, K.; Fukuda, R.; Hasegawa, J.; Ishida, M.; Nakajima, T.; Honda, Y.; Kitao, O.; Nakai, H.; Klene, M.; Li, X.; Knox, J. E.; Hratchian, H. P.; Cross, J. B.; Adamo, C.; Jaramillo, J.; Gomperts, R.; Stratmann, R. E.; Yazyev, O.; Austin, A. J.; Cammi, R.; Pomelli, C.; Ochterski, J. W.; Ayala, P. Y.; Morokuma, K.; Voth, G. A.; Salvador, P.; Dannenberg, J. J.; Zakrzewski, V. G.; Dapprich, S.; Daniels, A. D.; Strain, M. C.; Farkas, O.; Malick, D. K.; Rabuck, A. D.; K. Raghavachari, K.; Foresman, J. B.; Ortiz, J. V.; Cui, Q.; Baboul, A. G.; Clifford, S.; Cioslowski, J.; Stefanov, B. B.; Liu, G.; Liashenko, A.; Piskorz, P.; Komaromi, I.; Martin, R. L.; Fox, D. J.; Keith, T.; Al-Laham, M. A.; Peng, C. Y.; Nanayakkara, A.; Challacombe, M.; Gill, P. M. W.; Johnson, B.; Chen, W.; Wong, M. W.; Gonzalez, C.; Pople J. A., Gaussian 03 (Revision B.02), Gaussian Inc, Pittsburgh, PA, 2003.

Chapter 5

Effects of Electrode Structure on Photoelectrochemical Properties of ZnO Electrodes Modified with Porphyrin-Fullerene Composite Layers with an Intervening Fullerene Monolayer

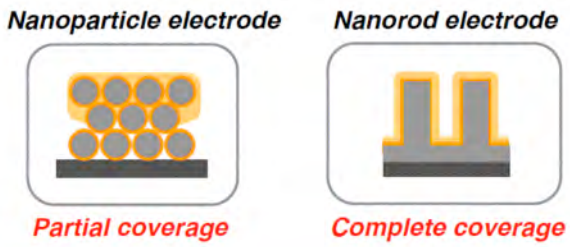

Abstract: ZnO nanorod and nanoparticle electrodes have been applied to solar cells possessing characteristics of both bulk heterojunction and dye-sensitized devices. Namely, first, the ZnO electrodes were covered with fullerene acid molecules to yield the monolayer on the electrodes. Then, zinc porphyrin and fullerene acid molecules were spin-coated on the modified surfaces to give the porphyrin-fullerene modified ZnO electrodes. The porphyrin-fullerene modified ZnO nanorod devices with the intervening fullerene monolayer exhibited efficient photocurrent generation compared to the reference systems without the fullerene monolayer. The significant improvement of the photocurrent generation efficiency by the fullerene monolayer may be associated with the efficient charge separation in the porphyrin-fullerene composite layer, followed by electron injection to a conduction band of the ZnO nanorod electrode together with the suppression of charge recombination between the separated charges by the fullerene monolayer. The cell performance was optimized by altering the length and diameter of the ZnO nanorods and the density of the ZnO nanorod array. The effects of ZnO electrode structures (i.e., nanorod versus nanoparticle) on the photoelectrochemical properties were also compared under the same conditions. Despite larger surface area of the ZnO nanoparticle electrode by a factor of three than that of the ZnO nanorod electrode, similar photocurrent generation efficiencies were noted. This can be rationalized by the facts that only the top surface of the porous ZnO nanoparticle electrode is covered by the porphyrin-fullerene composite layers, whereas all the surface of the ZnO nanorod electrode is wrapped in the composite layers. The photocurrent generation mechanism was also corroborated by the steady-state fluorescence and fluorescence lifetime measurements. The results obtained from this study will provide basic and valuable information on the design of electrode structures and donor-acceptor combination toward the improvement of cell performance in dye-sensitized bulk heterojunction solar cells.

Introduction

Recently organic solar cells have attracted much attention in terms of global warming and growing shortage of petroleum reserves.[1-10] Representative examples include dye-sensitized solar cells[1] and bulk heterojunction solar cells,[2-10] which exhibit power conversion efficiencies (η) in the range 7-11% and 4-7%, respectively. The production of electric power from light in organic solar cells involves the following processes: (i) photons are absorbed within a photoactive layer, leading to the formation of locally confined excitons, and then the excitons migrate to the interface of donor (D)-acceptor (A) heterojunction and dissociate to electron-hole pairs (bulk heterojunction solar cell) or photons are absorbed by the dye on the surface of semiconducting electrode and the resulting dye excited state leads to rapid formation of separated electron-hole pairs at the interface of dye-semiconducting electrode (dye-sensitized solar cell), and (ii) the separated charges move towards respective electrodes, thereby yielding photocurrent in an external circuit. To achieve the high efficiency in each process and ultimately the high cell performance of bulk heterojunction solar cells, it is crucial to control the morphology and mixing state of D-A heterojunction, which would influence on the efficiencies of exciton diffusion, charge separation, and charge collection to the electrodes. In the case of dye-sensitized solar cells, it is also important to regulate the electrode morphology and the dye surface coverage on the electrode, which would have a large impact on the efficiencies. Specifically, high-performance bulk heterojunction solar cells possess an interpenetrating network of D-A molecules in the D-A blend film sandwiched by two electrodes bearing different work functions.[2-7,10] It has been recognized that an intimate mixing of D-A components leads to an increase in the interface area and percolation of the components. To create a desirable D-A bicontinuous network in D-A blend films, which reveal efficient charge separation as well as hole and electron transportation through the network, various strategies have been proposed inclusive of a change in spin-coating solvents and annealing of the blend films.[2-10]

In previous studies, we have developed novel photoelectrochemical devices, i.e., dye-sensitized bulk heterojunction solar cells, which possess characteristics of both dye-sensitized and bulk heterojunction devices.[8,11-14] Typically, first, porphyrin as donor and fullerene as acceptor are self-assembled in a mixture of toluene and acetonitrile due to lyophobic interaction and π–π interaction between the porphyrin and fullerene, yielding porphyrin-fullerene aggregates with a size of ~100 nm in the mixed solvent. Then, the aggregates are electrophoretically deposited onto a sintered SnO_2 nanoparticle film with a particle size of 15 nm on a fluorine doped tin oxide transparent electrode (FTO). Illumination of the modified SnO_2 electrode results in charge separation between porphyrin and fullerene that is similar to one in bulk heterojunction solar cells. On the other hand, electron injection

from the reduced fullerene to a conduction band (CB) of the SnO_2 electrode and hole transfer from the resulting porphyrin radical cation to I^- in the electrolyte solution bear resemblance to that in dye-sensitized solar cell. To realize high performance in the photoelectrochemical device, it is essential to achieve both efficient electron injection into the CB and hole transfer to the I^- minimizing undesirable charge recombination through the porphyrin-fullerene film. Along this line, several attempts have been made to fulfill the requirement.[11-14] However, it is still difficult to achieve the requirement in terms of bottom-up self-organization of porphyrin and fullerene on the nanostructured semiconducting electrode owing to intrinsic difficulty to control each self-organization process. Moreover, the porphyrin-fullerene composite clusters (~100 nm) are so large that they would not incorporate into the porous semiconducting electrode to cover all the inside surfaces.

One possible way to overcome the problem is to use a one-dimensional (1-D) nanostructured semiconducting oxide that is vertically aligned with respect to a transparent conducting electrode.[15-17] Application of 1-D semiconducting oxides to dye-sensitized bulk heterojunction solar cells has the possibilities of increasing the interfacial area between the 1-D semiconducting oxide and the porphyrin-fullerene composite and creating an electron-transporting pathway through the 1-D semiconducting oxide that possesses very high electron mobility. In fact, electron mobility in single crystalline nanorods after charge collection is known to be several orders of magnitude larger than that in random polycrystalline networks.[18]

Among various semiconductor oxides, zinc oxide (ZnO) is an attractive material for preparing 1-D nanorods. 1-D ZnO possesses high electron mobility,[19] the availability of low-temperature synthesis, and the potential for controlling the morphology through simple processing from solution. Recently, ZnO nanorod has been applied to both dye-sensitized solar cells[18,20] and bulk heterojunction solar cells.[21] For instance, Hashimoto et al. have investigated the influence of ZnO nanorod length as an electrode on the device performance of poly(3-hexylthiophene)–6,6-phenyl-C_{61}-butyric acid methyl ester bulk heterojunction solar cells (denoted as ZnO/P3HT-PCBM), and improved the power conversion efficiency (η) up to 2.7%.[21c] In such cases, the promising performance of 1-D ZnO-nanorod photovoltaic devices is attributed in part to the ease of electron transport and collection. Furthermore, stepwise electron transfer (ET) from the P3HT excited state to PCBM, followed by electron injection from the reduced PCBM (4.3 eV) to the CB of the ZnO (4.4 eV) electrode, has been reported in analogous ZnO/P3HT-PCBM bulk heterojunction solar cells,[22] as in the case of dye-sensitized bulk heterojunction solar cells using SnO_2 and TiO_2 electrodes.[8,11-14] Therefore, utilization of 1-D ZnO nanorod electrode in dye-sensitized bulk heterojunction solar cells is an attractive methodology for improving the device performance.

Here we report the first preparation and photoelectrochemical properties of 1-D ZnO nanorod electrode modified with porphyrin-fullerene composites for dye-sensitized bulk heterojunction solar cells. The porphyrin (ZnP) and fullerene (C_{60}-acid) molecules used in this study are shown in Figure 1. A DMF solution of the porphyrin-fullerene composite was spin-coated onto the 1-D ZnO nanorods vertically aligned on a FTO (denoted as FTO/ZnO-r) to cover the electrode surface completely (denoted as FTO/ZnO-r/(ZnP+C_{60}-acid)$_m$). We expected that efficient charge separation would take place within the ZnP-C_{60}-acid composite film. To further facilitate electron injection from the resulting C_{60} radical anion to the CB of the ZnO electrode and retard charge recombination between electrons in the CB of the ZnO electrode and the porphyrin radical cation, a fullerene monolayer was incorporated between the ZnO electrode and the porphyrin-fullerene composite film by chemical adsorption of C_{60}-acid on the 1-D ZnO nanorods (denoted as FTO/ZnO-r/(C_{60}-acid)$_1$/(ZnP+C_{60}-acid)$_m$). ZnO nanorods were grown by the low-temperature hydrothermal solution method,[23] which allowed us to examine the effects of length and diameter of the ZnO nanorods as well as density of the whole array of the ZnO nanorods over the electrode surface on the photoelectrochemical properties. ZnO nanoparticle electrodes (denoted as FTO/ZnO-p) in which the mesoporous nanoparticle film thickness is comparable to the ZnO nanorod height and the diameter of the nanoparticles parallels that of the nanorods were also prepared to evaluate the effects of surface morphology of ZnO electrodes on the photoelectrochemical properties. Steady-state fluorescence and fluorescence lifetime measurements were performed to shed light on the photocurrent generation mechanism.

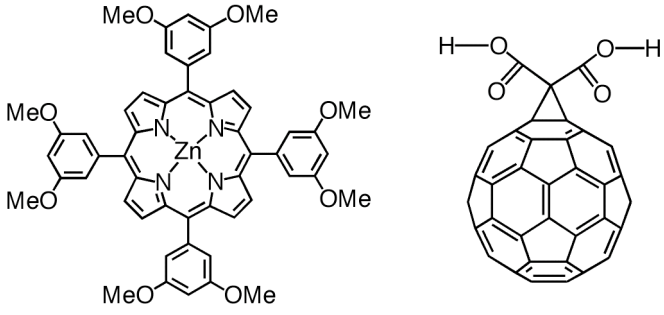

Figure 1. Porphyrin and fullerene derivatives used in this study.

Results and Discussion

Preparation of ZnO Electrodes. The growth of ZnO nanorods on a FTO electrode was controlled by changing the growth reaction time and the concentration of zinc acetate in ethanol for the aligned nanocrystal seeds on the FTO electrode. After the growth of the ZnO nanorods, the length and diameter of the ZnO nanorods as well as the density of the whole

array of the ZnO nanorods over the FTO electrode were characterized by using SEM analysis. At first, the effects of the growth reaction time on the length and diameter of the ZnO nanorods were examined at a fixed concentration of zinc acetate in ethanol (1.0×10^{-3} M). The cross-sectional SEM images reveal densely-packed ZnO nanorods that are grown vertically from the surface of the FTO electrode (Figure 2). The average length of the ZnO nanorods is increased from 0.6 to 1.6 μm with increasing the growth reaction time from 50 to 90 min, whereas the diameter remains constant (100 nm). The results are summarized in Table 1. Then, the effects of the concentration of zinc acetate in ethanol on the diameter of the ZnO nanorods and the density of the whole array of the ZnO nanorods over the FTO electrode were investigated at the fixed growth reaction time of 70 min. The top-down SEM images also disclose densely-packed ZnO nanorods on the FTO electrodes (Figure 3). With increasing the concentration of zinc acetate in ethanol, the average density of the whole array of the ZnO nanorods over the FTO electrode is initially increased and then leveled off, while the average diameter is decreased slightly (Table 1). It is noteworthy that the alignment of ZnO nanorods prepared at $[Zn(OAc)_2] = 1.0 \times 10^{-3}$ M is more uniform than that prepared at $[Zn(OAc)_2] = 1.0 \times 10^{-2}$ M. Furthermore, in the case of $[Zn(OAc)_2] = 1.0 \times 10^{-2}$ M, some of the close nanorods cling together. Therefore, ZnO nanorod electrodes prepared with the growth reaction time of 70 min at $[Zn(OAc)_2] = 1.0 \times 10^{-3}$ M were employed as a typical electrode for the following experiments. The ZnO nanoparticle electrode (FTO/ZnO-p) with a film thickness of 1.8 μm and a particle size of 110 nm was also prepared for comparison (see Experimental Section and Figure 4).

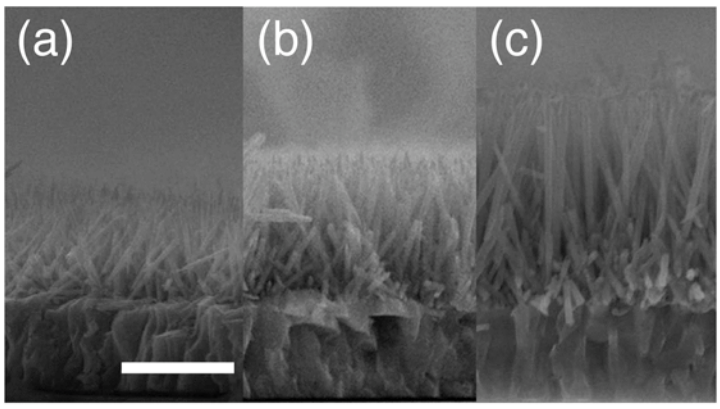

Figure 2. Cross-sectional SEM images of the ZnO nanorod arrays on FTO electrodes after the growth reaction time of (a) 50 min, (b) 70 min, and (c) 90 min with a fixed concentration of zinc acetate in ethanol (1.0×10^{-3} M). Scale bar: 1μm.

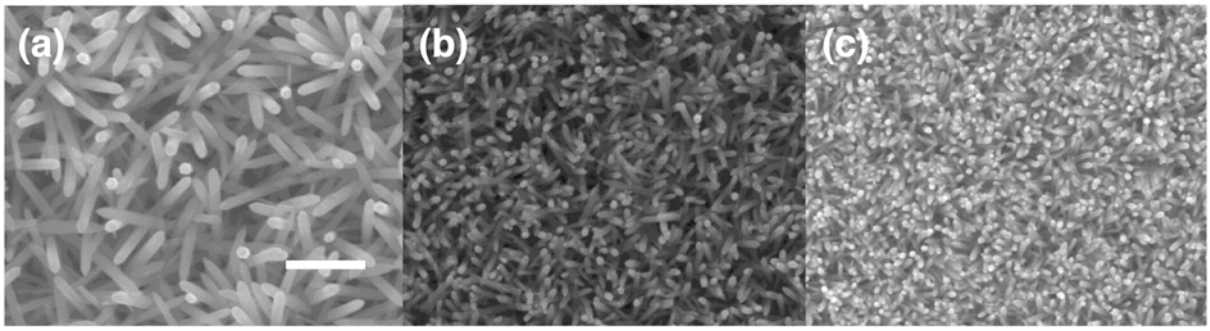

Figure 3. Top-down SEM images of the ZnO nanorod arrays on FTO electrodes after growth reaction time of 70 min with different concentrations of zinc acetate in ethanol: (a) 5.0×10^{-4} M, (b) 1.0×10^{-3} M, and (c) 1.0×10^{-2} M. Scale bar: 500 nm.

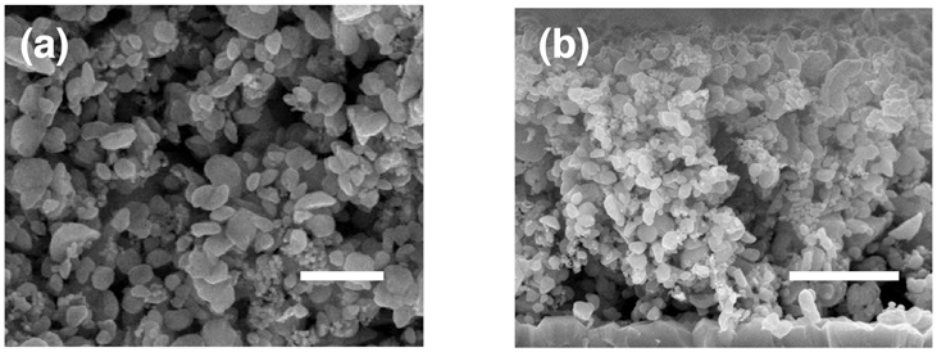

Figure 4. (a) Top-down SEM and (b) cross-sectional SEM images of the ZnO nanoparticle films on FTO electrodes. Scale bar (white line): (a) 500 nm, (b) 1 μm. The film thickness and the particle size were adjusted to be 1.8±0.3 μm and 110±20 nm, respectively, for comparison with the ZnO nanorod system.

TABLE 1: Length, Density, and Diameter of ZnO Nanorods Grown under Different Conditions.

growth reaction time / min	zinc acetate / M	length / μm	density / per cm^2	diameter / nm
70	5.0×10^{-4}	1.0±0.1	$(1\pm0.1) \times 10^9$	120±10
50	1.0×10^{-3}	0.6±0.1	a	100±5
70	1.0×10^{-3}	1.0±0.1	$(4\pm1) \times 10^9$	100±5
90	1.0×10^{-3}	1.6±0.2	a	100±5
70	1.0×10^{-2}	1.0±0.1	$(4\pm1) \times 10^9$	95±5

[a]Not measured.

Mott-Schottky analyses of impedance of the ZnO nanorod electrode were performed to estimate the CB potentials (E_{CB}).[28] Mott-Schottky plots (Cp^{-2} vs V) of the electrode were obtained at 100 Hz, which fell within the capacitive regime of the Bode plot at each electrolyte pH (Figure 5). The flat-band potential (E_{FB}) of the ZnO nanorod electrode is estimated as –0.07 V vs. NHE at pH = 7 from the x-intercepts of the Mott-Schottky plots.[29] It is generally known that the E_{CB} of many n-type semiconductors is 0.1–0.3 eV more negative than E_{FB}.[30] Therefore, the upper limit of the E_{CB} value of the ZnO nanorod electrode is calculated to be –0.37 V vs. NHE at pH = 7. The upper limit of the E_{CB} value of the ZnO nanorod electrode is slightly larger than the previously reported values (~ –0.5 V vs. NHE).[31] The upper limit of the valence band edge potential (E_{VB}) of the ZnO nanorod electrode is also calculated to be 2.93 V vs. NHE at pH = 7, from the onset of the UV-visible absorption spectrum of the electrode. Oxidation potential of the porphyrin excited singlet state ($ZnP^{\bullet+}/{}^1ZnP^*$) is determined to be –1.11 V from the E_{00} value (2.11 eV) and the first oxidation potential of ZnP ($ZnP^{\bullet+}$/ZnP = 1.00 V vs. NHE) in CH_2Cl_2. From these values, ET from the porphyrin excited singlet state to the CB of the ZnO as well as stepwise ET from the porphyrin excited singlet state to C_{60}-acid ($C_{60}/C_{60}^{\bullet-}$ = –0.43 V vs. NHE), followed by ET from the reduced C_{60}-acid to CB of the ZnO (>–0.37 V vs. NHE) is possible owing to the exothermic reaction.

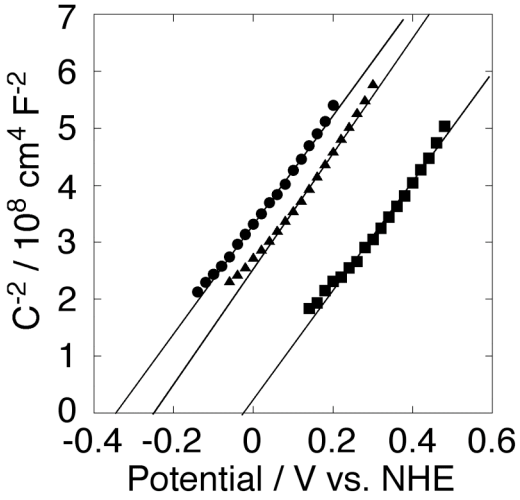

Figure 5. Mott-Schottky plots for the ZnO nanorod electrode at electrolyte pH = 4.3 (square), 9.1 (triangle), and 11.2 (circle). The ZnO electrode with a film thickness of 1.0 μm and a diameter of 100 nm was employed for the measurements.

Modification of ZnO Electrodes with C_{60}-acid Monolayer. The ZnO nanorod electrode was immersed into DMF containing 0.2 mM C_{60}-acid for a certain period of time (0.5 – 6 h) at 40 °C to give a FTO/ZnO-r/(C_{60}-acid)$_1$ electrode. The change in absorbance of the FTO/ZnO-r/(C_{60}-acid)$_1$ electrode at 430 nm arising from C_{60}-acid was monitored as a function of the immersing time (Figure 6a). The absorbance due to adsorbed C_{60}-acid onto the ZnO

nanorods is increased rapidly with increasing the immersing time to reach a maximum for 3-5 h, yielding the saturated coverage of C_{60}-acid on the ZnO nanorods. The total amount of the C_{60}-acid adsorbed onto the ZnO nanorod electrode was determined by measuring absorbance of C_{60}-acid (ε = 3.5 × 10^4 $M^{-1}cm^{-1}$ at 326 nm), which was dissolved from the C_{60}-acid-modified ZnO nanorod electrode into DMF containing 0.1 M HCl. Taking into account the roughness factor (12) of the ZnO nanorod electrode (see Experimental Section), the C_{60}-acid density on the actual surface area was determined to be 1.7 × 10^{-10} mol cm^{-2}. Assuming that the C_{60}-acid molecules are densely packed on the ZnO nanorod surface to which the carboxyl groups are bound, the C_{60}-acid density on the ZnO nanorods is estimated to be 1.7 × 10^{-10} mol cm^{-2}. The experimental value is in good agreement with the calculated one, implying formation of the densely-packed C_{60}-acid monolayer on the ZnO nanorod surface. Similar densely-packed monolayer of C_{60}-acid (1.8 × 10^{-10} mol cm^{-2}) was formed on the ZnO nanoparticle surface (Figure 6b), although the roughness factor (40) of the ZnO nanoparticle electrode (see Experimental Section) is three times as large as that of the ZnO nanorod electrode (vide infra).

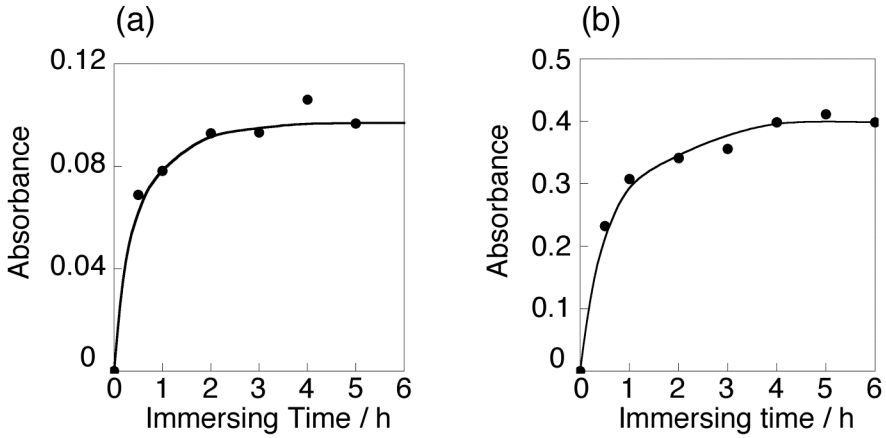

Figure 6. (a) Change in the absorbance of FTO/ZnO/$(C_{60}\text{-acid})_1$ electrode at a 430 nm rising from the adsorption of C_{60}-acid as a function of immersing time. The absorbance of FTO/ZnO was subtracted from that of FTO/ZnO/$(C_{60}\text{-acid})_1$. (b) Change in absorbance of the FTO/ZnO-p/$(C_{60}\text{-acid})_1$ electrode at 430 nm arising from the adsorption of C_{60}-acid as a function of immersing time. Absorbance of the FTO/ZnO-p electrode was subtracted from that of the FTO/ZnO-p/$(C_{60}\text{-acid})_1$ electrode.

Photoelectrochemical Properties of ZnO Nanorod Electrodes Modified with Porphyrin -Fullerene Composites. The FTO/ZnO-r/$(C_{60}\text{-acid})_1$ electrode was further modified with ZnP and C_{60}-acid composites by spin-coating the DMF solution to yield a FTO/ZnO-r/$(C_{60}\text{-acid})_1$/$(ZnP+C_{60}\text{-acid})_m$ electrode. Photoelectrochemical measurements were performed in acetonitrile containing 0.5 M LiI and 0.01 M I_2 with the FTO/ZnO-r/$(C_{60}\text{-acid})_1$/$(ZnP+C_{60}\text{-acid})_m$ as a working electrode, and a platinum counter

electrode, and an I^-/I_3^- reference electrode (See Experimental Section). For instance, Figure 7a displays anodic photocurrent response of the FTO/ZnO-r/$(C_{60}$-acid$)_1$/(ZnP+C_{60}-acid$)_m$ electrode illuminated at an excitation wavelength of 400 nm (1.35 μW cm^{-2}) at an applied potential of +0.55 V vs. NHE. Note that the initial ratio was [ZnP] : [C_{60}-acid] = 1 : 6 in DMF for the spin-coating. The photocurrent responses were prompt and steady and the experimental error of the reproducibility was ±5% during a second on/off cycle of visible light illumination, as observed for analogous photoelectrochemical devices consisting of porphyrin and fullerene.[8,11-14] Current vs. potential characteristic of the FTO/ZnO-r/$(C_{60}$-acid$)_1$/(ZnP+C_{60}-acid$)_m$ electrode was also measured at an excitation wavelength of λ > 380 nm (37.4 mW cm^{-2}), as depicted in Figure 7b. With increasing the positive bias, the photocurrent is increased compared to the dark current. Increased charge separation and facile transport of charge carrier under positive bias are responsible for enhanced photocurrent generation.

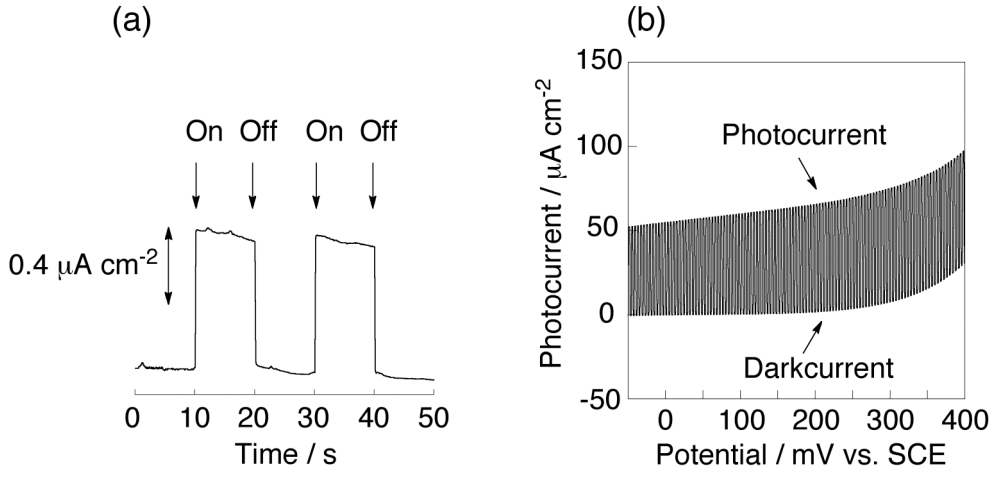

Figure 7. (a) The photoelectrochemical response of the FTO/ZnO-r/$(C_{60}$-acid$)_1$/(ZnP+C_{60}-acid$)_m$ device. Potential: +0.55 V vs. NHE; excitation wavelength: λ_{ex} = 400 nm (1.35 μW cm^{-2}). (b) Current vs. applied potential curve of the FTO/ZnO-r/$(C_{60}$-acid$)_1$/(ZnP+C_{60}-acid$)_m$ device; excitation wavelength: λ_{ex} > 380 nm (37.4 mW cm^{-2}). [ZnP] : [C_{60}-acid] = 1 : 6 ([ZnP] = 0.67 mM, [C_{60}-acid] = 4.00 mM); electrolyte: 0.5 M LiI and 0.01 M I_2.

To evaluate the photoelectrochemical response of the FTO/ZnO-r/(C_{60}-acid)$_1$/(ZnP+C_{60}-acid)$_m$ electrode, we examined the wavelength dependence of the incident photon-to-current efficiency (IPCE). The IPCE values were calculated by normalizing the photocurrent densities for incident light energy and intensity and by use of the expression (1):

$$\text{IPCE}\ (\%) = 100 \times 1240 \times i/(W_{\text{in}} \times \lambda) \qquad (1)$$

where i is the photocurrent density (A cm^{-2}), W_{in} is the incident light intensity (W cm^{-2}), and λ is the excitation wavelength (nm). Figure 8 shows the photocurrent action spectra for the FTO/ZnO-r/(C_{60}-acid)$_1$/(ZnP+C_{60}-acid)$_m$ device. The IPCE value of the FTO/ZnO-r/(C_{60}-acid)$_1$/(ZnP+C_{60}-acid)$_m$ device is increased with increasing the ratio of C_{60}-acid vs. ZnP to reach a maximum of 30% at 400 nm with the initial ratio of [ZnP] : [C_{60}-acid] = 1 : 6 in DMF for the spin-coating. The photocurrent action spectra largely agree with the absorption spectra of the FTO/ZnO-r/(C_{60}-acid)$_1$/(ZnP+C_{60}-acid)$_m$ electrodes (Figure 9).[26] Further increase in the C_{60}-acid ratio results in a decrease in the IPCE value. Therefore, the initial ratio of [ZnP] : [C_{60}-acid] = 1 : 6 ([ZnP] = 0.67 mM) in DMF was used for comparison of the photoelectrochemical properties under various conditions (vide infra).

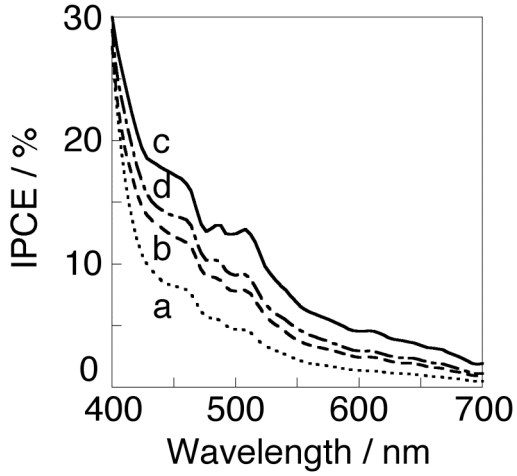

Figure 8. The photocurrent action spectra (IPCE vs. wavelength) of the FTO/ZnO/(C_{60}-acid)$_1$/(ZnP+C_{60}-acid)$_m$ devices. (a) [ZnP] : [C_{60}-acid] = 1 : 4 ([C_{60}-acid] = 2.00 mM), (b) [ZnP] : [C_{60}-acid] = 1 : 5 ([C_{60}-acid] = 3.35 mM), (c) [ZnP] : [C_{60}-acid] = 1 : 6 ([C_{60}-acid] = 4.00 mM), and (d) [ZnP] : [C_{60}-acid] = 1 : 7 ([C_{60}-acid] = 4.70 mM); Concentrations in DMF for the spin-coating: [ZnP] = 0.67 mM; Potentials: +0.30 V vs. SCE; electrolyte: 0.5 M LiI and 0.01 M I_2.

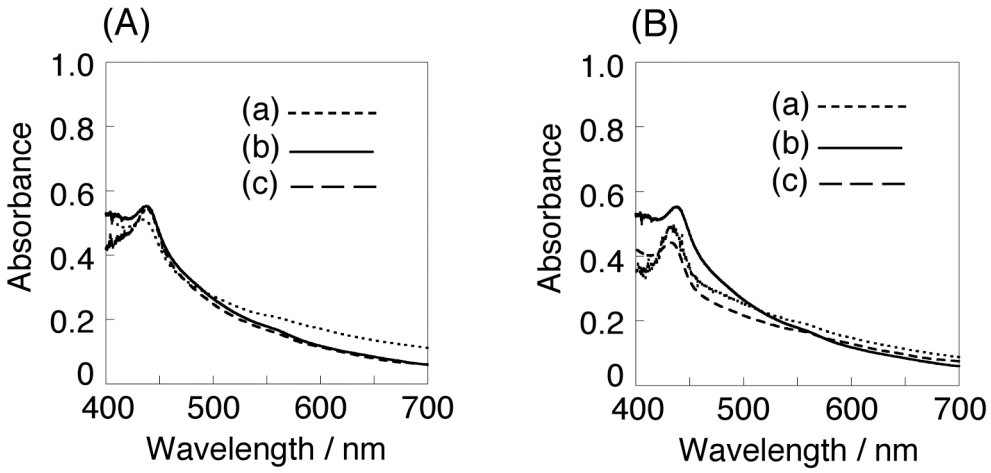

Figure 9. (A) The absorption spectra of FTO/ZnO-r/$(C_{60}\text{-acid})_1$/$(ZnP+C_{60}\text{-acid})_m$ electrodes. The lengths of ZnO nanorods: (a) 0.6 μm, (b) 1.0 μm, and (c) 1.6 μm. (B) The absorption spectra of FTO/ZnO-r/$(C_{60}\text{-acid})_1$/$(ZnP+C_{60}\text{-acid})_m$ electrodes. Concentrations of zinc acetate for seeding: (a) 5.0×10^{-4} M, (b) 1.0×10^{-3} M, (c) 1.0×10^{-2} M. Concentrations in the mixed DMF solution for spin-coating: [ZnP] = 0.67 mM, [C_{60}-acid] = 4.00 mM ([ZnP] : [C_{60}-acid] = 1 : 6).

Effects of C_{60}-acid Monolayer on Photoelectrochemical Properties. To investigate the effects of C_{60}-acid monolayer on the photocurrent generation efficiency, we compared the IPCE values of the photoelectrochemical devices with and without the C_{60}-acid monolayer (Figure 10). In the absence of the C_{60}-acid monolayer, the IPCE value of the FTO/ZnO-r/$(ZnP)_m$ device (Figure 10A(c)) is virtually similar to that of the FTO/ZnO-r device (Figure 10A(d)). This reveals that direct electron injection from the porphyrin excited singlet state to the CB of the ZnO has little impact on the photocurrent. On the other hand, the IPCE value of the FTO/ZnO-r/$(C_{60}\text{-acid})_m$ device (Figure 10A(b)) is considerably higher than that of the FTO/ZnO-r device. This means that ET occurs from I^- in the electrolyte to the C_{60} excited states, followed by electron injection from the reduced C_{60} to the CB of the ZnO, leading to notable photocurrent generation.[27] The IPCE value of the FTO/ZnO-r/$(ZnP+C_{60}\text{-acid})_m$ device (Figure 10A(a)) is further higher than the sum of the IPCE values of the FTO/ZnO-r/$(ZnP)_m$ and the FTO/ZnO-r/$(C_{60}\text{-acid})_m$ reference devices. This implies that charge separation between ZnP and C_{60}-acid contributes to the photocurrent generation significantly. In contrast, in the presence of the C_{60}-acid monolayer, the IPCE values of the FTO/ZnO-r/$(C_{60}\text{-acid})_1$/$(C_{60}\text{-acid})_m$ (Figure 10B(b)), the FTO/ZnO-r/$(C_{60}\text{-acid})_1$/$(ZnP)_m$ (Figure 10B(c)), and the FTO/ZnO-r/$(C_{60}\text{-acid})_1$ (Figure 10B(d)) are largely identical. This shows that electron injection from the excited states of the porphyrin or C_{60}-acid on the C_{60}-acid monolayer into the CB of the ZnO is not efficient via the lowest unoccupied molecular orbital (LUMO) of the C_{60}-acid

monolayer. Nevertheless, the IPCE value of the FTO/ZnO-r/(C_{60}-acid)$_1$/(ZnP+C_{60}-acid)$_m$ device (Figure 10B(a)) is much higher than those of the FTO/ZnO-r/(C_{60}-acid)$_1$/(ZnP)$_m$ and FTO/ZnO-r/(C_{60}-acid)$_1$/(C_{60}-acid)$_m$, reference devices. This demonstrates that charge separation between ZnP and C_{60}-acid in the presence of the C_{60}-acid monolayer has a notable impact on the improvement of photocurrent generation efficiency. More importantly, the IPCE value of the FTO/ZnO-r/(C_{60}-acid)$_1$/(ZnP+C_{60}-acid)$_m$ device is remarkably large compared with that of the FTO/ZnO-r/(ZnP+C_{60}-acid)$_m$ device. This corroborates that separated electrons are injected into the CB of the ZnO nanorods via the LUMO of the C_{60}-acid monolayer more efficiently than without the C_{60}-acid monolayer, leading to the improved photocurrent generation. During the spin-coating for the preparation of the FTO/ZnO-r/(ZnP+C_{60}-acid)$_m$ electrode some of C_{60}-acid molecules have possibilities to bind onto the surface of the ZnO nanorods directly. However, such direct binding may be minor as it takes a few hours to form the C_{60}-acid monolayer on the ZnO nanorod electrode (vide supra). Therefore, we can safely conclude that the C_{60}-acid monolayer on ZnO nanorod leads to the improvement of photocurrent generation. For the FTO/ZnO-r/(C_{60}-acid)$_1$/(ZnP+C_{60}-acid)$_m$ device, a short circuit photocurrent (J_{sc}) of 1.37 mA cm^{-2}, an open circuit potential (V_{oc}) of 0.26 V, and a fill factor (*ff*) of 0.40 yielded a η value of 0.14 % under standard AM 1.5 conditions (Figure 11).

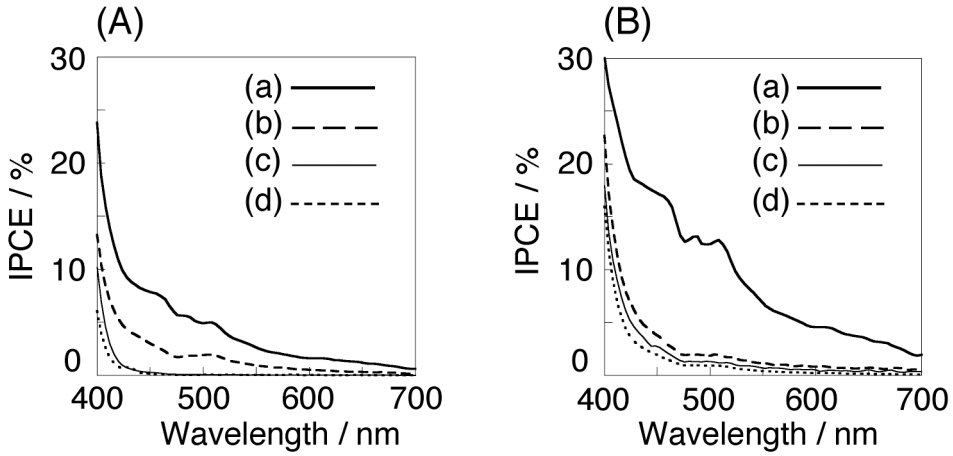

Figure 10. (A) The photocurrent action spectra of the (a) FTO/ZnO-r/(ZnP+C_{60}-acid)$_m$, (b) FTO/ZnO-r/(C_{60}-acid)$_m$, (c) FTO/ZnO-r/(ZnP)$_m$, (d) FTO/ZnO-r devices. (B) The photocurrent action spectra of the (a) FTO/ZnO-r/(C_{60}-acid)$_1$/(ZnP+C_{60}-acid)$_m$, (b) FTO/ZnO-r/(C_{60}-acid)$_1$/(C_{60}-acid)$_m$, (c) FTO/ZnO-r/(C_{60}-acid)$_1$/(ZnP)$_m$, (d) FTO/ZnO-r/(C_{60}-acid)$_1$ devices. Potentials: +0.55 V vs. NHE; electrolyte: 0.5 M LiI and 0.01 M I_2; Concentration in DMF for spin-coating: [ZnP] = 0.67 mM, [C_{60}-acid] = 4.00 mM ([ZnP] : [C_{60}-acid] = 1 : 6).

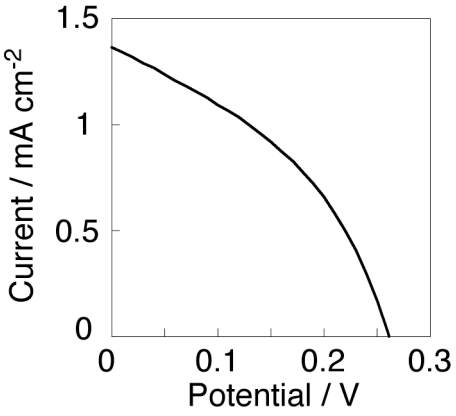

Figure 11. Current–voltage characteristic of the FTO/ZnO-r/$(C_{60}\text{-acid})_1$/$(ZnP+C_{60}\text{-acid})_m$ device under AM 1.5 irradiation (100 mW cm^{-2}).

Optical studies. Steady-state fluorescence spectra (λ_{ex} = 430 nm) were measured for the better understanding of the photodynamical behavior of the porphyrin-fullerene system on the ZnO electrodes (Figure 12). The FTO/ZnO-r/$(ZnP)_m$ (Figure 12b) and FTO/ZnO-r/$(C_{60}\text{-acid})_1$/$(ZnP)_m$ (Figure 12d) electrodes reveal characteristic porphyrin fluorescence with maxima at 610 nm and 660 nm. In marked contrast, the fluorescence intensities are intensively reduced and the emission maxima are different in the FTO/ZnO-r/$(ZnP+C_{60}\text{-acid})_m$ (Figure 12a) and FTO/ZnO-r/$(C_{60}\text{-acid})_1$/$(ZnP+C_{60}\text{-acid})_m$ (Figure 12c) electrodes. Taking into account the results on the photoelectrochemical properties together with the strong quenching in the $(ZnP+C_{60}\text{-acid})_m$ composite electrodes relative to the reference electrodes without the composite layer, the porphyrin excited singlet state is quenched rapidly by C_{60} in the composite via ET not by the C_{60}-monolayer, exhibiting little fluorescence in the FTO/ZnO-r/$(ZnP+C_{60}\text{-acid})_m$ and FTO/ZnO-r/$(C_{60}\text{-acid})_1$/$(ZnP+C_{60}\text{-acid})_m$ electrodes.[9d,e] Thus, the emission on the FTO/ZnO-r/$(ZnP+C_{60}\text{-acid})_m$ and FTO/ZnO-r/$(C_{60}\text{-acid})_1$/$(ZnP+C_{60}\text{-acid})_m$ electrodes could originate from the impurities or degradation of ZnP and/or C_{60}-acid in addition to the minor direct excitation of C_{60}-acid at λ_{ex} = 430 nm. It is noteworthy that the FTO/ZnO-r/$(ZnP+C_{60}\text{-acid})_m$ and FTO/ZnO-r/$(C_{60}\text{-acid})_1$/$(ZnP+C_{60}\text{-acid})_m$ electrodes exhibit no characteristic CT emission at 800-1000 nm due to the direct complexation between ZnP and C_{60}-acid.[28]

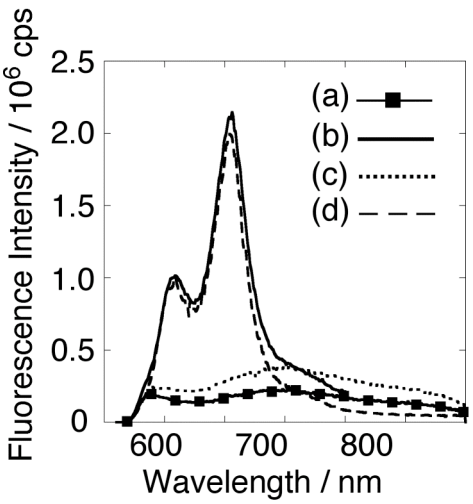

Figure 12. Steady-state fluorescence spectra of (a) FTO/ZnO-r/(ZnP+C_{60}-acid)$_m$, (b) FTO/ZnO-r/(ZnP)$_m$, (c) FTO/ZnO-r/(C_{60}-acid)$_1$/(ZnP+C_{60}-acid)$_m$, and (d) FTO/ZnO-r/(C_{60}-acid)$_1$/(ZnP)$_m$ electrodes with an excitation wavelength of 430 nm.

The porphyrin excited singlet state was probed by the picosecond fluorescence lifetime measurements for the FTO/ZnO-r/(ZnP+C_{60}-acid)$_m$, FTO/ZnO-r/(ZnP)$_m$, FTO/ZnO-r/(C_{60}-acid)$_1$/(ZnP+C_{60}-acid)$_m$, and FTO/ZnO-r/(C_{60}-acid)$_1$/(ZnP)$_m$ electrodes. The emission decay measurements were carried out using time-correlated single photon counting method at the wavelength of 660 nm at which ZnP emits. The time resolution is 60-70 ps on the basis of FWHM of instrument response function. As discussed in the steady-state fluorescence measurements, the porphyrin excited singlet state is strongly quenched by the C_{60} in the composite via ET, exhibiting little ZnP fluorescence at 660 nm. Thus, the multi-component fluorescence decays with rather long lifetimes of > 60 ps in the FTO/ZnO-r/(ZnP+C_{60}-acid)$_m$ and FTO/ZnO-r/(C_{60}-acid)$_1$/(ZnP+C_{60}-acid)$_m$ electrodes stem from the minor relaxation process probably due to the impurities or degradation of ZnP (Figure 13). We also performed transient absorption measurements for the modified ZnO electrodes using femtosecond pump-probe method with the excitation wavelength of 420 nm. Unfortunately, formation of the charge-separated state in the mixed films could not be detected because of a poor signal-to-noise ratio and the instability of the samples under the experimental conditions.

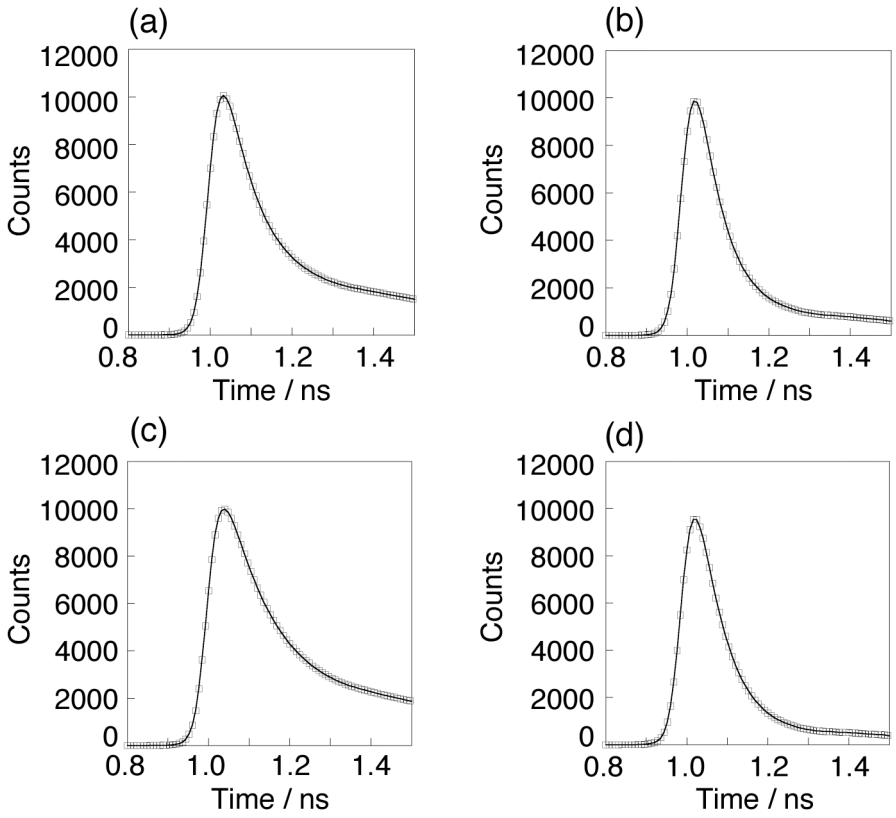

Figure 13. The fluorescence decay curves of the (a) FTO/ZnO-r/(ZnP+C_{60}-acid)$_m$, (b) FTO/ZnO-r/(ZnP)$_m$, (c) FTO/ZnO-r/(C_{60}-acid)$_1$/(ZnP+C_{60}-acid)$_m$, and (d) FTO/ZnO-r/(C_{60}-acid)$_1$/(ZnP)$_m$ electrodes observed at 660 nm with an excitation wavelength of 405 nm. The decays were analyzed with 3-exponential fit (τ_1 = 0.06 ns (74 %), τ_2 = 0.35 ns (24 %), τ_3 = 1.8 ns (2 %) for the FTO/ZnO-r/(ZnP+C_{60}-acid)$_m$, τ_1 = 0.05 ns (86 %), τ_2 = 0.24 ns (13 %), τ_3 = 1.56 ns (1 %) for the FTO/ZnO-r/(ZnP)$_m$, τ_1 = 0.09 ns (90 %), τ_2 = 0.05 ns (9 %), τ_3 = 1.7 ns (1 %) for the FTO/ZnO-r/(C_{60}-acid)$_1$/(ZnP+C_{60}-acid)$_m$, and τ_1 = 0.06 ns (90 %), τ_2 = 0.21 ns (9 %), τ_3 = 1.7 ns (1 %) for the FTO/ZnO-r/(C_{60}-acid)$_1$/(ZnP)$_m$ electrodes).

On the basis of the energetics of the photoactive and radical ion species involved in the FTO/ZnO-r/(C_{60}-acid)$_1$/(ZnP+C_{60}-acid)$_m$ device, the results obtained here, and the well-established photocurrent generation mechanism of analogous photoelectrochemical devices using SnO_2 and TiO_2 electrodes,[9d,e,11-14] we propose a photocurrent generation scheme (Scheme 1). First, ET takes place from $^1ZnP^*$ (ZnP: –1.11 V vs. NHE) to C_{60} (C_{60}-acid: –0.43 V vs. NHE) yielding the porphyrin radical cation ($ZnP^{\bullet+}$) and C_{60} radical anion ($C_{60}^{\bullet-}$). The generated $C_{60}^{\bullet-}$ gives electrons to the CB of the ZnO electrode (>–0.37 V vs. NHE) via the LUMO of the C_{60}-acid monolayer. On the other hand, the oxidized porphyrin (ZnP/$ZnP^{\bullet+}$ = 1.00 V vs. NHE) undergoes the ET reduction with the iodide (I^-/I_3^- = 0.5 V vs. NHE)[11-14] in the electrolyte system, resulting in photocurrent generation in the circuit. Direct electron injection from $^1ZnP^*$ to the CB of the ZnO as well as from $^1ZnP^*$ to the CB of ZnO via the LUMO of the

C_{60}-acid monolayer is a minor pathway for photocurrent generation considering the similar photocurrent generation efficiencies in the FTO/ZnO-r/$(C_{60}\text{-acid})_1/(ZnP)_m$ and the FTO/ZnO-r/$(C_{60}\text{-acid})_1$ as well as the FTO/ZnO-r/$(ZnP)_m$ and the FTO/ZnO-r devices (vide supra). The less efficient ET reactions from $^1ZnP^*$ to the ZnO and to the C_{60}-acid monolayer directly are consistent with the steady-state fluorescence in that the quenching in the $(ZnP+C_{60}\text{-acid})_m$ composite electrodes is far more efficient than the reference electrodes without the $(ZnP+C_{60}\text{-acid})_m$ composite layer (Figure 12).

Scheme 1. Plausible photocurrent generation mechanism for the FTO/ZnO-r/$(C_{60}\text{-acid})_1/(ZnP+C_{60}\text{-acid})_m$ device.

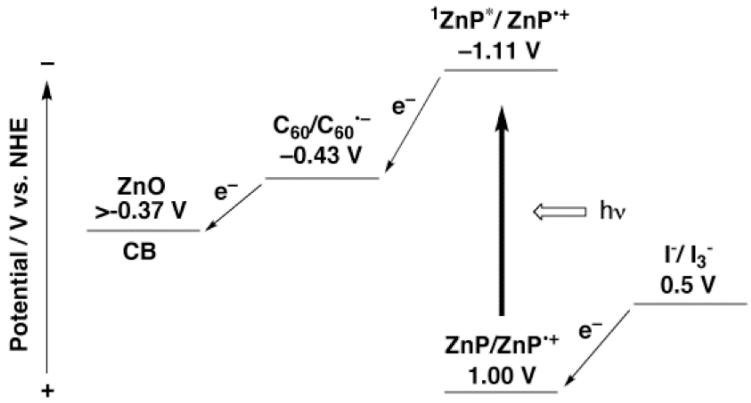

Effects of Length and Diameter of ZnO Nanorods and Density of Whole Array of ZnO Nanorods on Photoelectrochemical Properties. To examine the dependence of the photocurrent generation efficiency on the length of ZnO nanorods, the photoelectrochemical properties of the FTO/ZnO-r/$(C_{60}\text{-acid})_1/(ZnP+C_{60}\text{-acid})_m$ device were evaluated using the ZnO nanorods with different lengths of 0.6, 1.0, and 1.6 μm (vide supra). With increasing the length of ZnO nanorods, the IPCE value is increased initially, but a further increase in the length leads to a decrease in the IPCE value (Figure 14). Considering that the absorption spectra on the electrodes are comparable (Figure 9A), the ZnO nanorods with a suitable length of 1.0 μm may facilitate both charge separation between ZnP and C_{60}-acid and electron transportation through the ZnO nanorods, exhibiting the highest IPCE value of 30% at 400 nm.

The effects of the density of the whole array of the ZnO nanorods and the diameter of the ZnO nanorods were also investigated by using the ZnO nanorods prepared with the different concentrations of zinc acetate in ethanol for the seeding (vide supra). The IPCE value is increased remarkably as the concentration of zinc acetate is increased from 5.0×10^{-4} M to 1.0×10^{-3} M, whereas the IPCE value is decreased slightly as the concentration of zinc acetate is increased from 1.0×10^{-3} M to 1.0×10^{-2} M (Figure 14B). The corresponding absorption spectra are rather comparable irrespective of the difference in the seed concentration (Figure

9B). Thus, the amounts of ZnP and C_{60}-acid loaded on the surface of ZnO nanorods are largely equal for the different electrodes. In such a case the high density of the ZnO nanorod array and the small diameter of the ZnO nanorods are expected to reduce the thickness of the ZnP-C_{60}-acid composite film, thereby improving the photocurrent generation efficiency owing to efficient electron injection from the thin composite film to the ZnO nanorods. The slight decrease in the IPCE value at $[Zn(OAc)_2] = 1.0 \times 10^{-2}$ M relative to that at $[Zn(OAc)_2] = 1.0 \times 10^{-3}$ M may be associated with rather irregular alignment and close contact of the ZnO nanorods in the case of $[Zn(OAc)_2] = 1.0 \times 10^{-2}$ M (vide supra). These results corroborate that the photocurrent generation efficiency can be modulated by varying the length and diameter of the ZnO nanorods as well as the density of the whole array of the ZnO nanorods over the electrode surface.

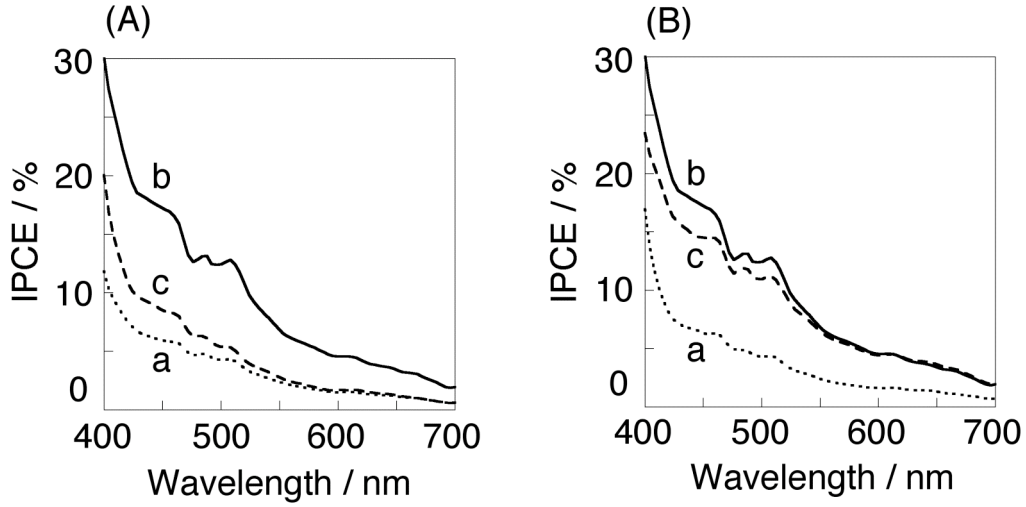

Figure 14. The photocurrent action spectra of the FTO/ZnO-r/$(C_{60}\text{-acid})_1$/$(ZnP+C_{60}\text{-acid})_m$ devices. (A) The length of ZnO nanorods: (a) 0.6 μm, (b) 1.0 μm, and (c) 1.6 μm. (B) The concentration of zinc acetate: (a) 5.0×10^{-4} M, (b) 1.0×10^{-3} M, and (c) 1.0×10^{-2} M. Potentials: +0.55 V vs. NHE; electrolyte: 0.5 M LiI and 0.01 M I_2; Concentration in the mixed DMF solution for spin-coating: [ZnP] = 0.67 mM, [C_{60}-acid] = 4.00 mM ([ZnP] : [C_{60}-acid] = 1 : 6).

Effects of Electrode Structure on Photoelectrochemical Properties. Finally, we compared the photoelectrochemical properties of the ZnO nanorod and the ZnO nanoparticle electrodes under the similar conditions (Figure 15A). Unexpectedly, the IPCE value of the FTO/ZnO-r/$(C_{60}\text{-acid})_1$/$(ZnP+C_{60}\text{-acid})_m$ device is comparable to that of the FTO/ZnO-p/$(C_{60}\text{-acid})_1$/$(ZnP+C_{60}\text{-acid})_m$ device. This is remarkable considering that the surface area of the ZnO nanoparticle electrode is ca. three times as large as that of the ZnO nanorod electrode. Although the adsorbed amount of C_{60}-acid on the ZnO nanoparticle electrode is also larger by a factor of three than that on the ZnO nanorod electrode, the

absorption spectra of the FTO/ZnO-r/(C_{60}-acid)$_1$/(ZnP+C_{60}-acid)$_m$ and the FTO/ZnO-p/(C_{60}-acid)$_1$/(ZnP+C_{60}-acid)$_m$ electrodes are rather comparable irrespective of the difference in the electrode structures (Figure 15B). Judging from the comparable absorbance at 440 nm stemming from ZnP mainly, the amounts of ZnP and C_{60}-acid loaded on the surfaces of the ZnO nanorods and ZnO nanoparticles covered with the C_{60}-acid monolayer are considered to be virtually similar. This may be explained by the difference in the fabrication processes (chemical adsorption vs. spin-coating). The long steeping time allows the complete monolayer coverage of both electrodes by C_{60}-acid, irrespective of the slow chemical adsorption of C_{60}-acid onto the ZnO surfaces in the C_{60}-acid solution. In marked contrast, rapid evaporation of the composite solution in the mesoporous ZnO nanoparticle film during the spin-coating hinders the infiltration of the composite molecules to the bottom of the ZnO nanoparticle film, whereas the composite solution covers the whole array of the smooth ZnO nanorods rapidly during the spin-coating process to yield the complete coverage of the composites on the electrode surface (vide infra).

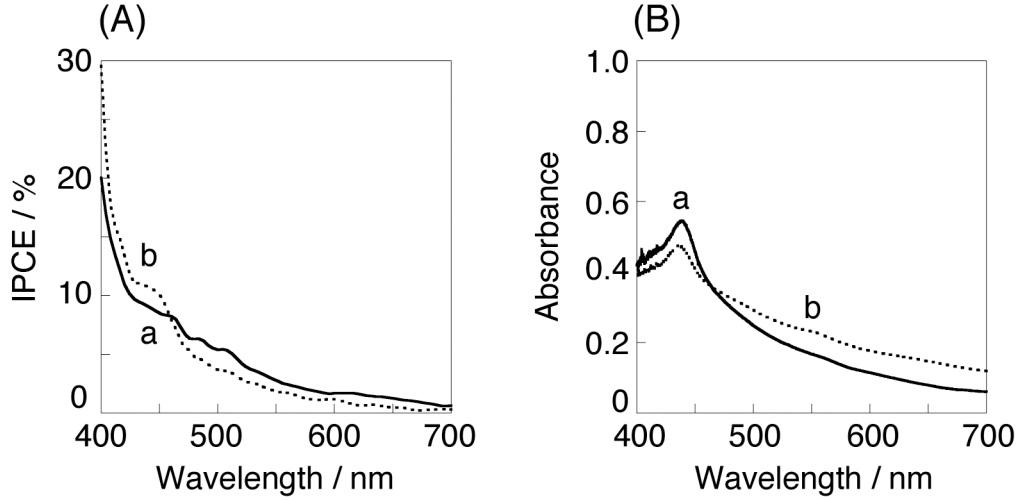

Figure 15. (A) The photocurrent action spectra of (a) FTO/ZnO-r/(C_{60}-acid)$_1$/(ZnP+C_{60}-acid)$_m$ and (b) FTO/ZnO-p/(C_{60}-acid)$_1$/(ZnP+C_{60}-acid)$_m$ devices. The film lengths of the ZnO nanorod and the ZnO nanoparticle electrodes are 1.6 μm and 1.8 μm, respectively. Potentials: +0.55 V vs. NHE; electrolyte: 0.5 M LiI and 0.01 M I_2; Concentration in the mixed DMF solution for spin-coating: [ZnP] = 0.67 mM, [C_{60}-acid] = 4.00 mM ([ZnP] : [C_{60}-acid] = 1 : 6). (B) The absorption spectra of the (a) FTO/ZnO-r/(C_{60}-acid)$_1$/(ZnP+C_{60}-acid)$_m$ and (b) FTO/ZnO-p/(C_{60}-acid)$_1$/(ZnP+C_{60}-acid)$_m$ electrodes. The film lengths of the ZnO nanorod and the ZnO nanoparticle electrodes are 1.6 μm and 1.8 μm, respectively. Concentration in the mixed DMF solution for spin-coating: [ZnP] = 0.67 mM, [C_{60}-acid] = 4.00 mM ([ZnP] : [C_{60}-acid] = 1 : 6). Absorbances of the FTO/ZnO-r/(C_{60}-acid)$_1$ and FTO/ZnO-p/(C_{60}-acid)$_1$ electrodes were subtracted from those of the FTO/ZnO-r/(C_{60}-acid)$_1$/(ZnP+C_{60}-acid)$_m$ and FTO/ZnO-p/(C_{60}-acid)$_1$/(ZnP+C_{60}-acid)$_m$ electrodes, respectively.

To obtain more insight into the similarity in the loaded amounts of ZnP and C_{60}-acid on the different ZnO electrodes, we carried out the cross-sectional SEM measurements for the FTO/ZnO-r/(C_{60}-acid)$_1$/(ZnP+C_{60}-acid)$_m$ and the FTO/ZnO-p/(C_{60}-acid)$_1$/(ZnP+C_{60}-acid)$_m$ electrodes. The ZnO nanorods are uniformly covered with thick porphyrin-fullerene composite layers from the top to the bottom of the ZnO nanorods (Figure 16). In the case of the FTO/ZnO-p/(C_{60}-acid)$_1$/(ZnP+C_{60}-acid)$_m$ electrode, however, only the top surface of the porous ZnO nanoparticle electrode is wrapped in the porphyrin-fullerene composite layers (Figure 17). These results imply that the spin-coating solvent containing the small molecules does not infiltrate into the porous ZnO nanoparticle electrode, resulting in incomplete coverage of the nanoparticle electrode surface with large surface area, whereas facile infiltration of the spin-coating solvent into the ZnO nanorod electrode leads to complete coverage of the nanorod electrode with small surface area. These results rationalize the similar photoelectrochemical properties of the ZnO nanorod and nanoparticle devices.

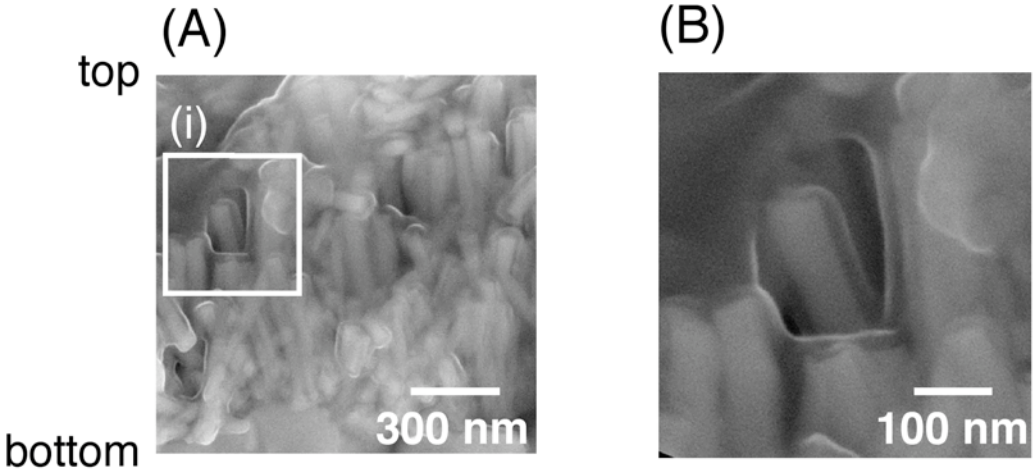

Figure 16. (A) Cross-sectional SEM images of the FTO/ZnO-r/(C_{60}-acid)$_1$/(ZnP+C_{60}-acid)$_m$ electrodes. The enlarged image of area (i) is shown as (B).

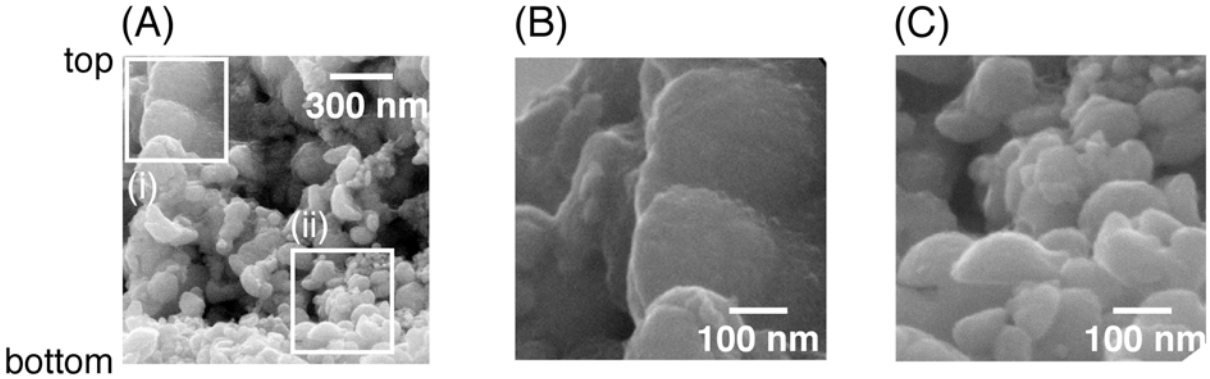

Figure 17. (A) Cross-sectional SEM images of the FTO/ZnO-p/(C_{60}-acid)$_1$/(ZnP+C_{60}-acid)$_m$ electrode. The enlarged images of area (i) and (ii) are shown as (B) and (C), respectively.

Conclusions

We have successfully prepared ZnO nanorod and ZnO nanoparticle electrodes, and applied them to dye-sensitized bulk heterojunction solar cells for the first time. The effects of the intervening fullerene monolayer between the porphyrin-fullerene composite multilayers and the ZnO nanorods on photocurrent generation efficiency were examined. The ZnO nanorod electrodes modified sequentially with the fullerene monolayer and the porphyrin-fullerene multilayers exhibited the high incident photon-to-current efficiency up to 30% at 400 nm as compared to the reference systems without the fullerene monolayer. The intervening fullerene monolayer between the porphyrin-fullerene composite multilayers and the ZnO nanorods may enhance the electron injection efficiency into the ZnO nanorod electrode and inhibit the charge recombination, leading to the improvement of photocurrent generation efficiency. Finally, the effects of ZnO electrode structures (nanorod vs. nanoparticle) on photocurrent generation efficiency were evaluated. Unfortunately, similar photocurrent generation efficiencies were noted despite of the difference in the electrode structures. This can be explained by the facts that only the top surface of the porous ZnO nanoparticle electrode is covered by the porphyrin-fullerene composite layers, whereas all the surface of the ZnO nanorod electrode is wrapped in the composite layers. Nevertheless, the results obtained from this study will provide basic and valuable information on the advanced design of organic solar cells if a combination of surface morphology of electrodes and donor-acceptor composites is modulated adequately to fulfill the requirements for high cell performance.

Experimental Section

General Procedure. ^{1}H NMR spectra were recorded on JEOL EX270 KS or JEOL AL300 NMR spectrometers. Matrix-assisted laser desorption ionization time-of-flight (MALDI-TOF) mass spectra were measured with a COMPACT MALDI II (SHIMADZU) mass spectrometer. High-resolution mass spectra (HRMS) were recorded on a JEOL JMS-HX 110A spectrometer. UV-visible absorption spectra were obtained on a Perkin Elmer Lambda 900UV/vis/NIR spectrometer. Steady-state fluorescence spectra were measured on a Fluorolog 3 spectrofluorimeter (ISA Inc.) equipped with a cooled IR sensitive photomultiplier (R2658). Field emission scanning electron microscopy (FE-SEM) observation was carried out by using a JSM6500F (JEOL). BET analysis was performed using nitrogen adsorption desorption analysis (BELSORP 18 PLUS).

Materials. All solvents and chemicals were of reagent grade quality, purchased commercially and used without further purification unless otherwise noted. Thin-layer chromatography and

flash column chromatography were performed with Alt. 5554 DC-Alufolien Kieselgel 60 F_{254} (Merck) and Silica-gel 60N (Kanto Chemicals), respectively. Porphyrin (ZnP)[29] and fullerene (C_{60}-acid)[30] compounds were synthesized by following previously reported procedures.

Preparation of ZnO Nanorods and ZnO Nanoparticles. ZnO nanorod arrays were grown on a FTO electrode (Asahi Glass, Japan) to give FTO/ZnO-r. First, an ethanol solution of zinc acetate was cast onto a FTO surface by spin-coating. The density of the whole array of the ZnO nanorods over the FTO electrode was altered systematically by changing the concentrations of zinc acetate in ethanol ($5 \times 10^{-4} - 1 \times 10^{-2}$ M).[31] Then, the FTO electrode was dried and annealed to form the aligned nanocrystal seeds on the surface. The annealing temperature was controlled in sequence of 130 °C for 60 min, 180 °C for 60 min, and 260 °C for 120 min in air. Finally, vertical ZnO nanorod arrays were grown from the aligned nanocrystal seeds by immersing the seeded FTO electrode into a precursor solution containing 0.04 M $Zn(NO_3)_2$ and 0.8 M NaOH at 80 °C for 50 – 90 min. The samples were carefully rinsed by deionized water and dried at 100 °C in air for 6 h. The roughness factor of the ZnO nanorod electrode was determined by SEM and BET analyses. The ZnO nanorod electrode prepared with the growth reaction time of 70 min at $[Zn(OAc)_2] = 1.0 \times 10^{-3}$ M was employed for the determination. The roughness factor of 12, determined by the SEM measurement, was the same as the value obtained from BET analysis.

To address the effects of electrode surface morphology on the photoelectrochemical properties, the ZnO nanoparticle electrode was also prepared by following previously reported procedure.[27] The particle size was adjusted to be 110 nm for the comparison of the ZnO nanorod electrode. The suspension was deposited on a FTO electrode by using doctor blade technique. The film was annealed at 400 °C for 30 min in air to form a nanostructured film electrode with a 1.8 μm-thick ZnO film for the comparison. The roughness factor of 40, determined by the SEM measurement, was identical to the value obtained from BET analysis.

Impedance of the ZnO nanorod electrode was measured using an ALS 630a electrochemical analyzer.[24,25,32-34] All measurements were performed in a three-electrode configuration using the ZnO nanorod working electrode, a Pt counter electrode and a Ag/AgCl (saturated KCl) reference electrode. The electrolyte was aqueous 0.1 M $Na_2B_4O_7$, the pH of which was adjusted with HCl and NaOH.

Modification of ZnO Nanorods and ZnO Nanoparticles with Fullerene Monolayer. ZnO nanorod and ZnO nanoparticle electrodes were modified with the fullerene monolayer to give FTO/ZnO-r/(C_{60}-acid)$_1$ and FTO/ZnO-p/(C_{60}-acid)$_1$. Firstly, FTO/ZnO-r or FTO/ZnO-p electrode was immersed into a DMF solution containing 0.2 M C_{60}-acid for 5 h. Then,

C_{60}-acid–coated FTO/ZnO-r or FTO/ZnO-p electrode was carefully rinsed with DMF repeatedly. The amounts of C_{60}-acid adsorbed on the electrodes were determined by measuring absorbance due to C_{60}-acid that was dissolved from the C_{60}-acid–coated FTO/ZnO-r or FTO/ZnO-p electrode into DMF containing 0.1 M HCl.

Formation of Porphyrin-Fullerene Multilayers on ZnO Electrodes. A known amount of ZnP, C_{60}-acid or the mixture in DMF was cast on the top surface of FTO/ZnO-r, FTO/ZnO-r/(C_{60}-acid)$_1$ or FTO/ZnO-p/(C_{60}-acid)$_1$ electrode. After standing for 90 sec, the electrode was spin-coated at 800 rpm for 60 seconds to yield the modified electrode.

Photoelectrochemical Measurements. Electrochemical measurements were carried out in a standard three-electrode system using CV-50W electrochemical analyzer.[11-14] The modified FTO/ZnO-r or FTO/ZnO-p as a working electrode was immersed into the electrolyte solution containing 0.5 M LiI and 0.01 M I_2 in acetonitrile. A Pt wire covered with a glass ruggin capillary, whose tip was located near the working electrode, and a Pt coil were used as quasi-reference and counter electrodes, respectively. The potential measured was converted to the normal hydrogen electrode (NHE) scale by adding +0.30 V. The stability of the reference electrode potential was confirmed under the experimental conditions. A 500 W xenon lamp (XB-50101AA-A; Ushio, Japan) was used as a light source. Potential versus current characteristics were measured with controlled-potential scan (0.001 V s^{-1}) under 0.5 Hz chopped white light (λ > 380 nm; input power: 37.4 mW cm^{-2}). The monochromatic light through a monochrometer (MC-10N; Ritsu, Japan) was illuminated on the modified area of the working electrode (0.20 cm^2) from the backside. The light intensity was monitored by an optical power meter (ML9002A; Anritsu, Japan) and corrected. The potential versus current characteristics of the porphyrin-fullerene modified electrodes were also measured with PEC-L11 solar simulator (Peccell, Japan) under standard two electrode conditions (100 mW cm^{-2} AM1.5). All experimental values are given as an average from five independent measurements.

Spectral Measurements. A pump-probe method was used to measure transient absorption spectra in sub-picosecond-nanosecond time domain. The measurements were carried out using the instrument described previously.[11d] The transient spectra were recorded by a CCD detector coupled with a monochromator in the visible and near infrared ranges. The second harmonic (420 nm) of Ti:sapphire laser was used for the excitation. A typical time resolution of the instrument was 200 fs (FWHM). Emission decays were measured using a time-correlated single photon counting (TCSPC) technique. The excitation wavelength was 405 nm and the

time resolution was 60-70 ps.[11d]

References and Notes

[1] (a) Hagfeldt, A.; Grätzel, M. *Acc. Chem. Res.* **2000**, *33*, 269. (b) Grätzel, M. *Nature* **2001**, *414*, 338. (c) Grätzel, M. *Pure Appl. Chem.* **2001**, *73*, 459. (d) Watson, D. F.; Meyer, G. J. *Ann. Rev. Phys. Chem.* **2005**, *56*, 119. (e) Anderson, N. A.; Lian, T. *Ann. Rev. Phys. Chem.* **2005**, *56*, 491. (f) Lewis, N. S. *Inorg. Chem.* **2005**, *44*, 6900. (g) Duncan, W. R.; Prezhdo, O. V. *Ann. Rev. Phys. Chem.* **2007***, 58*, 143. (h) Imahori, H.; Umeyama, T.; Ito, S. *Acc. Chem. Res.* **2009**, *42*, 1809.

[2] (a) Yu, G.; Gao, J.; Hummelen, J. C.; Wudl, F.; Heeger, A. J. *Science* **1995**, *270*, 1789. (b) Padinger, F.; Rittberger, R. S.; Sariciftci, N. S. *Adv. Funct. Mater.* **2003**, *13*, 85. (c) Hoppe, H.; Sariciftci, N. S. *J. Mater. Chem.* **2006**, *16*, 45. (d) Scharber, M. C.; Mühlbacher, D.; Koppe, M.; Denk, P.; Waldauf, C.; Heeger, A. J.; Brabec, C. J. *Adv. Mater.* **2006**, *18*, 789. (e) Kim, J. Y.; Lee, K.; Coates, N. E.; Moses, D.; Nguyen, T.–Q.; Dante, M.; Heeger, A. J. *Science* **2007**, *317*, 222. (f) Kim, K.; Liu, J.; Namboothiry, M. A. G.; Carroll, D. L. *Appl. Phys. Lett.* **2007**, *90*, 163511.

[3] (a) Shaheen, S. E.; Brabec, C. J.; Sariciftci, N. S.; Padinger, F.; Fromherz, T.; Hummelen, J. C. *Appl. Phys. Lett.* **2001**, *78*, 841. (b) Li, G.; Shrotriya, V.; Huang, J.; Yao, Y.; Moriarty, T.; Emery, K.; Yang, Y. *Nat. Mater.* **2005**, *4*, 864. (c) Ma, W.; Yang, C.; Gong, X.; Lee, K.; Heeger, A. J. *Adv. Funct. Mater.* **2005**, *15*, 1617. (d) Kim, Y.; Cook, S.; Tuladhar, S. M.; Choulis, S. A.; Nelson, J.; Durrant, J. R.; Bradley, D. D. C.; Giles, M.; Mcculloch, I.; Ha, C.–S.; Ree, M. *Nat. Mater.* **2006**, *5*, 197.

[4] (a) Schmidt-Mende, L.; Fechtenkötter, A.; Müllen, K.; Moons, E.; Friend, R. H.; MacKenzie, J. D. *Science* **2001**, *293*, 1119. (b) Halls, J. J. M.; Walsh, C. A.; Greenham, N. C.; Marseglia, E. A.; Friend, R. H.; Moratti, S. C.; Holmes, A. B. *Nature* **1995**, *376*, 498. (c) Sommer, M.; Lindner, S. M.; Thelakkat, M. *Adv. Funct. Mater.* **2007**, *17*, 1493.

[5] (a) Huynh, W. U.; Dittmer, J. J.; Alivisatos, A. P. *Science* **2002**, *295*, 2425. (b) Liu, J.; Tanaka, T.; Sivula, K.; Alivisatos, A. P.; Fréchet, J. M. J. *J. Am. Chem. Soc.* **2004**, *126*, 6550.

[6] (a) Hiramoto, M.; Fujiwara, H.; Yokoyama, M. *Appl. Phys. Lett.* **1991**, *58*, 1062. (b) Tsuzuki, T.; Shirota, Y.; Rostalski, J.; Meissner, D. *Solar Energy Mater. Solar Cells* **2000**, *61*, 1. (c) Gebeyehu, D.; Maennig, B.; Drechsel, J.; Leo, K.; Pfeiffer, M. *Solar Energy Mater. Solar Cells* **2003**, *79*, 81. (d) Xue, J.; Rand, B. P.; Uchida, S.; Forrest, S. R. *Adv. Mater.* **2005**, *17*, 66.

[7] (a) Wienk, M. M.; Kroon, J. M.; Verhees, W. J. H.; Knol, J.; Hummelen, J. C.; van Hal, P. A.; Janssen, R. A. J. *Angew. Chem., Int. Ed.* **2003**, *42*, 3371. (b) Eckert, J.–F.; Nicoud, J.–F.; Nierengarten, J.–F.; Liu, S. -G.; Echegoyen, L.; Barigelletti, F.; Armaroli, N.; Ouali, L.; Krasnikov, V.; Hadziioannou, G. *J. Am. Chem. Soc.* **2000**, *122*, 7467.

[8] (a) Imahori, H.; Fukuzumi, S. *Adv. Funct. Mater.* **2004**, *14*, 525. (b) Imahori, H. *J. Phys. Chem. B* **2004**, *108*, 6130. (c) Imahori, H. *J. Mater. Chem.* **2007**, *17*, 31. (d) Imahori, H. *Bull. Chem. Soc. Jpn.* **2007**, *80*, 621. (e) Umeyama, T.; Imahori, H. *Energy Environ. Sci.* **2008**, *1*, 120. (f) Umeyama, T.; Imahori, H. *J. Phys. Chem. C* **2009**, *113*, 9029. (g) Kamat, P. V. *J. Phys. Chem. C* **2007**, *111*, 2834. (h) Fukuzumi, S.; Kojima, T. *J. Mater. Chem.* **2008**, *18*, 1427.

[9] (a) Liu, Y.; Xiao, S.; Li, H.; Li, Y.; Liu, H.; Lu, F. Zhuang, J.; Zhu, D. *J. Phys. Chem. B* **2004**, *108*, 6256. (b) Huang, C.–H.; McClenaghan, N. D.; Kuhn, A.; Hofstraat, J. W.; Bassani, D. M.; *Org. Lett.* **2005**, *7*, 3409. (c) Imahori, H.; Liu, J.–C.; Hosomizu, K.; Sato, T.; Mori, Y.; Hotta, H.; Matano, Y.; Araki, Y.; Ito, O.; Maruyama, N.; Fujita, S. *Chem. Commun.* **2004**, 2066. (d) Imahori, H.; Liu, J.–C.; Hotta, H.; Kira, A.; Umeyama, T.; Matano, Y.; Li, G.; Ye, S.; Isosomppi, M.; Tkachenko, N. V.; Lemmetyinen, H. *J. Phys. Chem. B* **2005**, *109*, 18465. (e) Kira, A.; Tanaka, M.; Umeyama, T.; Matano, Y.; Yoshimoto, N.; Zhang, Y.; Ye, S.; Lehtivuori, H.; Tkachenko, N. V.; Lemmetyinen, H.; Imahori, H. *J. Phys. Chem. C* **2007**, *111*, 13618.

[10] (a) Ma, W.; Yang, C.; Gong, X.; Lee, K.; Heeger, A. J. *Adv. Funct. Mater.* **2005**, *15*, 1617. (b) Peet, J.; Kim, J. Y.; Coates, N. E.; Ma, W. L.; Moses, D.; Heeger, A. J. *Nat. Mater.* **2007**, *6*, 497. (c) Hoppe, M.; Niggemann, M.; Winder, C.; Kraut, J.; Hiesgen, R.; Hinch, A.; Meissner, D.; Sariciftci, N. S. *Adv. Funct. Mater.* **2004**, *14*, 1005. (d) Suemori, K.; Miyata, T.; Yokoyama, M.; Hiramoto, M. *Appl. Phys. Lett.* **2005**, *86*, 063509.

[11] (a) Hasobe, T.; Imahori, H.; Fukuzumi, S.; Kamat, P. V. *J. Phys. Chem. B* **2003**, *107*, 12105. (b) Kira, A.; Umeyama, T.; Matano, Y.; Yoshida, K.; Isoda, S.; Isosomppi, M.; Tkachenko, N. V.; Lemmetyinen, H.; Imahori, H. *Langmuir* **2006**, *22*, 5497. (c) Kang, S.; Umeyama, T.; Ueda, M.; Matano, Y.; Hotta, H.; Yoshida, K.; Isoda, S.; Shiro, M.; Imahori, H. *Adv. Mater.* **2006**, *18*, 2549. (d) Imahori, H.; Ueda, M.; Kang, S.; Hayashi, H.; Hayashi, S.; Kaji, H.; Seki, S.; Saeki, A.; Tagawa, S.; Umeyama, T.; Matano, Y.; Yoshida, K.; Isoda, S.; Shiro, M.; Tkachenko, N. V.; Lemmetyinen, H. *Chem.–Eur. J.* **2007**, *13*, 10182. (e) Kira, A.; Umeyama, T.; Matano, Y.; Yoshida, K.; Isoda, S.; Park, J.–K.; Kim, D.; Imahori, H. *J. Am. Chem. Soc.* **2009**, *131*, 3198.

[12] (a) Hasobe, T.; Kashiwagi, Y.; Absalom, M. A.; Sly, J.; Hosomizu, K.; Crossley, M. J.; Imahori, H.; Kamat, P. V.; Fukuzumi, S. *Adv. Mater.* **2004**, *16*, 975. (b) Hasobe, T.; Kamat, P. V.; Absalom, M. A.; Kashiwagi, Y.; Sly, J.; Crossley, M. J.; Hosomizu, K.;

Imahori, H.; Fukuzumi, S. *J. Phys. Chem. B* **2004**, *108*, 12865.

[13] Hasobe, T.; Kamat, P. V.; Troiani, V.; Solladié, N.; Ahn, T. K.; Kim, S. K.; Kim, D.; Kongkanand, A.; Kuwabata, S.; Fukuzumi, S. *J. Phys. Chem. B* **2005**, *109*, 19.

[14] (a) Hasobe, T.; Imahori, H.; Kamat, P. V.; Ahn, T. K.; Kim, S. K.; Kim, D.; Fujimoto, A.; Hirakawa, T.; Fukuzumi, S. *J. Am. Chem. Soc.* **2005**, *127*, 1216. (b) Imahori, H.; Fujimoto, A.; Kang, S.; Hotta, H.; Yoshida, K.; Umeyama, T.; Matano, Y.; Isoda, S. *Adv. Mater.* **2005**, *17*, 1727. (c) Imahori, H.; Fujimoto, A.; Kang, S.; Hotta, H.; Yoshida, K.; Umeyama, T.; Matano, Y.; Isoda, S.; Isosomppi, M.; Tkachenko, N. V.; Lemmetyinen, H. *Chem.-Eur. J.* **2005**, *11*, 7265. (d) Imahori, H.; Mitamura, K.; Umeyama, T.; Hosomizu, K.; Matano, Y.; Yoshida, K.; Isoda, S. *Chem. Commun.* **2006**, 406. (e) Imahori, H.; Mitamura, K.; Shibano, Y.; Umeyama, T.; Matano, Y.; Yoshida, K.; Isoda, S.; Araki, Y.; Ito, O. *J. Phys. Chem. B* **2006**, *110*, 11399. (f) Imahori, H.; Fujimoto, A.; Kang, S.; Hotta, H.; Yoshida, K.; Umeyama, T.; Matano, Y.; Isoda, S. *Tetrahedron* **2006**, *62*, 1955. (g) Hasobe, T.; Fukuzumi, S.; Hattori, S.; Kamat, P. V. *Chem.–Asian. J.* **2007**, *2*, 265.

[15] (a) Kang, Y.; Park, N.–G.; Kim, D. *Appl. Phys. Lett.* **2005**, *86*, 113101. (b) Wang, L.; Liu, Y. S.; Jiang, X.; Qin, D. H.; Cao, Y. *J. Phys. Chem. C* **2007**, *111*, 9538.

[16] (a) Wei, Q.; Hirota, K.; Tajima, K.; Hashimoto, K. *Chem. Mater.* **2006**, *18*, 5080. (b) Park, J. H.; Lee, T.–W.; Kang, M. G. *Chem. Commun.* **2008**, 2867.

[17] Kannan, B.; Castelino, K.; Majumdar, A. *Nano. Lett.* **2003**, 3, 1729.

[18] Galoppini, E.; Rochford, J.; Chen, H.; Saraf, G.; Lu, Y.; Hagfeldt, A.; Boschloo, G. *J. Phys. Chem. B* **2006**, *110*, 16159.

[19] Kaidashev, E. M.; Lorenz, M.; von Wenckstern, H.; Rahm, A.; Semmelhack, H.–C.; Han, K.–H.; Benndorf, G.; Bundesmann, C.; Hochmuth, H.; Grundmann, M. *Appl. Phys. Lett.* **2003**, *82*, 3901.

[20] Law, M.; Greene, L.; Johnson, J. C.; Saykally, R.; Yang, P. *Nat. Mater.* **2005**, *4*, 455.

[21] (a) Olson, D. C.; Piris, J.; Collins, R. T.; Shaheen, S. E.; Ginley, D. S. *Thin Solid Films* **2006**, *496*, 26. (b) Ravirajan, P.; Peiró, A. M.; Nazeeruddin, M. K.; Grätzel, M.; Bradley, D. D. C.; Durrant, J. R.; Nelson, J. *J. Phys. Chem. B* **2006**, *110*, 7635. (c) Takanezawa, K.; Hirota, K.; Wei, Q.–S.; Tajima, K.; Hashimoto, K. *J. Phys. Chem. C* **2007**, *111*, 7218. (d) Olson, D. C.; Lee, Y.–J.; White, M. S.; Kopidakis, N.; Shaheen, S. E.; Ginley, D. S.; Voigt, J. A.; Hsu, J. W. P. *J. Phys. Chem. C* **2007**, *111*, 16640. (e) Olson, D. C.; Lee, Y.–J.; White, M. S.; Kopidakis, N.; Shaheen, S. E.; Ginley, D. S.; Voigt, J. A.; Hsu, J. W. P. *J. Phys. Chem. C* **2008**, *112*, 9544.

[22] (a) White, M. S.; Olson, D. C.; Shaheen, S. E.; Kopidakis, N.; Ginley, D. S. *Appl. Phys. Lett.* **2006**, *89*, 143517. (b) Gilot, J.; Barbu, I.; Wienk, M. M.; Janssen, R. A. J. *Apply. Phys. Lett.* **2007**, *91*, 113520. (c) Yip, H.–L.; Hau, S. K.; Baek, N. S.; Jen, A. K.–Y. *Appl.*

Phys. Lett. **2008**, *92*, 193313.

[23] Green, L. E.; Law, M.; Goldberger, J.; Kim, F.; Johnson, J. C.; Zhang, Y. F.; Saykally, R. J.; Yang, P. D. *Angew. Chem., Int. Ed.* **2003**, *42*, 3031.

[24] (a) Fabregat-Santiago, F.; Garcia-Belmonte, G.; Bisquert, J.; Bogdanoff, P.; Zaban, A. *J. Electrochem. Soc.* **2003**, *150*, E293. (b) Chun, W.–J.; Ishikawa, A.; Fujisawa, H.; Takata, T.; Kondo, J. N.; Hara, M.; Kawai, M.; Matsumoto, Y.; Domen, K. *J. Phys. Chem. B* **2003**, *107*, 1798.

[25] (a) Matsumoto, Y.; Omae, K.; Watanabe, I.; Sato, E. *J. Electrochem. Soc.* **1986**, *133*, 711. (b) Matsumoto, Y. *J. Solid State Chem.* **1996**, *126*, 227.

[26] The fine structure (470-520 nm) of the photocurrent action spectra results from artifacts of our photocurrent measurement system.

[27] Hotta, H.; Kang, S.; Umeyama, T.; Matano, Y.; Yoshida, K.; Isoda, S.; Imahori, H. *J. Phys. Chem. B* **2005**, *109*, 5700.

[28] (a) Armaroli, N.; Marconi, G.; Echegoyen, L.; Bourgeois, J.–P.; Diederlich, F. *Chem.–Eur. J.* **2000**, *6*, 1629. (b) Tkachenko, N. V.; Guenther, C.; Imahori, H.; Tamaki, K.; Sakata, Y.; Fukuzumi, S.; Lemmetyinen, H. *Chem. Phys. Lett.* **2000**, *326*, 344. (c) Imahori, H.; Tkachenko, N. V.; Vehmanen, V.; Tamaki, K.; Lemmetyinen, H.; Sakata, Y.; Fukuzumi, S. *J. Phys. Chem. A* **2001**, *105*, 1750. (d) Armaroli, N.; Accorsi, G.; Song, F.; Palkar, A.; Echegoyen, L.; Bonifazi, D.; Diederlich, F. *ChemPhysChem* **2005**, *6*, 732.

[29] Geier, G. R.; Lindsey, J. S. *Tetrahedron* **2004**, *60*, 11435.

[30] (a) Hirsch, A,; Lamparth, I.; Karfunkel, H. R.; *Angew. Chem., Int., Ed. Engl.* **1994**, *33*, 437. (b) Hirsch, A.; Lamparth, I.; Grösser, T.; Karfunkel, H. R. *J. Am. Chem. Soc.* **1994**, *116*, 9385. (c) Lamparth, I.; Maichle-Mössmer, C.; Hirsch, A. *Angew. Chem., Int. Ed. Engl.* **1995**, *34*, 1607.

[31] (a) Song, J.; Lim, S. *J. Phys. Chem. C* **2007**, *111*, 596. (b) Li, C.; Fang, G.; Li, J.; Ai, L.; Dong, B.; Zhao, X. *J. Phys. Chem. C* **2008**, *112*, 990.

[32] Keis, K.; Vayssieres, L.; Rensmo, H.; Lindquist, S.–E.; Hagfeldt, A.; *J. Electrochem. Soc.* **2001**, *148*, A149.

[33] (a) Mott, N. F. *Proc. R. Soc. London, Ser. A* **1939**, *171*, 27. (b) Schottky, W. *Z. Phys.* **1942**, *118*, 539. (c) Bolts, J. M.; Wrighton, M. S. *J. Phys. Chem.* **1976**, *80*, 2641. (d) Watson, D. F.; Marton, A.; Stux, A. M.; Meyer, G. J. *J. Phys. Chem. B* **2004**, *108*, 11680.

[34] (a) Redmond, G.; O'Keeffe, A.; Burgess, C.; MacHale, C.; Fitzmaurice, D. *J. Phys. Chem.* **1993**, *97*, 11081. (b) Sayama, K.; Sugihara, H.; Arakawa, H. *Chem. Mater.* **1998**, *10*, 3825. (c) Noack, V.; Weller, H.; Eychmüller, A. *Phys. Chem. Chem. Phys.* **2003**, *5*, 384.

Chapter 6

Electron Transfer Cascade by Organic/Inorganic Ternary Composites of Porphyrin, Zinc Oxide Nanoparticle, and Reduced Graphene Oxide on a Tin Oxide Electrode that Exhibits Efficient Photocurrent Generation

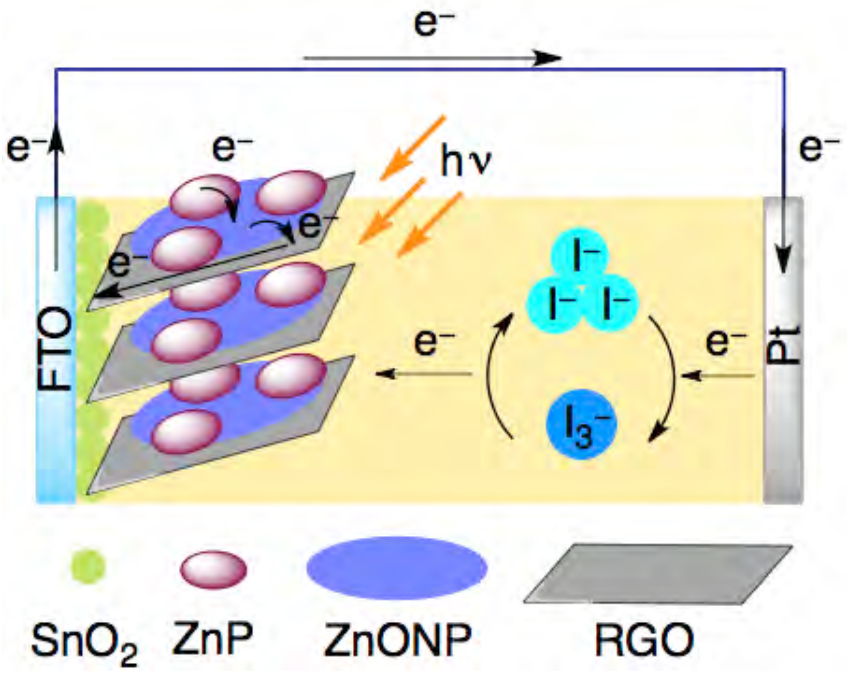

Abstract: A bottom-up strategy has been developed to construct a multiple electron transfer system composed of organic/inorganic ternary composites (porphyrin, zinc oxide nanoparticle, reduced graphene oxide) on a semiconducting electrode without impairing the respective donor-acceptor components. The hierarchical electron transfer cascade system exhibited remarkably high photocurrent generation with an incident-photon-to current efficiency of up to ca. 70%.

Introduction

Core to photosynthesis is the multistep electron transfer (ET) of supramolecularly assembled photofunctional chromophores in protein.[1] Such well-organized multistep ET systems allow photosynthesis to achieve efficient solar energy conversion. To mimic the multistep ET, various attempts have been made in artificial systems.[2] However, it is still a challenge to organize suitable organic/inorganic materials in a bottom-up manner, forming a hierarchical ET cascade on an electrode without impairing the intrinsic structures and functions. Here, we report an approach to construct a multistep ET system exhibiting efficient photocurrent generation. It utilizes porphyrin (ZnP, Figure 1),[3] zinc oxide nanoparticle (ZnONP), and reduced graphene oxide (RGO) as donor-acceptor components. They are sequentially organized on an electrode, that is, i) anchoring of the ZnONP on RGO as a two-dimensional (2D) scaffold, ii) adsorption of ZnP on the ZnONP on RGO, iii) electrophoretic deposition of the resulting organic/inorganic composites onto sintered SnO_2 nanoparticles on an FTO electrode (denoted as FTO/SnO_2) (Figure 1).

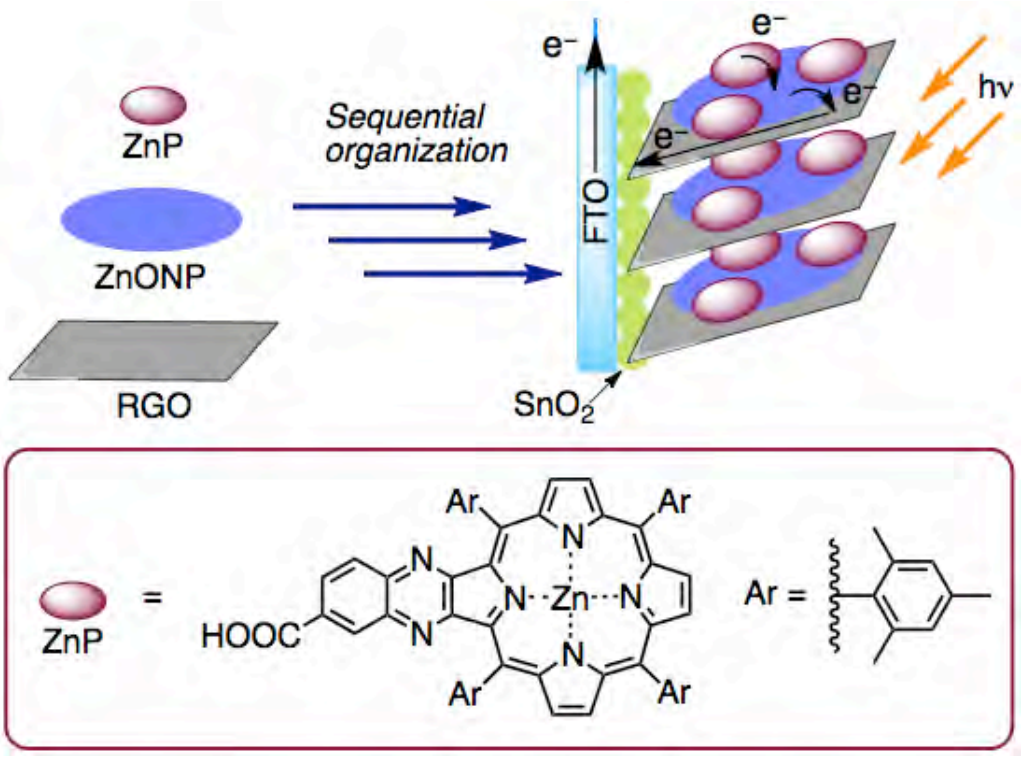

Figure 1. Hierarchical electron cascade system on an electrode.

An FTO/SnO_2 electrode was modified with ZnP, ZnONP, and RGO composites as follows. First, graphene oxide (GO) was prepared by the treatment of graphite powder with strong acid, followed by filtration.[4] This oxidation process introduces hydroxyl and epoxy groups into the graphene sheet, along with carbonyl and carboxyl groups into the edges.[5] The dried product was suspended in ethanol and mildly sonicated to disperse the GO sheets. Figure

2A displays an atomic force microscopy (AFM) image of GO after sonication process. The graphene sheets exist as fragments with an average area of 0.38 μm^2 owing to the oxidation process (Figure 2B). The average thickness of the GO sheet was determined as ca. 1.0 nm, which is consistent with that of fully exfoliated GO sheets[6] (Figure 2C).

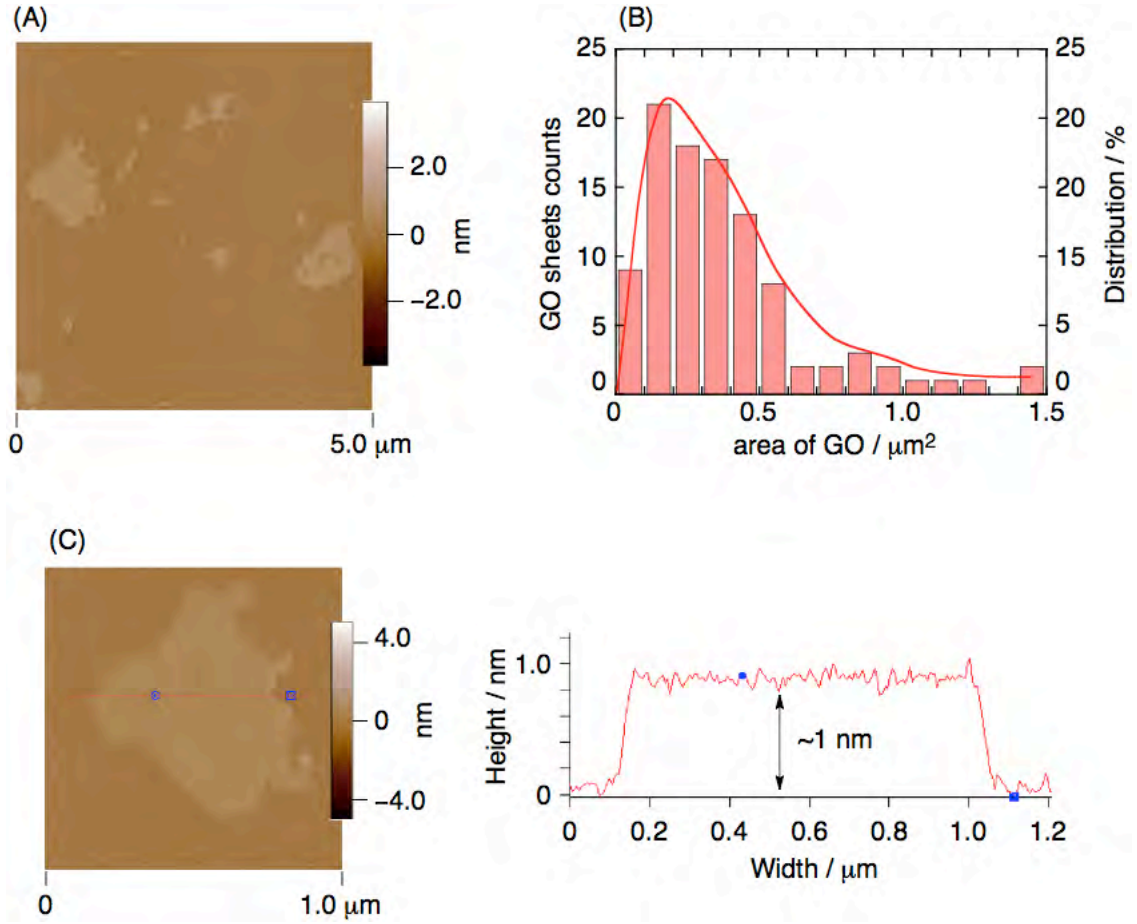

Figure 2. (A) AFM image of the GO. The GO sample was prepared by spin coating (2000 rpm, 60 s) on a freshly cleaved mica surface. (B) Area distribution of GO sheets measured by AFM. (C) Section profile of the AFM image of GO. The blue markers along the red trace represent a single GO sheet with a height of ~1 nm.

The next step is the anchoring of the ZnONP onto RGO. Initially, ZnONP were suspended in ethanol.[7] Then, an ethanol suspension of ZnONP with GO was mildly sonicated under N_2 saturated conditions to coat ZnONP on GO. UV-irradiation of GO–ZnONP has been previously shown to result in photocatalytic reduction of GO.[8] During the process, the suspension changed color from pale brown to pale black (Figure 3). This is rationalized by considerable restoration of the conjugated π network in graphene sheets via photoreduction by the excited ZnONP anchored on the graphene sheet. *n*-Heptane was added to the suspension so that RGO–ZnONP composites were precipitated from the solution. Transmission electron

microscopy (TEM) measurement was performed to evaluate the surface morphology. A typical TEM image of ZnONP anchored onto the RGO sheets is given in Figure 4. Both ZnONP and the edge of RGO are evident. ZnONP observed in the TEM image has small spherical structure with a size of ca. 7 nm.[7] It is noteworthy that the RGO sheets are densely covered by ZnONP. Such oxide nanoparticles anchored on the surfaces of RGO are favorable to prevent the exfoliated RGO sheets from direct stacking after photoreduction of GO.

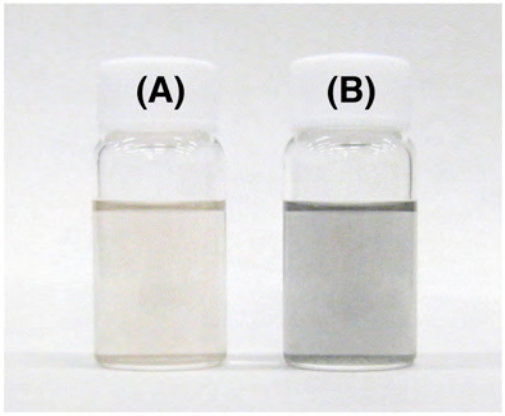

Figure 3. Photographs of the ethanol suspensions of GO and ZnONP (A) before, and (B) after the UV-irradiation for 1 h.

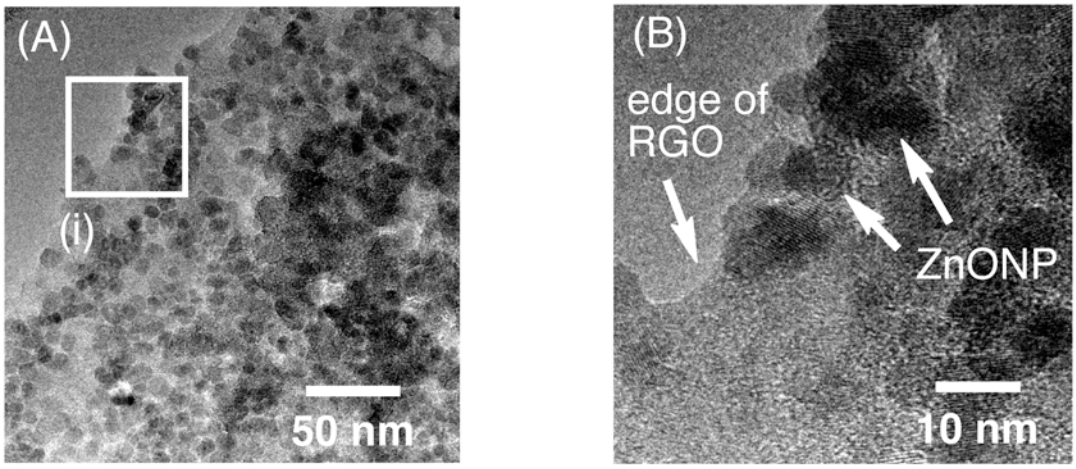

Figure 4. TEM images of ZnONP–RGO composite. The enlarged image of area (i) is shown as (B). A dilute sample was drop-cast on a carbon grid for the measurement.

Finally, the RGO–ZnONP composites were stirred in 0.2 mM ZnP methanol solution to adsorb ZnP molecules onto the RGO–ZnONP composites. The resulting composites were centrifuged and subsequently washed with methanol. To a toluene suspension of the composites, acetonitrile was injected rapidly, resulting in formation of the ternary composites $(RGO+ZnONP+ZnP)_m$ in the mixed solvents. The ternary composites were electrophoretically deposited onto a FTO/SnO_2 electrode (denoted as FTO/SnO_2/$(RGO+ZnONP+ZnP)_m$).[2e] The absorption spectrum of the FTO/SnO_2/$(RGO+ZnONP+ZnP)_m$ electrode shows the Soret and Q bands of ZnP, implying that ZnP molecules adsorb onto the composite film (Figure 5). Moreover, the FE-SEM and TEM measurements also reveal that the RGO sheets on the

electrode are wrapped with ZnO nanoparticles that are further coated with ZnP molecules (Figure 6). These results suggest that the RGO sheets serve as a 2D network, which would be able to facilitate electron flow from the ZnONP–ZnP composites to the FTO/SnO_2 electrode (vide infra). To further examine the morphology of the FTO/SnO_2/$(RGO+ZnONP+ZnP)_m$ electrode, cross-sectional FE-SEM measurement was employed.

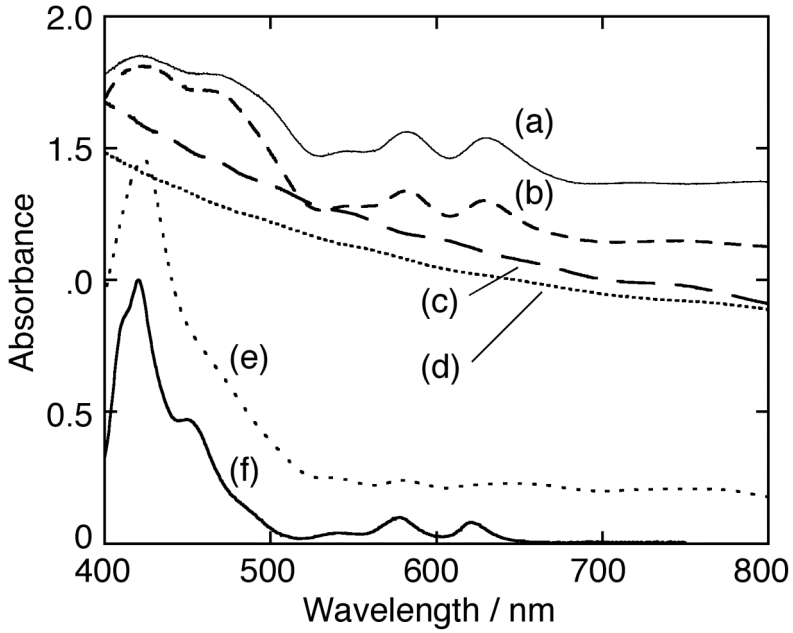

Figure 5. UV-visible absorption spectra of the (a) FTO/SnO_2/$(RGO+ZnONP+ZnP)_m$ electrode (thin solid line), and (b) FTO/SnO_2/$(ZnONP+ZnP)_m$ electrode (short dashed line), (c) FTO/SnO_2/$(RGO+ZnONP)_m$ electrode (long dashed line), (d) FTO/SnO_2/$(ZnONP)_m$ electrode (densely dotted line), (e) FTO/SnO_2/$(ZnP)_m$ electrode (sparsely dotted line), and (f) ZnP in ethanol (bold solid line).

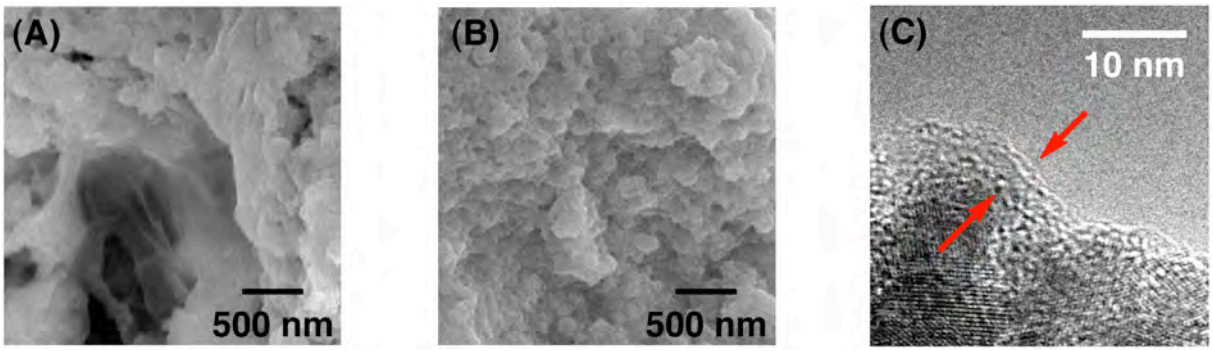

Figure 6. FE-SEM images of (A) the $(RGO–ZnONP–ZnP)_m$ composite and (B) the $(ZnONP–ZnP)_m$ composite on the FTO/SnO_2 electrode, and (C) TEM image of ZnONP modified with ZnP molecules on RGO. The red arrows show the ZnP layer. ZnONP exhibits distinct lattice fringes and well-developed patterns.

It is evident that the $(RGO+ZnONP+ZnP)_m$ composites are firmly deposited on the FTO/SnO_2 electrode (Figure 7). More importantly, we found that the RGO sheets covered by the ZnONP–ZnP composites facilitate electron transport within the composite film. The RGO sheets are randomly distributed in the composite film and this random network can still facilitate ET to the electrode after collecting electrons in the RGO sheets.[9] These results corroborate an electron-transport pathway to the FTO/SnO_2 electrode through the 2D RGO sheets incorporated during electrophoretic deposition method. This strategy is analogous to one dimensional (1D) fullerene–carbon nanotube (CNT) composite system employed in earlier study.[10]

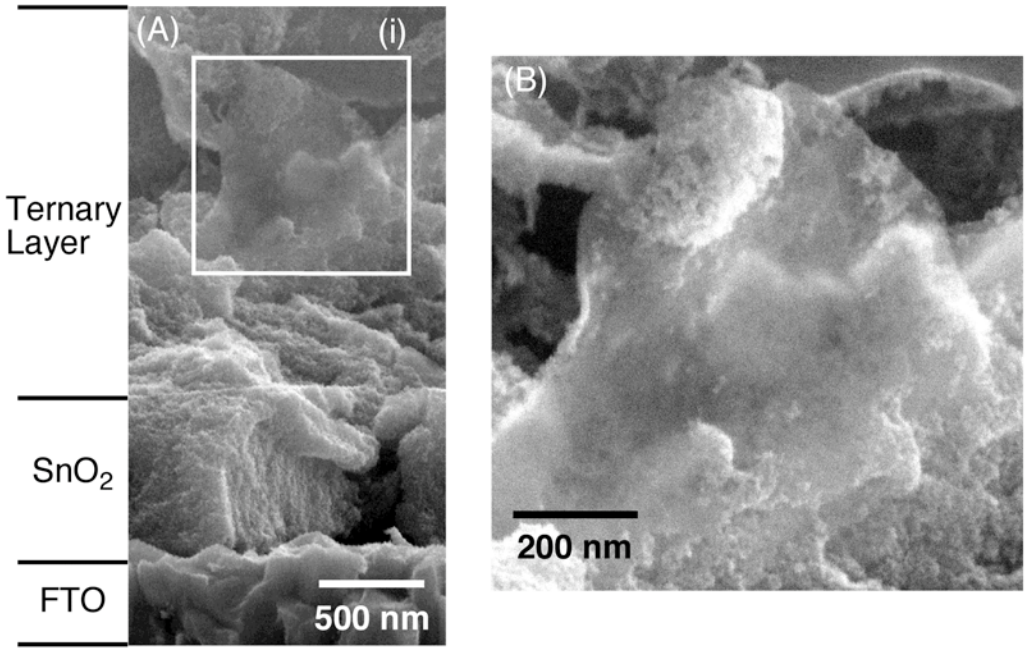

Figure 7. (A) Cross-sectional FE-SEM images of the $FTO/SnO_2/(RGO–ZnONP–ZnP)_m$ electrode. The enlarged image of area (i) is shown as panel (B).

To demonstrate the effects of the ET cascade on the photocurrent generation efficiency, we compared the incident photon-to-current efficiency (IPCE) of the photoelectrochemical devices. Figure 8 depicts the photocurrent action spectra for the modified electrodes. The action spectra closely resemble the corresponding absorption spectra of the electrodes (Figure 5). The IPCE value of the $FTO/SnO_2/(ZnP)_m$ device is considerably larger than that of the $FTO/SnO_2/(ZnONP)_m$ and $FTO/SnO_2/(RGO+ZnONP)_m$ electrodes. This implies that direct electron injection from the porphyrin excited singlet state (^{1}ZnP*) to a conduction band (CB) of the SnO_2 electrode has a significant impact on the photocurrent generation (Scheme 1) as established previously.[2d,11] The IPCE value of the $FTO/SnO_2/(ZnONP+ZnP)_m$ electrode is

enhanced remarkably compared with the FTO/SnO_2/$(ZnP)_m$ electrode. This improvement can be explained by the large contribution to the photocurrent from an additional pathway that electron injection occurs from the ^{1}ZnP* to the CB of the SnO_2 via ZnONP. More importantly, the IPCE value of the FTO/SnO_2/$(RGO+ZnONP+ZnP)_m$ electrode is further enhanced relative to the FTO/SnO_2/$(ZnONP+ZnP)_m$ electrode. This result unambiguously exemplifies that electron injection takes place from the ^{1}ZnP* to the CB of the SnO_2 via ZnONP and/or RGO, improving the photocurrent generation. It should be emphasized that the maximum IPCE value of the FTO/SnO_2/$(RGO+ZnONP+ZnP)_m$ electrode reaches ca. 70% at 440 nm under an applied potential of 0.05 V vs SCE. Considering that the adsorbed amounts of the ZnP molecules on the composites (6.0×10^{-8} mol cm^{-2}) are comparable for the FTO/SnO_2/$(RGO+ZnONP+ZnP)_m$ and FTO/SnO_2/$(ZnONP+ZnP)_m$ electrodes, we can safely conclude that the improvement result from the difference in the electron injection efficiency and/or electron collection efficiency due to the presence of the RGO and the better configuration for the photocurrent generation. These results imply that the hierarchical ET cascade system is responsible for the occurrence of multistep ET on the electrode, leading to efficient photocurrent generation through the ZnONP and RGO sheets in the device.

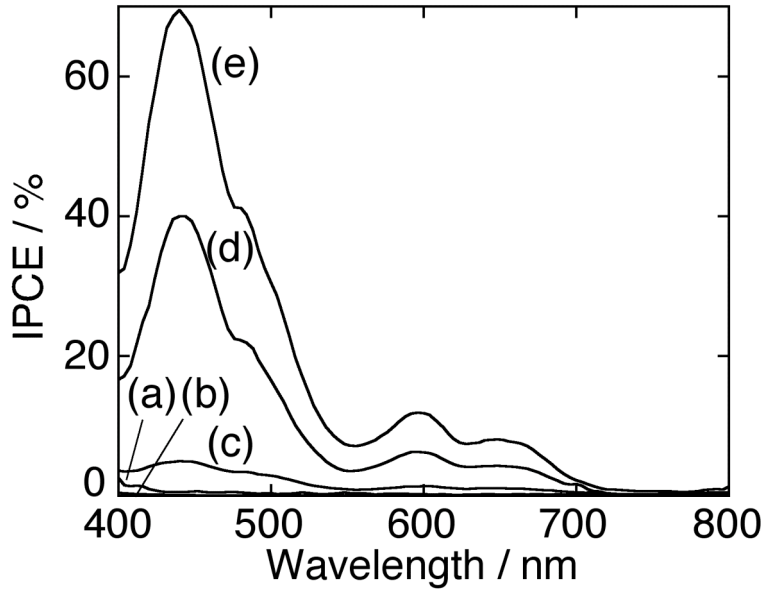

Figure 8. Photocurrent action spectra of the (a) FTO/SnO_2/$(ZnONP)_m$, (b) FTO/SnO_2/$(RGO+ZnONP)_m$, (c) FTO/SnO_2/$(ZnP)_m$, (d) FTO/SnO_2/$(ZnONP+ZnP)_m$, (e) FTO/SnO_2/$(RGO+ZnONP+ZnP)_m$ electrodes. Applied potential: 0.05 V vs SCE; 0.5 M LiI and 0.01 M I_2 in acetonitrile as an electrolyte. IPCE values were calculated by normalizing the photocurrent densities for incident light energy and intensity and by use of the expression: IPCE (%) = $100 \times 1240 \times i/(W_{in} \times \lambda)$ = (light harvesting efficiency) × (electron injection efficiency) × (electron collection efficiency), where i is the photocurrent density (A cm^{-2}), W_{in} is the incident light intensity (W cm^{-2}), and λ is the excitation wavelength (nm).

Scheme 1. Schematic Illustration for the Energy Diagram

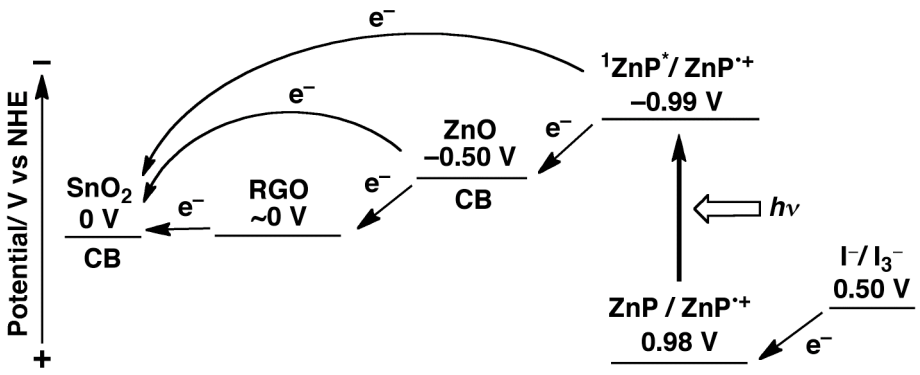

To shed light on the effect of the RGO on the photocurrent generation, we conducted photovoltage measurements by monitoring the cell potential response to on-off cycles of visible light illumination. Band gap excitation of ZnONP using UV-irradiation was used solely for the reduction of GO in the initial ZnONP–GO suspension. Photoelectrochemical characterization was carried out using visible light irradiation thus avoiding any direct excitation of ZnONP. Under open circuit conditions, the electrons are accumulated in the film by irradiation and then equilibrated with redox couple (I^-/I_3^-) in the electrolyte. Additionally, the charges in the device are retained within the film for longer time in deaerated solution. The rise in potential following the irradiation is observed in the FTO/SnO_2/(RGO+ZnONP+ZnP)$_m$ and the FTO/SnO_2/(ZnONP+ZnP)$_m$ electrodes in an acetonitrile solution containing 0.1 M *n*-tetrabutylammonium perchlorate (TBAP) as an electrolyte (Figure 9). In a previously reported CNT–TiO_2 composite system, the magnitude of the photovoltage of the FTO/CNT/TiO_2 electrode is lower than that of the FTO/TiO_2 electrode.[12] This reflects electron transport from TiO_2 to CNT, resulting in the lowering of Fermi level of the FTO/CNT/TiO_2 electrode. The photovoltage is similar in the FTO/SnO_2/(RGO+ZnONP+ZnP)$_m$ and FTO/SnO_2/(ZnONP+ZnP)$_m$ electrodes as the Fermi level of the working electrode is mainly dictated by the SnO_2 film. The slow rise of photovoltage of the FTO/SnO_2/(RGO+ZnONP+ZnP)$_m$ electrode is indicative of the fact that additional time required electron equilibration in the ZnONP–RGO composite. In addition, the photovoltage decay of the FTO/SnO_2/(RGO+ZnONP+ZnP)$_m$ electrode recorded upon stopping the illumination is slower than that of the FTO/SnO_2/(ZnONP+ZnP)$_m$ electrode. The photovoltage decay directly reflects the longer lifetime of accumulated electrons into the electrolyte. Since, RGO can be regarded as an electron storage material[12] similar to that of CNT,[12a] we expect charge recombination at the electrolyte interface to be less favored.[9,14] Given that the CB of SnO_2 is 0 V vs NHE and the Fermi level of RGO is ~0 V vs NHE,[15] difference in the photovoltage decay rate is expected to be small. The presence of RGO influences the overall

performance by (i) accepting electrons from the ZnONP–ZnP composites and (ii) providing a medium to store and shuttle electrons within the composite film,[13] as seen in CNT–TiO_2 composite system.[12] These results also support the occurrence of multistep ET cascade on the electrode.

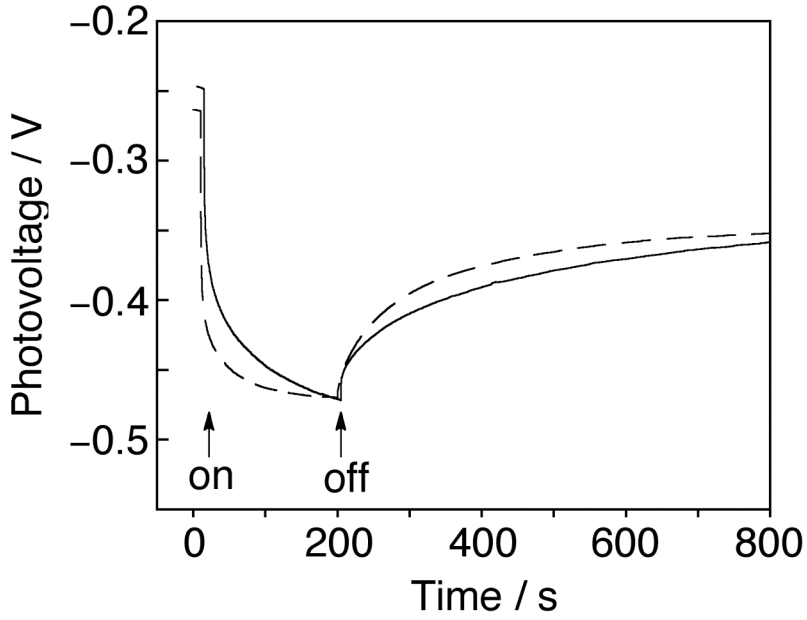

Figure 9. Photovoltage response of the FTO/SnO_2/(RGO+ZnONP+ZnP)$_m$ (solid line) and FTO/SnO_2/(ZnONP+ZnP)$_m$ (dashed line) electrodes under white light illumination (input power: 37.4 mW cm^{-2}, λ > 380 nm) in a deaerated acetonitrile solution containing 0.1 M TBAP.

On the basis of the film structures and the photoelectrochemical properties of the FTO/SnO_2/(RGO+ZnONP+ZnP)$_m$ systems together with the previously established photocurrent generation mechanism in analogous porphyrin-semiconducting oxide composites,[2e,11] we can propose a photocurrent generation diagram as illustrated in Scheme 1. First, electron injection from ^{1}ZnP* into the CB of ZnONP (–0.5 V vs NHE)[16] takes place,[17] in addition to minor electron injection from ^{1}ZnP* to the Fermi level of RGO (~0 V vs NHE)[15] and/or the CB of SnO_2 (0 V vs NHE).[2e,11] In the former case, the collected electrons in the CB of ZnONP are transferred into the CB of SnO_2 through the 2D RGO network in the ZnONP–ZnP composites, together with electron injection from ZnONP to the CB of SnO_2. Then, the oxidized porphyrin ($ZnP/ZnP^{+\bullet}$ = 0.98 V vs NHE)[3] undergoes ET reduction with the iodide (I^-/I_3^- = 0.5 V vs NHE)[2e,11] in the electrolyte solution, resulting in the photocurrent generation. Thus, the hierarchical ET cascade system for the FTO/SnO_2/(RGO+ZnONP+ZnP)$_m$ system is responsible for the high photocurrent generation.

In conclusion, we have successfully developed a promising strategy for constructing the

efficient hierarchical ET cascade system on a semiconducting electrode in a bottom-up manner by using RGO as a 2D sheet to anchoring organic/inorganic hybrid materials for the first time. The electrophoretically deposited film exhibited remarkably high photocurrent generation (IPCE = 70%) compared with the reference device without RGO sheets as well as ZnONP. These results will provide fundamental clue for the bottom-up construction of artificial photosynthetic systems utilizing organic/inorganic assemblies.

Experimental Section

General. UV-visible absorption spectra were obtained on a Perkin Elmer Lambda 900UV/vis/NIR spectrometer. AFM measurements were carried out using a MFP-3D (Asylum Research) in the AC mode. TEM micrographs were measured by applying a drop of the sample to a carbon grid. Images were recorded using a JEM-2200FS transmission electron microscope (JEOL). FE-SEM micrographs were recorded using JSM-6500F (JEOL). Transparent conducting glasses (FTO, SnO_2:F, 9.4 Ω/sq) were commercially available from Asahi Glass.

Synthesis and Materials. Synthesis of ZnP was carried out according to the previously reported method.[3] All solvents and chemicals were of reagent grade quality, purchased commercially and used without further purification.

Preparation of SnO_2 films on FTO electrodes. A 15% SnO_2 colloidal solution (particle size = 15 nm; Alfa Aesar) was deposited on the FTO electrode using the doctor blade technique. The electrode was annealed at 673 K for 1 h. The thickness (500 nm) of the SnO_2 film on FTO was estimated by FE-SEM measurements. Thin SnO_2 film for the photovoltage measurements was prepared by the spray-coated method described previously report.[18] The thickness (100 nm) of the SnO_2 film on FTO was estimated by using surface roughness/profile measuring instrument (SURFCOM 130A, ACCRETECH).

Synthesis of GO. GO was prepared by Hummer's method. First, the graphite powder (200 mg, Alfar Aesar) was oxidized: 200 mg of $NaNO_3$ and 9.2 mL of concentrated H_2SO_4 were added slowly in reaction vessel kept in an ice bath. This mixture was sonicated for 10 min. Then, the mixture was continuously stirred in an ice bath while 1.2 g of $KMnO_4$ was added slowly over 1h. Next, the reaction vessel was removed from the ice bath, and the temperature of the mixture was brought up to ~35ºC. After the mixture was stirred for 2 h, it changed color to brownish-gray. 100 mL of water was slowly added to the mixture, again stirring continuously

for 30 min. After adding 100 mL water with 3% H_2O_2 to the mixture, resulting oxidized material was filtered. Finally, the oxidized material was washed with 1 M HCl and deionized water repeatedly, and then dried.

Preparation of ZnO colloidal suspension in ethanol. A batch of ZnO colloidal suspension was obtained by dissolving 110 mg (0.5 mM) of $Zn(OAc)_2 \cdot 2H_2O$ in 25 mL ethanol with sonication for 5 min at 0ºC. 21 mg (0.5 mM) of $Li(OH) \cdot H_2O$ was then added and sonication was continued for another 5 min at 0ºC. A stable and optically transparent ZnO suspension was obtained. All of the experiments in the present study were carried out after stabilizing the colloidal ZnO for 2 h.

Preparation of the RGO–ZnONP–ZnP composite. 0.75 mg of GO was added to the ZnO colloidal suspension (resulting solution: 0.03 mg mL^{-1} GO and 20 mM ZnONP in ethanol) and sonicated for 20 min to produce dispersion of GO sheets coated with ZnONP. After purging the above ethanol solution with N_2 for 20 min, UV-irradiation of the ethanol solution was performed using high-pressure Hg arc lamp for 1 h. The solution was kept stirring during UV irradiation. The change in color from light brown to light black can be seen after UV-irradiation, suggesting conversion of GO to RGO. Then, four times the volume of *n*-heptane was added to the above solution so that ZnONP were precipitated out from the solution. This resulting precipitate was allowed to settle over night. The solvent was removed by centrifugation. 10 mL of 0.2 mM ZnP methanol solution was added, and then stirred for 1 h. The resulting composites were centrifuged and subsequent washed with methanol for several times.

Preparation of composite film. 10 mL of toluene was added to the RGO–ZnONP–ZnP composites. The colloid solution of RGO–ZnONP–ZnP composites was prepared in a 1 cm cuvette by injecting acetonitrile (1.2 mL) into a solution of the composites in toluene (0.6 mL, toluene/acetonitrile = 1:2, v/v). Two electrodes (i.e., FTO and FTO/SnO_2) were inserted into the cuvette with keeping at a distance of 6.0 mm by a Teflon spacer. A dc voltage (200 V) was applied for 2 min between these two electrodes using a power supply (ATTA model AE-8750). The deposition of the film could be visibly confirmed as the suspension became colorless with the simultaneous colorization of the FTO/SnO_2 electrode.

Determination of amount of ZnP adsorbed on the FTO/SnO_2/(RGO+ZnONP+ZnP)$_m$ and FTO/SnO_2/(ZnONP+ZnP)$_m$ electrode. The amount of ZnP molecule adsorbed on a FTO/SnO_2 electrode was determined by measuring absorbances due to ZnP [at 427 nm, ε

(DMF/0.1 M NaOH aqueous solution = 4 : 1) = 1.37×10^5 M^{-1} cm^{-1}], which were dissolved from the electrode surface into DMF containing 0.1 M NaOH aqueous solution.

Photoelectrochemical measurements. Photocurrent generation efficiencies of the electrode were measured in a one-compartment Pyrex UV cell (5 mL) with an electrolyte solution containing 0.5 M LiI and 0.01 M I_2 in acetonitrile. The samples were excited with monochromatic light using a 500 W Xe arc lamp (Ritsu UXL-500D-0) coupled with a monochromator (Ritsu MC-10N). The illuminated area on the modified surface was 0.20 cm^2. The light intensity was modulated with neutral density filters (HOYA). The film was immersed into the electrolyte solution as a working electrode. The photocurrent was measured in a three-electrode arrangement, the modified SnO_2 working electrode, a platinum wire counter electrode, and an I^-/I_3^- reference electrode using an ALS 630a electrochemical analyzer. The light intensity was monitored by an optical power meter (Anritsu ML9002A) and corrected. The I^-/I_3^- reference electrode was made from platinum wire covered with glass luggin capillary filled with the acetonitrile solution containing 0.5 M LiI and 0.01 M I_2. The potential measured was converted to the saturated calomel electrode (SCE) scale by adding +0.05 V. The stability of the reference electrode potential was confirmed under the experimental conditions.

Photovoltage measurements were also carried out in a one-compartment Pyrex UV cell (5 mL) with an electrolyte solution containing 0.1 M *n*-tetrabutylammonium perchlorate in acetonitrile. A 500 W xenon lamp (XB-50101AA-A; Ushio, Japan) was used as a light source. The illuminated area on the modified surface was 0.20 cm^2. The film was immersed into the electrolyte solution as a working electrode. The photovoltage was measured in a three-electrode arrangement, the modified SnO_2 working electrode, a platinum wire counter electrode, and an Ag/AgCl reference electrode using an ALS 630a electrochemical analyzer. In photovoltage measurements, we used thin SnO_2 layer (100 nm) as the working electrode prepared by spray coating method. The preparation method of SnO_2 electrode did not affect the cell performance of the modified electrode. The light intensity was monitored by an optical power meter (Anritsu ML9002A) and corrected. The stability of the reference electrode potential was confirmed under the experimental conditions.

References and Notes

[1] In Molecular Mechanism of Photosynthesis; Blankenship, R. E. Ed.; Willey-Blackwell: Dordrecht, **2002**.

[2] (a) Sun, L. C.; Hammarström, L.; Åkermark, B.; Styring, B. *Chem. Soc. Rev.* **2001**, *30*, 36.

(b) Alstrum-Acevedo, J. H.; Brennaman, M. K.; Meyer, T. J. *Inorg. Chem.* **2005**, *44*, 6802. (c) Sheeney-Haj-Ichia, L.; Basnar, B.; Willner, I. *Angew. Chem., Int. Ed.* **2005**, *44*, 78. (d) Sisson, A. L.; Sakai, N.; Banerji, N.; Fürstenberg, A.; Vauthey, E.; Matile, S. *Angew. Chem., Int. Ed.* **2008**, *47*, 3727. (e) Imahori, H.; Umeyama, T. *J. Phys. Chem. C* **2009**, *113*, 9029. (f) Gust, D.; Moore, T. A.; Moore, A. L. *Acc. Chem. Res.* **2009**, *42*, 1890. (g) Wasielewski, M. R. *Acc. Chem. Res.* **2009**, *42*, 1910. (h) D'Souza, F.; Ito, O. *Chem. Commun.* **2009**, 4913. (i) Ardo, S.; Meyer, G. J. *Chem. Soc. Rev.* **2009**, *38*, 115. (j) Schulz-Drost, C.; Sgobba, V.; Gerhards, C.; Leubner, S.; Calderon, R. M. K.; Ruland, A.; Guldi, D. M. *Angew. Chem., Int. Ed.* **2010**, *49*, 6425. (k) Sagawa, T.; Yoshikawa, S.; Imahori, H. *J. Phys. Chem. Lett.* **2010**, *1*, 1020. (l) D'Souza, F.; Sandanayaka, A. S. D.; Ito, O. *J. Phys. Chem. Lett.* **2010**, *1*, 2586. (m) Sakai, N.; Bhosale, R.; Emery, D.; Mareda, J.; Matile, S. *J. Am. Chem. Soc.* **2010**, *132*, 6923. (n) Bhosale, R.; Misek, J.; Sakai, N.; Matile, S. *Chem. Soc. Rev.* **2010**, *39*, 138. (o) Kamat, P. V. *J. Phys. Chem. Lett.* **2011**, *2*, 242.

[3] Eu, S.; Hayashi, S.; Umeyama, T.; Matano, Y.; Araki, Y.; Imahori, H. *J. Phys. Chem. C* **2008**, *112*, 4396.

[4] Hummers, W. S.; Offeman, R. E. *J. Am. Chem. Soc.* **1958**, *80,* 1339.

[5] Lerf, A.; He, H.; Forster, M.; Klinowski, J. *J. Phys. Chem. B* **1998**, *102*, 4477.

[6] (a) Stankovich, S.; Dikin, D. A.; Piner, R. D.; Kohlhass, K. A.; Kleinhammes, A.; Jia, Y.; Wu, Y.; Nguyen, S. T.; Ruoff, R. S. *Carbon* **2007**, *45*, 1558. (b) Gómez-Navarro, C.; Weitz, R. T.; Bittner, A. M.; Scolari, M.; Mews, A.; Burghard, M.; Kern, K. *Nano Lett.* **2007**, *7*, 3499.

[7] Spanhel, L.; Anderson, M. A. *J. Am. Chem. Soc.* **1991**, *113*, 2826.

[8] (a) Williams, G.; Seger, B., Kamat, P. V. *ACS Nano* **2008**, *2*, 1487. (b) Williams, G.; Kamat, P. V. *Langmuir* **2009**, *25*, 13869.

[9] Ng, Y. H.; Lightcap, I. V.; Goodwin, K.; Matsumura, M.; Kamat. P. V. *J. Phys. Chem. Lett.* **2010**, *1*, 2222.

[10] Umeyama, T.; Tezuka, N.; Fujita, M.; Hayashi, S.; Kadota, N.; Matano, Y.; Imahori, H. *Chem.–Eur. J.* **2008**, *14*, 4875.

[11] (a) Imahori, H.; Liu, J.–C.; Hotta, H.; Kira, A.; Umeyama, T.; Matano, Y.; Li, G.; Ye, S.; Isosomppi, M.; Tkachenko, N. V.; Lemmetyinen, H. *J. Phys. Chem. B* **2005**, *109*, 18465. (b) Imahori, H. *J. Mater. Chem.* **2007**, *17*, 31. (b) Kira, A.; Umeyama, T.; Matano, Y.; Yoshida, K.; Isoda, S.; Park, J. K.; Kim, D.; Imahori, H. *J. Am. Chem. Soc.* **2009**, *131*, 3198.

[12] (a) Kongkanand, A.; Kamat, P. V. *ACS Nano* **2007**, *1*, 13. (b) Brown, P.; Takechi, K.; Kamat, P. V. *J. Phys. Chem. C* **2008**, *112*, 4776.

[13] Lightcap, I. V.; Kosel, T. H.; Kamat, P. V. *Nano Lett.* **2010**, *10*, 577.

[14] Wojcik, A.; Kamat, P. V. *ACS Nano* **2010**, *4*, 6697.

[15] Czerw, R.; Foley, B.; Tekleab, D.; Rubio, A.; Ajayan, P. M.; Carroll, D. L. *Phys. Rev. B* **2002**, *66*, 033408.

[16] Subramanian, V.; Wolf, E. E.; Kamat, P. V. *J. Phys. Chem. B* **2003**, *107*, 7479.

[17] We performed transient absorption measurements for the FTO/SnO_2/(RGO+ZnONP+ZnP)$_m$ and FTO/SnO_2/(ZnONP+ZnP)$_m$ electrodes using the femtosecond pump-probe method with the excitation wavelength of 415 nm. However, formation of the charge-separated state in the mixed films could be detected because of a poor signal-to-noise ratio and the instability of the samples under the experimental conditions.

[18] (a) Kang, S.; Umeyama, T.; Ueda, M.; Matano, Y.; Hotta, H.; Yoshida, K.; Isoda, S.; Shiro, M.; Imahori, H. *Adv. Mater.* **2006**, *18*, 2549. (b) Imahori, H.; Ueda, M.; Kang, S.; Hayashi, H.; Hayashi, S.; Kaji, H.; Seki, S.; Saeki, A.; Tagawa, S.; Umeyama, T.; Matano, Y.; Yoshida, K.; Isoda, S.; Shiro, M.; Tkachenko, N. V.; Lemmetyinen, H. *Chem.–Eur. J.* **2007**, *13*, 10182.

Chapter 7

Segregated Donor-Acceptor Columns in Liquid Crystals that Exhibit Highly Efficient Ambipolar Transport

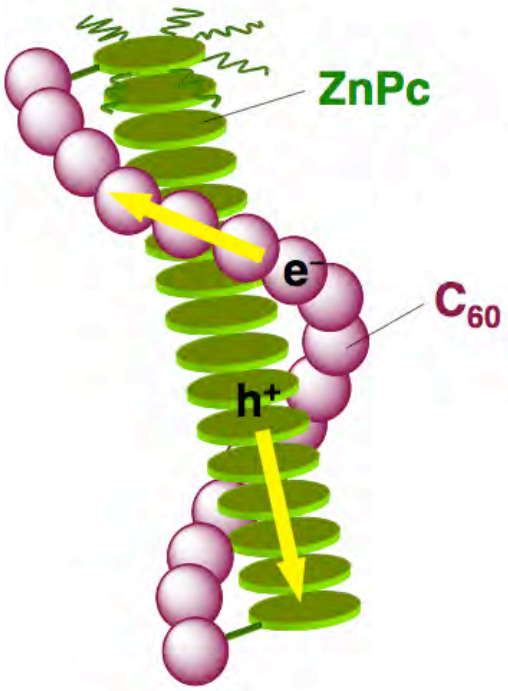

Abstract: Liquid crystalline donor (i.e., phthalocyanine) was covalently linked to acceptor (i.e, fullerene) to achieve efficient charge-transporting properties in a liquid crystalline phase. The columnar structure exhibited highly efficient ambipolar charge-transporting character, demonstrating the potential utility of the strategy in organic electronics.

Introduction

Recently liquid crystals (LCs) have drawn much attention as a promising type of molecular semiconductor because of the potential utility in organic electronics including organic thin-film transistors, organic light-emitting diodes, and organic solar cells.[1] Disc-like molecules functionalized with alkyl groups self-assemble into supramolecular one-dimensional (1D) columns that further self-organize into hexagonal, rectangular, and nematic phases as discotic liquid crystals (DLCs).[2] Hierarchical self-assembly from simple disc-like molecules to DLCs through the formation of 1D columns is a highly appealing strategy to organize donor-acceptor (D-A) molecules,[3] i.e., forming D-A heterojunction structures exhibiting ambipolar charge-transporting properties[4] and efficient photocurrent generation.[5]

As a donor phthalocyanines are some of the most widely investigated self-assembling molecules in DLCs.[2,6] On the other hand, as an acceptor fullerenes have been successfully incorporated into LC systems to give various LC phases.[7] Besides, some of the covalently functionalized fullerenes are known to form different columnar phases.[8] Therefore, a simultaneous application of phthalocyanine and fullerene to LCs is highly attractive to form such D-A heterojunction structures. Nevertheless, so far there have been a few examples of mesogenic phthalocyanine-fullerene linked dyads.[9] As such, relationships between the LC structures and charge-transporting properties have yet to be examined.

Herein we report the synthesis and LC and charge-transporting properties of a zinc phthalocyanine (ZnPc)-C_{60} dyad (Figure 1). Six 4-dodecyloxyphenoxy groups were introduced into the periphery of the central core to form discotic columnar structure of the ZnPc.[10] C_{60} was also tethered to the ZnPc core via a short semiflexible bridge. We expected that due to the strong π–π interaction between the C_{60} molecules and the covalent linkage the C_{60} molecules would be arranged successively along the ZnPc 1D column, leading to D-A bicontinuous structure in the LCs.

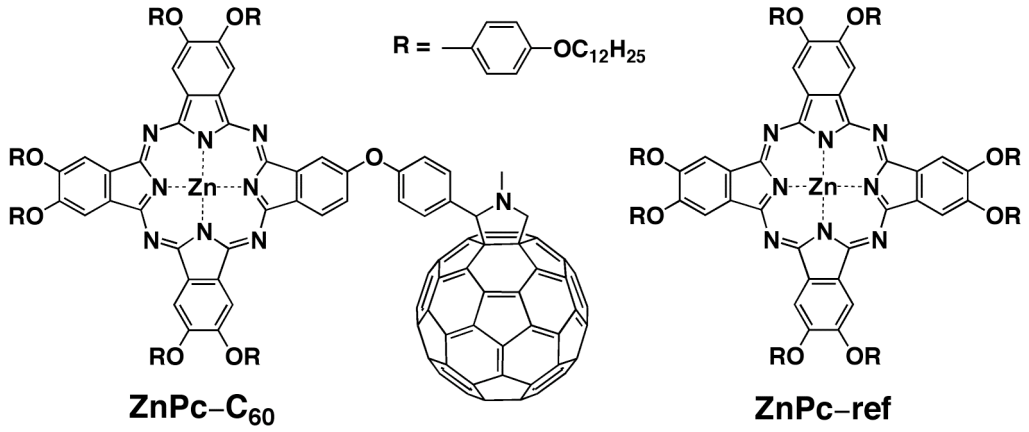

Figure 1. Phthalocyanine derivatives used in this study.

The synthesis and characterization of ZnPc-C_{60} and zinc phthalocyanine reference (ZnPc-ref) are described in the Experimental Section. The LC properties of ZnPc-C_{60} and ZnPc-ref were examined by a combination of differential scanning calorimetry (DSC), polarized optical microscopy (POM), and X-ray diffraction (XRD). Upon heating, only one broad endothermic curve (35 – 80ºC) with a peak of ca. 53ºC, corresponding to the LC-like phase-to-LC phase transition, is seen in ZnPc-C_{60}, whereas that to the crystal-to-LC phase transition is observed at 124°C in ZnPc-ref (Figure 2 and Table 1).

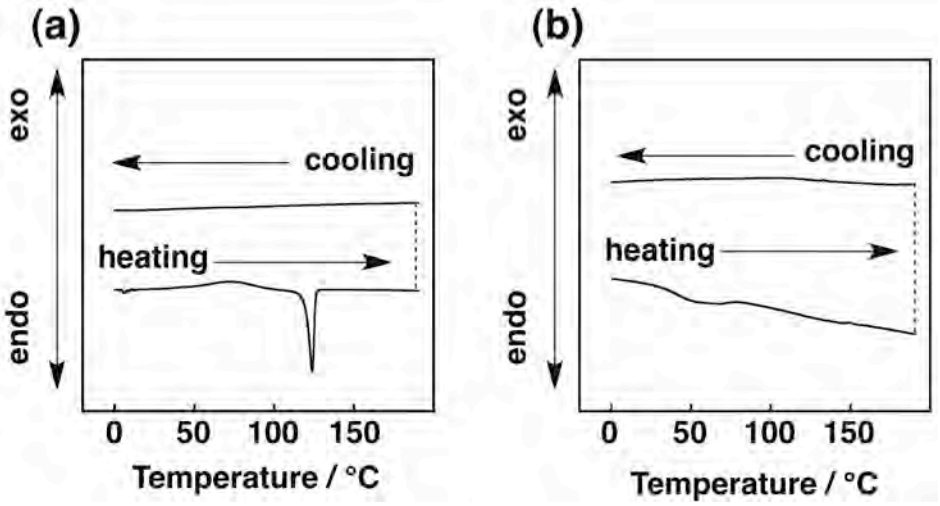

Figure 2. DSC thermograms of (a) ZnPc–ref and (b) ZnPc–C_{60} at 5.0°C min^{-1}. ZnPc–ref and ZnPc–C_{60} formed a glassy liquid crystalline state on cooling. T_g peak on cooling phase was undetectable even the cooling speed was slowed down to 1°C min^{-1}. ZnPc–ref and ZnPc–C_{60} were decomposed over 200°C.

Table 1. Phase transition temperatures and enthalpy changes.

compound	T / °C	ΔH / kJ mol^{-1}	phase sequence
ZnPc–ref	124	91.3	crystal / Col_h
ZnPc–C_{60}	35 – 80	17.5	LC–like / Col_r

Once ZnPc-C_{60} and ZnPc-ref were heated above the respective transition temperature, they formed a glassy liquid crystalline state at 25°C. Two POM images of ZnPc-ref at 25°C and 160°C show similar optical textures, while that of ZnPc-C_{60} reveals a birefringence texture upon heating 160°C (Figure 3). On cooling to 25°C, both ZnPc-ref and ZnPc-C_{60} showed birefringence images of textures that were similar to those at 160°C. These results corroborate that ZnPc-ref and ZnPc-C_{60} retain the mesophases consisting of the ordered structures (i.e., glassy LC state) at 25°C.

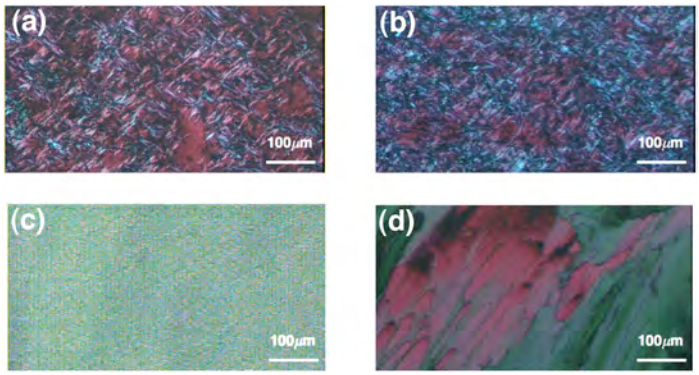

Figure 3. POM images of ZnPc–ref (a) at 25°C and (b) at 160°C on heating from 25°C with a rate of 10°C min^{-1} and ZnPc–C_{60} (c) at 25°C and (d) at 160°C on heating from 25°C with a rate of 10°C min^{-1}. On cooling from 160°C to 25°C with a rate of 10°C min^{-1} similar images of textures were obtained for ZnPc–ref and ZnPc–C_{60}, implying the retention of the mesoscopic phases.

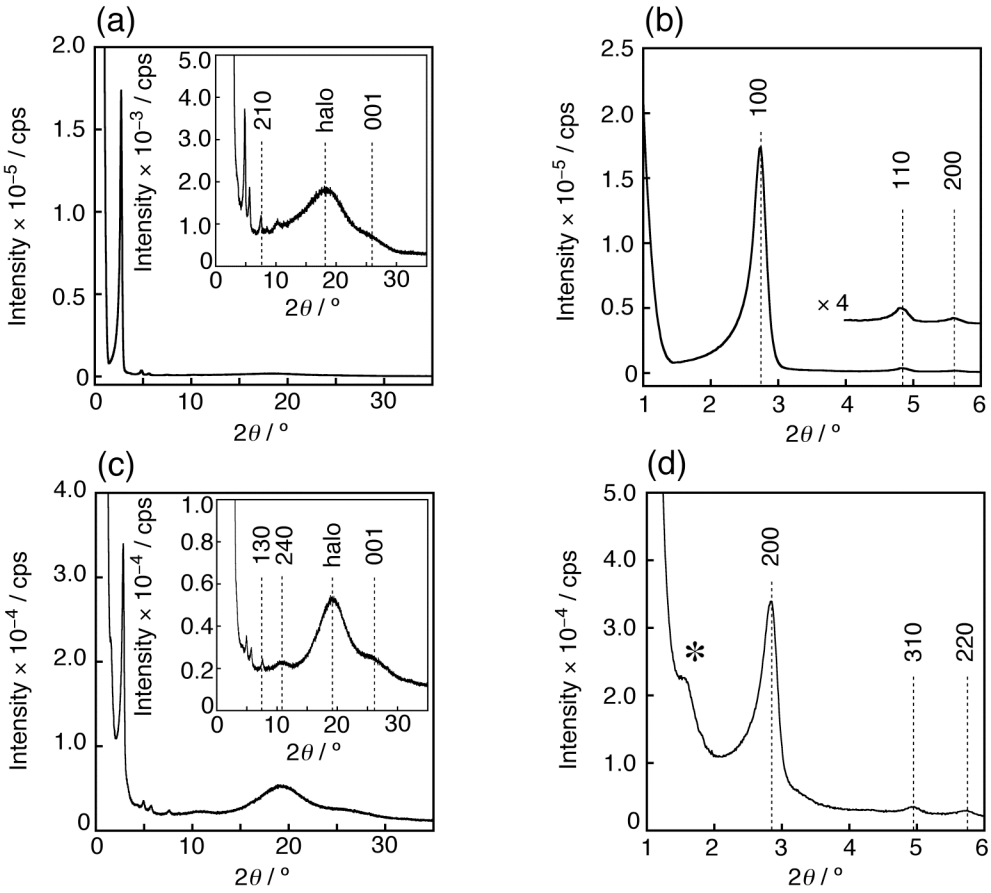

Figure 4. XRD patterns of ZnPc-ref in 2θ ranges of (a) 0-35° and (b) 1-6°. XRD patterns of ZnPc-C_{60} in 2θ ranges of (c) 0-35° and (d) 1-6°. Each sample was measured at 160°C. The intensified XRD patterns in 2θ ranges of 0-35° are also depicted as insets in figures (a) and (c). The mark * in Figure 4d is a peak arising from a helical pitch of C_{60} molecules along the ZnPc column.

These mesophases were identified by XRD (Figures 4 and 5, Table 2). By heating to 160°C the XRD patterns of ZnPc-ref exhibit hexagonal columnar (Col_h) mesophase (Figure 4a,b). On the other hand, XRD patterns of ZnPc-C_{60} at 25°C (Figure 5a,b) and 160°C (Figure 4c,d) are rather similar, but by heating to 160°C the peak intensities are remarkably enhanced, leading to the change from LC-like phase (Col_r1) to discotic rectangular columnar mesophase (Col_r2). Additionally, ZnPc-C_{60} retains this ordered structure after cooling to 25°C (Figure 5c,d). Considering a broad reflection peak of (001) in ZnPc-C_{60}, the ZnPc part in ZnPc-C_{60} may form disordered column in the Col_r2 mesophase, although such disordered columns of phthalocyanines are reported to reveal high hole mobility (ca. 10^{-1} cm^2 V^{-1} s^{-1}).[11] Furthermore, we measured the absorption spectra of the ZnPc-ref and ZnPc-C_{60} films to get the information on the packing geometries of the ZnPc moieties in the film after heating and cooling treatment (Figure 6). Both the spectra show blue-shift of the absorption arising from the ZnPc moiety relative to those in toluene, supporting the face-to-face stacking of the ZnPc moieties in the discotic columnar structures.

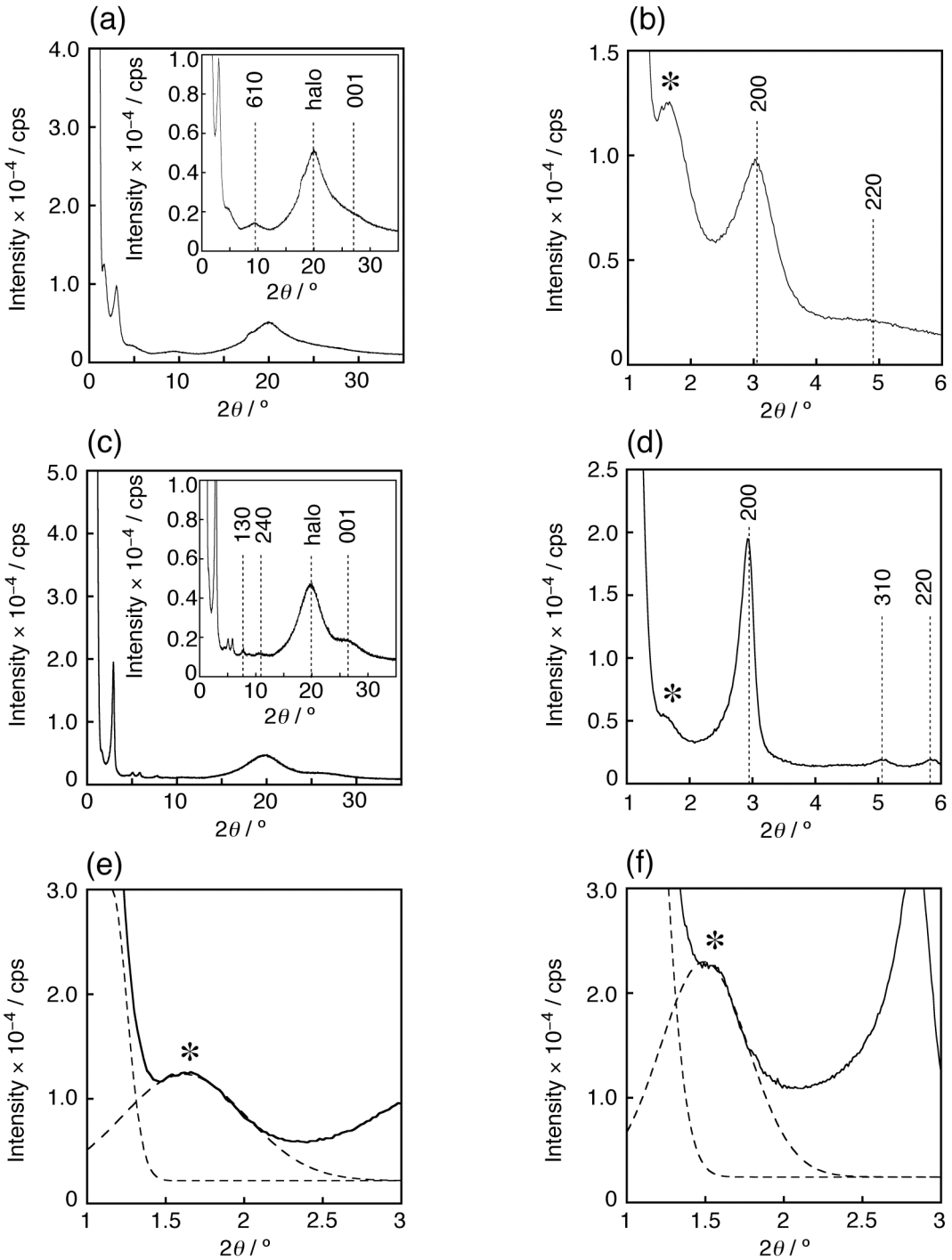

Figure 5. XRD patterns of ZnPc–C_{60} films in 2θ ranges of (a) 0 – 35° and (b) 1 – 6° at 25ºC without the heating and cooling treatment and of (c) 0 – 35° and (d) 1 – 6° at 25ºC where the sample was heated up to 160ºC, followed by cooling to 25ºC. The intensified XRD patterns in 2θ ranges of 0 – 35° are also depicted as insets in the figures (a) and (c). Peak fittings of the XRD patterns of the ZnPc-C_{60} films in 2θ ranges of 1 – 3º (e) at 25ºC without the heating and cooling treatment and (f) at 160ºC (solid line: XRD pattern, dashed line: fitting curves). The mark * in Figures 5b,d,e,f is a peak arising from a helical pitch of C_{60} molecules along the ZnPc column.

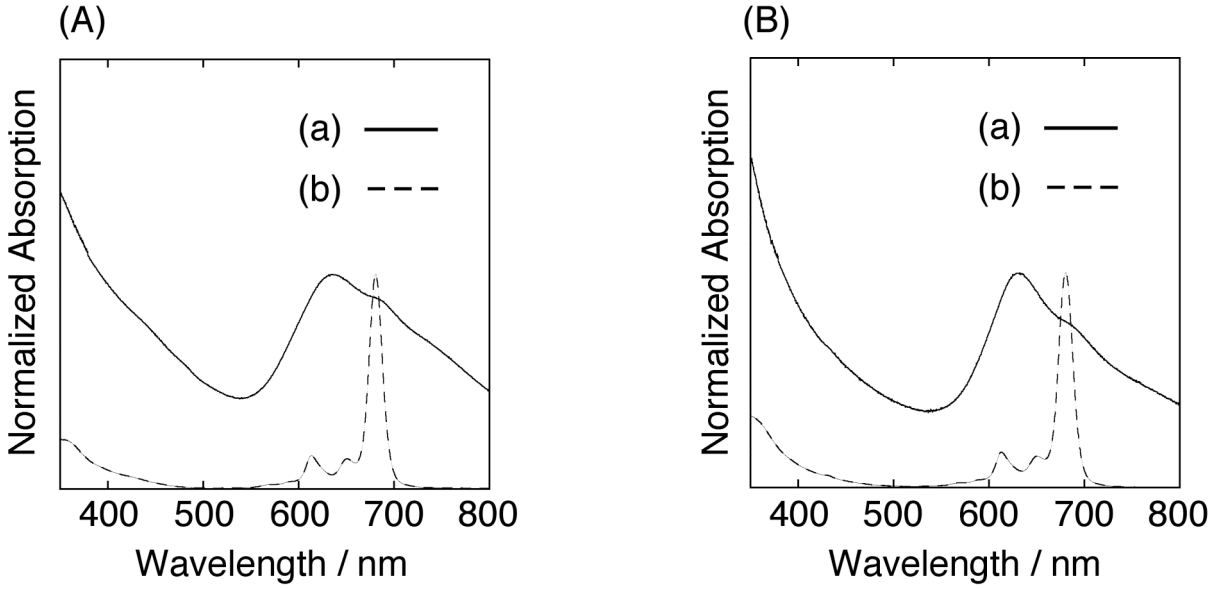

Figure 6. (A) Absorption spectra of (a) ZnPc-ref film, which was prepared by spin-coating of the toluene solution on a glass slide, at 25ºC where the sample was heated up to 160ºC for 20 min, followed by cooling to 25ºC (solid line) and of (b) ZnPc-ref in toluene (dashed line). (B) Absorption spectra of (a) ZnPc-C_{60} film, which was prepared by spin-coating of the toluene solution on a glass slide, at 25ºC where the sample was heated up to 160ºC for 20 min, followed by cooling to 25ºC (solid line) and of (b) ZnPc-C_{60} in toluene (dashed line). The spectra are normalized for comparison.

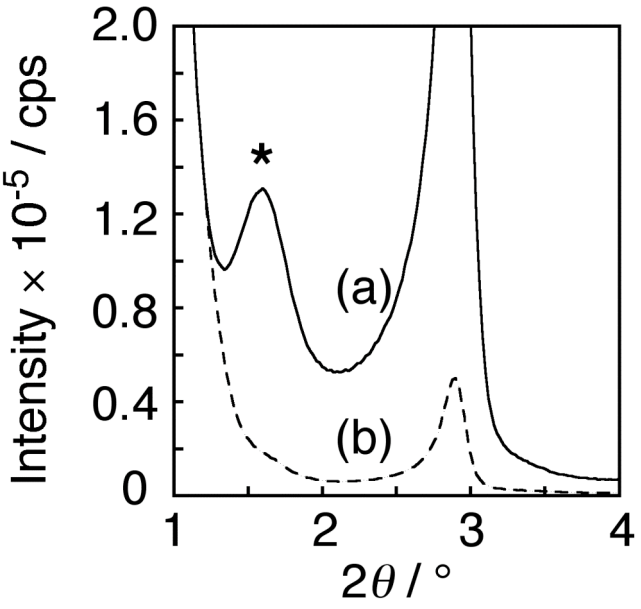

Figure 7. XRD patterns of ZnPc–C_{60} films oriented in the direction of (a) parallel to the X–ray beam (solid line) and (b) perpendicular to the X–ray beam (dashed line). The reflection peak assigned to the helical pitch (* mark) in curve (a) is not evident in curve (b). These samples were prepared by uniaxial shearing of the sample surface and measured at 160ºC.

Table 2. XRD Data of ZnPc–ref and ZnPc–C_{60}.

compound	lattice constants / Å	spacing / Å	Miller indices (hkl)
ZnPc–ref (Col_h at 160°C)	a = 36.1	31.3	(100)
Z = 1.0 for ρ^a = 1.1		17.9	(110)
		15.4	(200)
		11.8	(210)
		4.7	halo
		3.6	(001)
ZnPc–C_{60} (Col_r1 at 25°C without annealing)	a = 56.5	50.7	helical pitch
Z = 2.0 for ρ^a = 1.2	b = 46.8	28.5	(200)
$P2_1/m$		18.0	(220)
		9.2	(610)
		4.9	halo
		3.2	(001)
ZnPc–C_{60} (Col_r2 at 160°C)	a = 61.3	54.8	helical pich
Z = 2.0 for ρ^a = 1.3	b = 35.1	30.7	(200)
$P2_1/m$		17.7	(310)
		15.3	(220)
		11.5	(130)
		8.2	(240)
		4.6	halo
		3.4	(001)

[a]Assumed density (grams per cubic centimeter).

It is noteworthy that only ZnPc-C_{60} reveals a low angle peak at 1.59° (＊ mark in Figure 4d) that can be assigned as a helical pitch of molecules (5.48 nm) being 16 times the layer spacing of 0.34 nm.[12] These results suggest that due to the π–π interaction C_{60} molecules are also arranged linearly, showing the helical alignment along the ZnPc columnar structures. To shed light on the C_{60} arrangement, XRD measurements were also performed for the uniaxially oriented films of ZnPc-C_{60} (Figure 7).[13] These oriented films were prepared by uniaxial shearing of the sample surface. When the direction of the X-ray is parallel to the axis of the ZnPc column, the peak assigned to the helical pitch becomes more evident, supporting the helical C_{60} arrangement along the ZnPc column. Interestingly, the integrated areas of the peak

assigned to helical pitch extracted by peak fitting are rather comparable before and after heating treatment (Figure 5e,f). This implies that this helical C_{60} arrangement along the ZnPc column is formed even before heating treatment due to the plausible self-assembling process in the reprecipitation procedure by toluene and methanol as reported previously (vide infra).[4f,5a,c]

To correlate the LC structures with the charge-transporting properties, electron mobility (μ_e) and hole mobility (μ_h) were determined by the time-of-flight (TOF) method (Figures 8 and 9 and Experimental Section). Electron and hole mobilities under the electric field ($E = 0$) were obtained by extrapolation from the plots of the corresponding mobilities as a function of $E^{1/2}$ (Figures 8c,d). The μ_e and μ_h values of ZnPc-ref could not be obtained before heating the sample because of the poor film formation. After heating and cooling treatment, ZnPc-ref has a high μ_h value of 2.8 $cm^2\ V^{-1}\ s^{-1}$, but does not show electron mobility (Figure 9 and Table 3). In contrast, the current transients of ZnPc-C_{60} film before and after heating were observed under both the positive and negative bias modes (Figures 8a,b), suggesting ZnPc-C_{60} exhibits ambipolar charge-transporting character with rather comparable μ_h and μ_e values. The electron mobility of the ZnPc-C_{60} film before heating is larger than the hole mobility, showing that an electron-transporting pathway (i.e., the helical C_{60} arrangement along the ZnPc column) is formed before heating treatment (vide supra). It should be noted here that the respective μ_h and μ_e values increase by 26 times and 7 times after the heating and cooling treatment. This exemplifies that the heating allows the ZnPc-C_{60} molecules to adopt more regular arrangement, especially intra-column arrangement of the ZnPc moiety as well as the inter-column arrangement, leading to improvement of the ambipolar charge-transporting properties. More importantly, ZnPc-C_{60} displays remarkably high μ_h of 0.26 $cm^2\ V^{-1}\ s^{-1}$ and μ_e of 0.11 $cm^2\ V^{-1}\ s^{-1}$, which are the highest values ever reported for organic materials with D-A heterojunction.[4,5a] Meanwhile, the log charge mobilities decrease with increasing electric fields (Figure 8c, d). The negative E-field dependency of charge mobility indicates that carrier trapping occurs with a larger probability as the applied voltage is larger and generally arises when different hopping processes with different activation energies operate. Given that the macroscopic charge-carrier transport in the sample should involve both the intra-column (much less energy-demanding) and inter-column (much more energy-demanding) hopping events, the observed negative E-field dependency of the charge mobility seems reasonable.[4f,14]

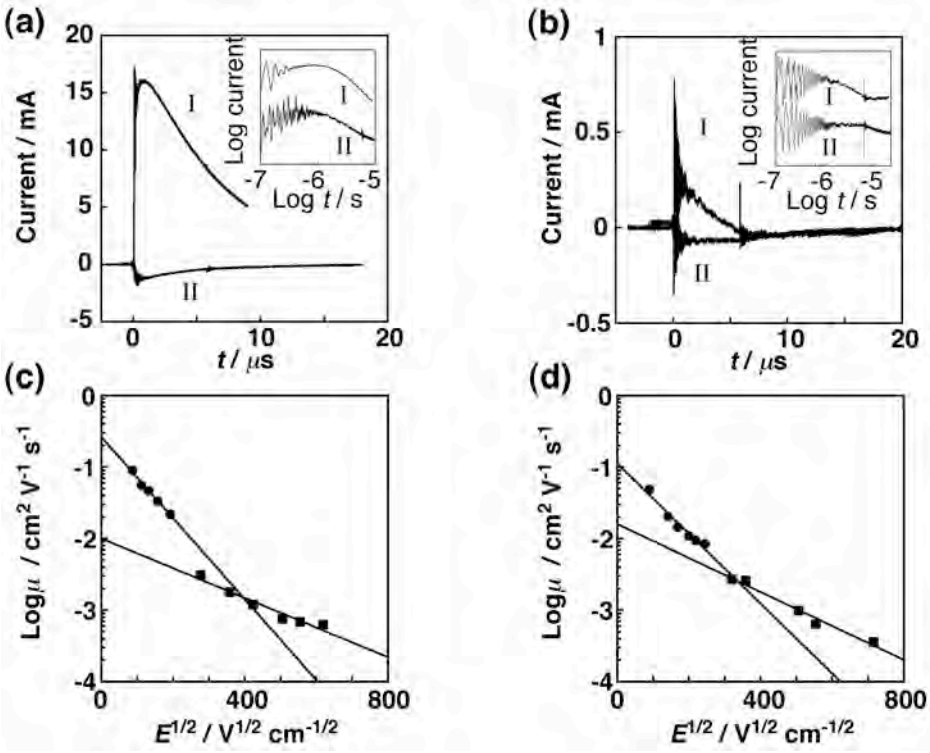

Figure 8. TOF current transients observed for ZnPc-C_{60} (a) before heating at an electric field strength (E) of 1.3×10^5 V cm^{-1} and (b) at 25ºC where the sample was heated up to 160°C for 10 min, followed by cooling to 25ºC at an electric field strength (E) of 7.7×10^3 V cm^{-1} after photoexcitation with 355 nm laser pulse. Curves I and II were observed under positive and negative bias modes, respectively. The log-log plots of TOF current transients vs time are also depicted as insets of the figures (a) and (b). (c) Log hole and (d) log electron mobilities observed for ZnPc-C_{60} as a function of $E^{1/2}$. Black square and circle represent before and after heating the sample, respectively.

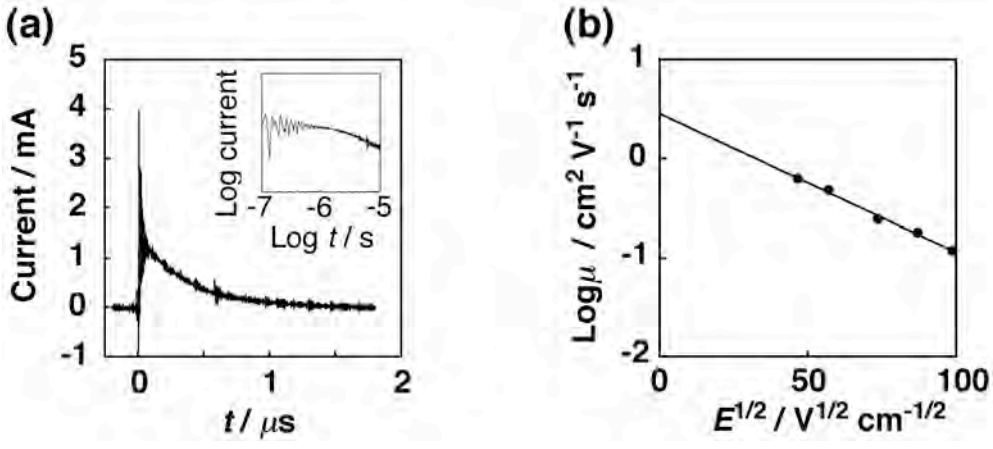

Figure 9. (a) TOF current transients observed for ZnPc–ref after annealing (160°C for 10 min, followed by cooling to 25°C) at an electric field strength (E) of 5.4×10^3 V cm^{-1} at 25°C (insets: log–log plot of TOF current transient vs time) under positive bias mode. (b) Plot of logarithmical hole mobilities observed for ZnPc–ref after annealing as a function of $E^{1/2}$.

Table 3. Charge Mobilities of ZnPc-ref and ZnPc-C_{60}.[a]

compound	TOF μ_h / $cm^2\ V^{-1}\ s^{-1}$	TOF μ_e / $cm^2\ V^{-1}\ s^{-1}$	TRMC $\Sigma\mu$ / $cm^2\ V^{-1}\ s^{-1}$
ZnPc-ref	2.8 (–)[b]	0 (–)[b]	3.0 (7.3)
ZnPc-C_{60}	0.26 (0.010)	0.11 (0.016)	0.52 (0.10)

[a]The value in parenthesis was obtained before the heating procedure. [b]Could not be measured.

With these contrasting long-range charge-transporting properties in mind, we measured flash-photolysis time-resolved microwave conductivities (TRMC) of ZnPc-ref and ZnPc-C_{60} (Figure 10 and Experimental Section). This electrodeless method allows for evaluating short-range transient conductivities of materials.[15] For instance, upon exposure to a 355 nm laser pulse at 25°C, ZnPc-ref reveals a prompt rise of a transient conductivity $<\phi\Sigma\mu>$, in which ϕ is the quantum efficiency of charge separation and $\Sigma\mu$ is the sum of mobility of all the transient-charge carriers, thus reaching maximum transient conductivities of 2.9×10^{-4} $cm^2\ V^{-1}\ s^{-1}$ before heating and of 1.2×10^{-4} $cm^2\ V^{-1}\ s^{-1}$ after heating and cooling treatment (Table S3). The ϕ values were also determined as 4.0×10^{-3} % before and after heating and cooling treatment by the current integration of TOF transients after heating. Accordingly, the hole mobilities of ZnPc-ref were obtained as 7.3 $cm^2\ V^{-1}\ s^{-1}$ before heating and of 3.0 $cm^2\ V^{-1}\ s^{-1}$ after heating and cooling treatment (Table 3). The larger value before heating than after heating and cooling treatment may result from the crystallinity nature of ZnPc-ref. That is, the annealing process of ZnPc-ref molecules causes transformation of crystal to liquid crystal, yielding the drop in the TRMC conductivity transient and the hole mobility. On the other hand, ZnPc-C_{60} exhibits maximum transient conductivities of 5.3×10^{-5} $cm^2\ V^{-1}\ s^{-1}$ before heating and of 1.5×10^{-4} $cm^2\ V^{-1}\ s^{-1}$ after heating and cooling treatment. From the ϕ values (5.2×10^{-2} % for before heating, 2.9×10^{-2} % for after heating and cooling treatment) of ZnPc-C_{60} (Table 4), the charge mobilities of ZnPc-C_{60} were obtained as 0.10 $cm^2\ V^{-1}\ s^{-1}$ before heating and of 0.52 $cm^2\ V^{-1}\ s^{-1}$ after heating and cooling treatment (Table 3). These short-range trends are consistent with long-range trends observed by the TOF method. These prompt rises of transient conductivities for the ZnPc-ref and ZnPc-C_{60} films arise from the photoresponse behavior of these films, in which free charge carriers, defined as charges escaped from recombination process, are generated by the laser excitation. On the other hand, in the decay part of the transient conductivity, the carriers are distributed randomly in the film, and subsequently undergo the recombination process.[16]

Table 4. Maximum Transient Conductivities ($\phi\Sigma\mu$) and Quantum Efficiency of Charge Separation (ϕ)[a]

compound	$\phi\Sigma\mu$[b] / cm^2 V^{-1} s^{-1}	ϕ[c] / %
ZnPc–ref	1.2×10^{-4} (2.9×10^{-4})	4.0×10^{-3} (4.0×10^{-3})
ZnPc–C_{60}	1.5×10^{-4} (5.3×10^{-5})	2.9×10^{-2} (5.2×10^{-2})

[a]The value in parenthesis was obtained before the heating procedure. [b]Maximum value of the transient conductivity upon photoirradiation at 355 nm (photon density: 2.8×10^{15} cm^{-2}). [c]Determined by the current integration of TOF transients.

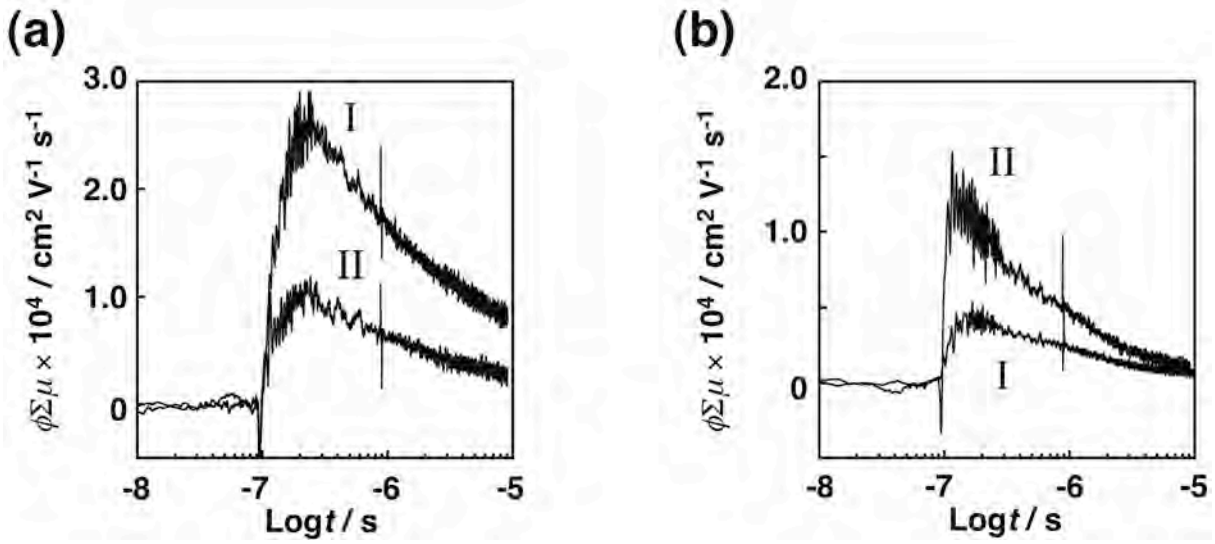

Figure 10. TRMC profiles of (a) ZnPc-ref before heating (curve I) and at 25ºC where the sample was heated up to 160°C for 10 min, followed by cooling to 25ºC (curve II), and (b) ZnPc-C_{60} before heating (curve I) and at 25ºC where the sample was heated up to 160°C for 10 min, followed by cooling to 25ºC (curve II), after photoexcitation with 355 nm laser pulse.

It should be noted that TRMC signals consist of the sum of charge mobilities for the negative and positive carriers, and we cannot extract respective electron and hole mobilities from the TRMC value accurately. The ZnPc-ref has a much higher TRMC charge mobility than does the ZnPc-C_{60} molecule. The presence of C_{60} moiety in the ZnPc-C_{60} film may disorder the ZnPc arrangement in the ZnPc-C_{60} column, lowering the TRMC value, especially the hole mobility.[12] In the TOF measurements the ZnPc-C_{60} film exhibits the high hole (0.26 cm^2 V^{-1} s^{-1}) and electron (0.11 cm^2 V^{-1} s^{-1}) mobilities in which the hole mobility is ca. two times larger than that of the electron mobility. Thus, both the charge mobilities would contribute to the TRMC value of ZnPc-C_{60} because of the comparable electron and hole

mobilities of ZnPc-C_{60} obtained by the TOF measurements as well as the expected short-range TRMC charge mobilities ($\geq$0.11 $cm^2\ V^{-1}\ s^{-1}$) that are typically higher than the long-range TOF charge mobilities. Some previous papers suggested that co-assembly of a D-A linked dyad with corresponding D or A molecules allows better packing of the molecular units and results in larger charge mobilities.[9b,17] We may be able to improve the charge-transporting properties of ZnPc-C_{60} by blending suitable phthalocyanine or fullerene derivatives.

Considering that TRMC and TOF measurements provide short-range and long-range charge-transporting properties, respectively, TRMC values depend on the degree of alignment for ZnPc-C_{60} molecules in the ZnPc-C_{60} intra-column, whereas TOF values correlate with that between ZnPc-C_{60} inter-columns as well as in the ZnPc-C_{60} intra-column. Note that the m_h and m_e values measured by TOF after the heating are 26 times and 7 times higher than those before the heating. On the other hand, the total charge mobility measured by TRMC after the heating and cooling treatment is 5 times higher than that before the heating. It is evident that the enhancement in the total charge mobility obtained by TOF is larger than that obtained by TRMC. More well-ordered alignment of the respective ZnPc-C_{60} columns in the LC by the heating may facilitate intra-charge transport between the ZnPc-C_{60} columns, leading to the improvement of the macroscopic charge mobilities.

In conclusion, we have successfully prepared a promising type of D-A linked dyad that is self-assembled to form segregated D-A columns in liquid crystals. The D-A heterojunction structure of ZnP-C_{60} molecules was found to exhibit highly efficient ambipolar charge-transporting properties. Such relationship between the liquid crystal structures and charge-transporting properties will provide basic and fundamental information on the rational design of high-performance liquid crystalline materials in organic electronics.

Experimental Section

General Procedures. ^{1}H NMR spectra were measured with a JEOL JNM–EX400 NMR spectrometer. Matrix-assisted laser desorption/ionization (MALDI) time-of-flight mass spectra were obtained using a SHIMADZU Biotech AXIMA–CFR with 1,8–dihydroxy–9(10*H*)–anthracenone (dithranol) as a matrix. High-resolution mass spectra (HRMS) were recorded on a JEOL JMS-HX110A spectrometer. IR spectra were recorded on a JASCO FT/IR-470 Plus spectrometer using KBr pellets. UV-vis-near infrared (NIR) spectra of solutions and films were measured with a Perkin–Elmer Lambda 900 UV/vis/NIR spectrometer. Steady–state fluorescence spectra were obtained by a HORIBA SPEX Fluoromax–3 spectrofluorometer.

Synthesis. C_{60} (99.98%) were obtained from MTR Ltd. and used as-received. All other solvents and chemicals were of reagent-grade quality, purchased commercially, and used without further purification unless otherwise noted. Thin layer chromatography (TLC) and column chromatography were performed with Silica gel 60 F_{254} (Merck) and SiliaFlash F60 (230–400 mesh; SiliCycle Inc.), respectively. Synthesis of ZnPc–C_{60} and ZnPc–ref was carried out according to the previously reported method (Scheme 1).[1] Condensation of 4,5–bis(4–dodecaoxyphenoxy)–1,2–dicynanobenzene **1**[18,19] and 4–(4–formyl-phenoxy)–1,2–dicyanobenzene **2**[20] afforded phthalocyanine derivative **3** and ZnPc–ref. Subsequent Prato reaction of **3** with C_{60} and sarcosine led to ZnPc–C_{60}.

Scheme 1. Synthesis of ZnPc–ref and ZnPc–C_{60}

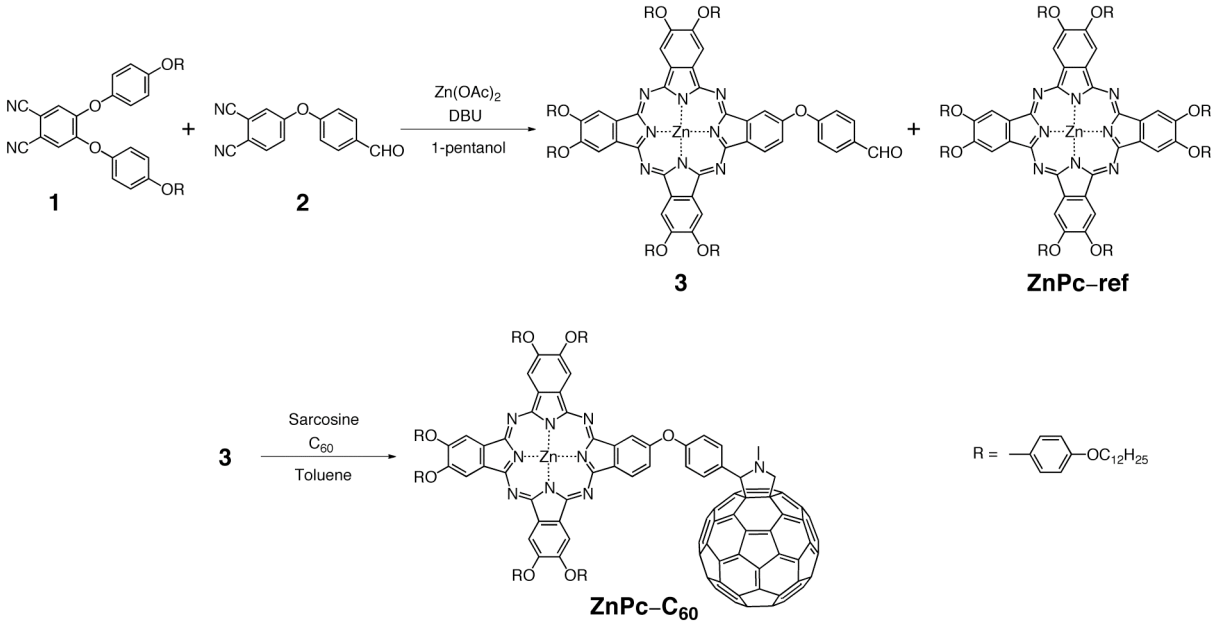

Phthalocyanine derivative (3)

A 300 mL of two-neck round-bottomed flask was charged with 4,5–bis(4–dodecaoxyphenoxy) –1,2–dicynanobenzene **1**[18,19] (4.7 g, 6.9 mmol), 4–(4–formylphenoxy)–1,2–dicyanobenzene **2**[20] (550 mg, 2.3 mmol), zinc acetate (450 mg, 2.5 mmol), 1,8–diazabicyclo[5.4.0]undec–7–ene (2.5 mL) and 1–pentanol (130 mL). The solution was stirred at 140°C for 24 h. After cooling to room temperature, the reaction mixture was extracted with dichloromethane (× 5). The combined organic layers were dried over anhydrous sodium sulfate and the solvent was removed by rotary evaporator. Purification by column chromatography (neutralized silica, toluene/THF = 20/1 with first fraction: R_f = 0.6, second fraction: R_f = 0.5) gave the first and second fractions as an eluent. Subsequent reprecipitation of the first and second residues (chloroform/methanol) afforded **ZnPc–ref** (353 mg, 0.12 mmol, 5.5% yield) and **3** (440 mg, 0.29 mmol, 8.2% yield) as brilliant green powders. **ZnPc–ref**: ^{1}H

NMR (400 MHz, CD_2Cl_2) δ 8.62 (s, 8H), 7.13 (d, J = 8.0 Hz, 16H), 6.85 (d, J = 8.0 Hz, 16H), 3.88 (t, J = 4.0 Hz, 16H), 1.73 (m, 16H), 1.41 (m, 16H), 1.19 (m, 128H), 0.79 (t, J = 7.2 Hz, 24H); HRMS found: 2785.646, $C_{147}H_{188}N_8O_{14}Zn$ requires 2785.750; IR data (KBr) ν 2922, 2852 (C–H), 1606 (C=C), 1504, 1457 (C–N), 1203 cm^{-1} (C–O); UV–vis (toluene) λ_{max} (ε / 10^3 M^{-1} cm^{-1}) 354 (65.3), 614 (44.3), 651 (40.3), 681 (280); Fluorescence (toluene) 685, 758 nm. **3**: ^{1}H NMR (400 MHz, CD_2Cl_2) δ 9.97 (s, 1H), 8.96 (d, J = 8.0 Hz, 1H), 8.74–8.55 (m, 7H), 7.93 (d, J = 8.0 Hz, 2H), 7.69 (d, J = 8.0 Hz, 1H), 7.44–7.36 (m, 4H), 7.27 (br, 12H), 7.05 (d, J = 8.0 Hz, 2H), 6.98–6.90 (m, 12H), 3.97 (br, 12H), 1.92 (br, 12H), 1.51–1.29 (m, 108H), 0.86 (br, 18H); HRMS found: 2354.360, $C_{147}H_{188}N_8O_{14}Zn$ requires 2353.354; IR data (KBr) ν 2923, 2853 (C–H), 1700 (C=O), 1598 (C=C), 1504, 1456 (C–N), 1200 cm^{-1} (C–O); UV–vis (toluene) λ_{max} (ε / 10^3 M^{-1} cm^{-1}) 352 (65.7), 613 (43.3), 651 (39.1), 680 (260); Fluorescence (toluene) 685, 758 nm.

ZnPc–C_{60}

A 300 mL of two-neck round-bottomed flask was charged with of **3** (140 mg, 0.06 mmol), C_{60} (86 mg, 0.12 mmol), and sarcosine (10 mg, 0.12 mmol) in toluene (120 mL). The solution was stirred at 120°C for 24 h, then the solvent was removed in vacuo. The crude product was purified by column chromatography (neutralized silica, toluene/THF = 20:1 with R_f = 0.05) and HPLC several times. Subsequent reprecipitation of the first residues (toluene/methanol) afforded **ZnPc–C_{60}** as a brilliant green powder (66 mg, 0.021 mmol, 36% yield): ^{1}H NMR (400 MHz, $C_2D_2Cl_4$) δ 9.22 (s, 1H), 8.88 (br, 7H), 8.50 (s, 1H), 7.86 (br, 2H), 7.86 (br, 2H), 7.65 (br, 1H), 7.28 (d, J = 8.0 Hz, 2H), 7.19–7.12 (m, 12H), 6.97–6.92 (m, 12H), 4.94 (m, 2H), 4.22 (d, J = 8.0 Hz, 1H), 4.40 (m, 12H), 1.77 (m, 12H), 1.44–1.31(m, 108H), 0.81 (m, 18H); HRMS found: 3100.297, $C_{209}H_{193}N_9O_{13}Zn$ requires 3100.401; IR data (KBr) ν 2924, 2852 (C–H), 1617 (C=C), 1503, 1456 (C–N), 1200 cm^{-1} (C–O); UV–vis (toluene) λ_{max} (ε / 10^3 M^{-1} cm^{-1}) 350 (100), 613 (50.9), 651 (46.2), 680 (303); Fluorescence (toluene) 688, 758 nm.

Mesomorphism Identification.[21]

The phase transition temperatures were measured by differential scanning calorimetry (DSC, TA instrument DSC2920) and from microscopic observations of the optical textures (Olympus BH2 and Mettler FP90 hot stage). The DSC measurements were carried out on 3-4 mg samples of recrystallized materials at a scanning rate of 1 and 5°C min^{-1}. The mesophases were identified by X–ray diffraction at temperatures corresponding to the mesophase and the glass or crystal phase using a Rigaku RINT 2000 HF equipped with a hand-made hot stage. Temperature-dependent electronic spectra were measured on a Shimadzu UV2500PC UV–vis spectrophotometer as a cast film sandwiched between two microscope glass slides.

Time-of-Flight (TOF) Charge Mobility Measurements.[22]

Electrical measurements were carried out by a two-probe method using a Keithley model 4200–SCS semiconductor parameter analyzer using 3 μm gap Au/Ti electrodes, fabricated by a photolithographic technique on a silicon wafer coated with a 300 nm thick insulating SiO_2 layer. The electrodes were 30 μm long and 50 nm thick, which were fully covered by a cast sample film with a thickness of ~1 μm. All the measurements were performed at 25ºC at a reduced pressure (<10^{-3} Pa) using a Nagase Electronic Equipment Service model GRAIL10–Helips–4–HT low-temperature prober. Photoirradiation was performed using an Asahi Spectra model MAX–301 xenon light source with a light power density of 15 mW mm^{-2}. Bulk charge carrier mobility was evaluated by means of a TOF technique. ZnPc–ref was mounted with a thickness of 92 μm (after annealed) on an Al substrate, sandwiched by a 360-nm-thick ITO grass, and ZnPc–C_{60} was mounted with a thickness of 3.9 μm (before annealed), 25 μm (after annealed with positive bias) and 41 μm (after annealed with negative bias) on an Al substrate, sandwiched by a 15-nm-thick Au, annealed at 160ºC for 1 h, and placed in a vacuum chamber (<10^{-4} Pa) during the TOF measurements. Current transients, generated in the samples upon exposure to a 355 nm laser pulse from a Spectra Physics model INDY–HG Nd:YAG laser through quartz–ITO windows, were recorded by a Tektronix model DPO 3034digital oscilloscope with a terminate resistance of 10 kΩ. Electron and hole mobilities under the zero electric field (E = 0) were obtained by extrapolation from the plots of the corresponding mobilities as a function of $E^{1/2}$, assuming a charge carrier transporting model in disordered molecular solid, where mobility μ is defined by the following equation, $\mu = \mu_o \exp[C\{(\rho/kT)^2 - \Sigma^2\}E^{1/2}]$.[23,24]

Time-Resolved Microwave Conductivity (TRMC) Measurements.[22]

Nanosecond laser pulses from a Nd:YAG laser (Spectra Physics, INDY–HG, third harmonic generation (THG), 355 nm) with FWHM of 3-5 ns were used as excitation sources. The photon density of the laser was set at 1.6 × 10^{15}–3.6 × 10^{16} photons cm^{-2}. For the TRMC measurements, a microwave frequency of 8.6–9.4 GHz and a power of 2.1–4.6 mW were employed so that the motion of charge carriers could not be disturbed by the low electric field of the microwaves. The TRMC signal, picked up by a diode (rise time < 1 ns), was monitored by a digital oscilloscope (Tektronix, TDS3032B, rise time ~1.2 ns). All the experiments were carried out at 25ºC. The transient photoconductivity of the samples is related to the reflected microwave power and the sum of the mobility of charge carriers via Gill equation (1):

$$\mu(T,E) = \mu_0 \exp\left(-\frac{\varepsilon_0 - \beta\sqrt{E}}{kT_{\text{eff}}}\right) \qquad 1/T_{\text{eff}} = 1/T - 1/T_0 \qquad (1)$$

where T (K) is the temperature, E is the negative electric field dependence of charge carrier mobility (μ), μ_0 is the mobility at T_0, T_0 is the temperature at which the Arrhenius plots of mobility at various electric fields intercept, β (eV(V cm^{-1})$^{-1/2}$) is the Poole-Frenkel coefficient, ε_0 is the activation energy, and k is the Boltzmann constant. The number of photons absorbed by the sample was estimated based on the power loss of incident laser pulses averaged over 200 shots. The ϕ values were determined by the current integration of TOF transients. The films, which were prepared by spin-coating of the toluene solution, were overcoated by Au semitransparent electrodes at 20 mm^2, vacuum evaporated to a thickness of 25 nm, and excited by laser pulses at 355 nm with a pulse duration of 3–5 ns and a photon density of 3.0×10^{15} photons cm^{-2}. Current transients were monitored by a digital oscilloscope (Tektronix, TDS3052B) through a 300 kΩ terminate resistance, and the charges were also accumulated by an electrometer of Keithley Instruments 6514.

References and Notes

[1] (a) Shimizu, Y.; Oikawa, K.; Nakayama, K.; Guillon, D. *J. Mater. Chem.* **2007**, *17*, 4223. (b) Rosen, B. M.; Wilson, C. J.; Wilson, D. A.; Peterca, M.; Imam, M. R.; Percec, V. *Chem. Rev.* **2009**, *109*, 6275.

[2] (a) Laschat, S.; Baro, A.; Steinke, N.; Giesselmann, F.; Hägele, C.; Scalia, G.; Judele, R.; Kapatsina, E.; Sauer, S.; Schreivogel, A.; Tosoni, M. *Angew. Chem., Int. Ed.* **2007**, *46*, 4832. (b) Kato, T.; Yasuda, T.; Kamikawa, Y.; Yoshio, M. *Chem. Commun.* **2009**, 729.

[3] (a) Percec, V.; Gloddle, M.; Bera, T. K.; Miura, Y.; Shiyanovskaya, I.; Singer, K. D.; Balagurusamy, V. S. K.; Heiney, P. A.; Schnell, I.; Rapp, A.; Spiess, H.–W.; Hudson, S. D.; Duan, H. *Nature* **2002**, *419*, 384. (b) Samori, P.; Yin, X.; Tchebotareva, N.; Wang, Z.; Pakula, T.; Jäckel, F.; Watson, M. D.; Venturini, A.; Müllen, K.; Rabe, J. P. *J. Am. Chem Soc.* **2004**, *126*, 3567. (c) Pisula, W.; Kastler, M.; Wasserfallen, D.; Robertson, J. W. F.; Nolde, F.; Kohl, C.; Müllen, K. *Angew. Chem., Int. Ed.* **2006**, *45*, 819. (d) Tasios, N.; Grigoriadis, C.; Hansen, M. R.; Wonneberger, H.; Li, C.; Spiess, H. W.; Müllen, K.; Floudas, G. *J. Am. Chem. Soc.* **2010**, *132*, 7478.

[4] (a) Shi, Q.; Hou, Y.; Jin, H.; Li, Y. *J. Appl. Phys.* **2007**, *102*, 073108. (b) Ballantyne, A. M.; Chen, L.; Dane, J.; Hammant, T.; Braun, F. M.; Heeney, M.; Duffy, W.; McCulloch, I.; Bradley, D. D. C.; Nelson, J. *Adv. Funct. Mater.* **2008**, *18*, 2373. (c) Li, W.–S.; Yamamoto, Y.; Fukushima, T.; Saeki, A.; Seki, S.; Tagawa, S.; Masunaga, H.; Sasaki, S.; Takata M.; Aida, T. *J. Am. Chem. Soc.* **2008**, *130*, 8886. (d) Bullock, J. E.; Carmieli, R.; Mickley, S. M.; Vura-Weis, J.; Wasielewski, M. R. *J. Am. Chem. Soc.* **2009**, *131*, 11919. (e) Charvet, R.; Acharya, S.; Hill, J. P.; Akada, M.; Liao, M.; Seki, S.; Honsho, Y.; Saeki,

A.; Ariga, K. *J. Am. Chem. Soc.* **2009**, *131*, 18030. (f) Hizume, Y.; Tashiro, K.; Charvet, R.; Yamamoto, Y.; Saeki, A.; Seki, S.; Aida, T. *J. Am. Chem. Soc.* **2010**, *132*, 6628.

[5] (a) Imahori, H.; Ueda, M.; Kang, S.; Hayashi, H.; Hayashi, S.; Kaji, H.; Seki, S.; Saeki, A.; Tagawa, S.; Umeyama, T.; Matano, Y.; Yoshida, K.; Isoda, S.; Shiro, M.; Tkachenko, N. V.; Lemmetyinen, H. *Chem.–Eur. J.* **2007**, *13*, 10182. (b) Kira, A.; Umeyama, T.; Matano, Y.; Yoshida, K.; Isoda, S.; Park, J. K.; Kim, D.; Imahori, H. *J. Am. Chem. Soc.* **2009**, *131*, 3198. (c) Umeyama, T.; Tezuka, N.; Kawashima, F.; Seki, S.; Matano, Y.; Nakao, Y.; Shishido, T.; Nishi, M.; Hirao, K.; Lehtivuori, H.; Tkachencko, N. V.; Lemmetyinen, H.; Imahori, H. *Angew. Chem., Int. Ed.* **2011**, *50*, 4615.

[6] Hanack, M.; Lang, M. *Adv. Mater.* **1994**, *6*, 819.

[7] (a) Nierengarten, J.–F.; Solladie, N.; Deschenaux, R. In *Fullerenes*; Langa, F.; Nierengarten, J.–F., Eds.; RSC Publishing: Cambridge, 2007; Chapter 5. (b) Campidelli, S.; Bourgun, P.; Guintchin, B.; Furrer, J.; Stoeckli-Evans, H.; Saez, I. M.; Goodby, J. W.; Deschenaux, R. *J. Am. Chem. Soc.* **2010**, *132*, 3574.

[8] (a) Lenoble, J.; Campidelli, S.; Maringa, N.; Donnio, B.; Guillon, D.; Yevlampieva, N.; Deschenaux, R. *J. Am. Chem. Soc.* **2007**, *129*, 9941. (b) Lenoble, J.; Maringa, N.; Campidelli, S.; Donnio, B.; Guillon, D.; Deschenaux, R. *Org. Lett.* **2006**, *8*, 1851. (c) Maringa, N.; Lenoble, J.; Donnio, B.; Guillon, D.; Deschenaux, R. *J. Mater. Chem.* **2008**, *18*, 1524. (d) Hoang, T. N. Y.; Pociecha, D.; Salamonczyk, M.; Gorecka, E.; Deschenaux, R. *Soft Mater* **2011**, *7*, 4948.

[9] (a) Bottari, G.; de la Torres, G.; Guldi, D. M.; Torres, T. *Chem. Rev.* **2010**, *110*, 6768. (b) de la Escosura, A.; Matínez-Díaz, M. V.; Barberá, J.; Torres, T. *J. Org. Chem.* **2008**, *73*, 1475. (c) Geerts, Y. H.; Debever, O.; Amato, C.; Sergeyev, S. *Beilstein J. Org. Chem.* **2009**, *5*, doi: 10.3762/bjoc.5.49. (d) Ince, M.; Martínez-Díaz, M. V.; Barberá, J.; Torres, T. *J. Mater. Chem.* **2011**, *21*, 1531.

[10] Ichihara, M.; Suzuki, A.; Hatsusaka, K.; Ohta, K. *Liquid Crystals* **2007**, *34*, 555.

[11] (a) Iino, H.; Takayashiki, J.; Hanna, J.; Bushby, R. J.; *Jpn. J. Appl. Phys.* **2005**, *44*, L1310. (b) Iino, H.; Hanna, J.; Bushby, R. J.; Movaghar, B.; Whitaker, B. J.; Cook, M. J. *Appl. Phys. Lett.* **2005**, *7*, 132102. (c) Miyake, Y.; Shiraiwa, Y.; Okada, K.; Monobe, H.; Hori, T.; Yamasaki, N.; Yoshida, H.; Cook, M. J.; Fujii, A.; Ozaki, M.; Shimizu, Y. *Appl. Phys. Express* **2011**, *4*, 021604.

[12] On the basis of the Col_r2 structure for ZnPc-C_{60}, the ZnPc plane is tilted by 7.4° against the axis of the ZnPc column. Given that the C_{60} helical pitch is 16 times the layer spacing, the separation distance between the C_{60} (0.7-0.9 nm) is estimated to be smaller than the shortest one between the the C_{60} (~1.0 nm). Such enhanced packing of the C_{60} may be achieved by the disordered wedge-shaped open stacked ZnPc in the ZnPc column.

[13] (a) Barberá, J.; Cavero, E.; Lehmann, M.; Serrano, J.; Sierra, T.; Vázquez, J. T. *J. Am. Chem. Soc.* **2003**, *125*, 4527. (b) Pisula, W.; Tomovic, Z.; Simpson, C.; Kastler, M.; Pakula, T.; Müllen, K. *Chem. Mater.* **2005**, *17*, 4296. (c) Lee, S.; Lin, H.; Lin, Y.; Chen, H.; Liao, C.; Lin, T.; Chu, Y.; Hsu, H.; Chen, C.; Lee, J.; Hung, W.; Liu, Q.; Wu, C. *Chem.–Eur. J.* **2011**, *17*, 792.

[14] (a) Seki, S.; Yoshida, Y.; Tagawa, S.; Asai, K.; Ishigure, K.; Furukawa, K.; Fujiki, M.; Matsumoto, N. *Phil. Mag. B* **1999**, *79*, 1631. (b) Kunimi, Y.; Seki, S.; Tagawa, S. *Solid State Commun.* **2000**, *114*, 469.

[15] Saeki, A.; Seki, S.; Koizumi, Y.; Sunagawa, T.; Ushida, K.; Tagawa, S. *J. Phys. Chem. B* **2005**, *109*, 10015.

[16] (a) Saeki, A.; Seki, S.; Sunagawa, T.; Ushida, K.; Tagawa, S. *Phil. Mag.* **2006**, *86*, 1261. (b) Saeki, A.; Seki, S.; Tagawa, S. *J. Appl. Phys.* **2006**, *100*, 023703.

[17] (a) Goldmann, D.; Janietz, D.; Schmidt, C.; Wendorff, J. H. *Angew. Chem., Int. Ed.* **2000**, *39*, 1851. (b) Reczek, J. J.; Villazor, K. R.; Lynch, V.; Swager, T. M.; Iverson, B. L. *J. Am. Chem. Soc.* **2006**, *128*, 7995.

[18] Lo, P. K.; Sleiman, H. F. *J. Am. Chem. Soc.* **2009**, *131*, 4182.

[19] Ichihara, M.; Suzuki A.; Hatsusaka, K.; Ohta, K. *Liquid Crystals*, **2007**, *34*, 555.

[20] Giuntini, F.; Raoul, Y.; Dei, D.; Municchi, M.; Chiti, G.; Fabris, C.; Colautti, P.; Jori, G.; Roncucci, G. *Tetrahedron Lett.* **2005**, *46*, 2979.

[21] Fabien, N.; Hirosato, M.; Motoo, S.; Shimizu, Y. *J. Mater. Chem.* **2007**, *17*, 2607.

[22] Hizume, Y.; Tashiro, K.; Charvet, R.; Yamamoto, Y.; Saeki, A.; Seki, S.; Aida, T. *J. Am. Chem. Soc.* **2010**, *132*, 6628.

[23] Borsenberger, P. M.; Pautmeier, L. T.; Bässler, H. *Phys. Rev.* **1992**, *46*, 12145.

[24] Bässler, H. *Phys. Status Solidi* **1993**, *175*, 15.

Concluding Remarks

This thesis has described the systematic investigation of the effects of porphyrin–TiO_2 geometry on the electron transfer kinetics and the cell performance of porphyrin-sensitized solar cell, and preparation and photoelectrochemical application of bottom-up self-assembled photofunctional materials aiming at exhibiting efficient charge-transporting properties. The results and findings in this work are summarized as follows.

Chapter 1

The author has systematically examined the effects of porphyrin substituents and adsorption conditions on the photovoltaic properties of the porphyrin-sensitized TiO_2 cells. The cell performance of the porphyrin-sensitized TiO_2 cells was affected greatly by the steric bulkiness around the porphyrin, the electronic coupling between the porphyrin core and the TiO_2 surface, the immersion solvent, and the immersion time. In particular, the high cell performance of the porphyrin-sensitized TiO_2 cells was realized when protic solvent (i.e., methanol) and short immersion time (0.5 – 1 h) were used for the conditions of the dye adsorption on TiO_2. This unique behavior is in marked contract with little dependence of the cell performance on ruthenium dye-sensitized TiO_2 cells as a function of the immersion solvent and immersion time. The TiO_2 electrode cell with 5-(4-carboxyphenyl)-10,15-20-tris-(2,4,6-trimethylphenyl)porphyrinatozinc(II) as a sensitizer exhibited the maximum cell performance: an incident photon-to-current efficiency (IPCE) value of 76%, a short circuit photocurrent density of 9.4 mA cm^{-2}, an open circuit voltage of 0.76 V, a fill factor of 0.64, and a power conversion efficiency of 4.6% under standard AM 1.5 sunlight. These results will provide basic and important information on the development of dye-sensitized solar cells with high performance.

Chapter 2

The author has investigated the photoinduced electron injection and charge recombination kinetics in porphyrin-sensitized TiO_2 electrodes using time resolved absorption spectroscopy as well as the binding geometry of poprhyrin/TiO_2 using transmission electron microscopy measurements. There is a heterogeneous dye/semiconductor binding geometry; the porphyrin molecules are attached to the TiO_2 surface with a distribution of tilt angles, where the angle determines the porphyrin-semiconductor electron transfer distance and charge transfer occurs via through-space, rather than through-bond connecting the porphyrin core and anchoring

COOH group. From measurements of transient absorption spectra of the dyes on TiO_2 and analysis of the spectral evolution, it was concluded that the oxidized dye, D^+, is the only photoproduct and its spectrum is quantified. For short sensitization time (1 h), there is a direct correlation between solar cell efficiency and amplitude of long-lived conduction band electrons, once variations in light-harvesting (surface coverage) have been taken into account. On the other hand, long immersion time (12 h) results in decreased solar cell efficiency because of decreased efficiency of electron injection.

Chapter 3

The author has successfully established CN-labeled molecules as probes of the binding geometry of non-labeled molecules by using vibrational sum frequency generation (SFG) spectroscopy and transient absorption spectroscopy. The transient absorption kinetic results of labeled and non-labeled molecules showed that they have very similar dynamics, demonstrating that the labeled molecules are good probes for binding geometry of non-labeled molecules. The SFG measurements revealed that all porphyrin molecules studied here are attached to the TiO_2 surface under an appreciable tilt angle, and this angle depends on the specifics of the porphyrin as well as properties of the immersion solvent and duration of the immersion. There is a linear correlation between average tilt angle and solar cell efficiency normalized for surface coverage (η_{rel}) – the smaller the angle the higher solar cell efficiency. Since electron transfer exhibits strong distance dependence, the rate of electron injection and recombination constitutes a complimentary measure (to SFG measured tilt angle) of sensitizer binding geometry. Long immersion time (i.e. 12 h vs. 1 h) of the TiO_2 electrode causes aggregation induced decrease of solar cell efficiency through two effects – changes of binding geometry and increased radiationless quenching decreasing injection efficiency.

Chapter 4

The author has characterized self-assembled amorphous D-A solids consisting of porphyrin derivatives and C_{60} by solid-state NMR. The fully-relaxed direct polarization/magic angle spinning ^{13}C NMR experiments without ^{1}H dipolar decoupling (DP/MAS/noDD), cross polarization magic angle spinning ^{13}C NMR experiments without ^{1}H dipolar decoupling (CP/MAS/noDD), and ^{1}H–^{13}C heteronuclear correlation (HETCOR) experiments provided molecular-level information on the disordered tetraphenylporphyrin/C_{60} composites, which explains the remarkable difference in organic solar cell performances arising from subtle structural difference. Such analyses for amorphous solids will become increasingly important in organic electronics as well as in supramolecular chemistry.

Chapter 5

The author has successfully prepared ZnO nanorods and ZnO nanoparticle electrodes and applied them to photoelectrochemical devices. The effects on photocurrent generation efficiency of the intervening fullerene monolayer between the porphyrin-fullerene composite multilayers and ZnO nanorods were examined. The ZnO nanorod electrodes modified sequentially with the fullerene monolayer and porphyrin-fullerene multilayers exhibited high incident photon-to-current efficiency up to 30% at 400 nm compared to that of the reference systems without the fullerene monolayer. The intervening fullerene monolayer between the porphyrin-fullerene composite multilayers and ZnO nanorods may enhance the electron injection efficiency into the ZnO nanorod electrode and inhibit charge recombination, leading to improvement in photocurrent generation efficiency. Finally, the effects of ZnO electrode structures (nanorod versus nanoparticle) on photocurremt generation efficiency were evaluated. Unfortunately, similar photocurrent generation efficiencies were noted despite of the difference in the electrode structures. This can be explained by the facts that only the top surface of the porous ZnO nanoparticle electrode is covered by the porphyrin-fullerene composite layers, whereas the entire surface of the ZnO nanorod electrode is wrapped in the composite layers. Nevertheless, the results obtained from this study will provide basic and valuable information on the advanced design of organic solar cells, if a combination of surface morphology of electrodes and donor-acceptor composites is modulated adequately to fulfill the requirements for high cell performance.

Chapter 6

The author has successfully developed a promising strategy for constructing the efficient hierarchical electron transfer cascade system on a semiconducting electrode in a bottom-up manner by using reduced graphene oxide (RGO) as a two-dimensional sheet to anchoring organic/inorganic hybrid materials. The electrophoretically deposited film exhibited remarkably high photocurrent generation (incident photon-to-current generation efficiency = 70%) compared with the reference device without RGO sheets as well as zinc oxide nanoparticles. These results will provide a fundamental clue for the bottom-up construction of artificial photosynthetic systems utilizing organic/inorganic assemblies.

Chapter 7

The author has successfully prepared a promising type of D-A linked dyad that is self-assembled to form segregated D-A columns in liquid crystals. The D-A heterojunction

structure of zincphthalocyanine-fullerene molecules was found to exhibit highly efficient ambipolar charge-transport properties. This relationship between the liquid crystalline structures and charge transport properties will provide basic and fundamental information on the rational design of high-performance liquid crystalline materials for use in organic electronics.

List of Publications

Chapter 1

Effects of Porphyrin Substituents and Adsorption Conditions on Photovoltaic Properties of Porphyrin-Sensitized TiO_2 Cell

Imahori, H.; Hayashi, S.; Hayashi, H.; Oguro, A.; Eu, S.; Umeyama, T.; Matano, Y.

J. Phys. Chem. C **2009**, *113*, 18406-18413.

Chapter 2

Photoinduced Charge Carrier Dynamics of Zn-Porphyrin-TiO_2 Electrodes: The Key Role of Charge Recombination for Solar Cell Performance

Imahori, H.; Kang, S.; Hayashi, H.; Haruta, M.; Kurata, H.; Isoda, S.; Canton, S. E.; Infahsaeng, Y.; Kathiravan, A.; Pascher, T.; Chábera, P.; Yartsev, A. P.; Sundström, V.

J. Phys. Chem. A **2011**, *115*, 3679-3690.

Chapter 3

Role of Binding Structures of Zn-Porphyrin on TiO_2 Surface in Dye-Sensitized Solar Cells: Systematic Investigation by Ultrafast Spectroscopy and Sum Frequency Generation

Kathiravan, A.; Hayashi, H.; Tong, Y.; Ye, S.; Infahsaeng, Y.; Chabera, P.; Pascher, T.; Yartsev, A.; Isoda, S.; Imahori, H.; Sundström, V.

To be submitted.

Chapter 4

Local Stoichiometry in Amorphous Supramolecular Composites Analyzed by Solid-State ^{13}C Nuclear Magnetic Resonance

Kaji, H.; Hayashi, H.; Yamada, T.; Fukuchi, M.; Fujimura, S.; Ueda, M.; Kang, S.; Umeyama, T.; Matano, Y.; Imahori, H.

Appl. Phys. Lett. **2011**, *98*, 113301-1–113301-3.

Chapter 5

Effects of Electrode Structures on Photoelectrochemical Properties of ZnO Electrodes Modified with Porphyrin-Fullerene Composite Layers with Intervening Fullerene Monolayer

Hayashi, H.; Kira, A.; Umeyama, T.; Matano, Y.; Charoensirithavorn, P.; Sagawa, T.;

Yoshikawa, S.; Tkachenko, N. V.; Lemmetyinen, H.; Imahori, H.
J. Phys. Chem. C **2009**, *113*, 10819-10828.

Chapter 6

Electron Transfer Cascade by Organic/Inorganic Ternary Composites of Porphyrin, Zinc Oxide Nanoparticle, and Reduced Graphene Oxide on Tin Oxide Electrode that Exhibits Efficient Photocurrent Generation
Hayashi, H.; Lightcap, I. V.; Tsujimoto, M.; Takano, M.; Umeyama, T.; Kamat, P. V.; Imahori, H.
J. Am. Chem. Soc. **2011**, *133*, 7684-7687.

Chapter 7

Segregated Donor–Acceptor Columns in Liquid Crystals That Exhibits Highly Efficient Ambipolar Charge Transport
Hayashi, H.; Nihashi, W.; Umeyama, T.; Matano, Y.; Seki, S.; Shimizu, Y.; Imahori, H.
J. Am. Chem. Soc. **2011**, *133*, 10736-10739.

Other Publications

Effects of Porphyrin Substituents on Film Structure and Photoelectrochemical Properties of Porphyrin/Fullerene Composite Clusters Electrophoretically Deposited on Nanostructured SnO_2 Electrodes
Imahori, H.; Ueda, M.; Kang, S.; Hayashi, H.; Kaji, H.; Seki, S.; Saeki, A.; Tagawa, S.; Umeyama, T.; Matano, Y.; Yoshida, K.; Isoda, S.; Shiro, M.; Tkachenko, N. V.; Lemmetyinen, H.
Chem. –Eur. J. **2007**, *13*, 10182-10193.

Light-Harvesting and Energy Transfer in Multiporphyrin-Modified CdSe Nanoparticles
Kang, S.; Yasuda, M.; Miyasaka, H.; Hayashi, H.; Umeyama, T.; Matano, Y.; Yoshida, K.; Isoda, S.; Imahori, H.
ChemSusChem **2008**, *1*, 254-261.

Fused Five-Membered Porphyrin for Dye-Sensitized Solar Cells
Hayashi, S.; Matsubara, Y.; Eu, S.; Hayashi, H.; Umeyama, T.; Matano, Y.; Imahori, H.
Chem. Lett. **2008**, *37*, 846-847.

Naphthyl-Fused π-Elongated Porphyrins for Dye-Sensitized TiO_2 Cells
Hayashi, S.; Tanaka, M.; Hayashi, H.; Eu, S.; Umeyama, T.; Matano, Y.; Araki, Y.; Imahori, H.
J. Phys. Chem. C **2008**, *112*, 15576-15585.

meso-3,5-Bis(trifluoromethyl)phenyl Substituted Expanded Porphyrins: Synthesis, Characterization, and Optical, Electrochemical, and Photophysical Properties
Kang, S.; Hayashi, H.; Umeyama, T.; Matano, Y.; Tkachenko, N. V.; Lemmetyinen, H.; Imahori, H.
Chem. Asian. J. **2008**, *3*, 2065-2074.

Oligothiophene Bearing 1-Hydroxy-1-oxodithieno[2,3-*b*:3',2'-*d*]phosphole as a Novel Anchoring Group for Dye-sensitized Solar Cells
Kira, A.; Shibano, Y.; Kang, S.; Hayashi, H.; Umeyama, T.; Matano, Y.; Imahori, H.
Chem. Lett. **2010**, *39*, 448-450.

Bisquinoxaline-Fused Porphyrins for Dye-Sensitized Solar Cells
Imahori, H.; Iijima, H.; Hayashi, H.; Toude, Y.; Umeyama, T.; Matano, Y.; Ito, S.
ChemSusChem **2011**, *4*, 797-805.

Effects of Fullerene Encapsulation on Structure and Photophysical Properties of Porphyrin-Linked Single-Walled Carbon Nanotubes
Umeyama, T.; Mihara, J.; Hayashi, H.; Kadota, N.; Chukharev, V.; Tkachenko, N. V.; Lemmetyinen, H.; Yoshida, K.; Isoda, S.; Imahori, H.
Chem. Commun. **2011**, *47*, 11781-11783.

Thermal Conversion of Precursor Soluble Polymer to Insoluble Low Bandgap Conjugated Polymers Containing Isothianaphthene Dimer Subunits
Umeyama, T.; Hirose, K.; Noda, K.; Matsushige, K.; Shishido, T.; Hayashi, H.; Matano, Y.; Ono, N.; Imahori, H.
J. Phys. Chem. C **2012**, *116*, 1256-1264.

Effects of Carbon-Metal-Carbon Linkages on the Optical, Photophysical, and Electrochemical Properties of Phosphametallacycle-Linked Coplanar Porphyrin Dimers

Matano, Y.; Matsumoto, K.; Hayashi, H.; Nakao, Y.; Kumpulainen, T.; Chukharev, V.; Tkachenko, N. V.; Lemmetyinen, H.; Shimizu, S.; Kobayashi, N.; Sakamaki, D.; Ito, A.; Tanaka, K.; Imahori, H.
J. Am. Chem. Soc. **2012**, *134*, 1825-1839.

Self-Assembled Porphyrins on Modified Zinc Oxide Nanorods: Development of Model Systems for Inorganic-Organic Semiconductor Interface Studies
Saarenpää, H.; Sariola-Leikas, E.; Perros, A. P.; Kontio, J. M.; Efimov, A.; Hayashi, H.; Lipsanen, H.; Imahori, H.; Lemmetyinen, H.; Tkachenko, V. N.
J. Phys. Chem. C **2012**, *116*, 2336-2343.

A Photoconductive, Thiphene-Fullerene Double-Cable Polymer, Nanorod Device
Imahori, H.; Kitaura, S.; Kira, A.; Hayashi, H.; Nishi, M.; Hirao, K.; Isoda, S.; Tsujimoto, M.; Takano, M.; Zhe, Z.; Miyato, Y.; Noda, K.; Matsushige, K.; Stranius, K.; Tkachenko, N. V.; Lemmetyinen, H.; Qin, L.; Hurst, S. J.; Mirkin, C. A.
J. Phys. Chem. Lett. **2012**, *3*, 478-481.

Reviews

Novel π Expanded Porphyrin for Dye-Sensitized Solar Cells
Imahori, H.; Hayashi, H.
Kagakukogyo **2009**, *60*, 33-37.

Research Development and Trend of Optoelectronics Materials for Bulk Heterojunction Solar Cells
Imahori, H.; Hayashi, H.
Display **2010**, *16*, 9-14.

Acknowledgment

The studies presented in this thesis have been carried out under the direction of Professor Hiroshi Imahori at the Department of Molecular Engineering, Graduate School of Engineering, Kyoto University, during the period of *2006 – 2012*.

The author would like to express my gratitude to Professor Hiroshi Imahori for his kind guidance, invaluable suggestions, and encouragement throughout this study. The author enjoyed the discussion with him every weekend and it helps his research proceed smoothly. The author is also deeply grateful to Professor Yoshihiro Matano and Assistant Professor Tomokazu Umeyama for their constant advice and helpful discussions during the course of this work.

The author is indebted to Professor Noboru Ono, Assistant Professor Tatsuya Murakami, Assistant Professor Kei Kurotobi, Assistant Professor Yuta Takano, Dr. Masanobu Tanaka, Dr. Simon Mathew, Dr. Yuki Shibano, Dr. Kohei Hosomizu, Dr. Seunghun Eu, Dr. Aiko Kira, Dr. Takashi Nakabuchi, Dr. Noriyasu Tezuka, and Dr. Abeda Sultana Touchy for their helpful suggestions and technical assistance. Special thanks go to Dr. Soonchul Kang for teaching me how the research works when the author started his Ph. D. in Imahori group.

The author would like to thank Professor Hironori Kaji (*Kyoto University*), Dr. Tomonori Yamada, Dr. Tatsuya Fukushima, Professor Seiji Isoda (*Kyoto University*), Dr. Masahiko Tsujimoto (*Kyoto University*), Professor Shu Seki (*Osaka University*), Professor Shen Ye (*Hokkaido University*), Dr. Yujin Tong (*Hokkaido University*), and Dr. Yo Shimizu (*AIST*) for their kind guidance and helpful comments.

The author also wishes to express his special gratitude to Professor Prashant V. Kamat at Radiation Laboratory, Department of Chemistry and Biochemistry, University of Notre Dame for his kind support and changing the author's perspective on researcher. Great thanks go to Dr. Alexsandra Wojcik, Mr. Ian Lightcap, Mr. Kevin Tvrdy, and Mr. Sean Murphy for their kind support, valuable suggestions and fruitful discussions in the author's stay in U.S.A. (September–November, *2009*).

The author also wishes to express his special gratitude to Professor Nikolai V. Tkachenko, Professor Helge Lemmetyinen, Dr. Vladimir Chukharev, Ms. Hanna Saarenpää, and Ms. Kati Stranius at Department of Chemistry and Bioengineering, Tampere University of Technology for their kind support, valuable suggestions, and fruitful discussions in the author's stay in

Finland (June–July, *2011*).

Great thanks go to Professor Villey Sundström, Prof. Arkady Yartsev, Dr. Arunkmar Kathiravan, Mr. Yingyot Infahsaeng at Department of Chemical Physics, Lund University for their kind support, valuable suggestions, and fruitful discussions in the author's stay in Sweden (July–August, *2011*).

The author acknowledges the Research Fellowship of Japan Society for the Promotion of Science for Young Scientists and 21th Century COE on Kyoto University Alliance for Chemistry for financial supports.

Thanks also go to the all members of the laboratory of Photoorganic Chemistry at Department of Molecular Engineering, Graduate School of Engineering, Kyoto University and the people who the author has come to know through my research for their help, valuable suggestions, and heartwarming friendship.

Finally, the author would like to thank heartily his father, mother, sister, grandfathers, and grandmothers for their encouragements and supports.

Hironobu Hayashi

Kyoto, Japan
2012